

A Thesis Submitted for the Degree of PhD at the University of Warwick

Permanent WRAP URL:

<http://wrap.warwick.ac.uk/166785>

Copyright and reuse:

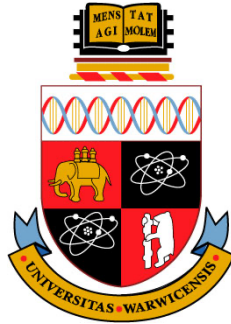
This thesis is made available online and is protected by original copyright.

Please scroll down to view the document itself.

Please refer to the repository record for this item for information to help you to cite it.

Our policy information is available from the repository home page.

For more information, please contact the WRAP Team at: wrap@warwick.ac.uk



Quantifying Iron in the Brain using Magnetic Resonance Imaging

by

Jierong Luo

**Submitted for the degree:
Doctor of Philosophy in Engineering**

**School of Engineering
The University of Warwick**

Jan 2022

Table of Contents

Acknowledgements	VII
Declaration	VIII
Publications.....	IX
Abstract.....	X
List of Figures	XIII
List of Tables	XVIII
List of Abbreviations	XX
Chapter 1: Introduction	1
1.1 Iron in the brain	4
1.1.1 Brain iron storage and ferritin	4
1.1.2 Brain iron homeostasis	5
1.1.3 Brain iron concentration	6
1.2 Alteration of brain iron level.....	7
1.2.1 Ageing	7
1.2.2 Pathological changes.....	9
1.3 Imaging brain iron using MRI	12
Chapter 2: MRI signals and pulse sequences.....	16
2.1 MRI signal.....	16
2.1.1 Spin	16
2.1.2 Free precession and Larmor frequency	17
2.1.3 Thermal equilibrium and Boltzmann distribution.....	17
2.1.4 Effect of RF pulses.....	18
2.1.5 Free induction decay (FID) and relaxation	18
2.1.6 MR signal detection	19
2.1.7 Spatial encoding, Fourier transform and image formation.....	20

2.2 MR pulse sequence	21
2.2.1 Spin echo.....	21
2.2.2 Gradient Echo	28
2.3 Magnetic susceptibility	28
2.3.1 Magnetisation mechanisms	29
2.3.2 Bulk susceptibility quantification using MRI	31
Chapter 3: Literature Review of quantitative MRI methods for measuring iron	33
3.1 R_2 , R_2^* relaxometry and R_2'	33
3.2 Field-dependent R_2 increase	35
3.3 SWI and QSM	35
3.4 Other phase-related MRI techniques.....	38
Chapter 4: Research methodology for the quantitative MRI.....	39
4.1 <i>In vitro</i> phantom MRI.....	39
4.2 <i>In vivo</i> human brain MRI	39
4.2.1 Iron estimation for <i>in vivo</i> human brain MRI	40
4.2.2 Group comparison using <i>in vivo</i> human brain MRI	41
4.3 MR imaging and reconstruction.....	41
4.4 Post-processing.....	42
4.4.1 Quantitative MRI parametric mapping	42
4.4.2 QSM framework.....	43
4.5 Image analysis.....	47
Chapter 5: Effective transverse relaxation rate, derived from dual-contrast fast-spin-echo (FSE) MRI, enables detection of hemisphere differences in iron level and function in Parkinson's disease and healthy brain	49
5.1 Introduction	49
5.2 Methods.....	51

5.2.1 PPMI subjects.....	51
5.2.2 Retrospective MR data selection	52
5.2.3 MR acquisition	52
5.2.4 DaTScan acquisition and calculation of Striatal Binding Ratio (SBR).....	52
5.2.5 Calculation of the effective transverse relaxation rate (effective R_2)	53
5.2.6 Segmentation.....	54
5.2.7 Estimation of the brain iron concentrations	55
5.2.8 Data processing and statistical analysis	56
5.3 Results.....	58
5.3.1 Subject information	58
5.3.2 Effective R_2 in various brain regions at baseline	59
5.3.3 Correlation of the effective R_2 with estimated iron concentration in the brain.....	60
5.3.4 Comparison of median effective R_2 values between groups	64
5.3.5 Relationship between the effective R_2 and SBR in the putamen and caudate	67
5.3.6 Longitudinal changes of the effective R_2 in various brain regions	72
5.4 Discussion	80
5.4.1 Effective R_2 is linearly proportional to the iron level across investigated brain regions, can be used as an alternative to conventional R_2	80
5.4.2 Effective R_2 can reveal the asymmetrical disease manifestation in PD brain hemispheres	82
5.4.3 Putaminal effective R_2 in PD corresponds to the local DaT dysfunction severity at early stage of PD	85
5.4.4 Effective R_2 measurement of individual brain region is limited in distinguishing HC and PD	85

5.4.5 Longitudinal change of effective R_2 is overall consistent with the age-dependent non-haemin iron accumulation in HC, but associated with pathological iron alternation and microstructural changes in PD	87
5.5 Conclusions	89
5.6 Acknowledgements.....	90
Chapter 6: Evaluation of QSM contrast and quantitative measurement of iron in phantoms and human brains on 3.0 T MRI: comparison with transverse relaxation.	91
6.1 Introduction	91
6.2 Methods.....	93
6.2.1 MR phantom	93
6.2.2 Healthy volunteers.....	94
6.2.3 MR acquisition	95
6.2.4 Image processing and analysis.....	97
6.2.5 Data analysis	101
6.3 Results.....	103
6.3.1 Susceptibility contrast in phantoms and human brains.....	103
6.3.2 Anatomical contrast of deep grey matter in proton density-, T_2 -weighted images and QSM	104
6.3.3 Correlation of the susceptibility with the Fe^{3+} concentration in phantoms	113
6.3.4 Correlation of the susceptibility with the prior-published iron concentration in healthy brains	116
6.3.5 Comparison of different quantitative MRI measures of brain iron	120
6.3.6 Reproducibility of quantitative susceptibility mapping	131
6.4 Discussion	132
6.4.1 QSM can enhance iron-induced anatomical contrast.....	132

6.4.2 QSM can faithfully measure the ferric iron concentration in agarose gel phantoms, with the linear correlation	133
6.4.3 <i>In vivo</i> brain susceptibility was linearly correlated with the putative iron concentration, and with the transverse relaxation rates (R_2^* , R_2 , effective R_2), but variations existed.....	134
6.4.4 Potential variation in <i>in vivo</i> quantitative MRI correlations may be reduced by using the putative iron concentration in healthy brains with age adjustment.....	137
6.4.5 Reproducibility of the susceptibility varies among subcortical nuclei ...	138
6.5 Conclusions	139
Chapter 7: Transverse relaxation rate R_2^* and quantitative susceptibility mapping (QSM) of $A\beta(1-42)$ and ferritin-bound iron in MR phantoms for 9.4 T preclinical MRI	141
7.1 Introduction	141
7.2 Method	143
7.2.1 Construction of the $A\beta(1-42)$ + ferritin-bound iron and control phantoms	143
7.2.2 Preparation for imaging the phantom in 9.4 T preclinical MRI system..	146
7.2.3 Hardware set up for 9.4 T preclinical MRI	147
7.2.4 MR acquisition	149
7.2.5 Image processing	151
7.2.6 Data analysis	160
7.3 Results.....	161
7.3.1 Assessment of QSM implementation for 9.4 T preclinical MRI	161
7.3.2 Quantitative R_2^* and susceptibility of the $A\beta(1-42)$ and ferritin-bound iron	172
7.3.3 Relationship between pixel-wise R_2^* and susceptibility in different phantoms.....	181

7.3.4 Correlation of R_2^* with the ferritin-bound iron level	185
7.3.5 Correlation of the susceptibility with the ferritin-bound iron level	187
7.4 Discussion	189
7.4.1 QSM of $A\beta(1-42)$ and ferritin-bound iron with 9.4 T small-animal MRI system.....	189
7.4.2 Correlation between R_2^* and susceptibility	190
7.4.3 R_2^* of $A\beta(1-42)$ and ferritin-bound iron level.....	191
7.4.4 Susceptibility of $A\beta(1-42)$ and ferritin-bound iron level	192
7.4.5 Effect of the mineral form and distribution of the iron, on UHF R_2^* and susceptibility MRI.....	194
7.4.6 Comparison with <i>in vivo</i> and <i>ex vivo</i> UHF MRI.....	196
7.5 Conclusions	196
Chapter 8: Conclusions and future work	198
References	201
Appendix A Empirical prediction of iron concentrations of brain regions by Hallgren and Sourander	i
Appendix B Effective R_2 measurements in reported PPMI subjects	ii
Appendix C DaT SBR results of reported PPMI subjects	xii
Appendix D Magnitude signal decays in 3D GRE, MESE and dual-contrast FSE sequences for 3.0 T clinical study at UHCW, Coventry	xv
Appendix E Agarose gel preparation, protein aggregation and gelation.....	xvi
Appendix F Pre-scan adjustments and shimming strategies for 9.4 T preclinical MRI	xxiii
Appendix G Assessment of QSM reconstruction on 9.4 T preclinical MRI.....	xxx
Appendix H Summary of linear regression analyses between R_2^* and ferritin levels, and between susceptibility and ferritin level in $A\beta$ +Ftn, Ftn and $A\beta$ phantoms.	xxxviii
Appendix I Ethical approval documentation.....	xxxix

Acknowledgements

Until the moment of writing, I could not find words that are enough to describe my appreciation and gratitude to everything and everyone that have helped me, not only to complete this work toward the degree but also to take the journey in this place as a person. I would like to thank my family from away, and my supervisor Joanna Collingwood, who support me, encourage me, and believe in me. And I would like to thank my friends, especially Surya Rajan, and Daniel Roth, who understand me and support me from near and far during the whole time.

I would like to thank all the scientists and colleagues from the University of Warwick, Jake Brooks, and others from the Trace Metal in Medicine research group; to Davide Piaggio and Elisa Baioni, as my housemates and friends and colleagues, and everyone from the Biomedical Engineering office, with whom I have worked closely and have talked about work and life.

I would also like to thank the scientists and colleagues from the University Hospital Coventry and Warwickshire, Sarah Wayte, Andrew Weedall, and Michael Diokono.

I would also like to thank many people that I have met and talked to and played volleyball together with, during the time being. Those are many, but especially Terry and Dot Monnington, Declan Perry, James Massey, Ronny Genieser, and Muinuddin Maharun. Without you, I would not have been able to go so far.

Thank you.

Declaration

This thesis is submitted to the University of Warwick in support of my application for the degree of Doctor of Philosophy. It has been composed by myself and has not been submitted in any previous application for any degree to this, or any other university.

The data acquisition for the 3.0 T MRI at the local NHS Trust hospital, University Hospital Coventry and Warwickshire (UHCW) were with the help of Dr. Sarah Wayte, MRI clinical scientist Andrew Weedall, and MRI research radiographer Michael Diokono, from the Radiology Physics Department, UHCW.

Publications

The following papers have arisen from work related to this thesis:

J. Luo, J. F. Collingwood. Magnetic resonance imaging evaluation of regional brain iron in Parkinson's disease and normal ageing: a cross-sectional and longitudinal study. Conference poster presentation. The 14th International Conference on Alzheimer' & Parkinson's Disease. 2019. Lisbon, Portugal.

J. Luo, J. Everett, J. Donnelly, F. Slade, N. Telling, J. Collingwood. Transverse relaxation rate R_2^* and quantitative susceptibility mapping of beta-amyloid and ferritin-bound iron with 9.4 T preclinical MRI. Oral presentation. The 17th International Conference on Alzheimer' & Parkinson's Disease. 2022. Barcelona, Spain.

The following manuscript is in submission to Journal of Neuroscience Methods:

J. Luo, J. F. Collingwood. Effective R_2 relaxation rate, derived from dual-contrast FSE MRI, enables detection of hemisphere differences in iron level and function in Parkinson's disease and healthy brain. In submission.

Abstract

As accumulating post-mortem evidence indicates the involvement of iron dyshomeostasis in neurodegeneration, the need to measure iron levels in the living human brain is more urgent than ever before. Magnetic resonance imaging (MRI) provides a non-invasive tool to detect brain iron in clinical and preclinical settings, by exploiting the magnetic properties of tissue iron using different pulse sequences. However, the question remains open, as to whether existing quantitative MRI techniques can be used as a robust technique to measure iron in a complex biological system like brains. Therefore, this PhD thesis seeks to extend this understanding by assessing existing techniques and developing original quantitative methods for improved iron measurement in clinical and preclinical MRI. After briefly revising the efforts that have been made in the literature to quantify brain iron using quantitative MRI, the original contribution of the PhD thesis is composed of three experiments:

The first project was to investigate whether the measurement derived from the 3.0 T dual-contrast fast-spin-echo (FSE) MRI, termed 'effective R_2 ' in this work, may be used as a quantitative MRI method, an alternative to the time-consuming conventional transverse relaxation rate (R_2) to evaluate the iron level in healthy (HC) and Parkinson's disease (PD) brains. Retrospective 3.0 T FSE *in vivo* MRI data from case-control HC and PD subjects were selected from the Parkinson's Progression Markers Initiative (PPMI) database, and the effective R_2 was calculated from exponential fitting of these data. Linear regression analysis was then performed between the effective R_2 and independently-estimated brain iron concentration (derived from the subject's age using the empirical age-dependent formulae reported by Hallgren and Sourander). To further investigate its potential clinical use, the effective R_2 was compared between groups, and linear correlation analysis was performed between the effective R_2 and the functional dopamine transporter (DaT) results. The findings of the project suggested a strong linear correlation between the effective R_2 and the estimated brain iron concentration, as well as a strong correlation between the putaminal effective R_2 and the DaT dysfunction in PD. Therefore, it can be concluded the effective R_2 may be used as a fast, quantitative

MRI method to aid the evaluation of iron and DaT functions with 3.0 T clinical MRI, as an alternative to conventional R_2 .

To exceed the constraints of R_2 and effective R_2 , in this subsequent research, the state-of-art quantitative susceptibility mapping (QSM) MRI technique was assessed for measuring iron concentration, at the local NHS Trust hospital. This project aimed to answer if a QSM method using nonlinear morphology enabled dipole inversion with L_1 -regularisation (nMEDI- L_1) can quantify iron in ferric iron (Fe^{3+}) phantoms and human brains accurately, using a local clinical 3.0 T MRI scanner. Using a 3D gradient-echo (GRE) sequence, the images of phantoms and healthy volunteers were obtained, and processed using the nMEDI- L_1 QSM method. The resulting susceptibility images of human brains were compared with routine clinical anatomical scans, and with the (effective) transverse relaxation rates (R_2 , R_2^* , effective R_2) mapping. Linear regression analysis was performed between the susceptibility measured in the phantom and the Fe^{3+} concentration, and between the brain susceptibility and the brain iron concentration estimated using Hallgren and Sourander's formulae. A very strong linear correlation was found between the susceptibility and the Fe^{3+} concentration in the phantom, with the Fe^{3+} -associated susceptibility increase that excellently matched the theoretical prediction of 1.30 ppb/ $\mu g \cdot g^{-1}$. As the results showed enhanced iron contrast in the QSM images, compared with the routine anatomical scan, a significant, strong, positive linear correlation between the susceptibility and the estimated iron concentration were also observed, with a smaller iron-associated susceptibility increase, compared to the phantom. The result is consistent with the literature, supporting the assertion that QSM may be used to measure iron concentration.

Lastly, to investigate the preclinical value of ultra-high-resolution QSM, the scope of QSM for measuring ferritin-bound iron and amyloid- β ($A\beta$), a misfolded protein strongly associated with Alzheimer's disease (AD) pathology, is studied *in vitro*, with 9.4 T preclinical MRI. Assessment of a selection of phase-processing techniques was performed, and automatic parameter optimisation techniques were tested for the nMEDI- L_1 , to optimise QSM for 9.4 T small-animal MRI system for the first time. R_2^*

and QSM of ferritin, A β , and A β +ferritin aggregates were measured *in vitro*, and linear regression analysis was performed between the ferritin (A β) level and the R₂^{*} and susceptibility. Linear regression analysis was also performed between pixel-wise R₂^{*} and susceptibility. An optimal QSM pipeline was devised after assessments. The results show ferritin-associated R₂ and susceptibility increase, which is particularly significant in A β +ferritin aggregates, showing in detail how QSM offers scope as a sensitive tool to detect iron-laden A β aggregates at ultra-high-field MRI.

List of Figures

Chapter 2:

Fig. 2.1 Effect of RF pulse, T_1 recovery and T_2 decay.

Fig. 2.2 An example 2D Cartesian k-space.

Fig. 2.3 SE pulse sequence.

Fig. 2.4 Multi-echo spin-echo (MESE) pulse sequence.

Fig. 2.5 An example 2D Cartesian segmented k-space.

Chapter 4:

Fig. 4.1 Image post-processing pipeline with QSM.

Chapter 5:

Fig. 5.1 Effective R_2 values measured in various brain regions.

Fig. 5.2 Example segmentation of *in vivo* human brain MRI obtained from PPMI.

Fig. 5.3 Linear correlation of the effective R_2 with the estimated iron concentration in HC.

Fig. 5.4 Observed effective R_2 (markers) in comparison with the predicted iron concentrations during normal ageing (regression lines) in HC (top), PD contralateral (middle) and ipsilateral (bottom) hemispheres.

Fig. 5.5 Effective R_2 measured in globus pallidus (left), putamen (middle), and substantia nigra (right) at 0, 12, 24, 48 months.

Fig. 5.6 Effective R_2 measured in red nucleus and caudate nucleus at 0, 12, 24, 48 months.

Fig. 5.7 Correlation between the effective R_2 and DaT SBR in the putamen and caudate at baseline.

Fig. 5.8 Correlation between the hemispheric difference of the effective R_2 and DaT SBR in the putamen (left) and caudate (right) at baseline.

Fig. 5.9 Relationship between the effective R_2 and DaT SBR (upper) and between their hemispheric differences (lower) of PD in the putamen (left) and caudate (right).

Fig. 5.10 Longitudinal changes of the effective R_2 within caudate nucleus.

Fig. 5.11 Longitudinal changes of the effective R_2 within putamen.

Fig. 5.12 Longitudinal changes of the effective R_2 within substantia nigra.

Fig. 5.13 Longitudinal changes of the effective R_2 within red nucleus.

Fig. 5.14 Longitudinal changes of the effective R_2 within globus pallidus.

Fig. 5.15 Effective R_2 percentage change in various brain regions after 12, 24, 48 months from baseline.

Chapter 6:

Fig. 6.1 Chelated Fe^{3+} MR phantom construction.

Fig. 6.2 Example segmentation of *in vivo* human brain MRI on QSM.

Fig. 6.3 Axial view of the magnitude (left), RDF (middle) and susceptibility map (right) of the iron phantom.

Fig. 6.4 Axial view of the magnitude (left), RDF (middle) and susceptibility map (right) of an example human brain (male, age = 24 yrs).

Fig. 6.5 Contrast comparison between proton density-weighted, T_2 -weighted and susceptibility images in the basal ganglia.

Fig. 6.6 Contrast comparison between proton density-weighted, T_2 -weighted and susceptibility images in the midbrain.

Fig. 6.7 Demonstration of the location of the horizontal line profiles of the midbrain on the inferior-middle level.

Fig. 6.8 The horizontal line profiles of the signal intensity measured on proton density-weighted, T_2 -weighted images and the susceptibility map of the midbrain on the inferior-middle level.

Fig. 6.9 Demonstration of the location of the crossline profiles of the midbrain on the middle level.

Fig. 6.10 The crossline profiles of the signal intensity measured on proton density-weighted, T_2 -weighted images and the susceptibility map of the midbrain on the middle level.

Fig. 6.11 Regression analysis of the observed susceptibility with Fe^{3+} -EDTA.

Fig. 6.12 Regression analysis of the observed susceptibility with Fe^{3+} -NTA.

Fig. 6.13 Linear regression (A) and residual (B) analyses between susceptibility and estimated iron concentration in caudate nucleus (CN), globus pallidus (GP), putamen (PUT), red nucleus (RN), and substantia nigra (SN).

Fig. 6.14 Linear regression (A) and residual (B) analyses between susceptibility and estimated iron concentration in caudate nucleus (CN), globus pallidus (GP), and putamen (PUT).

Fig. 6.15 Linear regression analysis of the measured susceptibility in selected brain regions.

Fig. 6.16 Relationship between the measured susceptibility and the age against expected iron concentration in different brain regions.

Fig. 6.17 Reconstructed brain images with QSM, R_2^* , R_2 , and effective R_2 .

Fig. 6.18 Paramagnetic and diamagnetic structures in the susceptibility map (left) and the R_2^* map (right) of the brain of a subject.

Fig. 6.19 Comparison between quantitative MRI measurements within ROIs.

Fig. 6.20 Comparison of the prior-published average iron concentrations in different brain regions.

Fig. 6.21 Comparison of quantitative MRI measurements with reported iron concentrations.

Chapter 7:

Fig. 7.1 Peptide suspensions (A) and $A\beta(1-42)$ and ferritin samples after 100 hrs incubation (B).

Fig. 7.2 An example of the gel assembly MR phantoms for the small animal coil.

Fig. 7.3 Imaging container and sample installation.

Fig. 7.4 UHF MRI hardware set-up.

Fig. 7.5 Example examination of the MR signal behaviour within PV6.

Fig. 7.6 Example reconstructed magnitude (top) and phase (bottom) images of the Ftn phantom acquired by the multi-echo 3D GRE pulse sequence.

Fig. 7.7 Example temporal unwrapping of Ftn phantom.

Fig. 7.8 Susceptibility images of phantom $A\beta$ +Ftn (top row), Ftn (middle row) and $A\beta$ (bottom row) with varying regularisation parameter λ .

Fig. 7.9 Example ROIs (magenta circles) on the phantom for 9.4 T preclinical MRI.

Fig. 7.10 Spatially unwrapped phase of Ftn (top), A β +Ftn (middle) and A β (bottom) phantoms using the Laplacian (left) and region-grow (right) unwrapping.

Fig. 7.11 Background field removal of A β +Ftn phantom using PDF, LBV and SHARP techniques.

Fig. 7.12 RDFs (top) and background fields (bottom) of the A β +Ftn phantom calculated using LBV (left) and PDF (middle), and the comparison (right).

Fig. 7.13 RDFs of A β +Ftn phantom calculated by SHARP with varying SMV filter radius.

Fig. 7.14 RDFs of A β +Ftn phantom calculated by SHARP with varying truncation value.

Fig. 7.15 RDFs of the phantoms generated using LBV.

Fig. 7.16 λ values calculated using automatic optimisation methods for A β +Ftn (A), Ftn (B), and A β (C) phantoms.

Fig. 7.17 Susceptibility images of each phantom generated with the λ optimised using different methods.

Fig. 7.18 Susceptibility measurements of 'A β +Ftn 0' sample with varying λ .

Fig. 7.19 Average susceptibility measured in the samples of A β +Ftn (top), Ftn (middle) and A β (bottom) phantoms with varying λ .

Fig. 7.20 The distribution of R_2^* measured within the ROIs of A β +Ftn phantom.

Fig. 7.21 The distribution of R_2^* measured within the ROIs of Ftn phantom.

Fig. 7.22 The distribution of R_2^* measured within the ROIs of A β phantom.

Fig. 7.23 The distribution of susceptibility measured within the ROIs of A β +Ftn phantom.

Fig. 7.24 The distribution of susceptibility measured within the ROIs of Ftn phantom.

Fig. 7.25 The distribution of susceptibility measured within the ROIs of A β phantom.

Fig. 7.26 Distributions of R_2^* (left) and susceptibility (right) of samples in each phantom.

Fig. 7.27 Correlation between pixel-wise R_2^* and susceptibility (A), with the corresponding distribution of each sample (B, C) within A β +Ftn phantom.

Fig. 7.28 Correlation between pixel-wise R_2^* and susceptibility (A), with the corresponding distribution of each sample (B, C) within Ftn phantom.

Fig. 7.29 Correlation between pixel-wise R_2^* and susceptibility (A), with the corresponding distribution of each sample (B, C) within A β phantom.

Fig. 7.30 Linear regression analysis of the ferritin ($A\beta$) concentration with R_2^* measured in $A\beta$ +Ftn (A), Ftn (B), and $A\beta$ (C) phantoms, and the comparison of the correlations (D).

Fig. 7.31 Linear regression analysis of the ferritin ($A\beta$) concentration with the susceptibility measured in $A\beta$ +Ftn (A), Ftn (B), and $A\beta$ (C) phantoms.

List of Tables

Chapter 1:

Table 1.1 Post-mortem iron concentrations within unfixed healthy brains from selected prior-reported studies.

Chapter 4:

Table 4.1 Contrasts of selected brain regions on different MR images.

Chapter 5:

Table 5.1 Subject information at baseline.

Table 5.2 Effective R_2 in different brain regions at baseline in comparison with the prior-published brain iron concentration.

Table 5.3 Comparison of effective R_2 between different brain regions at baseline.

Table 5.4 Summary of the regression analysis between effective R_2 values and estimated iron concentration in different groups.

Table 5.5 Comparison of the effective R_2 with the DaTScan results of subjects at baseline.

Table 5.6 Median effective R_2 percentage change (%) in the various brain regions.

Chapter 6:

Table 6.1 Summary of the regression analysis between susceptibility and iron concentration in phantom.

Table 6.2 Summary of the regression analysis between susceptibility and iron concentration in various brain regions.

Table 6.3 Comparison of the prior-published iron concentrations with quantitative MRI measurements within ROIs.

Table 6.4 Summary of the susceptibility reproducibility in ROIs.

Chapter 7:

Table 7.1 Summary of final 2 % w/v agarose-protein gel samples.

Table 7.2 Summary of R_2^* and susceptibility measurements of phantoms.

List of Abbreviations

1D	one-dimensional
^1H	hydrogen proton
2D	two-dimensional
3D	three-dimensional
AAS	atomic absorption spectroscopy
AD	Alzheimer's disease
ADC	analogue-to-digital converter
ADNI	Alzheimer's Disease Neuroimaging Initiative
ALS	amyotrophic lateral sclerosis
ANOVA	analysis of variance
APP	amyloid precursor proteins
ARLO	auto-regression on linear operations
ASSET	array coil spatial sensitivity encoding
ATP	adenosine triphosphate
A β	amyloid- β
A β (1-42)	amyloid- β (1-42)
B $_0$	external magnetic field
B $_1$	RF pulse magnitude
BBB	blood-brain barrier
BW	bandwidth
CG	conjugate gradient
cgs	centimetre, gram, second
CN	caudate nucleus
CNR	contrast-to-noise ratio
CNS	central nervous system
CP	Carr-Purcell
CPMG	Carr-Purcell-Meiboom-Gill
cryo-	cryogenic
DaT	dopamine transporter

DaTScan	functional SPECT imaging of striatal dopamine transporters
DMT1	divalent iron transporter 1
DWR	dry-to-wet ratio
EDTA	ethylenediaminetetraacetic acid
effective R_2	New term, defined in Chapter 5, effective transverse relaxation derived from dual-echo FSE MRI
ESP	inter echo time, echo spacing
ETL	echo train length
EVT	enhanced variable temperature
FA	flip angle
FDM	frequency difference mapping
FDRI	field-dependent R_2 increase
FE	frequency encoding
Fe^{2+}	ferrous iron
Fe^{3+}	ferric iron
FID	free induction decay
FLASH	fast low angle shot
FOV	field of view
FSE	fast-spin-echo
FT	Fourier transform
Ftn	ferritin
G	external magnetic field gradient
GAAS	graphite furnace atomic absorption spectroscopy
GM	grey matter
GP	globus pallidus
GRE	gradient echo
H	height
H-ferritin	ferritin heavy-chain subunit
H&Y	Hoehn and Yahr
HC	healthy volunteer/subject/control
HCl	hydrochloric acid

HD	Huntington's disease
HEIDI	homogeneity enabled incremental dipole inversion
ICP-MS	inductively coupled plasma mass spectrometry
ID	inner diameter
IEP	inter echo time, inter echo spacing
IFT	inverse Fourier transform
IRE	iron-responsive element
IRP	iron-regulatory protein
ISF	interstitial fluid
KH	Krebs-Henseleit
k_x, k_y, k_z	x, y, z axes in k-space
L-ferritin	ferritin light-chain subunit
LB	Lewy body
LBV	Laplacian boundary value
LF	loading factor
LIC	liver iron concentration
LIP	labile iron pool
LSQR	the least-squares
M_0	net magnetization vector
MCI	mild cognitive impairment
MEDI	morphology enabled dipole inversion
MEDI+0	morphology enabled dipole inversion with zero-susceptibility reference
MESE	multi-echo spin-echo
MFC	magnetic field correction
MoCA	Montreal cognitive assessment
MR	magnetic resonance
MRI	magnetic resonance imaging
MRM	magnetic resonance microscopy
mRNA	messenger ribonucleic acid
MS	multiple sclerosis

MSA	multiple system atrophy
MT	magnetisation transfer
MWF	myelin water fraction
N _A	number of averages
NAA	neutron activation analysis
NaOH	sodium hydroxide
NBIA	neurodegeneration with brain iron accumulation
NEX	number of excitations
NFT	neurofibrillary tangle
nMEDI-L ₁	nonlinear morphology enabled dipole inversion with L ₁ -regularisation
NMR	nuclear magnetic resonance
N _{PE}	number of phase encoding steps
NTA	nitrilotriacetic acid
O ₂	oxygen
OASIS	open access series of imaging study
OD	outer diameter
PD	Parkinson's disease
PDc	PD contralateral hemisphere
PDE	partial differential equation
PDF	projection onto dipole fields
PDi	PD ipsilateral hemisphere
PE	phase encoding
PE	polystyrene
PET	positron emission tomography
PIPES	piperazine-N,N'-bis(2-ethanesulfonic acid)
PIXE	particle-induced X-ray emission
PP	polypropylene
ppb	part per billion
ppm	part per million
PPMI	Parkinson's Progression Markers Initiative

PrP	prion protein
PS	polystyrene
PTFE	polytetrafluoroethylene
PUT	putamen
PV6	Paravision 6.0.1
QSM	quantitative susceptibility mapping
R_1	longitudinal relaxation rate
R_2	transverse relaxation rate
R_2'	transverse relaxation rate by local field inhomogeneity
R_2^*	transverse relaxation rate with field inhomogeneity
RARE	rapid acquisition with relaxation enhancement
RDF	relative difference field
RF	radiofrequency
RMSE	root mean squares errors
RN	red nucleus
ROI	region of interest
SAR	specific absorption rate
SBR	striatal binding ratio
SDK	software development kit
SE	spin-echo
SENSE	sensitivity encoding
SHARP	sophisticated harmonics artifact reduction for phase data
SLR	Shinnar–Le Roux
SMV	spherical mean value
SN	substantia nigra
SNR	signal-to-noise ratio
SOD1	superoxide dismutase 1
SPECT	single-photon emission computed tomography
SSE	sum of squared errors
SVD	singular value decomposition

SWAN	susceptibility weighted angiography
SWI	susceptibility-weighted imaging
T ₁	longitudinal relaxation time
T ₂	transverse relaxation time
T ₂ [*]	transverse relaxation time with field inhomogeneity
TDA-43	TAR DNA binding protein 43
T _E	echo time
TEM	transmission electron microscopy
TKD	truncated k-space division
T _R	repetition time
TSE	turbo-spin-echo
UHCW	University Hospital Coventry and Warwickshire
UHF	ultra-high-field
UPDRS	unified Parkinson's disease rating scale
UPSIT	University of Pennsylvania smell identification test
UTR	untranslated region
WM	white matter
ww	wet weight
XRF	X-ray fluorescence
α-syn	α-synuclein
λ	regularisation parameter
χ	susceptibility

Chapter 1: Introduction

Iron is the most abundant transition metal in the body, and its homeostasis is important for maintaining the basic functions of the organism [1, 2]. As a component of haemoglobin, iron is essential for oxygen transport by combining and releasing oxygen molecules into the circulatory system via redox reactions. It also participates in the synthesis of adenosine triphosphate (ATP) and energy generation in cytochromes, in the forms of cytochrome oxidases and iron-sulphur complexes [3]. In the brain, iron takes part in oxygen transportation, myelin and neurotransmitter biosynthesis, oxidative phosphorylation, and nitric oxide metabolism as an essential cofactor [4]. Therefore, iron homeostasis and the involvement of iron dysregulation in the neurodegenerative diseases' pathologies [5, 6], have drawn great interest from scientists and physicians.

Several analytical tools have historically been developed to investigate the chemical forms, magnetic properties, physiological and pathological distribution, and dynamic changes of iron in human brains and tissue [7-11]. These techniques rely on analysing post-mortem specimens, or biopsies from living patients, which are invasive and particularly impractical for diagnosis of brain disorders [12]. Exploiting the magnetic properties of tissue iron under an external magnetic field, magnetic resonance imaging (MRI) has been used for imaging and detecting iron in the human brains and tissues [13, 14], as a non-invasive technique in the clinical and preclinical settings. By applying different magnetic resonance (MR) pulse sequences [15, 16], MRI can demonstrate a variety of contrasts within the tissue, and therefore has great versatility in neuroimaging. As MRI has become a routine clinical tool for whole-brain imaging, it is also used as a useful preclinical technique for small-animal, specimens, and molecular imaging. At the time of writing, however, due to the complexity of biological systems, the debate remains active on whether the quantitative MRI method can be used as a reliable and reproducible approach to measuring the iron content in healthy and diseased brains.

Guided by this question, this PhD project, therefore, seeks to extend the understanding of brain iron quantification using quantitative MRI methods, in the typical clinical and preclinical settings. The aim of this work is to develop and assess novel MRI techniques and applications for measuring iron content in the brain (*in vivo*) or in the comparable *in-vitro* system, based on the currently viable clinical or preclinical MRI systems; also to identify the scope of these techniques, to quantify iron species in the complex biological system, the brain.

Hence, the PhD project is addressed from both theoretical (Chapter 2-4) and experimental (Chapter 5-7) perspectives, as presented in this thesis. In '*Chapter 1: Introduction*', the background is given to the iron homeostasis in the healthy brain, and brain with neurodegenerative diseases, *i.e.*, Parkinson's disease (PD) and Alzheimer's disease (AD), followed by a brief introduction to the relevant applications of iron contrast in MRI. In '*Chapter 2: MRI signals and pulse sequences*', the signal formation, detection, and the MR pulse sequences generally related to the iron contrast and quantification are examined. A thorough literature review of quantitative MRI methods for measuring tissue iron is given in *Chapter 3*, including the transverse relaxation rates (R_2 , R_2^* , and R_2'), Field-Dependent R_2 Increase (FDRI), Susceptibility-Weighted Imaging (SWI) and Quantitative Susceptibility Mapping (QSM) and other phase-related MRI techniques. Then '*Chapter 4: Research methodology for the quantitative MRI*' provides the general principle and justification of the quantitative MRI study design, and an overview of the research methodology for the following experiment chapters (Chapter 5-7).

In '*Chapter 5: Effective transverse relaxation rate, derived from dual-contrast fast-spin-echo (FSE) MRI, enables detection of hemisphere differences in iron level and function in PD and healthy brain*', the method of generating a quantitative MRI measurement, which we term 'effective R_2 ', is proposed. Utilising FSE MRI, which is commonly limited to anatomical applications, the method of calculating the quantitative effective R_2 is demonstrated and examined, using retrospective 3.0 T dual-contrast FSE data from the cohort study Parkinson's Progression Markers Initiative (PPMI). The effective R_2 enables a fast approach for the quantitative MRI

analysis, as an alternative to time-consuming conventional R_2 relaxometry. It is demonstrated in this work, for the first time, that the effective R_2 at 3.0 T can indicate the asymmetrical pathological changes of brain tissue caused by PD progression.

In '*Chapter 6: Evaluation of QSM contrast and quantitative measurement of iron in phantoms and human brains on 3.0 T MRI: comparison with transverse relaxation*', the state-of-the-art MRI technique, QSM, is established on the 3.0 T clinical MR scanner at the local NHS hospital, the University Hospital Coventry and Warwickshire (UHCW), Coventry, United Kingdom. In this study, an MR acquisition protocol, and an image post-processing pipeline using nonlinear morphology enabled dipole inversion with L_1 -regularisation (nMEDI- L_1) [17-19] QSM are successfully set up and tested for susceptibility contrast. The QSM method for iron quantification was compared with R_2 , R_2^* , and effective R_2 , and validated using in-house built iron-containing MR phantoms, and in healthy, living human brains.

In the last stage of this research project, the QSM technique is investigated in-depth with preclinical ultra-high-field (UHF) MRI, as presented in '*Chapter 7: Transverse relaxation rate R_2^* and quantitative susceptibility mapping (QSM) of amyloid- β (1-42) and ferritin-bound iron in MR phantoms for 9.4 T preclinical MRI*'. In this study, a comprehensive assessment and comparison of QSM phase processing methods on 9.4 T UHF small-animal MRI system, is established for the first time. Subsequently, with ultra-high resolution, the quantitative R_2^* and optimised QSM of the ferritin-bound iron and amyloid- β (1-42) (*i.e.*, $A\beta$ (1-42), the main component of the amyloid plaques observed in AD neuropathology), is performed *in vitro*. Moreover, by demonstrating the different quantitative correlation of the susceptibility and R_2^* with the ferritin iron level, in the presence and absence of $A\beta$ (1-42), the susceptibility and R_2^* are found to be sensitive to the mineral form and spatial distribution of the iron content, in addition to the concentration. These new results provide valuable information for wider research concerning $A\beta$ -associated pathologies and neurodegenerative diseases, to advance the accurate interpretation of R_2^* and QSM observations *in vivo* and *ex vivo*.

Finally, the findings of this PhD project are summarised alongside key conclusions in the last chapter '*Chapter 8: Conclusions and future work*', where the limitations of the study are discussed, and recommendations are made for future research.

1.1 Iron in the brain

In biological systems, the majority of iron is found in haemoglobin in the blood, involved in oxygen transportation and enzyme reactions [20]. Non-haemin iron, which was first found by Zaleski [21], accounts for about one-third of the total iron in the human body. In the human brain, iron ions are mostly conjugated with other molecules or stored in proteins in the ferric form (Fe^{3+}), which is chemically stable. Excessive unbound ferrous iron (Fe^{2+}) ions are toxic to the tissue, unselectively, because the highly reactive ferrous iron can take part in the Fenton reaction, which generates free radicals and causes oxidative stress [22].

1.1.1 Brain iron storage and ferritin

In healthy brains, the non-haemin iron is mainly stored in ferritin, in the form of 2- or 6-line ferrihydrite [22-25]. With a 2 nm-thick, ~12 nm-diameter spherical protein shell, every ferritin molecule has the capacity to store up to 4500 iron ions [22, 26, 27]. It regulates iron ions by oxidising excessive Fe^{2+} into Fe^{3+} via biomineralization, at its ferroxidase centre within the 8 nm-diameter internal cavity [24, 28, 29]. In mammals, ferritin consists of two types of subunits, defined by the difference in the peptide chains, the heavy chain (H-ferritin) and the light chain (L-ferritin). The functions of H- and L-ferritin are distinctive, and the ratio of the two subunits within the ferritin appears to be tissue-specific and age-dependent, where H-ferritin oxidises Fe^{2+} into Fe^{3+} while the L-ferritin subunit facilitates the formation of the ferritin's ferrihydrite (in Fe^{3+} form) core via nucleation [24, 26, 27]. As the primary protein for iron storage, ferritin is prevalent in the intracellular environment, sequestering excess iron ions in biological systems [24]. In serum, ferritin levels may be used as a measure of body iron stores, and increased serum ferritin can indicate inflammation [2]. In the brain, high ferritin concentrations have been found in oligodendrocytes, microglia, neurons, and some astrocytes [21, 30, 31]. The exception was found in dopaminergic neurons in nigrosome 1 and 3 within the

substantia nigra and noradrenergic neurons within the locus caeruleus, where most of the iron deposits were found to be stored in the neuromelanin [32]. Often considered as a by-product of ferritin, haemosiderin is observed in pathological iron overload, containing iron deposits that were reported to be in a form similar to ferrihydrite or wüstite [33, 34]. In addition to those iron storage complexes, a very small amount of iron is bound to transferrin, the primary iron transporting protein [35].

1.1.2 Brain iron homeostasis

The iron transportation across the blood-brain barrier (BBB) involves uptake and release of iron (Fe^{3+}) by transferrin into the labile iron pool (LIP), through the capillary endothelial cells [5]. The intracellular iron (Fe^{2+}) can then be exported into the interstitial fluid (ISF) by ferroportin. In the ISF, Fe^{2+} can then be oxidised into Fe^{3+} by the ceruloplasmin secreted from primary pericytes and astrocytes, or via transmembrane ceruloplasmin or hephaestin [4, 36]. At the cellular level, binding to transferrin, iron (Fe^{3+}) can be imported, in the form of diferric transferrin, into the intracellular environment via receptor-mediated endocytosis [5, 37]. The release of iron (Fe^{2+}) from the endosome into the cytoplasmic LIP occurs via divalent iron transporter 1 (DMT1), after the reduction of Fe^{3+} to Fe^{2+} by STEAP metalloreductases [38]. Then the iron ions (Fe^{2+}) can be utilised by proteins in the cytosol, but mostly by mitochondria; excessive iron may be stored in ferritin (or haemosiderin), or be exported via ferroportin [2, 4, 5]. Cellular iron homeostasis is regulated by the iron regulatory protein (IRP)/iron-responsive element (IRE) system [2]. IREs are located at the untranslated regions (UTRs) of the messenger ribonucleic acids (mRNAs) that encode proteins related to the iron metabolism [39, 40]. The binding of IRP to the IRE on 3'-UTRs (*e.g.*, transferrin receptor) can stabilise the mRNA and up-regulate protein translation, while binding to the 5'-UTRs (*e.g.*, ferritin, ferroportin) causes the translational repression and down-regulate the protein expression [5]. As the binding affinity of IRP to IRE is sensitive to the iron level, the IRP/IRE system could elegantly modulate the expression of iron-regulating proteins and maintain the intracellular iron level. At the systemic level, iron homeostasis also involves hepcidin,

released by hepatocytes, and macrophages, to modulate iron export and recycling [2].

1.1.3 Brain iron concentration

Hosting intensive oxidative metabolism activities, the central nervous system (CNS) maintains an overall high iron concentration with brain region-specific distributions [5, 22, 29, 37, 41]. The heterogeneous iron distribution was first illustrated post-mortem by Perls' Prussian blue staining [11, 13, 42], and confirmed by other analytical techniques years later. The highest iron concentration is found in the basal ganglia nuclei (globus pallidus [42-44], caudate [7, 43, 44], putamen [11, 43, 44]), the deep grey matter (GM) nuclei associated with motor function, cognition and learning [45]. In contrast, the iron concentration was reported to be lower in the cortex [10, 13, 46]. In the midbrain, a high level of iron concentration is found in the red nucleus and substantia nigra [44, 47]. Compared with the iron level of the GM, the iron analysis of white matter (WM) shows controversial results between reports of Perls' staining [48] and analytical assay [7, 9, 10, 43, 44, 49-51], and the latter reveals comparable WM iron levels to the cortex GM.

As a landmark work quantifying brain iron concentration, Hallgren and Sourander [11] measured the non-haemin iron from 81 unfixed, post-mortem brains using the orthophenanthroline method, after iron extraction from homogenised tissue samples by acid treatment. Studies that employed comparable methods also include the post-mortem iron concentration measurement in the brain carried out by Sofic *et al.* [47], in which the total iron, Fe^{2+} and Fe^{3+} were determined respectively using a modified ferrozine-based spectrophotometric method. These measurements of various brain regions are summarised in Table 1.1. With other analytical techniques, studies were carried out to measure the brain iron concentration in post-mortem tissue, using techniques including atomic absorption spectroscopy (AAS) [7, 10, 44, 49, 50], inductively coupled plasma mass spectrometry (ICP-MS) [9, 43, 51], neutron activation analysis (NAA) [8], and graphite furnace atomic absorption spectroscopy (GAAS) [52]. Recently, X-ray fluorescence (XRF) [53, 54], and particle-induced X-ray emission (PIXE) [55-57] were also used to investigate the spatial distribution of iron

content in post-mortem brain specimens. Although a somewhat large variation of the absolute iron concentrations presents between these post-mortem studies [46], the relative iron concentrations between the brain regions within each study is mostly consistent [7, 9, 10, 43, 44, 49-52].

1.2 Alteration of brain iron level

Iron in the human brain experiences dynamic changes throughout the lifetime and with the physiological condition of the biological system. Iron accumulation in brain regions has been observed in normal ageing [10, 11, 46]. At the same time, the pathological changes in iron levels, and the disruption of iron homeostasis, have also been associated with various neurodegenerative diseases [52, 58-62].

1.2.1 Ageing

In the literature concerning post-mortem brain iron measurements, the largest cohort continues to be the 81 unfixed human brains studied by Hallgren and Sourander [11] in 1958, at the time of writing. In this historical work, the concentration of non-haemin iron and its age-dependent accumulation in 11 brain regions was reported. Chen *et al.* [7] later investigated 9 unfixed frozen brains from subjects aged between 23 yrs and 83 yrs, using AAS, and reported a similar increasing trend of iron concentrations in multiple brain regions. In recent decades, an age-related increase of iron and ferritin concentration in the substantia nigra was reported by Zecca *et al.* [8], where a continuous increase of neuromelanin over the whole lifespan was observed. A recent post-mortem study on a large number of unfixed human brains was carried out by Ramos and colleagues [10] in 2014. Using AAS, the authors [10] measured the iron levels of 42 adult brains with the age ranging from 53 to 101 yrs. Fourteen brain regions were assessed, and a general age-related iron accumulation was found, with the most significant age-dependent increase in the basal ganglia. Concerning the brain regions of interest in this PhD thesis, Table 1.1 summarises the post-mortem iron concentrations within unfixed healthy brains from selected prior-reported studies [11, 47, 63].

Table 1.1 Post-mortem iron concentrations within unfixed healthy brains from selected prior-reported studies.

Iron concentration ($\mu\text{g/g}$ wet weight) in mean \pm standard deviation (number of measurements)											Tissue	Age (yrs)	Study
Globus pallidus	Red nucleus	Substantia nigra	Putamen	Dentate nucleus	Caudate nucleus	Thalamus	Cerebellar cortex	Frontal cortex	Hippocampus	Frontal white			
213.0 \pm 34.9 (55)	194.8 \pm 68.6 (44)	184.6 \pm 65.2 (52)	133.2 \pm 34.3 (56)	103.5 \pm 48.6 (45)	92.8 \pm 21.4 (58)	47.6 \pm 11.6 (52)	33.5 \pm 8.7 (53)	29.2 \pm 4.1 (58)		42.4 \pm 8.8 (59)	Unfixed	30-100	[11]
81 \pm 18 Fe ²⁺ : 27 \pm 6.3 Fe ³⁺ : 53 \pm 12 (6)		48 \pm 8.2 Fe ²⁺ : 32 \pm 7.0 Fe ³⁺ : 16 \pm 4.2 (8)	96 \pm 19 Fe ²⁺ : 65 \pm 14 Fe ³⁺ : 31 \pm 5.6 (8)						24 \pm 3.3 Fe ²⁺ : 10 \pm 0.8 Fe ³⁺ : 15 \pm 2.7 (6)		Frozen	71.3 \pm 12.5 (51-91)	[47]
42.3 (16) YC: 55.3 (8) EC: 29.7 (8)		50.2 (16) YC: 36.7 (8) EC: 60.7 (8)	41.6 (16) YC: 33.8 (8) EC: † (8)		25 (16) YC: 19.4 (8) EC: 29.1 (8)			10.7 (16) YC: 9.8 (8) EC: 11.4 (8)			Frozen	61 \pm 18.4 (27-88)	[63]†

† $\mu\text{g Fe/g ww}$ tissue was calculated by multiplying iron/protein and protein/ww tissue, the total value was pooled average from younger controls (YC, age below 65 yrs) and elderly controls (EC).

In measurements on formalin-fixed tissues obtained from 13 healthy brains, Krebs *et al.* [9] investigated the concentration of trace metals, including copper, iron, magnesium, and manganese of various brain regions using ICP-MS, but no age-dependency of iron concentration in the brain regions was found. Although a recent study suggested that a 5-month formalin fixation had negligible effect on the concentration of magnetic carriers in brain tissue [64], continued concerns about the impact of chemical fixation on metal ion distribution and concentration [65-69], mean that unfixed tissue samples are considered a more reliable source of information.

1.2.2 Pathological changes

Pathological alterations of iron content in particular brain regions have been reported in neural system degeneration, such as in Alzheimer's disease (AD), Parkinson's disease (PD), Huntington's disease (HD), multiple sclerosis (MS), multiple system atrophy (MSA) and neurodegeneration with brain iron accumulation (NBIA) [52, 58-62, 70]. Iron overload is also associated with multiple symptoms of neurodegeneration in animal models [71, 72]. Excess unliganded or poorly liganded Fe^{2+} in LIP can act as a strong catalyst in the Fenton reaction [73], which generates highly reactive hydroxyl and superoxide radicals. They can then cause tissue damage by engaging in secondary reactions as a non-selective oxidant [29]. Moreover, due to the high proportion of polyunsaturated fatty acids in the membranes [74], and the lack of the natural antioxidant glutathione in neurons [75], the CNS is highly vulnerable to oxidative damage from the accumulating reactive oxygen species [76].

Recently, with the increasing understanding of misfolded proteins that present in neurodegenerative diseases [77, 78], the involvement of iron dyshomeostasis in the molecular pathways to the pathogenesis is being elucidated [34, 79-91]. For instance, *in vitro*, both Fe^{2+} and Fe^{3+} can bind α -synuclein (α -syn) [92], a 140-amino-acid protein expressed in presynaptic terminals and neuronal cytosol [93]. Its misfolded aggregated form is one of the main components of Lewy bodies (LBs) [83, 94], associated with the LB pathology and related neurodegeneration, such as PD [93, 95]. Evidence also suggests an iron-modulated α -syn translation via the potential binding of IRP to the human α -syn mRNA [96, 97], and an iron-mediated α -syn cell-to-cell transmission [98]. In AD, iron accumulation was found colocalised with the disease's neurological hallmarks extracellular amyloid- β ($\text{A}\beta$) plaques [34, 90] and intercellular neurofibrillary tangles (NFTs) [99]. *In situ*, chemically reduced iron was found in the amyloid plaque core in human brain specimens diagnosed with AD [100], and this $\text{A}\beta$ -ferritin interaction was also observed *in vitro*, with horse spleen ferritin [88] and synthetic ferrihydrite particles [87]. Moreover, *in vitro* findings also suggest an iron-mediated increase of $\text{A}\beta$ release, via the interaction between Fe^{3+} and amyloid precursor proteins (APP) [101]. On the other hand, NFTs in AD contain

hyperphosphorylated tau, a pathologically misfolded form of tau protein, whose aggregation might be triggered by direct interaction with iron via a putative binding motif [102, 103]. Under normal physiological conditions, soluble tau proteins are involved in axonal transport and protein trafficking in axons and dendrites, to stabilise the microtubule assembly [104].

Additionally, iron's contribution to the aggregation of aberrant proteins, including A β , α -syn, tau, TAR DNA binding protein 43 (TDA-43), superoxide dismutase 1 (SOD1), and prion protein (PrP), has been recently reviewed elsewhere [102]. Besides, although neurodegenerative diseases, such as AD [105, 106], PD [79, 107], amyotrophic lateral sclerosis (ALS) [108], are primarily marked by different misfolded proteins, the aggregation of one particular protein is not disease-specific [80, 109, 110], which suggests common pathways and may explain the heterogeneity of some diseases' phenotypes and symptoms [111-113]. At the same time, ferroptosis as a form of iron-mediated cell death has also been highlighted as a factor [84, 97, 114]. Treatments to remove the excessive liganded iron with chelators have been suggested [115-117], with some showing potential to significantly delay disease progression [117].

1.2.2.1 Parkinson's disease

PD is the most common neurodegenerative movement disorder, characterised and associated with the progressive loss of the neuromelanin-containing [118-120], dopaminergic neurons within the substantia nigra pars compacta of the brain [121, 122]. Within the affected brain region, the disease is histologically marked by the presence of LBs, which are cytoplasmic inclusions of fibrillar, misfolded proteins consisting of aggregated α -syn [79, 83]. Solely relying on conventional clinical assessments [123-126], it is challenging to achieve early diagnosis of PD, because the impact of the neuron loss is usually insignificant until the advanced stage of the disease [121, 127]. Moreover, the disease progression is often monitored by assessing clinically the motor and non-motor Parkinsonism symptoms, while

accurate and sensitive objective testing for the diagnosis of early-stage idiopathic PD has not yet been developed in routine clinical practices. Recently, functional neuroimaging, including single-photon emission computed tomography (SPECT) [128, 129] and positron emission tomography (PET) [130-133], have shown potential in disease diagnosis in some preclinical and clinical settings. Using dopaminergic radiotracers, these imaging techniques have shown advantages in diagnosing early and uncertain cases [134, 135]. However, exposing patients to ionising radiation restricts the application in vulnerable patients, and in longitudinal studies, where the risk of undesirable impact may increase with repeated scans.

At the same time, consistently reported, post-mortem measurement of iron concentration in PD brains, suggested a significantly elevated iron level in the substantia nigra [43, 44, 47, 52, 136-138], with around double the concentration compared with healthy subjects. Using a semi-quantitative staining method, Jellinger *et al.* [139] reported increased Fe³⁺ and ferritin concentrations in the substantia nigra pars compacta of PD brain, in comparison with healthy controls. On the other hand, Wypijewska *et al.* [140] reported an increased LIP iron in the Parkinsonian brains, compared with the healthy brains, but no significant difference was found in the total iron concentration. However, some studies [63, 141, 142] did not observe the statistically different iron concentration of the substantia nigra between PD and healthy brains. Loeffler *et al.* [63] measured iron concentrations in the basal ganglia nuclei, substantia nigra and frontal cortex of PD, AD and age-matched healthy brains, and increased iron concentrations was observed in globus pallidus of PD, in comparison with the healthy brains. Chen *et al.* [42] reported increased iron and ferritin concentration in the putamen samples of PD, compared with the healthy control brains.

1.2.2.2 Alzheimer's disease

AD is the most common neurodegenerative disease in the world, and it accounts for about 60-80% of cases of dementia [143]. In the brain, neurological changes are

characterised by neuron loss within the hippocampus and cerebral cortex, and accumulation of extracellular amyloid plaques and intercellular NFTs [144]. As the molecular pathway has been elucidated, a long preclinical phase of AD has been recognised among the research field in the recent decade, that a 20-yrs or longer period of disease pathogenesis is likely to exist before the clinical diagnosis of AD [145-147]. Associated with mild cognitive impairment (MCI) [148] and neuropsychiatric symptoms [149], functional and structural changes of the associated brain regions may be detected using PET and MRI [109, 133, 150, 151].

In AD, the post-mortem measurements of iron concentrations within the brain are mostly unchanged, compared with healthy brains, while the results in some brain regions are inconsistent. Nevertheless, compared with normal ageing brains, several studies [63, 152-154] reported an increase in iron concentration within the frontal cortex, and House *et al.* found significantly higher iron concentration in frontal cortex GM [154]. A recent study [155] showed increased iron concentration in the neocortex of the brain with severe AD, compared with healthy brains. Loeffler *et al.* [63] observed higher iron concentration in the globus pallidus and frontal cortex of AD brains than healthy controls. In contrast, Griffiths *et al.* measured iron concentrations in AD's neocortex and basal ganglia nuclei, and found decreased iron concentration in the globus pallidus and unchanged in the neocortex, when compared with healthy brains [44].

1.3 Imaging brain iron using MRI

Since the nuclear magnetic resonance (NMR) techniques [156-159] were developed during the 1950s-1980s, MRI soon emerged [160] and has been applied as a clinical imaging technique [48]. The MRI signal directly arises from the hydrogen of water, under an external magnetic field, after applying a non-ionising, radiofrequency (RF) radiation. Realised with complex Fourier transforms (FT), in the combination of different RF pulse sequences and gradients of the external magnetic field (see

Chapter 2), the physical evolution of the characteristic signal transverse relaxation of protons (for ^1H NMR and MRI) can be well-described [15, 16, 156, 161-164].

In presence of paramagnetic ions, *e.g.*, Fe^{3+} , the proton transverse relaxation time (T_2) in solution is shortened, due to the electron spins relaxation of the paramagnetic ions [165, 166]. In the brain, primarily stored in ferritin, the iron core (ferrihydrite, described in Section 1.1.1) is antiferromagnetic and possesses a superparamagnetic moment at body temperature [167], which can be described by Néel relaxation (Section 2.3.1, also see Vuong *et al.*'s review [168] of theoretical models describing the MR relaxation induced by superparamagnetic particles). *In vitro*, ferritin demonstrates a significant T_2 -shortening effect, and a linear magnetic field-dependence [167, 169-171]. Therefore, NMR (^1H NMR, unless specified in this thesis) and MRI provide a potential tool to measure and analyse brain iron *in vivo*.

In human brain MRI, the iron-laden brain regions demonstrate hypointensity (darkening) on T_2 -weighted images, presumably due to the T_2 -shortening effect [48]. Compared to other transition metal ions in brain tissue, iron content has a dominant effect on the MRI, due to the relatively high concentration and the superparamagnetic mechanism. Hence, in healthy adult human brains, the iron content is normally found sufficient to be measured by quantitative MRI techniques at clinical field strengths [13, 172], and the quantitative correlations between tissue iron concentration with different MRI measurements have been reported in the literature (see Chapter 3).

Imaging iron content in the tissue shows the clinical value of supporting disease assessment and evaluation, especially in iron-laden organs and tissues, such as the liver and brain [137, 151, 173-181]. At 1.5 T, *in vivo* MRI examinations of the liver iron concentration (LIC), using transverse relaxation rate ($R_2 = 1/T_2$) has been well established, calibrated with LIC measured by needle biopsy from living patients, and has been applied for detecting liver iron overload [174], *e.g.*, hereditary hemochromatosis and thalassemia disorders [181, 182]. However, due to the

heterogeneous tissue compartments within human brains, efforts have been made to establish a baseline measurement, mostly brain region-specific (addressed as regions-of-interest, ROIs, see Chapter 4), of healthy and normal ageing brains [176, 183-190]. Using different *in vivo* quantitative (or semi-quantitative) MRI methods (see Chapter 3), those measurements in healthy volunteers can be compared with brain diseases associated with iron dyshomeostasis (see Section 1.2.2), such as PD [191-198], AD [199, 200], MS [201-204], or with their clinical symptoms. Presented in *Chapter 5* of this PhD thesis, the *in vivo* human brain QSM (Section 3.3 and Section 4.4.2) using 3.0 T clinical MRI was validated and compared with other quantitative MRI techniques at the local hospital UHCW, Coventry. Additionally, open-access neuroimaging databases have provided opportunities to study large global cohorts, healthy and diseased, such as Open Access Series of Imaging Study (OASIS) [205], Alzheimer's disease neuroimaging initiative (ADNI) [206] and PPMI [207]. Utilising the structural MRI data of the PPMI participants, together with their dopaminergic transporter (DaT) functional imaging results (SPECT), *Chapter 4* of the PhD thesis presents a new quantitative application of the 3.0 T dual-contrast FSE MRI, which is commonly restricted to anatomical imaging and assumed to be qualitative at clinical field strength. The reported effective R_2 is correlated with the iron level in the brain regions and can indicate the asymmetrical putaminal DaT dysfunction in PD patients.

On the other hand, the quantitative MRI using preclinical scanners, *e.g.*, equipped with microimaging, small-animal probe or cryo-probe (cryogenic probe), and ultra-high field (UHF, 7.0 T and above) imaging, enable a great range of applications. Brains of small (model) animals, especially transgenic mice, that manifested with human diseases' phenotypes, have been intensively studied [208-214]. Compared with human brain clinical MRI, the preclinical small-animal MRI allows a direct comparison between *in vivo* and *ex vivo* examination [214], unfortunately, by sacrificing the animal. Alternatively, post-mortem tissue specimens or MR phantoms could be examined with ultra-high resolution (or MR microscopy, MRM), under UHF [54, 208, 215-218]. Additionally, compared with MRI in clinical settings, some preclinical MRI scanners that are equipped with advanced shimming and temperature control

systems, allow elaborate control of the experiment (MR acquisition) conditions [68, 219, 220]. As the human brain MRI is entering a UHF era (7.0 T) [217, 221-226], this ultra-high-resolution information obtained from the preclinical UHF MRI is becoming more important than ever before, especially for susceptibility-related contrast, which is in theory enhanced by the increasing external magnetic field [227-230]. Therefore, in *Chapter 7* of the thesis, using 9.4 T preclinical MRI, the transverse relaxation rate with field inhomogeneity, R_2^* , as well as QSM of ferritin-bound iron and A β (1-42) were examined with ultra-high resolution *in vitro*. For the first time, the quantitative relationship between the ferritin-bound iron level and the QSM susceptibility, was reported, in dispersed ferritin and co-aggregated A β (1-42) and ferritin.

Chapter 2: MRI signals and pulse sequences

In this chapter, the physical and mathematical principles underlying the NMR and MRI signal formation, as well as the MR pulse sequences that are relevant to this thesis, are briefly revised (Section 2.1-2). It is then followed by the theoretical background of the magnetic susceptibility and how bulk (volume) susceptibility can be detected by MR. Although some of these theories have been well-established for several decades, the fundamental knowledge presents in this chapter is complementary to this PhD thesis. It is because these theories provide the basis for choosing the pulse sequences and MR acquisition parameters, image reconstruction and post-processing (Chapter 4), and the correct interpretation of the observation in the MRI literature (Chapter 3) and in the experiments of the PhD project (Chapter 5-7). Therefore, the reference materials for the equations in this chapter are from the NMR and MRI textbooks [15, 16, 166, 231], if not specified. Vectors are presented in bold.

2.1 MRI signal

2.1.1 Spin

Spin and magnetism are intrinsic properties possessed by atomic and subatomic particles. For atoms made up of electrons and nuclei, their atomic nuclei may be described by their fundamental physical properties, including mass, electric charge, magnetism and spin [166]. As a highly abstract concept, the spin of an atomic nucleus describes how it interacts with the electromagnetic field, and its magnitude is quantised and determined by its spin angular momentum quantum number, I . Each elementary particle has a particular value for I , and the particle with spin I has $(2I + 1)$ sublevels (spin state), ranging from $-I$ to I with integer interval. The sublevels of the particle are associated with different energy levels when a magnetic field is applied. For hydrogen (^1H , proton), $I = \frac{1}{2}$, there are two energy states for ^1H , $+\frac{1}{2}$, known as spin-up, and $-\frac{1}{2}$, spin-down, each spin state may be described to have a quantised angular momentum \mathbf{J} :

$$\mathbf{J} = \frac{\hbar I}{2\pi} \quad \text{Eq. (2.1)}$$

where h denotes the Planck's constant, I the sublevel of each spin state.

2.1.2 Free precession and Larmor frequency

In the presence of an external magnetic field \mathbf{B}_0 , the spin can be described to have a magnetic moment $\boldsymbol{\mu}$, which is proportional to the angular momentum \mathbf{J} :

$$\boldsymbol{\mu} = \gamma \mathbf{J} \quad \text{Eq. (2.2)}$$

and precesses along the direction of \mathbf{B}_0 . where γ denotes the nucleus-specific gyromagnetic ratio, for ^1H proton, $\gamma = 42.56 \text{ MHz} \cdot \text{T}^{-1}$. The spin precesses around the external field \mathbf{B}_0 , and the precession is associated with the energy E :

$$E = \boldsymbol{\mu} \cdot \mathbf{B}_0 \quad \text{Eq. (2.3)}$$

therefore, the difference between the above two spin states ($+\frac{1}{2}$, and $-\frac{1}{2}$) of the proton can be calculated by Eq.(2.1) and Eq.(2.3):

$$\Delta E = E_{spin-up} - E_{spin-down} = \frac{\gamma h}{2\pi} \left[\frac{1}{2} - \left(-\frac{1}{2} \right) \right] \mathbf{B}_0 = \frac{\gamma h \mathbf{B}_0}{2\pi} \quad \text{Eq. (2.4)}$$

according to the wave equation:

$$\Delta E = \frac{h\omega}{2\pi} \quad \text{Eq. (2.5)}$$

therefore, the precession frequency ω associated with ΔE of the spin, is defined as the Larmor frequency ω_0 :

$$\omega_0 = \gamma \mathbf{B}_0 \quad \text{Eq. (2.6)}$$

2.1.3 Thermal equilibrium and Boltzmann distribution

The two stable energy states of the spin coexist under an external magnetic field B_0 , and the spin can jump between the high-energy and the low-energy states by losing or gaining ΔE in the form of photons. In the absence of disturbance for a long enough time, the collection of spins can reach a state of thermal equilibrium. In this state of equilibrium, the low energy state is slightly favoured, and the statistic distribution of the difference between the two spin populations follows the Boltzmann function, at a given temperature T in Kelvin:

$$\frac{N_{spin-up}}{N_{spin-down}} = e^{\frac{\mu \mathbf{B}_0}{kT}} = e^{\frac{\gamma h \mathbf{B}_0}{2\pi kT}} \quad \text{Eq. (2.7)}$$

where $N_{spin-up}$ is the number of spins in the state of spin-up or parallel (almost align with \mathbf{B}_0), and $N_{spin-down}$ are the number of spins in the state of spin-down or anti-

parallel (almost opposite to \mathbf{B}_0), $\boldsymbol{\mu}$ denotes the magnetic moment of the spin, k is the Boltzmann constant, γ the gyromagnetic ratio, and h denotes the Planck's constant. In the equilibrium state, all spins are out-of-phase. Because a slight difference of the spin populations between the two states exists, when treating each individual spin as a vector with the magnetic moment $\boldsymbol{\mu}$ the direction, the sum of a spin ensemble (isochromats) is non-zero [232], which can be described in classical mechanics as a net magnetisation vector \mathbf{M}_0 , which satisfies:

$$\mathbf{M}_0 = \chi \mathbf{B}_0 \quad \text{Eq. (2.8)}$$

with χ represent the (microscopic) nuclear susceptibility, and \mathbf{B}_0 the external magnetic field.

2.1.4 Effect of RF pulses

When an RF pulse that generates a specific oscillation at the Larmor frequency of the observing nucleus to generate a small magnetic field \mathbf{B}_1 is applied to the spin ensemble, the state of thermal equilibrium is disturbed, and the energy of the spin system changed consequently. To the net magnetisation vector \mathbf{M}_0 , in a rotating frame reference at the Larmor frequency, its motion can be described by:

$$\frac{d\mathbf{M}}{dt} = \gamma \mathbf{M} \times \mathbf{B}_1 \quad \text{Eq. (2.9)}$$

and the flip angle (FA) α between \mathbf{M} and its original direction (\mathbf{B}_0), before applying \mathbf{B}_1 is given by [16]:

$$\alpha = \gamma \int_0^t \mathbf{B}_1(t) dt \quad \text{Eq. (2.10)}$$

with $\mathbf{B}_1(t)$ the amplitude of the RF pulse and t denotes the duration of the pulse. Therefore, depending on the amplitude of the RF pulse and its function with time, the spin populations can change, and the coherence can be generated, demonstrated as the \mathbf{M}_0 is tilted away from the direction of \mathbf{B}_0 , towards the x-y plane (Fig. 2.1).

2.1.5 Free induction decay (FID) and relaxation

When the oscillating magnetic field \mathbf{B}_1 generated by the RF pulse is removed, a very fast signal decay may be observed on the x-y plane, which is the free induction decay (FID). At the same time, the spin system starts the process of regaining the thermal

equilibrium under the main external magnetic field, via the interaction with the thermal molecular environment [166]. Known as longitudinal relaxation, spin-lattice relaxation describes the re-establishment of Boltzmann distribution of the spin populations. The characteristic time associated with the longitudinal recovery, is the longitudinal relaxation time (T_1). On the other hand, spin-spin relaxation describes the process of coherence decay (dephase), namely, transverse decay, and it is associated with the transverse relaxation time (T_2).

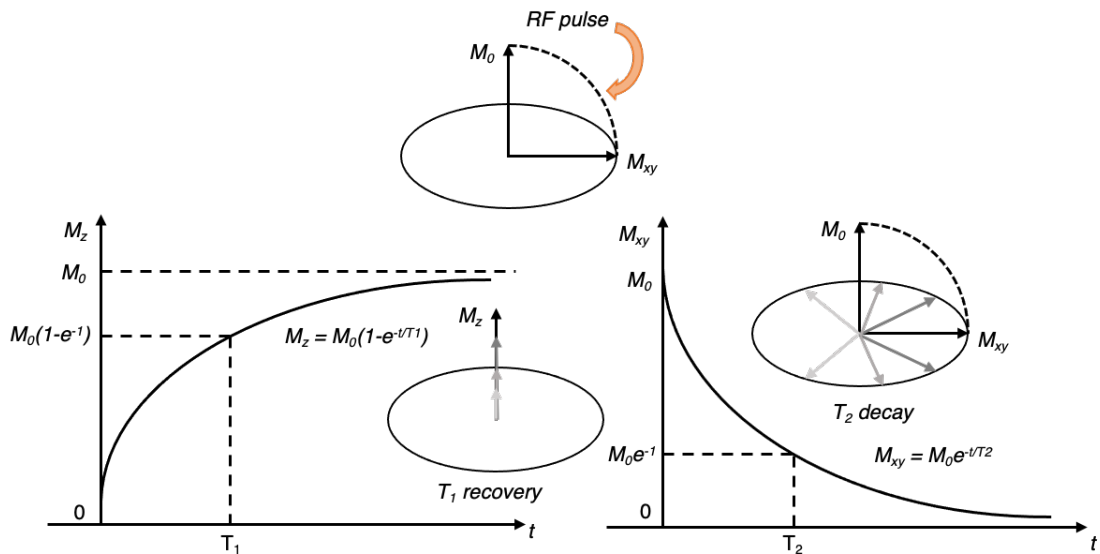


Fig. 2.1 Effect of RF pulse, T_1 and T_2 relaxation.

2.1.6 MR signal detection

Usually, the FID is not directly measured in NMR or MRI because of the fast decaying of the signals. In contrast, the intrinsic information of the system of spins, is indirectly obtained by detecting the signal generated by rephasing, using additional π -RF pulses or reversing the magnetic field gradient (G) depending on the MR pulse sequence. When the isochromats are in-phase again, this oscillating signal is then detected, via quadrature detection by the receive coil. The quadrature detector consists of two channels, real (Q) and imaginary (I) perpendicular to each other, detecting the magnetic flux on the x-y plane with a $\pi/2$ phase shift [16]. Hence, the detected MR signal is complex, and can be reconstructed by each channel, or combined into magnitude or phase data from the Q and I components.

2.1.7 Spatial encoding, Fourier transform and image formation

For one-dimensional (1D) acquisition, the MR signal is detected as an oscillating decay with time or as a spectrum in the frequency domain; and additional magnetic field gradients are required to form two-dimensional (2D) images or three-dimensional (3D) volumes, by superposing linearly varied magnetic field G_x , G_y , G_z on the main external field B_0 , spatially along x-, y- and z- direction. The spatially varied magnetic field enables spins at different locations to precess at different frequency, and the signal can be sampled (encoded) into a 2D or 3D frequency domain, known as k-space (Fig. 2.2). Typically, in 2D k-space, a Cartesian space is employed, with two perpendicular axes k_x and k_y , often indicating the frequency encoding (FE) and phase encoding (PE) directions, and for true 3D acquisition, an additional PE direction is along z-axis (k_z). These k-space data are eventually transformed into MR images via Fourier transform [16].

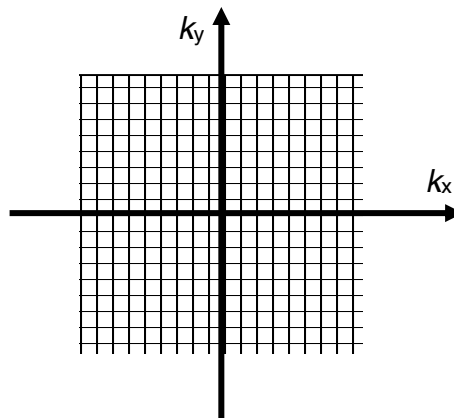


Fig. 2.2 An example 2D Cartesian k-space.

k_x : x-direction in the k-space; k_y : y-direction in the k-space.

The k-space trajectory is an active research field in MRI and more sophisticated k-space filling schemes are beyond the scope of this work, but the entire MR sequence has to be repeated multiple times to obtain a full k-space, as the signal generated after each RF pulse is sampled along the FE direction (k_x) within the repetition time (T_R), until the next RF pulse with a different PE (k_y) applied, in a conventional MR acquisition. Therefore, the acquisition time for a 2D k-space in the above example is:

$$\text{Scan time} = N_A \times N_{PE} \times T_R \quad \text{Eq. (2.11)}$$

and for 3D acquisition:

$$\text{Scan time} = N_A \times N_{PE1} \times N_{PE2} \times T_R \quad \text{Eq. (2.12)}$$

with N_A denotes the number of averages, N_{PE} the number of PE steps (along each PE direction for 3D acquisition), and T_R the repetition time of the MR acquisition [15]. The acquisition can be accelerated by using various fast imaging pulse sequences, or by employing parallel imaging and sensitivity encoding (SENSE) technique [233].

2.2 MR pulse sequence

MRI is one of the most versatile and flexible medical imaging techniques, because its signal and contrast can be adapted for the purpose of imaging, utilising different pulse sequences. For structural MRI, many MR pulse sequences are widely used in the clinical setting, to enhance contrasts between different tissue types, provide information about anatomy, or reveal the tissue parameters on different microscopic or macroscopic levels. Mostly, they are derived from two basic pulse sequences: 1) spin echo (SE) and 2) gradient echo (GRE).

It should be noted that different MR vendors often use their own commercial names and acronyms for these pulse sequences, but the physics underlying is the same for each type of basic sequence. For instance, the fast-spin-echo is called FSE by GE Healthcare, but TSE (Turbo Spin Echo) by Philips and Siemens. Sometimes the manufacturer's acronym does not directly reveal the type of the sequence, for example, RARE (Rapid Acquisition with Relaxation Enhancement) in Bruker is made available for the fast-spin-echo sequence, and SWAN (susceptibility weighted angiography) provided by GE Healthcare applies a 3D gradient echo for acquisition.

2.2.1 Spin echo

2.2.1.1 Spin echo and multiple spin echoes

Historically, the term SE is initially described by Hahn [234] in 1950, to indicate the spontaneous nuclear induction signals that appeared after two consecutive RF pulses. Hahn used a pair of $\pi/2$ -RF pulses to create an 'echo' of the spin's transient FID, which provides a firm basis for the investigation of nuclear magnetic resonance phenomena. This study established the method to measure nuclear relaxation times in liquid that

water molecules diffuse through the local inhomogeneous external field, using a pair of RF pulses with different the time interval τ , under the condition that FID does not interfere with the echo. Sometimes referred to as 'Hahn echo' in current days, this type of SE is generated when a pair of RF pulses are applied, whose signal intensity is considered to be relatively weak, compared to the modern SE sequence employed in MRI. Adapting from Hahn's method, Carr and Purcell developed the SE sequence (Carr-Purcell sequence or CP sequence) [157] that the literature often refers to nowadays, which employs a combination of a $\pi/2$ -RF pulse, followed by a π -RF pulse.

Described in Section 2.1.3, the collection of spins is in its thermal equilibrium under the external magnetic field B_0 , in which the population of two states are governed by the Boltzmann distribution, and the net magnetisation vector of the spin collection is aligned with the B_0 field. When a $\pi/2$ -pulse is applied to the ensemble of the spins at $t = 0$, mathematically, it equalises the populations of the spins with high and low energy states and converts this previously existing population difference into coherences (in-phase). In the most conventional analogue of the SE sequence, the first $\pi/2$ -excitation pulse seems to 'rotate' the net magnetization vector (M_0) from the z-axis to the x-y (transverse) plane, resulting in a magnetization that has the same magnitude of M_0 on the transverse plane. Diverted from the thermal equilibrium by the excitation pulse, in the absence of the RF field, the ensemble of spins will gradually return to the thermal equilibrium via relaxation, in which process the population difference of spins with two energy states re-establishes, and the coherences gradually dephase. It is described as the magnetisation vector M precesses around the z-axis while returning to be aligned with the main external magnetic field again. After the time interval τ , the following π refocusing pulse is applied, which reverses the coherence phases, and so the spins rephase to form an echo at $t = 2\tau$ (Fig. 2.3).

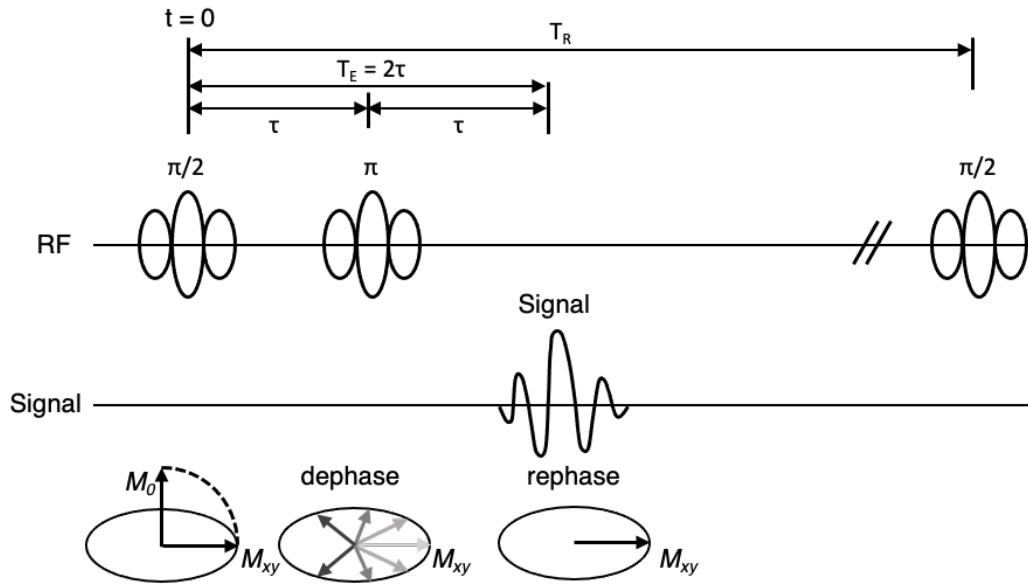


Fig. 2.3 SE pulse sequence.

Using the following π -refocusing pulse, the SE method reverses the coherence dephasing that is caused by time-invariant sources and eliminates the effect of the inhomogeneous external field on measured nuclear induction signals, which dominates the FID, and therefore recover the transverse relaxation time constant (T_2) of the ensemble of spins on the x-y plane. By repeatedly applying multiple pairs of the $\pi/2$ - π RF pulses on a sample with varying time interval τ between the $\pi/2$ and the π pulses, and allowing the full relaxation of the signal after each $\pi/2$ - π pulse pair, Carr and Purcell demonstrated that multiple spin-echoes can be generated, and the amplitude of the NMR signal can be used to determine the diffusion coefficient and the time constant T_2 with diffusion in water samples.

2.2.1.2 Multi-echo spin-echo

To eliminate the effect of diffusion in the measurement of NMR transverse relaxation, especially when a non-viscous sample with large T_2 is used, and so the sample's self-diffusion is no longer negligible, Carr and Purcell developed an alternative method [157] to reveal the 'natural' transverse relaxation of the NMR signal. In a Carr-Purcell (CP) sequence, instead of multiple exposures to the $(\pi/2)$ - π RF pair, a single exposure to a series of RF pulses is employed (Fig. 2.4).

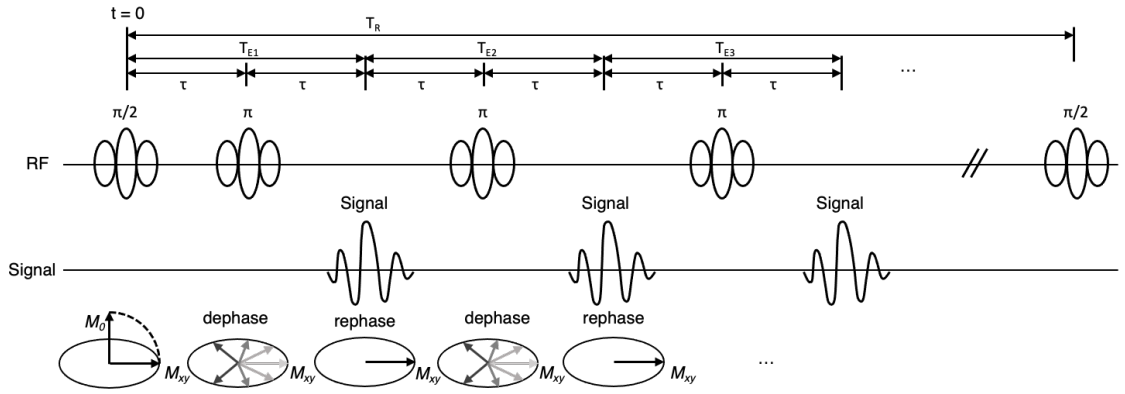


Fig. 2.4 Multi-echo spin-echo (MESE) pulse sequence.

Often referred as multi-echo spin-echo (MESE) in MRI literature, it applies a $\pi/2$ -pulse to 'flip' the net polarisation to the transverse x-y plane (at $t = 0$), then after time τ the dephased spins are refocused with n ($n = 1, 2, 3, 4, 5, \dots$) successive π -RF pulses to generate echoes after each π -pulse. The time interval between two consecutive π -pulses is fixed and equal to 2τ , and the spin echoes can be observed at $t = n\tau$, midway between each two refocusing pulses and trailing after the last π -RF pulse. In the case when the effect of diffusion is moderate, the decay on the transverse plane that is caused by diffusion can be calculated by:

$$M_{y'}(t) = M_0 e^{\frac{-\gamma^2 G^2 D t^3}{12n^2}} \quad \text{Eq. (2.13)}$$

where G is the gradient along FE-direction, D denotes the diffusion coefficient, n the number of refocusing RF pulses, known as the echo train length (ETL) in the MRI literature. Taking the natural transverse relaxation into account, the NMR signal amplitude obtained by $\pi/2$ - π sequence is therefore given by:

$$M_{y'}(t) = M_0 e^{-\frac{t}{T_2} + \frac{(-\gamma^2 G^2 D t^3)}{12n^2}} \quad \text{Eq. (2.14)}$$

For the SE sequence, $n = 1$. This well described the NMR signal intensity of liquid samples observed by using multiple SE (Fig. 2.3) and MESE (Fig. 2.4). Additionally, it explains the discrepancy in the transverse relaxation time constant T_2 of non-viscous samples measured by the above two methods [157], whose results are identical when measuring a viscous sample because of the restricted diffusion.

Hence, the above quantitative theory has revealed that the effect of diffusion on the observed decay can be effectively minimised by increasing or decreasing the inter-

echo-time (also known as IEP, inter echo spacing or ESP, echo spacing) 2τ in the CP sequence. In addition, another advantage of the CP sequence is that any potential molecular convection effect is made the most observable when the time interval between consecutive π -pulses is set as twice as the time between the $\pi/2$ -pulse and the first π -pulse. The convection effect is shown as the diminished signal amplitude of odd-number echoes [157], which can be easily identified and eliminated in calculation by using the even-number echo, where theoretically the coherences are perfectly refocused, and the net magnetic moment is in phase.

In the CP sequence, the amplitude adjustment of the refocusing π -RF pulse is the most important for the accuracy of the relaxation time measurement, because an ideal refocusing pulse should 'flip' all moments the exact angle of π so that all coherences previously dephasing on the x-y plane can be re-clustered (rephased) again, and a 'full' echo can be formed on the transverse plane. In practice, however, a perfect π pulse is not easy to achieve, and even a small refocusing error could accumulate and exaggerate through the long echo train in the CP sequence. To address this issue, Meiboom and Gill improved the sequence by shifting the phase of the excitation pulse by $\pi/2$, relative to the phase of the refocusing π -pulse [163]. To visualise the difference between two methods, considering a right-hand system, at first assume one same $(\pi/2)_x$ -excitation pulse rotate the net magnetization by $\pi/2$ about +x' axis onto the -y' axis of the rotating frame. In the original CP sequence [157], successive $(\pi)_x$ -pulses are then carried out to refocus the coherences and the spin echoes are form (in-phase) on +y' and -y' axis alternatively. Proposed by Meiboom and Gill [163], the $(\pi/2)_x$ -excitation pulse is followed by coherent and successive $(\pi)_y$ pulses, which means the coherences are 'flipped' by the π -pulses about +y' axis and always refocused on -y' axis, and all the echoes generated by this pulse sequence have the same phase. Known as Carr-Purcell-Meiboom-Gill (CPMG) sequence, this method can correct the imperfect refocus angle by 'flipping back' the coherences onto the transverse plane and forming the echo with the correct amplitude after every even-numbered refocusing pulse.

In NMR, the SE techniques are often regarded as the gold standard for relaxometry, and the CPMG sequence has been widely applied to study T_2 relaxation and the spectrum broadening, especially for spin $\frac{1}{2}$ nuclei, *e.g.*, ^1H . Compared to NMR, however, the CPMG-based MRI applications are more sensitive to the acquisition parameters and imaging systems, because of the interaction between the signal and the spatial encoding gradients. Therefore, the MR relaxometry measured with MRI is often not directly comparable to the NMR measurement of a sample. However, the relaxation measured using MRI can still be highly reproducible when the pulse sequence and acquisition parameters are consistent. As the CPMG sequence is widely employed in the clinical MRI scanner, it is still the most common and practical method for T_2 measurement in the body and brain.

2.2.1.3 Fast spin echo

As another variation of the SE sequence, the fast-spin-echo (FSE or TSE, for turbo-spin-echo) [235] may seem similar to MESE in a sense of the RF pulse sequence, because both of them have a series of multiple π -pulses after the initial $\pi/2$ -excitation RF pulse, to generate corresponding echoes. However, the data acquisition scheme in terms of k-space filling for FSE is entirely different. In SE or MESE sequence, the same PE step is applied to the echo(es) generated within one T_R , but different PE steps are used in FSE sequence for each echo generated after the π -pulse in the echo train. The latter PE scheme in the FES sequence enables multiple lines to be filled in the k-space during one T_R , which accelerate the acquisition by a 'turbo factor' that is equal to the ETL, compared to SE. The scan time of an FSE sequence is:

$$\text{Scan time} = \frac{T_R \times N_{PE} \times N_A}{ETL} \quad \text{Eq. (2.15)}$$

where T_R is the repetition time, N_{PE} denotes the number of PE steps, N_A the number of averages.

By sampling multiple lines of the k-space within one T_R , FSE 'fills up' the k-space in a much faster manner (Fig. 2.5), at the same time, its contrast behaviour is inherently more complicated. Composed by several segments (or portions), FSE's k-space contains the information of signals (echoes) obtained at different echo times (T_E).

Although some details and contrast of FSE image are compromised due to the mixing of signals, by taking advantage of the fact that the main contrast of an MR image is dominated by the signal near the k-space centre, the contrast and the weighting of the FSE image is determined by the echo acquired at the central portion of the k-space, and the corresponding T_E is called the effective T_E ($T_{E(\text{eff})}$). The control of contrast can be done by manipulating the phase encoding scheme, moreover, dual- and triple-echo FSE can be achieved more efficiently by assigning the echoes within one T_R to two or three images with varied $T_{E(\text{eff})}$.

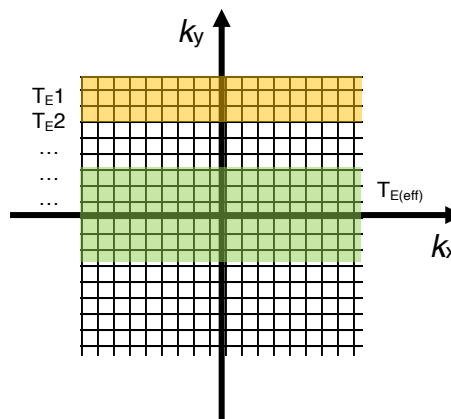


Fig. 2.5 An example 2D Cartesian segmented k-space.

The central k-space is highlighted in green. k_x : x-direction in the k-space; k_y : y-direction in the k-space. T_{E1} , T_{E2} , $T_{E(\text{eff})}$: 1st echo time, 2nd echo time, and effective echo time, respectively.

Compared to the image obtained by using conventional SE sequence, the one from FSE has some noticeable differences in the contrast behaviour and image quality, for example, the brighter appearance of fat (J-decoupling due to the short ESP), stronger magnetisation transfer (MT) effect (due to the long ETL that saturates the bound pool, showed as darker soft tissues and therefore relatively brighter veins), and somewhat reduced details [236, 237]. In clinical, to reduce the specific absorption rate (SAR) that is generated by the long echo train, a reduced FA ($\alpha < \pi$) of the refocus pulses is often applied, which further induces deviation from the conventional SE.

2.2.2 Gradient Echo

Instead of using the RF pulse that refocuses the coherences to form a spin echo, gradient echo (GRE) sequences rephase (and dephase) the spins to generate the MR signal (echo) by 'reversing' the gradient after the FID. Without the π -pulse, the field inhomogeneity is not compensated, and the induction nuclear signal decay is not only determined by T_2 , but also by the magnetic field and local susceptibility and diffusion. Another main difference between the SE sequence and the GRE sequence is that the latter applies a small FA ($\alpha < \pi/2$) to the spins to generate the net magnetization on the transverse plane. The low flip angle allows the GRE sequence to employ a short T_R , and therefore makes the pulse sequence faster relative to most of the SE sequences.

2.2.2.1 3D Gradient echo

The short scan time of the GRE sequence has made it a perfect candidate for 3D acquisition. In 2D MR acquisition, to localise the signal along the main magnetic field for instance (although it can be applied to any direction), a slice-selective gradient on z-direction is employed to excite a single slice each time when the RF pulse is applied. However, by exciting a 3D volume and applying an extra phase encoding along the conventional 'slice' direction, 3D acquisition can be achieved in MRI to obtain thinner slices and a better slice profile.

In 3D sequences, it takes longer time to acquire the MR signal due to the additional phase encoding step in each T_R , but the improved SNR and the resultant continuous scan volume have made 3D acquisition preferable in some clinical applications, especially when the isotropic voxel is desirable. It should be noticed that the artefacts that are possibly involved in the in-plane phase encoding, e.g., phase wrapping, could also be observed in the slice-direction when applying 3D GRE sequences.

2.3 Magnetic susceptibility

On the microscopic level, the magnetic susceptibility was demonstrated as the response of the spins of nuclei and the orbital electrons to the applied magnetic field, and the overall magnetic susceptibility χ of material is dominated by the orbital

motion and the spins of the electrons rather than the nuclei because of the relative density of the spins, with:

$$M = \chi B \quad \text{Eq. (2.16)}$$

where M denotes the magnetisation, B is the magnitude of the applied magnetic field. In general, when the induced magnetisation is aligned with the applied field, where $\chi > 0$, the material is paramagnetic, otherwise diamagnetic ($\chi < 0$). There are many mechanisms underlying the magnetisation of the material in presence of an external magnetic field, and the apparent magnetic susceptibility demonstrates a sum of these contributions and is generally determined by experiments [238-240].

2.3.1 Magnetisation mechanisms

Langevin diamagnetism. This mechanism exists in all materials, as it is caused by the electron motion in filled orbitals when a magnetic field is applied. A weak magnetisation field with a direction opposite to the applied magnetic field is produced within the material by the Langevin diamagnetism. It is temperature-independent, and it is the main mechanism of the diamagnetic property presented in water, stable salts, and most biological materials.

Curie paramagnetism. It is the magnetism presented in molecules with unpaired electrons. Under the applied magnetic field, it generates a positive magnetisation along the same direction as the external field, which is several magnitudes larger than the Langevin diamagnetic effect. It exists in the salts or solutions of transition metals such as iron and copper, as well as actinides, lanthanides and rare earth elements such as gadolinium, which has been widely studied in NMR and MRI research, and gadolinium in particular, also utilised in clinical MRI as a contrast agent. Some molecules with unpaired electrons or spins, e.g., O_2 , NO_2 , also demonstrate Curie paramagnetism. The Curie paramagnetism is temperature-dependent and it increases as the temperature T decreases, known as Curie's Law:

$$\chi = \frac{C_{Curie}}{T} \quad \text{Eq. (2.17)}$$

with C_{Curie} denotes Curie's constant.

Nuclear paramagnetism. The NMR visible nucleus with non-zero spins, *e.g.*, ^1H , ^{13}C , generate a very small positive magnetisation under the applied magnetic field, as described in the previous Section 2.1.2.3, Eq.(2.8). The nuclear paramagnetism also obeys Curie's Law and increase as the temperature decreases.

Magnetic domain and superparamagnetism. Some materials can form magnetic domains within their structure when an external magnetic field is applied. Within the magnetic domain, the spins are spontaneously magnetised and aligned in an ordered phase, and the introduced magnetisation remains even after the removal of the external field. The magnetically ordered state of the material is termed ferromagnetism, with different subtypes depending on the pattern of spins. Some ferromagnetic materials demonstrate a very large positive susceptibility and generate an enormous demagnetising field, usually considered unsafe in MR. However, when the physical size of the magnetically ordered material decreases under a certain level, these particles with a single magnetic domain demonstrate superparamagnetism – it generates a demagnetising field with the same direction of the applied magnetic field, with a greater susceptibility than for Curie paramagnetism [239, 241, 242].

The Néel relaxation time is used to characterise the relaxation of the electronic moment of a superparamagnetic particle, which is differed from the proton relaxation (described in Section 2.1.5). For a superparamagnetic particle, the Néel relaxation time $\tau_{\text{Néel}}$ is given by:

$$\tau_{\text{Néel}} = \tau_0 e^{\frac{KV}{kT}} \quad \text{Eq. (2.18)}$$

with τ_0 a pre-exponential factor that is on the order of 0.1 to 100 ns, K denotes the anisotropy constant, V denotes the volume of the particle, k the Boltzmann constant, and T the temperature in Kelvin. For a given volume, there is a blocking temperature for the particle, above which the material demonstrates superparamagnetism and no remanent magnetisation sustains after the external magnetic field is removed [170, 239, 241, 242].

2.3.2 Bulk susceptibility quantification using MRI

2.3.2.1 Relations between demagnetisation field and the susceptibility

Under the external magnetic field $\mathbf{B}_0(\mathbf{r})$, the proton nucleus experience [243]:

$$\mathbf{B}(\mathbf{r}) = \mathbf{B}_0(\mathbf{r}) + \mathbf{B}_{demag}(\mathbf{r}) \quad \text{Eq. (2.19)}$$

with $\mathbf{B}_{demag}(\mathbf{r})$ denotes the associated demagnetisation field that presents in the subject being imaged at location \mathbf{r} , and usually is determined by dipole approximation $\mathbf{B}_{demag}(\mathbf{r}) = \sum_i \mathbf{b}(\mathbf{r} - \mathbf{r}_i)$, with \mathbf{b} is the unit dipole function. Hereby, chemical shift effect is neglected.

Using Lorentz approach, the demagnetisation field $\mathbf{B}_{demag}(\mathbf{r})$ can be calculated by virtually separating the area surrounding the unit dipole into a near and a distant region, and the field contributed [244]:

$$\mathbf{B}_{demag}(\mathbf{r}) = \mathbf{B}_{near}(\mathbf{r}) + \mathbf{B}_{distant}(\mathbf{r}) \quad \text{Eq. (2.20)}$$

When assuming the unit dipoles are randomly distributed, and observed susceptibility χ is constant throughout the near region defined above (usually a sphere, named Lorentz sphere), the near field vanishes, and the distant field is given by [245]:

$$\mathbf{B}_{demag}(\mathbf{r}) = \mathbf{B}_{distant}(\mathbf{r}) = \mathbf{B}_0(\mathbf{r}) \cdot \{\chi(\mathbf{r}) \otimes \mathbf{b}(\mathbf{r})\} \quad \text{Eq. (2.21)}$$

where \otimes denotes 3D convolution. Therefore:

$$\mathbf{B}(\mathbf{r}) = \mathbf{B}_0(\mathbf{r}) + \mathbf{B}_0(\mathbf{r}) \cdot \{\chi(\mathbf{r}) \otimes \mathbf{b}(\mathbf{r})\} \quad \text{Eq. (2.22)}$$

This forms the foundation of quantifying susceptibility using MRI. Using the Fourier convolution theorem, the above equation can be transformed into a pointwise multiplication in the Fourier domain [17]:

$$\mathcal{F}(\chi(\mathbf{r})) \cdot \mathcal{F}(\mathbf{b}(\mathbf{r})) = \mathcal{F} \left\{ \frac{\mathbf{B}(\mathbf{r}) - \mathbf{B}_0(\mathbf{r})}{\mathbf{B}_0(\mathbf{r})} \right\} \quad \text{Eq. (2.23)}$$

with \mathcal{F} indicates Fourier transform. The right-hand side is sometimes referred as the Relative Difference Field (RDF) [246]:

$$RDF = \frac{\mathbf{B}(\mathbf{r}) - \mathbf{B}_0(\mathbf{r})}{\mathbf{B}_0(\mathbf{r})} \quad \text{Eq. (2.24)}$$

2.3.2.2 Relations between the MR phase and local field perturbation

Using a GRE sequence with multiple T_E , the phase observed by a right-hand MR system is given by:

$$\varphi(\tau) = \varphi_0 + \Delta\varphi_{MR}(\tau) = \varphi_0 + \Delta f_{MR} \cdot 2\pi\tau \quad \text{Eq. (2.25)}$$

where φ_0 is the transceiver phase offset, $\Delta\varphi_{MR}(\tau)$ denotes the phase evolved with time τ , and Δf_{MR} the frequency in the rotating frame that is inherently wrapped within 2π , calculated from:

$$\Delta f_{MR}(\mathbf{r}) = -\frac{\gamma}{2\pi} (B_{demag}(\mathbf{r}) + B_{background}(\mathbf{r})) \quad \text{Eq. (2.26)}$$

with $B_{background}(\mathbf{r})$ denotes the global field inhomogeneity [244].

Chapter 3: Literature Review of quantitative MRI methods for measuring iron

A variety of MRI parameters have been studied to measure iron stores in brain tissues in the past. The T_1 - and T_2 -shortening effects of the brain iron have been observed at different magnetic field strength [156, 162, 165, 247]. As the significant T_2 -shortening effect of the brain iron allows the visualisation of the relative iron levels on T_2 -weighted images, the transverse relaxation rates obtained with SE (R_2) [154, 247, 248] and GRE (R_2^*) [249] both show a positive correlation with post-mortem brain iron concentrations in healthy brains. Although it is time-consuming to obtain the accurate measurement of R_2 by using the SE pulse sequence, it reflects the characteristic microscopic properties of samples and does not need additional diffusion coefficient corrections for multi-echo MRI sequences [250]. Using scans obtained at two different field strengths, the field-dependent R_2 increase (FDRI) is sensitive to brain iron concentrations, especially to ferritin-bound iron oxide nanoparticles [251]. However, this method is rather impractical in clinical settings because it requires scanning patients twice using different scanners with high- and low-field strength, respectively. Utilising the MR phase information, susceptibility-weighted imaging (SWI) [252] was initially proposed for angiography but sometimes was reported as a semi-quantitative method for the brain iron level. Several advanced approaches to map brain iron have been developed recently as research tools but are not yet in clinical use, including quantitative susceptibility mapping (QSM) [253] and magnetic field correlation (MFC) [254].

3.1 R_2 , R_2^* relaxometry and R_2'

The transverse relaxation rate R_2 was one of the first quantitative MRI parameters being investigated in both *in vivo* and *in vitro* human brains, based on the underlying mechanism of (super)paramagnetic (ferritin) iron-induced proton relaxation [156, 161, 162, 165, 255, 256]. Derived from NMR, the SE and MESE pulse sequences (Section 2.2.1) have been used to obtain the R_2 values in tissue, and the relationship between R_2 and tissue iron concentration has been studied in post-mortem mouse,

monkey, and human brains, or in the liver [13, 174, 186, 248, 257]. The linear correlations usually contain an iron-dependent (slope) coefficient, which is mostly linearly proportional to the field strength (tested up to 14.0 T) [247, 258], and an iron-independent offset. Therefore, this field-dependency of the coefficient enables the comparison of the R_2 measured at different field strengths. House *et al.* [50] reported a threshold at 55 $\mu\text{g/g}$ (ww) in brain tissues as a lower detection limit for iron at 4.7 T. At UHF (7.0 T), or with a very high iron concentration, Hocq *et al.* [247] observed an IEP(ESP)-dependent (see Section 2.2.1.2) T_2 in tissue samples. Nevertheless, the quantitative R_2 is insensitive to artifacts introduced by the magnetic field inhomogeneity and generally robust against sequence parameters but sensitive to the changing water coefficient in the tissue [154]. Because of the varied amount of water between the WM and GM, R_2 is limited in quantifying iron content in the brain [154, 249]. At the same time, pathological alteration of water has been observed, it also explains the reducing correlation of R_2 with brain iron when disease groups were considered [42]. To eliminate the impact of water content in brain tissue, a predictive model for R_2 was proposed [50, 154], where a non-iron related tissue parameter, dry-to-wet ratio (DWR), was introduced.

By applying the GRE pulse sequence (Section 2.2.2), the exponential decay rate of transverse relaxation with the field inhomogeneity R_2^* can be obtained. The T_2^* -weighted images and R_2^* maps of iron-loaded tissues such as liver and brains usually showed a higher contrast-to-noise ratio (CNR) between the iron-rich region and the surrounding tissue, compared to T_2 -weighted images or R_2 maps [178, 259-261]. It is primarily caused by the cellular distribution of the iron content, which is encapsulated and compartmentalised within certain regions, generates the local field inhomogeneity, and accelerates dephasing in the GRE sequence. This effect is described by the static dephasing regime of the MR signal [227].

One disadvantage of R_2^* originates from the employed GRE pulse sequence. As it is very sensitive to the spin dephasing caused by local and global field inhomogeneity, the image quality and the reproducibility of the quantitative measurement can be

compromised by imperfect shimming, B_1 effect, and susceptibility artifact. An R_2' method was later proposed to correct some of the effects by eliminating the global field inhomogeneity from the measured parametric map, by subtracting R_2 from the R_2^* maps by definition $\frac{1}{T_2^*} = \frac{1}{T_2} + \frac{1}{T_2'}$, where $\frac{1}{T_2'} = R_2'$ [186, 200]. This normally requires a specific SE-GRE sequence, and accurate modelling of R_2 from the hybrid SE-GRE sequence [228, 262]. Ordidge *et al.* [263] reported a method to estimate iron content in the neurodegeneration by using local susceptibility R_2' .

3.2 Field-dependent R_2 increase

Another attempt to overcome the limitation of pathological changes of water content in brain tissue was proposed by Bartzokis *et al.* [251, 264], FDRI, which is calculated by the R_2 measurements obtained under one high magnetic field and one low magnetic field, respectively. The age-related increase of iron content in the human brain was later validated via *in vivo* MRI imaging by the same group [265]. By using the FDRI, the non-haemin iron content in the frontal WM, caudate nucleus, putamen, and globus pallidus were estimated among subjects with the age ranging from 20 to 81 yrs, and the relationship between the quantitative MRI measurement was found highly correlated with the post-mortem observation of non-haemin iron content.

3.3 SWI and QSM

In the recent decade, the use of the phase information obtained from the GRE sequence is found to be able to generate novel contrast that is related to the bulk susceptibility of the tissue. Both qualitative and quantitative methods exist, namely SWI (susceptibility-weighted imaging) [13, 266, 267] and QSM (quantitative susceptibility mapping), respectively. Rarely, some research utilising quantitative or numerical measurements of SWI signals were also termed QSM in the literature, though the SWI does not necessarily reveal the true range of the imaged subject's susceptibility. It is because the SWI image is generated by masking the conventional magnitude weighted image using a high-pass filtered phase image, where the slow-

varying background phase was removed by filtering [267]. In this thesis, the term QSM is exclusively used for the methods described below.

Recall Section 2.3.2, the phase information and the bulk magnetic susceptibility distribution of brain tissue can be reconstructed based on the phase image of MR by applying a gradient echo pulse sequence. Several approaches [18, 51, 268-273] have been proposed to quantitatively reconstruct the susceptibility image and may be categorised based on the two crucial QSM processing steps employed: different methods of processing phase data (generating RDF), and different approaches to solving the field-to-source (RDF-to-susceptibility) inverse problem. The phase processing usually consists of the phase-unwrapping and the background field removal, which are crucial to revealing the accurate RDF from the raw phase data.

For the phase-unwrapping, several methods have been proposed to resolve the inherently wrapped phase: path-following, Laplacian phase unwrapping and unwrapping within time-domain [274, 275]. Generally, the unwrapping relies solely on temporal technique is found inadequate to resolve the wrapped phase and the spatial unwrapping is also required. Previously proposed methods to remove the background (global) field contribution includes projection onto dipole fields (PDF), sophisticated harmonics artifact reduction for phase (SHARP) [245] and the Laplacian boundary value (LBV) method [276]. Those methods are found to be superior to homodyne filtering, as they treat the observed total field authentically as a superposition of the local field caused by the subject, and the background field by the hardware or material outside of the FOV. Variations of SHARP methods have also been reported in the literature [273, 277], usually by dynamically varying the size of the convolution kernel employed in the method, based on information provided by the magnitude images. For the multi-coil acquisition and parallel imaging, the SENSE-based approach [233] is found to generate the most reliable phase results [274]. These phase processing methods had been reviewed carefully in numerical phantoms and human brains somewhere else [274, 275].

Although methods exist for solving the field-to-source ill-posed inverse problem [278] by direct matrix inversion without employing constraints, it requires repeated MR acquisitions of the subject, with varying direction for each acquisition with regard to the external magnetic field [224, 279]. As the orientation of the main magnetic field of the scanner is fixed, this requires rotation of the subject undergoing MR examination, which is impractical in clinical MRI. Additional co-registration steps are therefore required, which could introduce variations of the resulting susceptibility, especially near structural boundaries. Single-orientation QSM using regularisation or inverse filtering to overcome the ill-posed problem that is caused at the magic angle Φ where the unit dipole function $\mathbf{b}(\mathbf{r})$ in the k-space equals zero [18, 19]:

$$\mathbf{b}(\mathbf{k}) = \mathcal{F}\{\mathbf{b}(\mathbf{r})\} = \frac{1}{3} - \cos^2\Phi \quad \text{Eq. (3.1)}$$

and the associated values generate errors that follow the wave-propagation, demonstrated as cone-shaped streaking artifacts in the susceptibility. Historically, this method was proposed to regularise the solution in the k-space by employing a modified inverse filter, which is usually referred as truncated k-space division (TKD) method [13, 217].

Least-squares based algorithms were proposed to solve this problem in the spatial domain, by minimising the error between the RDF calculated from the susceptibility χ as a pseudo-solution and the measured RDF, using the least-squares (LSQR) algorithm [280]. This method is mathematically unbiased, but the result does not always show sufficient suppression of the streaking artifacts. To solve this problem, approaches with regularisation with *a priori* were proposed, using a sophisticated algorithm that reformulates the inverse problem into a constraint minimisation. One of the most influential algorithms based on this method is the nonlinear morphology enabled dipole inversion (nMEDI) [17-19], where the magnitude edge information is used as *a priori* for the solution. It has been theoretically analysed and shown to be able to sufficiently suppress the streaking artifact in the susceptibility images. It was also reported to generate superior contrast and numerical results in human brain MRI to TKD-based methods [19, 224, 281]. However, introducing the regularisation

term generates bias in the solution, and the influence of the selection of the regularisation parameter on the resulting susceptibility map has not yet been systematically studied at the time of writing.

Nevertheless, the susceptibility maps generated using the QSM methods can have visually appealing contrast that could reveal additional information, which is not usually evident on the conventional weighted images or parametric maps. Langkammer *et al.* [51] reported a post-mortem validation of the QSM method using the iron measurement from the same fixed 13 post-mortem brains reported by Krebs *et al.* [9], and it showed a good linear correlation. Since then, the number of clinical studies that used the QSM method to image the brain iron, has greatly increased, where the measured susceptibility was often used for comparison between groups of subjects. With better accuracy and sensitivity in classifying and differentiating disease cohorts based on the brain iron content, the state-of-art QSM method appeared to have potential in quantitative brain iron in future research [191, 282].

3.4 Other phase-related MRI techniques

Sharing similar signal formation as QSM, MFC [283] is also generated from the local phase shift using the GRE pulse sequence. It was demonstrated to be able to quantify iron content via the field inhomogeneity [284]. Other potential methods for measuring the brain iron include the frequency difference mapping (FDM) [225], which does not require the use of phase unwrapping or sophisticated image processing compared with QSM.

Chapter 4: Research methodology for the quantitative MRI

This chapter provides the principles for selecting the quantitative MRI approach and techniques employed in this thesis, and the justification. Hereby it presents the overview of the research methodology in the MRI study design, acquisition, image processing and statistics in this work, while the specific materials and scientific methods used for the individual experiment were described in respective chapters (Chapter 5, 6 and 7).

4.1 *In vitro* phantom MRI

Physical MR phantoms are regularly used to validate quantitative measurements acquired using MRI. Historically, it derived from the phantom for ^1H NMR, usually consisting of water doped with paramagnetic ions [165]. In MRI, a large variety of phantoms exist, and more sophisticated phantoms can be constructed [228, 285-290]. In general, it can be constructed with materials with known and controlled electromagnetic properties, to predict observed MR signal behaviour. Or by changing its composition, it can mimic a particular *in vivo* microenvironment or can be used to investigate the interaction within the phantom by adopting physiological buffers and biomolecules and/or biomaterials, native or synthetic [283, 285, 289, 291-293]; or to realise *in vivo* microstructures of organisms [294, 295]. The advantages of using MR phantoms to investigate a quantitative MRI method include: 1) the relatively simple system, compared with the biological tissue, and 2) the maximisation of controlling the materials being imaged, which enables direct comparison between the physics models and the experiment results. However, the MR phantom is also intrinsically limited by the simplification of the systems, compared with the realistic tissue or organisms.

4.2 *In vivo* human brain MRI

Unlike iron quantification in the liver, where a biopsy can be performed relatively easily [173, 174], validation of the *in vivo* brain imaging is intrinsically challenging. An alternative method in imaging iron in the brain is to perform post-mortem validation (examples given in Chapter 3). In this method, the deceased brains are usually

imaged first, using the MRI technique to be tested, and the brains or tissue specimens are then dissected, and the iron concentration of the specimens measured using other analytical methods. By comparing with the exact iron concentration measurement obtained from the analytical technique with high reliability and reproducibility [78], post-mortem validation is considered the most robust method to associate the MRI observation with the tissue properties at the time of writing. However, limitations and challenges remain for this method, of translating the conclusion to *in vivo* MRI, including the effect of post-mortem fixation, tissue handling and segmentation, the imaging condition (*e.g.*, temperature, shimming, B_1) [64-69, 296].

4.2.1 Iron estimation for *in vivo* human brain MRI

To investigate the tissue properties *in vivo*, and the longitudinal changes for individuals, it is necessary to image living subjects using MRI. As brain biopsy for iron quantification is relatively impractical [12], an alternative is to estimate the iron concentration of the living patient's brain. Specifically, it involves estimation of the brain iron using retrospective post-mortem measurements. Selected studies were presented in Section 1.2.1, whereas a more comprehensive summary was previously reported by Haacke *et al.* [13], and a recent systematic review of trace elements (including iron) in the brain was reported elsewhere [46]. In the quantitative MRI literature, the most prevalent and widely employed source is the iron measurement work done by Hallgren and Sourander [11] in 1958 (also see Section 1.2.1). In this work, Hallgren and Sourander examined 81 unfixed healthy human brains from subjects with the age from 0 to 100 yrs, and measured and analysed the non-haemin iron concentrations in 11 brain regions. The empirical predictions of iron concentrations of various brain regions, as a function of the subject's age, are provided in Appendix A, and selected models for the brain regions related to this PhD project are given by [11]:

Caudate nucleus:

$$y = 96.6 \times (1 - e^{-0.05x}) + 3.3 \quad \text{Eq. (4.1)}$$

Globus pallidus:

$$y = 214.1 \times (1 - e^{-0.09x}) + 3.7 \quad \text{Eq. (4.2)}$$

Putamen:

$$y = 146.2 \times (1 - e^{-0.04x}) + 4.6 \quad \text{Eq. (4.3)}$$

with y denoted the non-haemin iron in $\mu\text{g/g}$ wet weight (ww), x the subject's age in years.

4.2.2 Group comparison using *in vivo* human brain MRI

The quantitative MRI measurement (summarised in Chapter 3) acquired from the *in vivo* human brain MRI, therefore, may be utilised as an indirect measure of iron content, for the comparison between groups of subjects (patients) [13, 14]. Although the iron content represented by the quantitative MRI measurement may be indirect, rather than exact (absolute), the comparison can be valid and reproducible, when appropriate MRI techniques are applied, and the MR acquisition conditions are controlled.

For comparing groups of patients with healthy subjects or volunteers, matched age and gender between groups are in general necessary, and rigorous clinical assessments with up-to-date and regularly revised standards should be performed, on all participants, to control the subject-related variable. For instance, PD symptoms and severity may be assessed with the Unified Parkinson's Disease Rating Scale (UPDRS) [123, 124] and the University of Pennsylvania Smell Identification Test (UPSIT) [125], together with the Parkinsonism progression staging assessment, Hoehn and Yahr (H&Y) year [126], established by Hoehn and Yahr. Additionally, the Braak's staging method [121, 127] can be employed for Parkinsonism, which incorporates Lewy body pathology, and the Montreal Cognitive Assessment (MoCA) [297] is also routinely used to clinically measure mild cognitive impairment (MCI).

4.3 MR imaging and reconstruction

The imaging acquisition methods applied in this research are designed and adjusted,

so that they are comparable across the platforms and systems provided by different vendors (Siemens, GE Healthcare, Bruker), and for different magnetic field strengths (3.0 T and 9.4 T). For non-retrospective data acquired in the PhD study (Chapter 6 and 7), within the individual platform, the MR images were obtained using the same coverage, slice locations and corresponding slice thickness among 2D and 3D acquisition and across different modalities, to ensure the correspondence of the signal location and to minimise the co-registration error in the later analysis. Principally, the dual-contrast FSE (TSE) sequence was applied for the effective R_2 mapping, the CPMG-based MESE sequence for conventional R_2 relaxometry, and the 3D GRE sequence for R_2^* mapping and QSM. The exact parameters of each pulse sequence are presented in the following experiment chapters (Chapter 5-7), correspondingly.

To ensure the pre-condition of the images satisfied the requirements for the QSM post-processing, and to minimise vendor-dependent contrast filtering and geometry correction, off-line reconstruction was conducted for non-retrospective MRI (Chapter 6 and 7), using MATLAB (R2019b, MathWorks). The off-line reconstruction of each acquisition is detailed in the *Methods* sections of Chapter 6 and 7, respectively. Online reconstruction was performed at the scanner after the acquisition only for inspection purposes.

4.4 Post-processing

4.4.1 Quantitative MRI parametric mapping

Longitudinal relaxation time T_1 may be calculated from the SE-based saturation recovery pulse sequence by fitting the signal intensity (magnitude) to the mono-exponential function:

$$S(T_R) = M_0 \left(1 - e^{-\frac{T_R}{T_1}} \right) + C \quad \text{Eq. (4.4)}$$

where $S(T_R)$ is the observed T_R -dependent magnitude MR signal, M_0 indicates the proton density, T_1 is the longitudinal relaxation time to be estimated, and C is a constant offset related to the hardware system and the experiment condition. The longitudinal relaxation rate R_1 can be calculated by the reciprocal of T_1 value:

$$R_1 = \frac{1}{T_1} \quad \text{Eq. (4.5)}$$

The transverse relaxation rates R_2 and R_2^* can be calculated from the magnitude data of the MESE and 3D GRE pulse sequences respectively. The observed signal with the given relaxation rates are assumed to follow the mono-exponential decay:

$$S(T_E) = M_0 e^{-\frac{T_E}{T_2}} + C \quad \text{Eq. (4.6)}$$

where $S(T_E)$ is the T_E -dependent magnitude MR signal, M_0 indicates the proton density, T_2 (T_2^*) indicates the transverse relaxation time constant to be calculated and C is a constant offset related to the hardware and the experiment condition. The transverse relaxation rate R_2 (R_2^*) is then given by:

$$R_2 = \frac{1}{T_2} \quad \text{Eq. (4.7)}$$

4.4.2 QSM framework

Employed in this PhD research (Chapter 6 and 7), the general post-processing framework that incorporates QSM, is depicted in Fig. 4.1. The general QSM pipeline consisted of phase processing and dipole inversion.

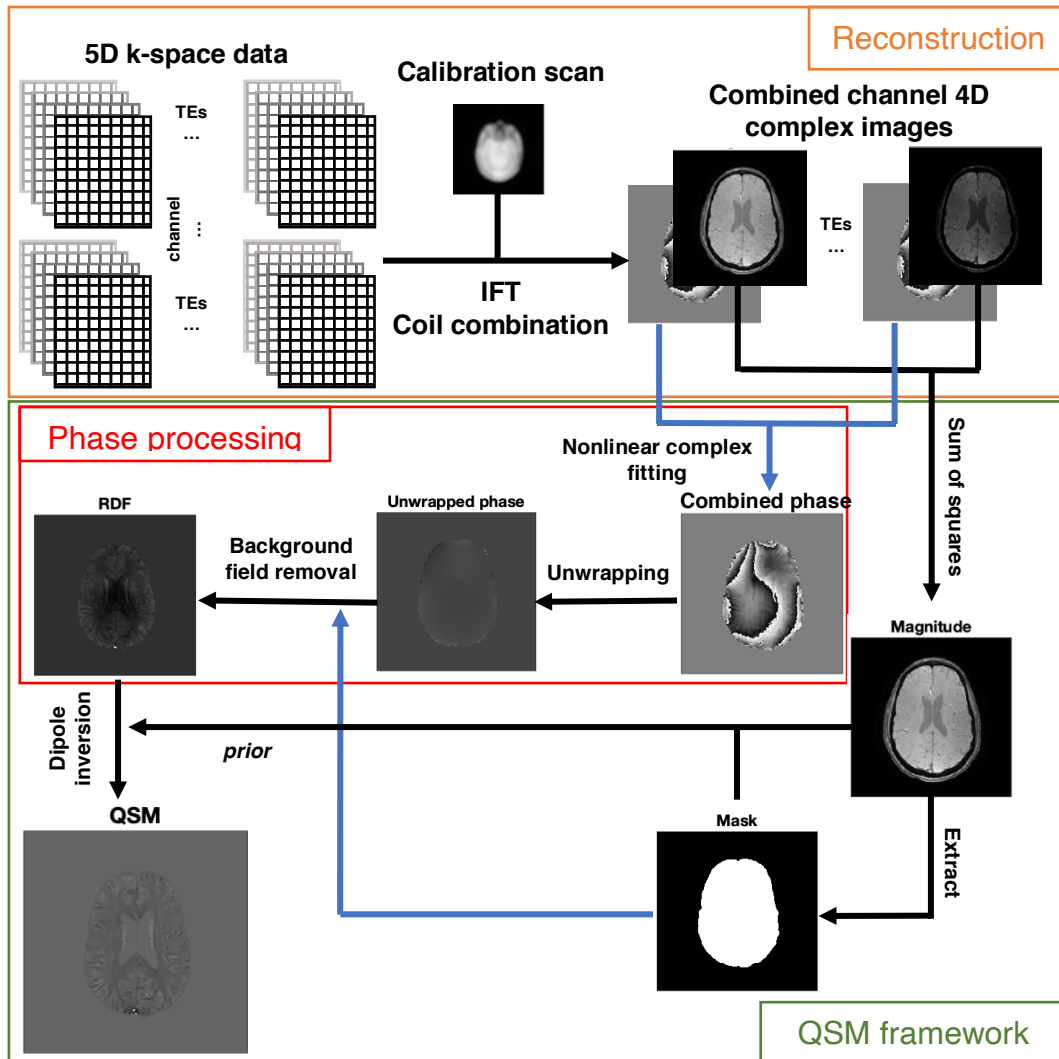


Fig. 4.1 Image post-processing pipeline with QSM.

4.4.2.1 Phase correction and normalisation

A pre-processing step can be carried out before the main QSM processing, including the correction of echo-to-echo phase inconsistency and data normalisation [298]. The correction of the echo-dependent phase can remove the inherent readout phase correction, which may be performed during the acquisition. Then the complex MR signal intensity can be normalised by the standard deviation of the background noise level and signal-to-noise ratio (SNR) is calculated according to:

$$SNR = \frac{mean_{signal}}{\sigma_{noise}} \quad \text{Eq. (4.8)}$$

The magnitude image of the reconstructed complex image data can be generated by the sum-of-squares method, summing along the echo direction, and a binary phantom mask for the brain or phantoms may be generated by thresholding.

4.4.2.2 Phase unwrapping and frequency map estimation

To resolve the true total phase shift of each pixel from the raw phase image, which is intrinsically wrapped within $(-\pi, \pi]$ due to the nature of quadrature detection of the MR signal (see Eq.(2.25) in Section 2.3.2.2), temporal and spatial unwrapping need to be performed. The temporal technique exploits the T_E -dependency of the phase evolution, and estimated the unaliased phase via a non-linear complex fitting [298]. The spatial unwrapping attempts to resolve the true phase of each voxel, by testing the neighbouring data point, based on a reliability map derived from the magnitude images (region-growing method [299]) or based on the Laplacian condition (Laplacian operator method [300]).

To remove the global field inhomogeneity, which is often a few orders of magnitude larger than the frequency shift caused by the subject, a procedure called background field removal, is required to reveal the frequency map when a reference scan [243, 276, 301] is not available or impractical to acquire (*e.g.*, *in vivo* imaging). Various background field removal techniques have been reported in the literature [245, 246, 276, 277, 302-304], and reviewed elsewhere [275]. The technique development remains an active research field, which exceeds the scope of the PhD thesis. Essentially, this step is to separate the contribution from the source inside (*e.g.*, subject or phantom) and outside of the imaging volume (*e.g.*, main magnetic field drift, imperfect shimming, RF coil's shape and material, subject-environment interface). The background field removal techniques built upon the same principle, that the field perturbation generated by the source from outside of the imaging volume (background field) satisfied the sets of harmonic functions.

Therefore, it can be removed by either modelling the harmonic function of the background field (*e.g.*, PDF [246]), or directly eliminating the term that satisfied the spherical mean value (SMV) theorem via deconvolution (*e.g.*, SHARP [245]). For instance, PDF (projection onto dipole fields) method [246] uses a conjugate gradient (CG) algorithm, to solve the least-squares minimisation problem of the background field, with the weight derived from the sum-of-squares magnitude mask in the Fourier domain. It models and mitigates the 0th- and 1st-order spherical harmonic

terms in the field expansion, which are assumed to be the result of insufficient shimming. The SHARP (sophisticated harmonic artifact reduction for phase data) algorithm [245] and the methods derived from it, *e.g.*, RESHARP [277], V-SHARP [302, 303], R-SHARP [304], remove the background field by applying one or multiple SMV filters to the masked total field. It is followed by k-space truncation as an additional regularisation step, to compensate for the non-harmonic contributions, from unaccounted transmitter frequency offset during the deconvolution [245]. The background removal by solving the LBV (Laplacian boundary value) problem [276] exploits the solution of Laplace’s equation by assuming simple boundary conditions to efficiently remove the background field. By transforming the problem into a boundary value problem of Poisson’s equation, the LBV background removal applied a finite difference method by employing a full multigrid algorithm to solve the partial differential equations (PDEs). After the background field removal, the resulting frequency map (or RDF, see Section 2.3.2.2) is the input of the following dipole inversion.

4.4.2.3 Field-to-susceptibility dipole inversion with nMEDI-L₁ [18]

Introduced in Section 3.3, nMEDI-L₁ [18] is one of the most influential and sophisticated algorithms available for QSM post-processing, based on a regularised approach to suppress the artifact generated by the single-orientation acquisition. It is also one of the fundamental frameworks for many lately developed pipelines for the human brain QSM [271, 273, 305-307]. Compared with the early attempts that relied on the k-space truncation [13], the susceptibility source is estimated using a Bayesian estimation approach. It uses the magnitude *a priori* to find the general solution to the forward source-to-field problem, which is treated as a partial differential equation. Alternative approaches to this inversion problem also exist [245, 272, 273, 308-310], but the resulting susceptibility accuracy [18, 19, 281], reproducibility at different field strengths [311] are only well documented for nMEDI-L₁. The inverse problem is reformulated to a constrained L₁-norm optimisation in nMEDI-L₁ [18]:

$$\operatorname{argmin}_{\chi} \frac{1}{2} \| W(e^{-i\Phi} - e^{-iF^{-1}DF\chi}) \|_2^2 + \lambda \| M\nabla\chi \|_1 \quad \text{Eq. (4.9)}$$

where χ is the susceptibility, W a weight matrix of the noise that is estimated from the magnitude image, Φ the local phase, F and F^{-1} denote the Fourier operator and its inverse, D indicates the unit dipole function, λ the regularisation parameter, M the binary mask obtained from the magnitude image, and ∇ denotes the gradient operator that indicates the smoothness of the solution. Moreover, for the *in vivo* human brain data, an additional L_2 -term can be employed in the minimisation problem, to enable a solution with homogeneous CSF as a zero-susceptibility reference (MEDI+0) [271]:

$$\operatorname{argmin}_{\chi} \frac{1}{2} \| W(e^{-i\Phi} - e^{-iF^{-1}DF\chi}) \|_2^2 + \lambda_1 \| M\nabla\chi \|_1 + \lambda_2 \| M_{CSF}(\chi - \overline{\chi_{CSF}}) \|_2^2$$

Eq. (4.10)

where λ_1 and λ_2 denote the regularisation parameters for the L_1 - and L_2 -optimisations respectively, M_{CSF} indicate the binary mask for CSF, and $\overline{\chi_{CSF}}$ the average susceptibility measured within the CSF mask.

4.5 Image analysis

In quantitative MRI, both pixel-wise analysis and ROI analysis can be applied. The pixel-wise analysis often employed in multi-modal measurements, when images acquired by different techniques can be aligned and co-registered, to extract structural and functional information [109, 151]. It also enables histogram analysis, to investigate the distribution of the pixel-wise data, which is valuable for inspection and interpretation of heterogeneity. On the other hand, ROI analysis can extract the representative information from the image, and is routinely used in human brain MRI, to measure parameters within certain brain nuclei or regions. Segmentation on human brain MRI, the procedure of drawing the ROI that overlaps the anatomical region of the brain, requires an understanding of the MR pulse sequences, corresponding tissue contrast mechanism, and human brain anatomy [312]. Regarding this PhD project, the basic MR contrast of the brain ROI, on relevant MR images, are summarised in Table 4.1.

Table 4.1 Contrasts of selected brain regions on different MR images.

ROI	Proton density-weighted image	T ₂ -weighted image	susceptibility map
caudate nucleus	hyperintensity to surrounding tissue		
globus pallidus	hypointensity to surrounding tissue	hypointensity to surrounding tissue	hyperintensity to surrounding tissue
putamen	hyperintensity to surrounding tissue	hyperintensity of the anterior-medial part, hypointensity of the posterior-lateral part to surrounding tissue	hyperintensity to surrounding tissue
red nucleus	hypointensity to surrounding tissue	hypointensity to surrounding tissue	hyperintensity to surrounding tissue
substantia nigra	hypointensity to surrounding tissue on the middle- superior levels, mixed contrast on the inferior-middle level	hyperintensity to surrounding tissue	hyperintensity to surrounding tissue

Chapter 5: Effective transverse relaxation rate, derived from dual-contrast fast-spin-echo (FSE) MRI, enables detection of hemisphere differences in iron level and function in Parkinson's disease and healthy brain

5.1 Introduction

Iron and its homeostasis are closely associated with the basic functions of organisms [1] (see Section 1.1). In human brains, the concentration and distribution of iron vary among different brain regions [13, 46], and experience dynamic changes, and the accumulation of iron content in the brain was observed in the normal ageing [7-11]. A landmark post-mortem work of the non-haemin iron concentration in human brains was performed by Hallgren and Sourander, and the age-dependent predictions of non-haemin iron concentration in various brain regions were reported [11]. The authors measured and analysed the non-haemin iron concentrations in 11 brain regions, after examining 81 unfixed brains from subjects with the age from 0 to 100 yrs. Other post-mortem research also investigated the brain iron change with normal ageing more recently [7-10], using different techniques including ICP-MS and AAS. Pathological changes of iron content in particular brain regions also have been observed in several neurodegeneration (Section 1.1.2) [52, 58-62, 70].

Hence, increasing interest has been drawn to how to detect the iron level in living brains, utilising clinically available techniques such as MRI. Primarily stored in ferritin, non-haemin brain iron demonstrates superparamagnetism under an applied external magnetic field at normal body temperature [239], accelerating neighbouring proton's relaxation [239, 241, 242]. Detailed in *Chapter 3*, several MRI measurements have been reported to quantify brain (tissue) iron in the past, including R_2 derived from SE sequence [50, 174, 186, 248, 257], R_2^* calculated from GRE [178, 259-261]. Elaborate methods such as FDRI [251, 264, 265] and R_2' [186, 200, 263] require multiple acquisitions or refine sequences. Emerging in the recent decade, the advanced QSM technique [51] employs sophisticated post-processing steps, but it is sensitive to acquisition parameters and processing algorithms. On the other hand, robust against the acquisition parameters and systems, the conventional transverse relaxation rates

R_2 remains as a reliable approach among existing MRI methods for tissue iron quantification.

Nevertheless, the long acquisition time of the SE sequence has been the main disadvantage of the conventional R_2 method (Section 2.2.1.1-2) in clinical settings, preventing it from being used as a routine clinical MRI technique. Attempts to overcome this limitation, include the dual-echo SE method [248], by minimising the number of echoes required to fit the observed signal to the exponential decay of the apparent transverse relaxation, which has shown satisfactory results when the T_E were selected carefully. Meanwhile, TSE (turbo-spin-echo) [313, 314], also known as FSE (fast-spin-echo) [236] (Section 2.2.1.3) has been employed as a routine clinical MRI sequence, due to its versatility in generating MRI contrast and its rapid acquisition. Utilising k-space segmentation, FSE accelerates the scan time by the factor of the ETL (echo train length, see Eq.(2.15) in Section 2.2.1.3), compared with the SE sequence. The MRI contrast of FSE is dominated by the TE, at which the MR signal fills in the central k-space. These advantages have enabled FSE to be a routine pulse sequence in clinical MRI, widely available as current and archived data. It is also found prevalent in large cohort studies [206], such as PPMI (Parkinson's Progression Markers Initiative) [207].

At the clinical field strength, FSE MRI had been almost exclusively used for anatomical imaging in the past, and the sensitivity of the whole brain quantitative FSE-derived T_2 was reported to be insufficient for diagnosis purposes at 1.5 T [315]. Recently, attempts were made to recover the 'true' T_2 from the MR images obtained by the FSE sequence by modelling the signal decay [316-318]. However, accurate results require exhaustive details of acquisition parameters, including the shape of the RF pulse and the actual FA, but this information is often lost for the retrospective data. Therefore, an alternative method of calculating a quantitative MRI measure is presented in this work, termed effective R_2 , derived from dual-contrast FSE MRI sequence, to evaluate the iron level within healthy and PD brains, using *in vivo* human brain 3.0 T MRI data from PPMI, and with reference to the prior-published post-mortem data for regional brain iron concentrations. Demonstrating in case-

control cross-sectional and longitudinal studies, this work also investigated the extend of the effective R_2 as a quantitative MRI method to indicate functional changes in the brain with PD.

5.2 Methods

5.2.1 PPMI subjects

All participants were screened by the study core of PPMI before the enrolment and satisfied the inclusion and exclusion criteria of the PPMI cohort study (<http://ppmi-info.org/>). Any motor, neuropsychiatric and cognitive clinical symptoms were assessed by the PPMI clinical core for each subject, including UPDRS [123, 124], UPSIT [125], and MoCA [297] (introduced in Section 4.2.2). Neuroimaging scans, including structural MRI and DaT SPECT imaging, were performed by the imaging core for each subject at screening.

PPMI's inclusion criteria for PD participants required subjects: 1) had been diagnosed as Parkinson's disease for 2 years or less than 2 years at screening; 2) aged 30 years or older at time of PD diagnosis; 3) at Hoehn and Yahr Stage I or II at PPMI study baseline (0-month); 4) must have had at least two of the following symptoms: resting tremor, bradykinesia, rigidity (must have either resting tremor or bradykinesia) or either asymmetric resting tremor or asymmetric bradykinesia; 5) have had confirmation from the PPMI imaging core that screening dopamine transporter SPECT scan was consistent with dopamine transporter deficit; 6) not expected to require PD medicine within at least 6 months since the baseline. The exclusion criteria were: 1) subjects taking PD medication (levodopa, dopamine agonists, MAO-B inhibitors, or amantadine) at the screening, or had taken PD medication within 60 days or for more than a total of 60 days prior to the screening; 2) received medicines (neuroleptics, metoclopramide, alpha methyl dopa, methylphenidate, reserpine, or amphetamine derivative) that might interfere with dopamine transporter SPECT imaging with 6 months of screening; 3) had use of investigational drugs or devices within 60 days of baseline (screening).

Inclusion for healthy subjects (HC) required that subjects must be 30 years old or above at screening. Exclusion criteria were the following: 1) active clinically significant neurological disorder at the screening, or previously obtained MRI scan with evidence of clinically significant neurological disorder; 2) received medicines that might interfere with dopamine transporter SPECT imaging with 6 months of screening; 3) had use of investigational drugs or devices within 60 days of baseline; 4) MoCA score less than or equal to 26; 5) first degree relative with idiopathic PD.

5.2.2 Retrospective MR data selection

All retrospective MR data obtained and analysed in this PhD project are screened and selected from the PPMI MRI database for rigorous case-control analysis, therefore, criteria are applied to minimise the potential bias introduced by the magnetic field strength, vendors, age, gender, and matched longitudinal data availability. Three Tesla (3.0 T) retrospective clinical MR data are selected to ensure the highest possible image resolution and SNR, and the images acquired by Siemens TrioTim system (syngo MR B15) are selected for processing and analysis, after considering the cross-sectional and longitudinal data availability. The MRI data of 12 early-stage drug-free PD (age range 39.2-60.3 yrs, 7 males and 5 females) and 12 age- and gender-matched healthy controls (HC, age range 40.6-60.1 yrs, 7 males and 5 females) are selected, processed, and analysed.

5.2.3 MR acquisition

The retrospective MR data obtained from PPMI were acquired by a dual-contrast 2D FSE pulse sequence on Siemens TrioTim system, 'Axial PD-T2 FSE'. The resulting proton density-weighted and T₂-weighted images were acquired using following acquisition parameters: T_R = 3000 or 3270 ms, ESP = 11.2 ms, ETL = 14, effective T_E = 11.2 and 101 ms, FA = 150 °, acquisition plane = axial, FOV = 256 × 228 mm, matrix size = 256 × 228, in-plane resolution = 1 × 1 mm², bandwidth (BW) = 47.6 kHz, percent phase FOV = 0.9, slice thickness = 3 mm, number of slices = 52 or 54.

5.2.4 DaTScan acquisition and calculation of Striatal Binding Ratio (SBR)

As reported in the PPMI imaging and analysis protocols, functional SPECT imaging of

striatal dopamine transporters (DaTScan) was acquired from the participants after ^{123}I -ioflupane injection. The SPECT data were reconstructed and processed prior to the SBR calculation by the PPMI imaging core. SBR used in this work was provided by the PPMI study documentation, which was calculated as the uptake density of (ROI/the occipital cortex- 1), where the occipital cortex was used as a reference. In the study, SBR was calculated for the bilateral caudate and putamen, indicating the dopamine receptor associated with dopamine transporters (DaT) uptake in the brain regions.

5.2.5 Calculation of the effective transverse relaxation rate (effective R_2)

Compared with the conventional R_2 , which is obtained from the T_2 decay using SE or MESE (see Section 2.2.1.1-2), the effective R_2 termed here in this PhD project, is calculated from the MR images acquired by the dual-contrast FSE sequence (Fig. 5.1).

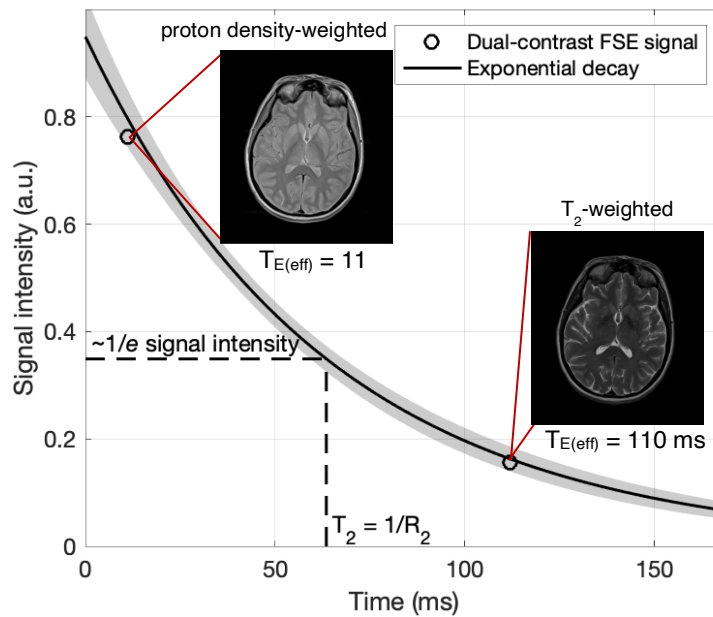


Fig. 5.1 MR signal decay in the dual-contrast FSE pulse sequence.

In an FSE pulse sequence, the observed signal is dominated by the T_E located at the central k-space, effective T_E ($T_{E(eff)}$):

$$S(T_{E(eff)}) = M_0 e^{-\frac{T_{E(eff)}}{T_2}} \quad \text{Eq. (5.1)}$$

where $S(T_{E(eff)})$ is the magnitude MR signal that is dominated by $T_{E(eff)}$, M_0 the effective proton density, and therefore T_2 is the corresponding effective transverse relaxation time (effective T_2) to be estimated. For a dual-contrast sequence, there are

$$\begin{aligned} S_{PD}(T_{E(eff1)}) &= M_0 e^{-\frac{T_{E(eff1)}}{T_2}}, \text{ and} \\ S_{T_2}(T_{E(eff2)}) &= M_0 e^{-\frac{T_{E(eff2)}}{T_2}} \end{aligned} \quad \text{Eq. (5.2)}$$

for the proton density-weighted MR signal and the T_2 -weighted signal respectively, demonstrated in Figure 5.1. Hence the effective R_2 is defined by the reciprocal of the effective T_2 :

$$\text{effective } R_2 = \frac{\ln\left(\frac{S_{PD}}{S_{T_2}}\right)}{\Delta T_{E(eff)}} \quad \text{Eq. (5.3)}$$

where

$$\Delta T_{E(eff)} = T_{E(eff2)} - T_{E(eff1)}. \quad \text{Eq. (5.4)}$$

Due to the high sensitivity of the logarithm to the background noise, the data are pre-processed to obtain a zero-mean background before fitting.

5.2.6 Segmentation

The ROIs are delineated manually and measured within ImageJ (Fig. 5.2), based on the human brain atlas [312]. The ROIs include bilateral caudate nucleus head (CN), globus pallidus (GP), putamen (PUT), red nucleus (RN) and substantia nigra (SN). The segmentation is carried out on the consecutive slices of the proton density- T_2 weighted image series acquired by the 'Axial PD- T_2 FSE' sequence. For repeated measurements in human brains, a set of ROIs for the individual is delineated based on the baseline acquisition, and is translated to the follow-up scans, and refined when necessary.

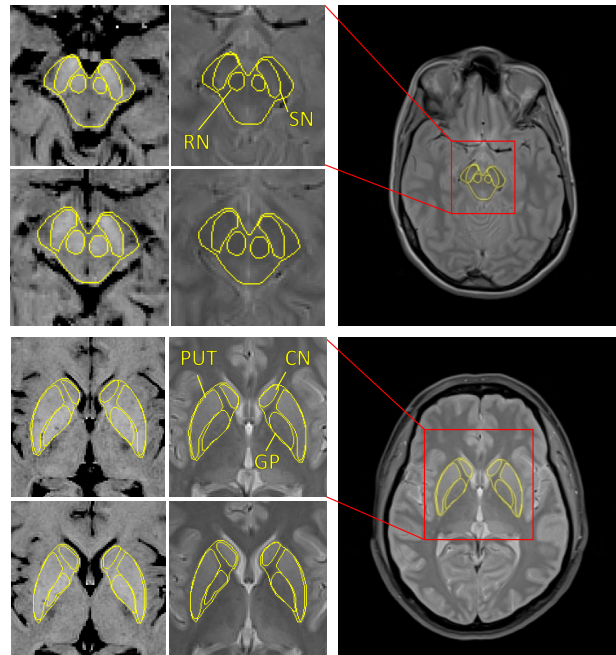


Fig. 5.2 Example segmentation of *in vivo* human brain MRI obtained from PPMI.

ROIs overlay on the effective R_2 parametric maps (left column) derived from $T_{E(\text{eff})} = 11$ ms and 101 ms. CN – caudate nucleus, GP – globus pallidus, PUT – putamen, RN – red nucleus, SN – substantia nigra.

5.2.7 Estimation of the brain iron concentrations

The average iron concentrations in various brain regions have been reviewed elsewhere [13, 46]. Although the variation of the absolute brain iron concentrations was observed, across the results in the literature, the relative concentrations between the brain regions reported from multiple sources were generally consistent. However, the iron concentration in the healthy brain is known to be dynamic as a function of the subject's age [7-11]. Therefore, in this PhD study, the age-dependent iron concentrations of different brain regions are estimated, from Hallgren and Sourander's post-mortem study on unfixed tissue [11], which contains the largest sample size and the widest age span in the literature.

The iron concentrations in the caudate nucleus, globus pallidus, and putamen, are calculated according to the regression equations between iron level and the age of the subject, provided in Hallgren and Sourander's work [11]. The regression formulas of the iron concentrations of substantia nigra and red nucleus with age were not

reported by the authors [11], so the average iron concentrations of the regions (measured from 52 and 44 healthy subjects respectively, age 30-100 yrs) reported in the same study [11], are employed in our work for the analysis.

5.2.8 Data processing and statistical analysis

The mean, median, standard deviation of each measurement within the bilateral ROIs are extracted, and the histogram of the pixel values are examined and tested for normality using Shapiro–Wilk test. The mean values and the median values of the effective R_2 are compared and the mean effective R_2 values are used for subsequent analysis.

Any difference in the age, gender, clinical assessment results at baseline (0-month) between HC and PD are tested using independent t-test for the subject selection. Any difference in the effective R_2 measurements between left and right hemispheres are tested using paired two-samples t-test, in HC and PD group respectively. To investigate the feasibility of differentiating the brain regions with the effective R_2 , the baseline (0-month) measurements of the effective R_2 from bilateral brain regions of participants are combined by averaging. Then Friedman’s two-way analysis of variance (ANOVA) is employed for all 5 brain regions, with diagnostic groups (*i.e.*, HC and PD) as the between-group variable, subsequently, the difference of mean effective R_2 values between each two brain regions is tested by paired two-samples t-test.

For the remaining analysis, the measured effective R_2 from both hemispheres are combined by each brain regions in the HC group. However, for the PD group, the measurements are rearranged by the hemispheres, according to their asymmetrical laterality of Parkinsonism. The unilaterality of the motor symptoms and the neurodegeneration of PD has been widely observed at the onset [319-321], which could affect neuroimaging measurements such as MRI [196, 322] and SPECT [128, 134, 135, 323]. Hence, in this work, the lateral effective R_2 measurements of each brain region in PD patients are then analysed in two hemispheric groups: the hemisphere contralateral to the individual’s PD symptom predominance at onset (PD

contralateral), and the ipsilateral hemisphere (PD ipsilateral). The disease unilaterality for individual PD patient that is referred in our work, is directly and individually determined by PPMI at their study enrolment, and the laterality is reported as a part of the subject's clinical assessment result.

Linear regression analysis with the least-squares method is performed between the measured effective R_2 values and the estimated iron concentration based on the subject's age [11], in HC, PD contralateral and PD ipsilateral groups respectively. As the prediction regression models for substantia nigra and red nucleus with subject's age was not reported in the literature, the average iron concentrations published in the same study [11] within these two brain regions are used for the current analysis. A linear model: $Effective R_2(s^{-1}) = k[Fe](mg/100 g \text{ wet weight}) + C$, with the slope coefficient k and the intercept offset C is employed for the regression analysis. The individually observed effective R_2 measurements employed for the analysis, are weighted by $\frac{1}{\sigma^2(effective R_2)}$, where σ denotes the standard deviation of the pixel-wise measurement within the individual ROI on the effective R_2 maps. Regression analysis is also performed to investigate any relationship between the effective R_2 measurement and the motor dysfunction, measured as the score of the UPDRS Part III. Regression analysis is also performed between the PD brain hemisphere difference of the effective R_2 (left-right) and the corresponding SBR ratio difference in the caudate nucleus and the putamen. Regression analysis is performed in MATLAB (R2019b, MathWorks).

For each brain region, the distribution of the effective R_2 measurement in each group is tested for normality using the Lilliefors test. For between-group comparison, the equal variance is tested by a two-sample F-test. The independent-samples Mann-Whitney U test is performed between the effective R_2 values obtained from HC and each PD hemispheric group, to test for the equal median. Any difference between the two hemispheres (contralateral vs. ipsilateral) of PD patients is tested by the related-samples Wilcoxon signed-rank test. The null hypothesis is rejected at the 5% significance level ($p < 0.05$) for all hypothesis testing. The analysis is carried out cross-

sectionally for the measurements obtained at the baseline and each follow-up visit at 12, 24 and 48 months where data were available (N = 11/12, 5/12, 6/11 for HC/PD at 12, 24, 48 months respectively). For the longitudinal trend analysis, the unavailable longitudinal data are imputed for visualisation purposes (not for hypothesis testing), to minimise the missing data bias. The correction uses the corresponding individual's available longitudinal data, to estimate the missing values, by the shape-preserving piecewise cubic spline interpolation. As the longitudinal trajectories of the absolute effective R_2 values measured within each brain region for each group are demonstrated graphically, the absolute effective R_2 values measured between each visit are compared. The related-samples Wilcoxon signed-rank test is performed between the effective R_2 measurements at each visit for individuals from each group respectively, to detect any longitudinal changes of the effective R_2 . To demonstrate the time-dependent trend for each brain region, the longitudinal change of the effective R_2 for the individual participant is also calculated as a percentage change of 12-, 24- and 48-month follow-up studies, with respect to the individual baseline measurement (0-month). All statistical analysis is performed within MATLAB (R2019b, MathWorks).

5.3 Results

5.3.1 Subject information

The retrospective MR data included in the current study are carefully screened to avoid potential bias introduced by the vendor and acquisition difference, and the subjects between diagnostic groups are matched to minimise the effect of age and gender on iron quantification in the analysis. The subjects' baseline information and the clinical assessment results are summarised in Table 5.1. The gender and age between the two diagnostic groups show no significant difference (independent two-samples t-test, $p > 0.05$). Compared with HC, the early-stage (average Hoehn & Yahr = 1.55 ± 0.52 yrs) PD patients show significant olfactory degeneration difference (UPSIT, $p < 0.05$), but no significant cognitive declination (MoCA, $p > 0.05$).

Table 5.1 Subject information at baseline.

	HC (N=12)	PD (N=12)	<i>p</i>
Gender (M/F)	7/5	7/5	n/a
Age (year)	49.48 ± 5.55	49.62 ± 6.10	> 0.5
Hoehn & Yahr year	n/a	1.55 ± 0.52	n/a
Disease duration (month)	n/a	2.82 ± 2.44	n/a
UPDRS Total	1.33 ± 1.41	27.82 ± 9.80	< 0.001
UPSIT Total	35.22 ± 2.54	21.63 ± 9.04	< 0.001
MoCA	28.92 ± 1.08	28.25 ± 2.60	> 0.4

5.3.2 Effective R_2 in various brain regions at baseline

Then the bilateral measurements of each brain region are averaged and combined for the between-regions analysis, as the effective R_2 of the left-right hemisphere difference is found statistically insignificant in these regions ($p > 0.1$, pair two-samples t-test). The effective R_2 values measured in various brain regions at baseline are summarised in Table 5.2, presented as average ± standard deviation, and separated by disease groups HC and PD. For the investigated brain region, the effective R_2 difference between HC and PD groups does not reach statistical significance ($p > 0.1$).

Table 5.2 Effective R_2 in different brain regions at baseline in comparison with the prior-published brain iron concentration [11].

Brain regions	Prior-published average brain iron concentration (mg/100 g wet weight) in healthy brains [11]	Observed effective R_2 (s^{-1}) at baseline [†]	
		HC (N = 12)	PD (N = 12)
CN	9.28 ± 2.14 (N = 58)	10.48 ± 0.28	10.52 ± 0.56
PUT	13.32 ± 3.43 (N = 56)	12.78 ± 0.65	12.56 ± 0.83
SN	18.46 ± 6.52 (N = 52)	14.21 ± 1.02	14.43 ± 0.91
RN	19.48 ± 6.86 (N = 44)	14.29 ± 0.74	14.04 ± 0.69
GP	21.30 ± 3.49 (N = 55)	15.82 ± 0.81	16.22 ± 0.76

CN – caudate nucleus, GP – globus pallidus, PUT – putamen, RN – red nucleus, SN – substantia nigra.

At baseline, however, the differences of the effective R_2 measurements between those brain regions are statistically detectable (Friedman’s two-way ANOVA, $F > 1$, $p < 0.05$) among all participants. In HC, the differences of measured effective R_2 between brain regions are found significant (paired 2-sample t-test, $p < 0.05$), with an exception found in the mean effective R_2 values between the substantia nigra and the red nucleus (Table 5.3). Compared with the prior-published iron concentration difference [11] between the brain regions, the observed effective R_2 difference the substantia nigra and the putamen (SN - PUT) is statistically significant ($p = 0.001$) but lower than expected, with a value smaller than those for globus pallidus vs. substantia nigra (GP - SN) and for putamen vs. caudate nucleus (PUT - CN).

Table 5.3 Comparison of effective R_2 between different brain regions at baseline.

Comparison between brain regions	Prior-published iron concentration difference in healthy brains [11]		Observed effective R_2 difference in HC (N=12)	
	Difference (mg/100 g wet weight)	p	Difference (s^{-1})	p^\dagger
GP – SN	2.84	< 0.01	1.61	< 0.001
SN – PUT	5.14	< 0.001	1.43	0.001
PUT – CN	4.04	< 0.001	2.3	< 0.001
SN – RN	n/a	n/a	-0.08	0.72
GP – RN	n/a	n/a	1.53	< 0.001

CN – caudate nucleus, GP – globus pallidus, PUT – putamen, RN – red nucleus, SN – substantia nigra.

5.3.3 Correlation of the effective R_2 with estimated iron concentration in the brain

Due to the unilaterality of PD [319-321], the effective R_2 measurements in the brains with PD are analysed by the hemispheres contralateral and ipsilateral to the body side of symptomatic predominance at onset for all following analysis. Figure 3 shows the linear correlation between the iron concentrations estimated as a function of age, from prior-published post-mortem iron concentration data for healthy brains [11], and the effective R_2 measurements (N=175) pooled from all ROIs of healthy individuals for all visits (0/12/24/48 month). The markers and error bars denote the median and the range of the measurements in each ROI (Fig. 5.3). The age-dependent

brain iron concentrations are calculated based on Hallgren & Sourander's study [8], except for the substantia nigra and red nucleus, where the corresponding average iron concentrations reported from the same study are employed.

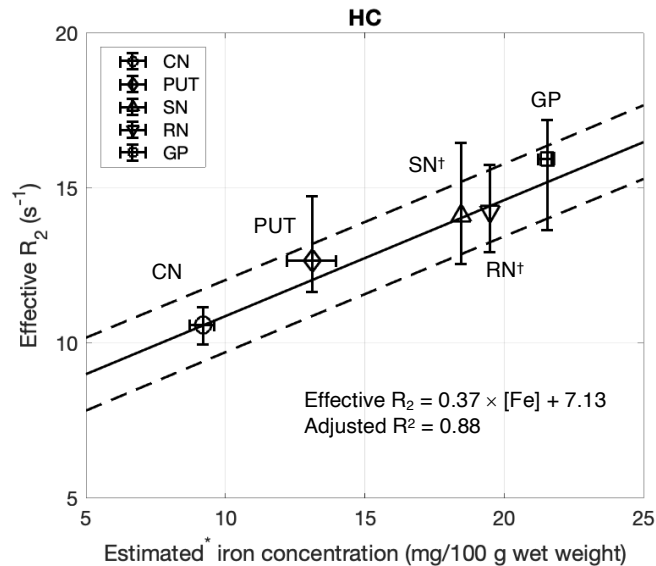


Fig. 5.3 Linear correlation of the effective R₂ with the estimated iron concentration in HC.

CN – caudate nucleus, GP – globus pallidus, PUT – putamen, RN – red nucleus, SN – substantia nigra.

In HC, the regression analysis suggests the presence of linear correlation (Pearson's $\rho > 0.88$, $F \gg 1$, $p \ll 0.001$) between the observed effective R₂ values and the estimated iron concentration (Table 5.4). However, compared with the HC group (adjusted R² = 0.88), the correlation between the measured effective R₂ values and the estimated iron concentration shows degraded linearity in the PD contralateral (adjusted R² = 0.81) and PD ipsilateral (adjusted R² = 0.81) groups. In HC, stronger correlation (adjusted R² = 0.91) is also found between effective R₂ and the estimated iron levels of the regions caudate (CN), putamen (PUT), and globus pallidus (GP).

Table 5.4 Summary of the regression analysis between effective R_2 values and estimated iron concentration in different groups.

Group	N	Pearson's ρ	Slope (k)	Intercept (C)	Adjusted R^2	RMSE
HC	175	0.8864	0.37 ± 0.01	7.13 ± 0.15	0.88	0.587
HC (CN, PUT, GP only)	105	0.9126	0.42 ± 0.01	6.73 ± 0.16	0.91	0.534
PD contralateral	235	0.8821	0.37 ± 0.01	7.22 ± 0.17	0.81	0.739
PD ipsilateral	235	0.8699	0.38 ± 0.01	7.08 ± 0.17	0.81	0.764

N = number of observations. CN – caudate nucleus, GP – globus pallidus, PUT – putamen, RN – red nucleus, SN – substantia nigra.

The robustness of the correlation between the effective R_2 and the estimated iron concentration is also reflected in Figure 5.4, when the measured effective R_2 values (left-hand side y-axis) are plotted against the subject's age, in comparison with the age-dependent iron level prediction (right-hand side y-axis). In the HC group (Fig. 5.4, top panel), the relative relationship between the effective R_2 in the caudate nucleus, putamen, and globus pallidus is generally in line with the predicted iron concentration, with larger variation observed in globus pallidus and putamen of older subjects (age > 54 yrs). In putamen, the measured effective R_2 also shows a slight overestimation among younger HC (age < 50 yrs). Compared with HC, the effective R_2 demonstrates larger variation in all three brain regions in both contralateral (Fig. 5.4, middle panel) and ipsilateral (Fig. 5.4, lower panel) PD hemispheres, against the iron level prediction in normal ageing. An overall higher effective R_2 values are observed in the globus pallidus, in comparison with the age-dependent estimation. Moreover, a decline trend is observed in the effective R_2 measurements of putamen, in contrast with the predicted slow accumulation of the putamen iron concentration.

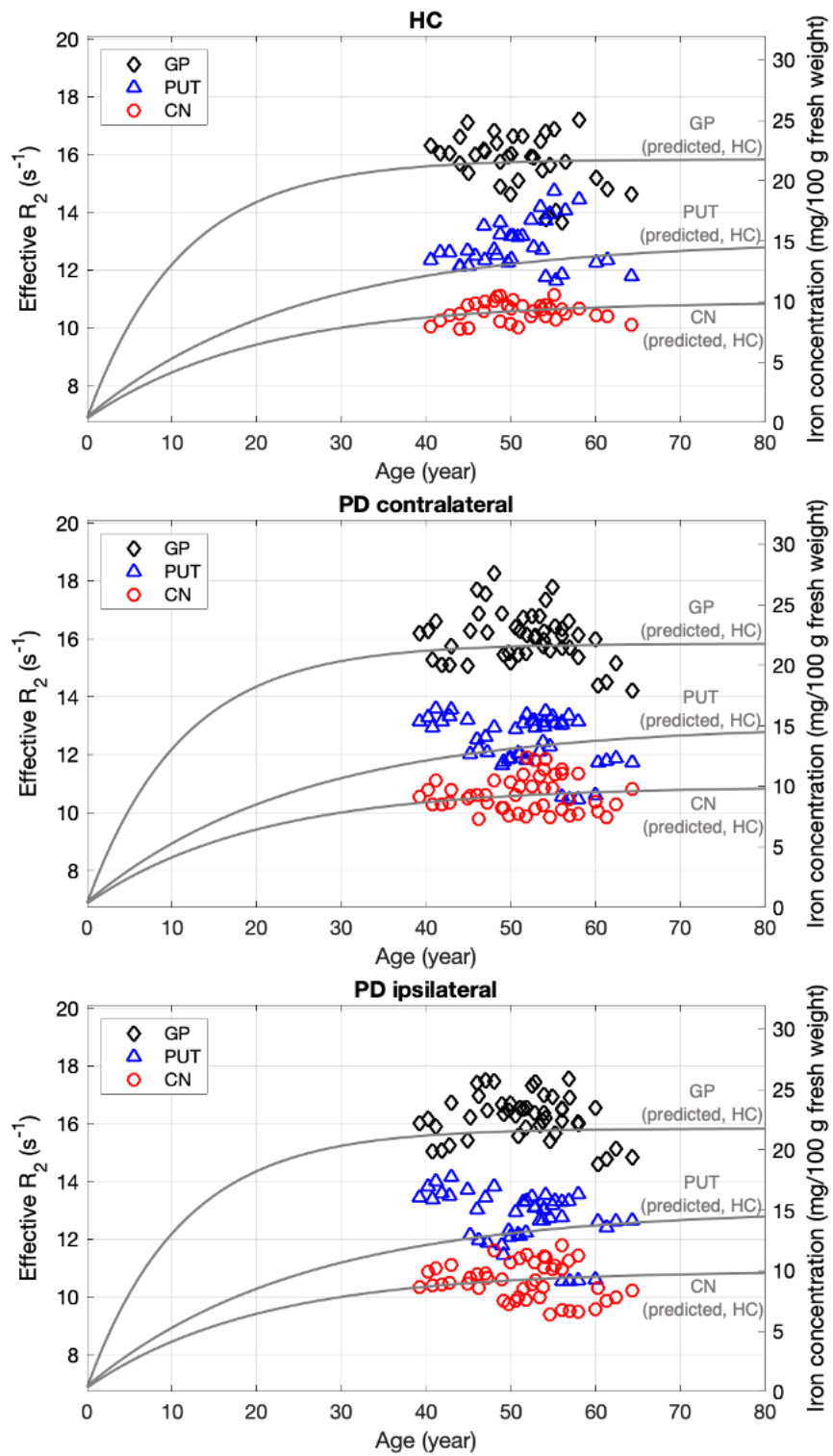


Fig. 5.4 Observed effective R_2 (markers) in comparison with the predicted iron concentrations during normal ageing (regression lines) in HC (top), PD contralateral (middle) and ipsilateral (bottom) hemispheres.

5.3.4 Comparison of median effective R_2 values between groups

Figure 5.5-6 show the individual effective R_2 measurements in putamen, globus pallidus, substantia nigra, caudate nucleus and red nucleus of HC subjects, the contralateral and the ipsilateral hemispheres of the PD subjects, at baseline (0-month), 12-month, 24-month, and 48-month, respectively.

When comparing the hemisphere first showing onset of PD changes (ipsilateral, PDi) with the contralateral hemisphere (PDc), the PD ipsilateral data show higher effective R_2 values in putamen at baseline, 12-month, and 24-month measurements (each significant at $p < 0.05$), and evidence suggesting higher effective R_2 at the 48-month visit (approaching significance at $p < 0.068$), in comparison with the PD contralateral putamen (Fig. 5.5, left column). Evidence (borderline significance, $p = 0.05$) for higher effective R_2 (ipsilateral vs. contralateral) is also found in the globus pallidus at the 48-month scan (Fig. 5.5, middle column). Conversely, the effective R_2 of the substantia nigra (Fig. 5.5 right column) appears to be lower for ipsilateral versus contralateral, but the statistical evidence for this is not as strong ($p < 0.092$ at the 24-month scan) as for the differences observed for putamen or globus pallidus. In the red nucleus (Fig. 5.6, left column) and the caudate nucleus (Fig. 5.6, right column), equivalent effective R_2 values are observed between the hemispheres.

For the comparison of the HC group with either PD hemispheric group, statistically significantly higher effective R_2 is only found in the globus pallidus of the PD ipsilateral group at the 24-month visits ($p < 0.05$), compared with the HC. This difference of the effective R_2 measurements is dominated by the female subject, due to the lack of available data in HC subjects at 24-month ($N = 5$).

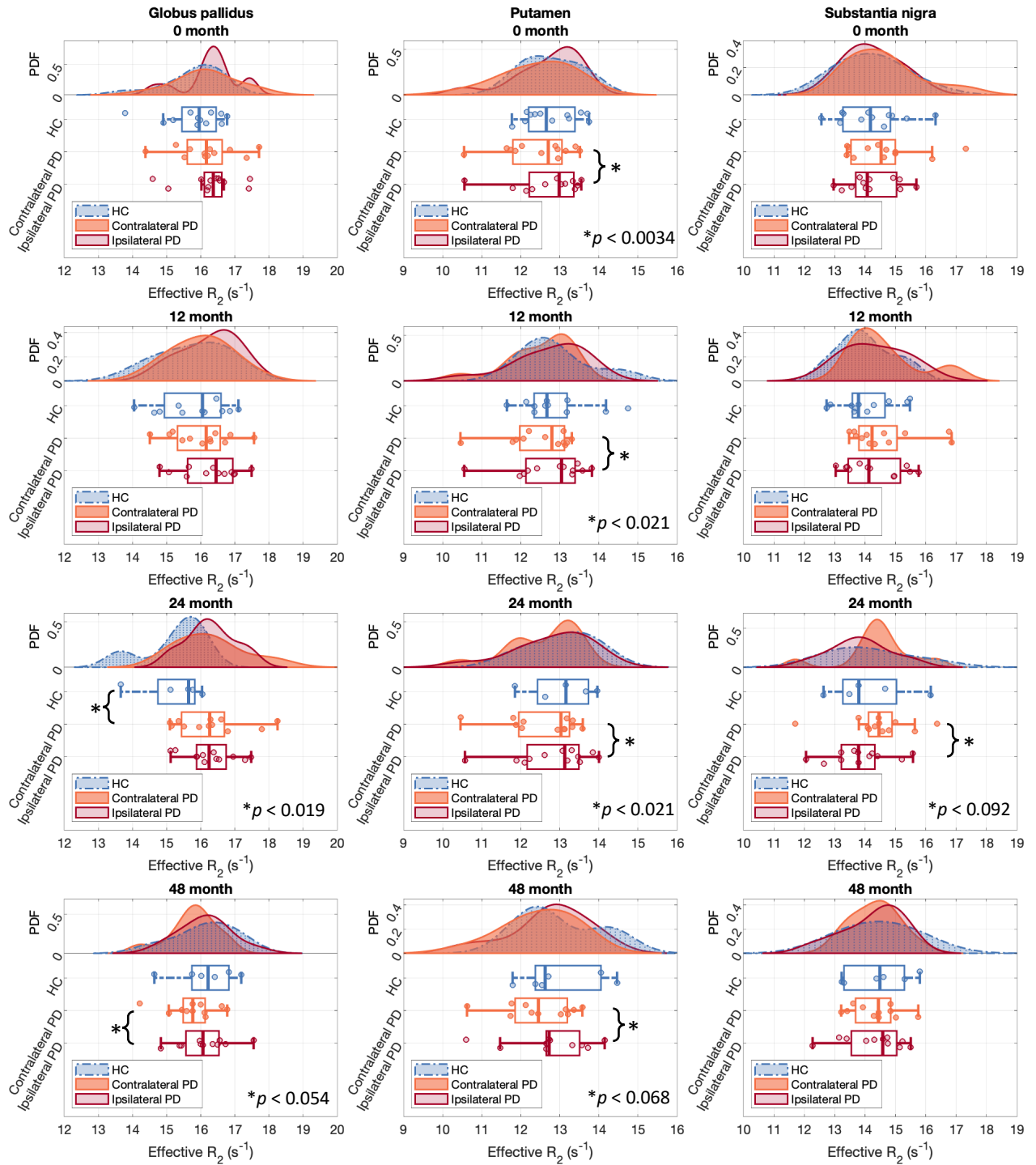


Fig. 5.5 Effective R_2 measured in globus pallidus (left), putamen (middle), and substantia nigra (right) at 0, 12, 24, 48 months.

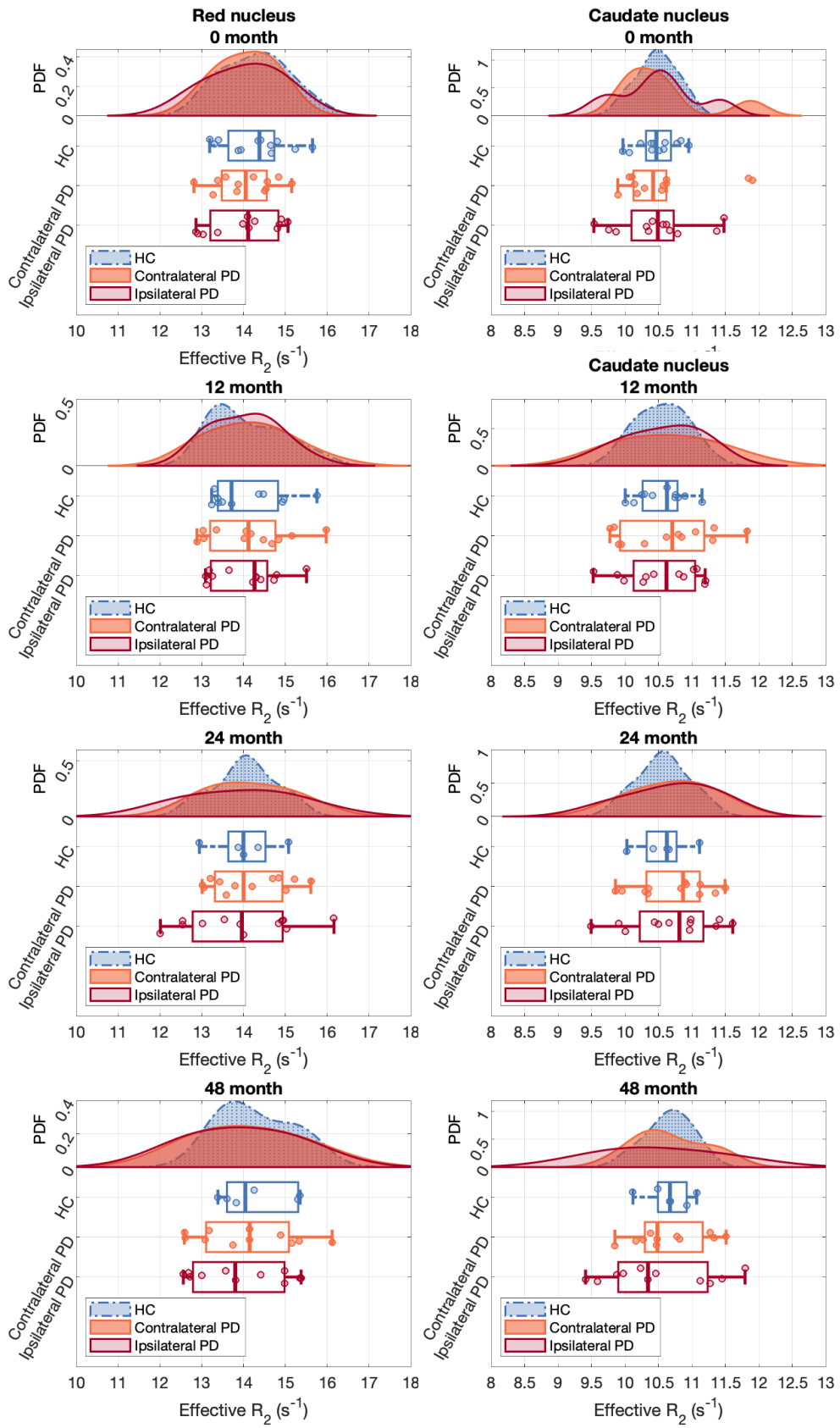


Fig. 5.6 Effective R_2 measured in red nucleus (left) and caudate nucleus (right) at 0, 12, 24, 48 months.

Although the effective R_2 of single brain region appears to be limited to distinguish PD patients from HC regarding the statistical significance level ($p > 0.1$), the consistent relative relation of the group medians from the repeated scans at baseline (0 month) and 12 month, suggests the observed difference between groups is not caused by the random noise. At the baseline and 12-month visits, the group medians of the effective R_2 values show a rank of PD ipsilateral $>$ PD contralateral $>$ HC in the globus pallidus and in the putamen. In the substantia nigra, the median effective R_2 value is found higher in the PD contralateral hemisphere, compared with the ipsilateral PD hemisphere and with HC.

5.3.5 Relationship between the effective R_2 and SBR in the putamen and caudate

As the difference of the effective R_2 is observed between the PD hemispheres contralateral and ipsilateral to the body side of symptomatic predominance at onset, this observation is investigated against the functional SPECT results of the caudate and the putamen, reported by PPMI (Appendix C). Shown in Figure 5.7, demonstrated as the decreased SBR at baseline, the decreased presynaptic tracer uptake suggests the dysfunction of DaT in the putamen and caudate of PD bilateral hemispheres, compared with HC. At baseline, a moderate but significant positive linear correlation (Pearson's $\rho = 0.467$, $p < 0.05$) between the effective R_2 and DaT SBR in putamen is found in the PD subjects (Fig.5.7, blue circles), compared with a trend of negative relationship (Pearson's $\rho = -0.2$) in HC (Fig.5.7, black squares). However, these correlations are not observed in caudate, for either HC or PD subjects ($-0.2 < \text{Pearson's } \rho < 0.2$, $p > 0.1$), at baseline (Fig.5.7, bottom).

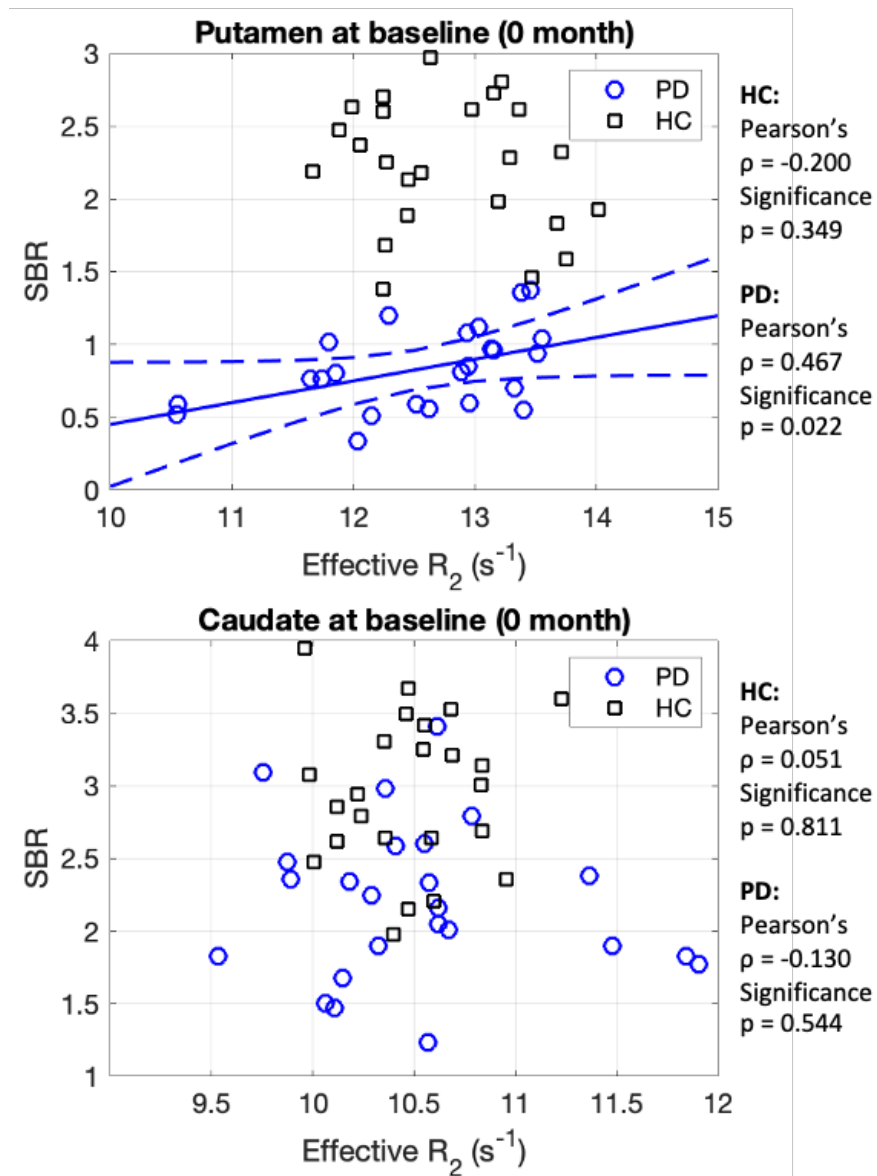


Fig. 5.7 Correlation between the effective R_2 and DaT SBR in the putamen and caudate at baseline.

In PD, the SBR reduction is more prominent in the hemisphere contralateral to the body side of symptomatic predominance at onset, than the hemisphere ipsilateral to the PD predominant laterality at onset (Table 5.5). Hence, the relationships between the effective R_2 and the DaT SBR in putamen and caudate, are further investigated by the hemispheric difference (left-right) of individual subjects at baseline.

Table 5.5 Comparison of the effective R_2 with the DaTScan results of subjects at baseline.

Subject	PD symptom predominant laterality at onset	SBR difference _(Left-Right)		Effective R_2 difference _(Left-Right) (s^{-1})	
		Caudate	Putamen	Caudate	Putamen
HC1	-	0.3	-0.47	-0.36	-0.55
HC2	-	0.08	0.23	-0.09	0.19
HC3	-	0.87	0.07	-0.02	0.25
HC4	-	0.17	-0.3	0.07	-0.02
HC5	-	0.15	-0.24	0.36	0.07
HC6	-	-0.32	-0.29	0.01	-0.11
HC7	-	0.46	-0.35	0.48	0.35
HC8	-	0.07	0.08	0.12	-0.17
HC9	-	0.46	-0.28	-0.24	-0.09
HC10	-	-0.17	-0.3	0.55	0.06
HC11	-	-0.02	-0.3	-0.22	0.34
HC12	-	0.38	0.12	0.31	-0.22
Average absolute difference		0.29 ± 0.24	0.25 ± 0.12	0.23 ± 0.18	0.20 ± 0.15

Subject	PD symptom predominant laterality [^] at onset	SBR difference _(Left-Right)		Effective R_2 difference _(Left-Right) (s^{-1})	
		Caudate	Putamen	Caudate	Putamen
PD1	Right	-0.13	-0.15	0.43	0.07
PD2	Right	-0.78	-0.17	-0.10	-0.11
PD3	Right	-0.34	-0.51	-0.12	-0.44
PD4 [†]	Left	0.4	-0.2	0.26	0.88
PD5	Right	-0.36	-0.07	0.57	-0.01
PD6	Left	0.74	0.53	0.17	0.51
PD7	Left	1.07	0.26	0.43	0.15
PD8	Left	0.38	0.41	-0.19	0.30
PD9	Left	0.73	0.4	-0.14	0.43
PD10	Left	0.32	0.27	-0.75	0.05
PD11	Right	-0.65	-0.37	-0.42	-0.18
PD12	Left	0.55	0.1	-0.48	0.04
Average absolute difference		0.54 ± 0.26	0.28 ± 0.16	0.34 ± 0.21	0.26 ± 0.26

[^]Body side with predominant symptoms. [†]Data were removed from the fitting in Fig. 5.8 as an outlier.

In putamen, the linear correlation between the hemispheric difference of the effective R_2 and of the SBR in PD (Fig. 5.8, blue circles) are positive (Pearson's $\rho = 0.524$), but less significant ($p = 0.08$). It is caused by an outlier (Fig. 5.8, arrow-pointed circle, PD4 in Table 5), whose predominant laterality indicated by the putaminal SBR is found unstable during the 48-month longitudinal study (Appendix C). After removing the outlier, a very strong (Pearson's $\rho = 0.932$), significant ($p < 0.001$) positive linear correlation (Fig. 5.8, blue regression line) of the hemispheric SBR difference with the effective R_2 difference, is found in PD putamen. In HC, a positive trend (Pearson's $\rho = 0.315$) is observed between the hemispheric difference of SBR and the effective R_2 in putamen (Fig. 5.8, black squares), but not statistically significant ($p > 0.1$). In caudate, no linear correlation is found ($p > 0.1$), between the hemispheric difference of the effective R_2 and DaT SBR.

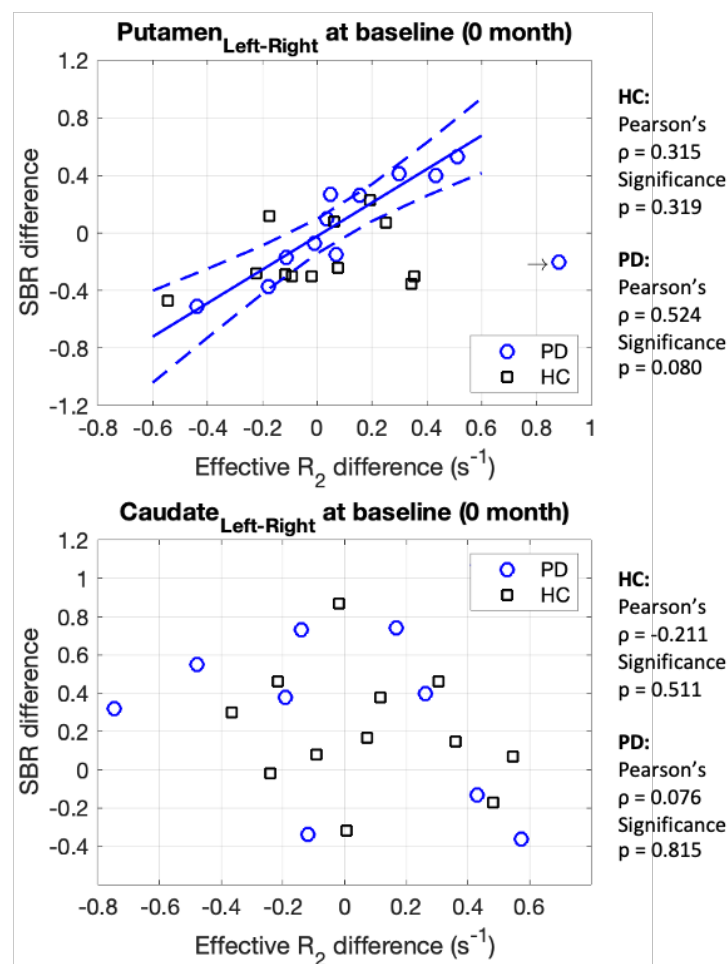


Fig. 5.8 Correlation between the hemispheric difference of the effective R_2 and DaT SBR in the putamen and caudate at baseline.

In PD, the positive linear correlations between the putaminal effective R_2 and the DaT SBR, and between their hemispheric differences, remain statistically significant ($p < 0.05$) when the measurements of baseline (0 month), 12 month, 24 month and 48 month are pooled together (Fig. 5.9, left column). However, compared with the baseline (left image in Fig. 5.7 and Fig. 5.8), the positive relationships became weaker between the putaminal effective R_2 and the DaT SBR (Pearson's $\rho = 0.467$ vs. 0.359), and between their hemispheric differences (Pearson's $\rho = 0.524$ vs. 0.371), as smaller SBR, and SBR hemispheric difference are observed in the later visits. Nevertheless, in caudate, the correlation between the effective R_2 and the DaT SBR, or between their hemispheric differences, is insignificant (Fig. 5.9, right column).

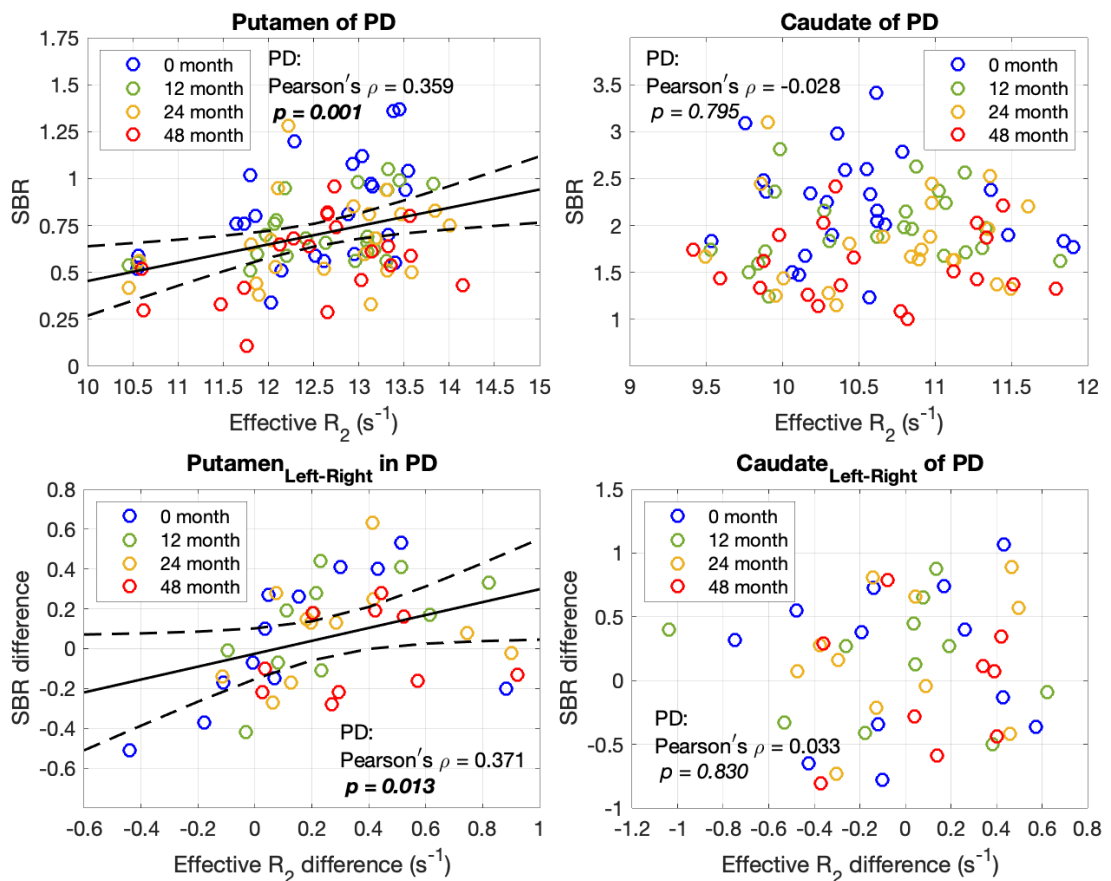


Fig.5.9 Relationship between the effective R_2 and DaT SBR (upper) and between their hemispheric differences (lower) of PD in the putamen (left) and caudate (right).

5.3.6 Longitudinal changes of the effective R_2 in various brain regions

After correcting the bias caused by the MRI data unavailability, the following results show the longitudinal changes of the effective R_2 measured in the caudate nucleus (Fig. 5.10), putamen (Fig. 5.11), substantia nigra (Fig. 5.12), red nucleus (Fig. 5.13) and globus pallidus (Fig. 5.14). The results are presented as the individual trajectories of the effective R_2 from different groups (upper panel), as well as group medians (lower panel, asterisks) and distributions (lower panel, coloured patches).

In caudate nucleus, HC group shows a small increase of effective R_2 median with slight fluctuation over the 48-month period (Fig. 5.10, green line in the lower panel). Largely overlapping with HC at 0- and 12-month measurements, the median values of the effective R_2 observed in the contralateral and ipsilateral (Fig. 5.10, yellow and peach lines in the lower panel) PD hemispheric groups, however, decrease after 24 months. In PD ipsilateral group, the increase of effective R_2 from the 12-month to the 24-month study is statistically significant ($p < 0.05$), and the decrease from the 24-month to the 48-month study is approaching statistical significance at $p = 0.067$. Fluctuations of the individual trajectories are observed in all three groups (Fig. 5.10, upper panel), but larger variances are observed among the measurements for PD hemispheric groups (Fig. 5.10, orange and red lines in the upper panel, patches in the lower panel), compared with HC. The difference in the observed data variance are statistically significant ($p < 0.05$) at baseline (0 month), between HC and PD contralateral groups, as well as between HC and PD ipsilateral groups.

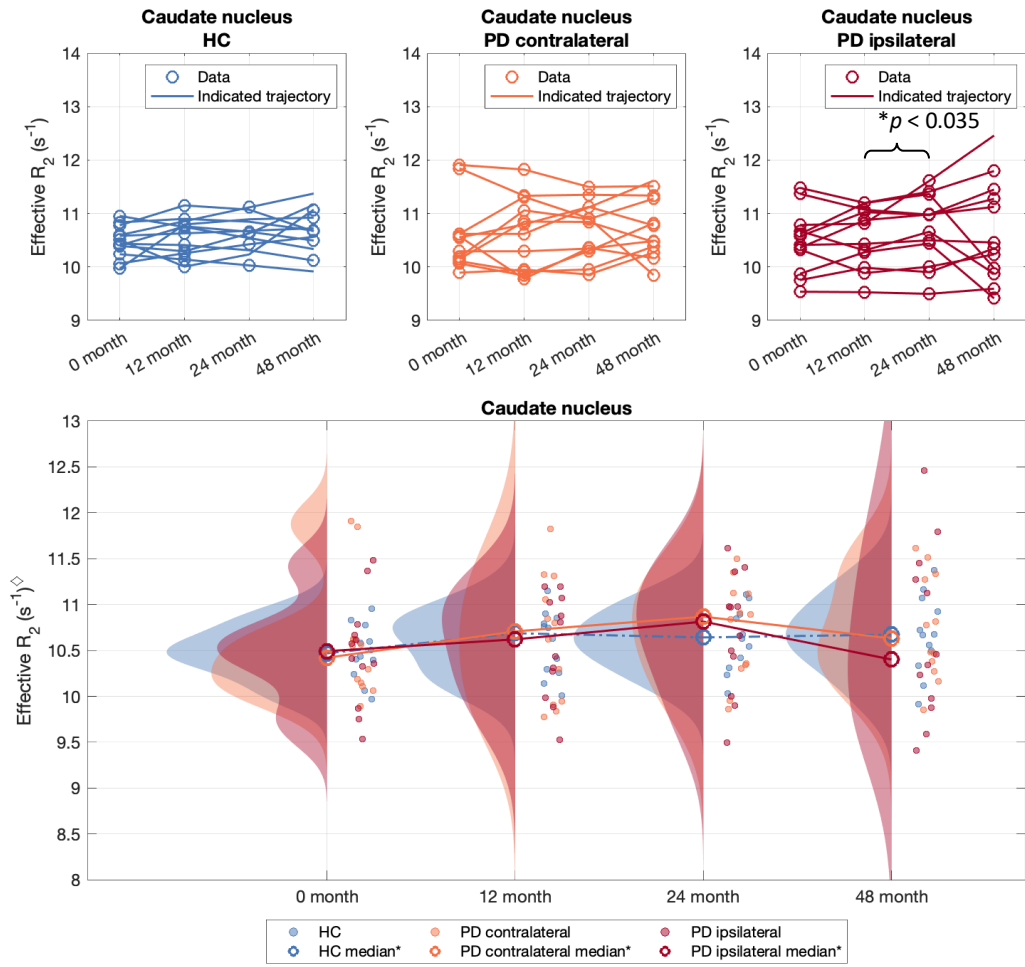


Fig. 5.10 Longitudinal changes of the effective R_2 within caudate nucleus.

Upper panel: trajectories of individual; lower panel: group medians and distributions.

◇ plotted with imputed values for missing data, for visualisation (not for hypothesis testing).

In comparison with caudate nucleus, the individual trajectories of the effective R_2 in the putamen is less fluctuated during the 48 months, in all three groups (Fig. 5.11, upper panel). The group median values suggest an unchanged putamen effective R_2 in the HC group (Fig. 5.11, blue line in the lower panel), but increase in PD contralateral and ipsilateral hemispheres (Fig. 5.11, orange and red lines in the lower panel). At 48-month, the effective R_2 in both PD contralateral and ipsilateral hemispheres show an overall decrease, compared to the 24-month measurements. These longitudinal changes do not show statistical significance ($p > 0.1$), possibly because the small magnitude difference is masked by the heterogeneous trajectories (Fig. 5.11, yellow and peach lines in the upper panel) observed within the group.

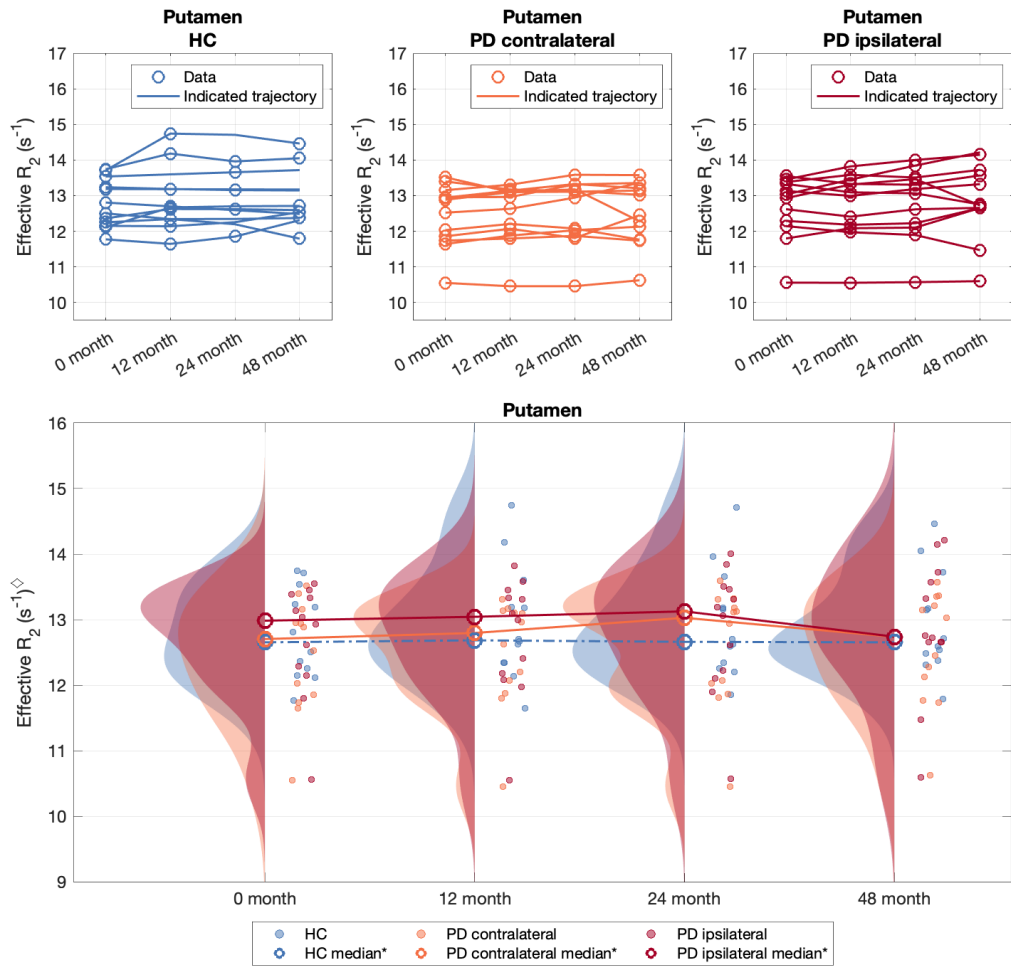


Fig. 5.11 Longitudinal changes of the effective R_2 within putamen.

Upper panel: trajectories of individual; lower panel: group medians and distributions.

◇ plotted with imputed values for missing data, for visualisation (not for hypothesis testing).

The greatest longitudinal variation of the effective R_2 is observed in the substantia nigra (Fig. 5.12, upper panel). In HC, the group median effective R_2 of the substantia nigra shows an increase at the 48th month, after fluctuating around the baseline level in the first 24 months (Fig. 5.12, blue line in the lower panel). A similar trend is observed in the PD contralateral hemispheric group (Fig. 5.12, orange line in the lower panel), compared with HC, but with larger effective R_2 median measurement. At the 48th month, the median effective R_2 of PD contralateral group drops back to its baseline level. In the ipsilateral hemisphere of PD, the median effective R_2 also experiences rise and fall along the timeline (Fig. 5.12, red line in the lower panel), altering in an opposite trend compared with the contralateral PD hemisphere. In both

hemispheric groups of PD, large longitudinal variations and individual difference are found when examining the effective R_2 trajectories of each patient (Fig. 5.12, middle and right-hand side images in the upper panel), which possibly contributes to the overall stability of the median effective R_2 of the groups by cancelling out each other's effect.

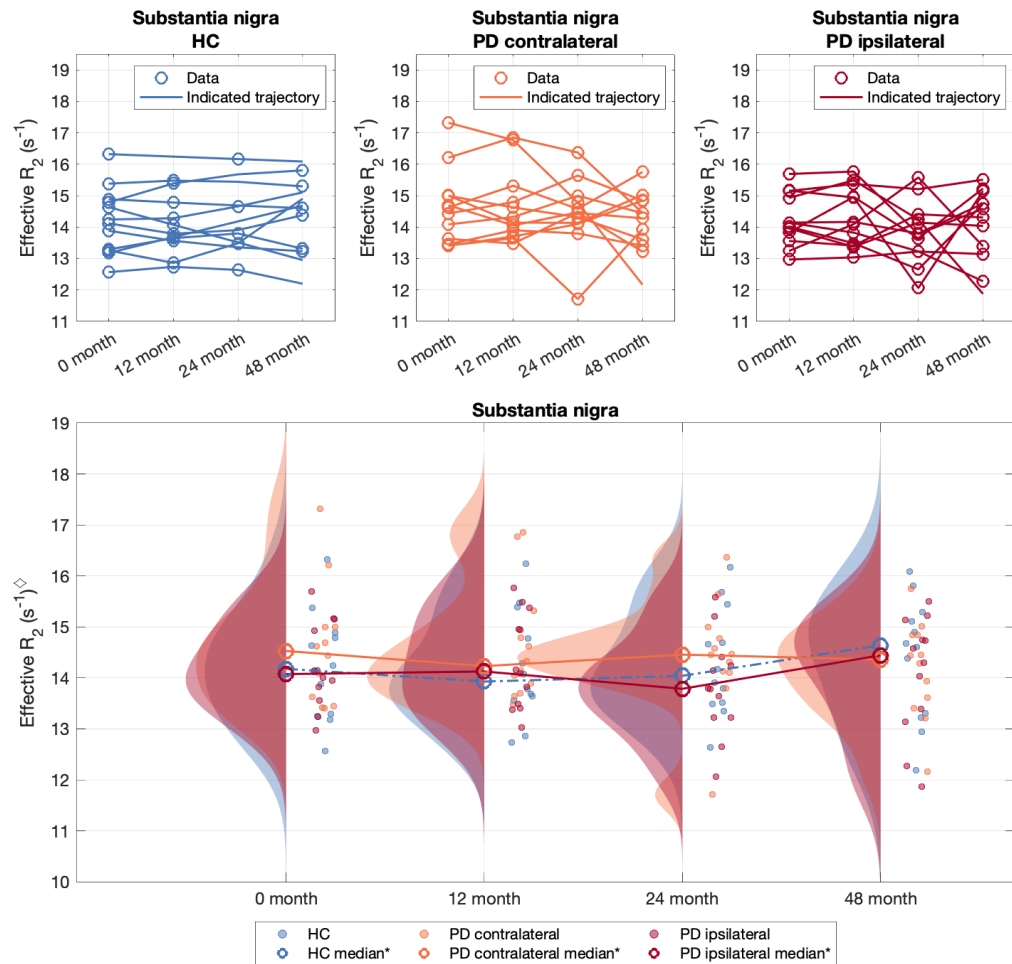


Fig. 5.12 Longitudinal changes of the effective R_2 within substantia nigra.

Upper panel: trajectories of individual; lower panel: group medians and distributions.

◇ plotted with imputed values for missing data, for visualisation (not for hypothesis testing).

In red nucleus, the median effective R_2 values of all groups fluctuate slightly around their baseline levels, over the 48 months (Fig. 5.13, lines in the lower panel). Compared with the HC, the median effective R_2 in PD contralateral and ipsilateral hemispheric groups are slightly lower at most of the times of visit (MRI examination), except for the 24-month study. The spread of the effective R_2 measurements,

however, is wider in both PD contralateral and ipsilateral groups (Fig. 5.13, orange and red patches in the lower panel) at 24th month and 48th month, in comparison with HC. The increasing effective R_2 variation with time corresponds to the heterogeneity of the longitudinal trajectories of the subjects within the group, which appears to be more prominent in PD hemispheres (contralateral and ipsilateral, the orange and red lines in the upper panel of Fig. 5.13).

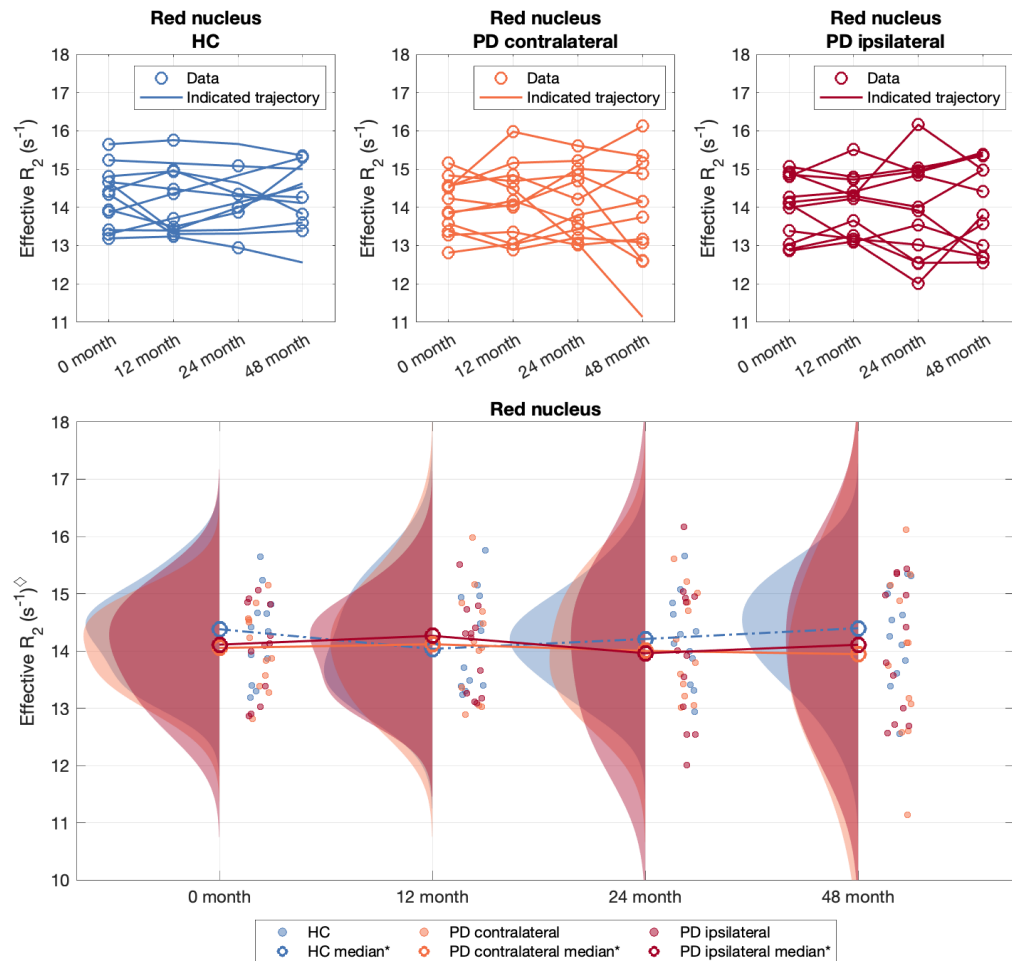


Fig. 5.13 Longitudinal changes of the effective R_2 within red nucleus.

Upper panel: trajectories of individual; lower panel: group medians and distributions.

◇ plotted with imputed values for missing data, for visualisation (not for hypothesis testing).

The median effective R_2 of the globus pallidus shows an overall unchanging trend with time, in all groups (Fig. 5.14, lines in the lower panel). With small fluctuations, the measurements of the PD contralateral and ipsilateral hemispheres (Fig. 5.14, orange and red lines in the lower panel) demonstrate larger median effective R_2 , in

comparison with HC (Fig. 5.14, blue line in the lower panel), at 0-month, 12-month, and 24-month visits. At the 48th month, the median effective R_2 of the contralateral PD hemispheres drops below the measurement of HC. It is contributed by the slight decrease of the effective R_2 trajectories observed in several individual data in the PD contralateral group (Fig. 5.14, middle image in the upper panel), but this change is not statistically significant possibly due to the within-group heterogeneity of the longitudinal trend.

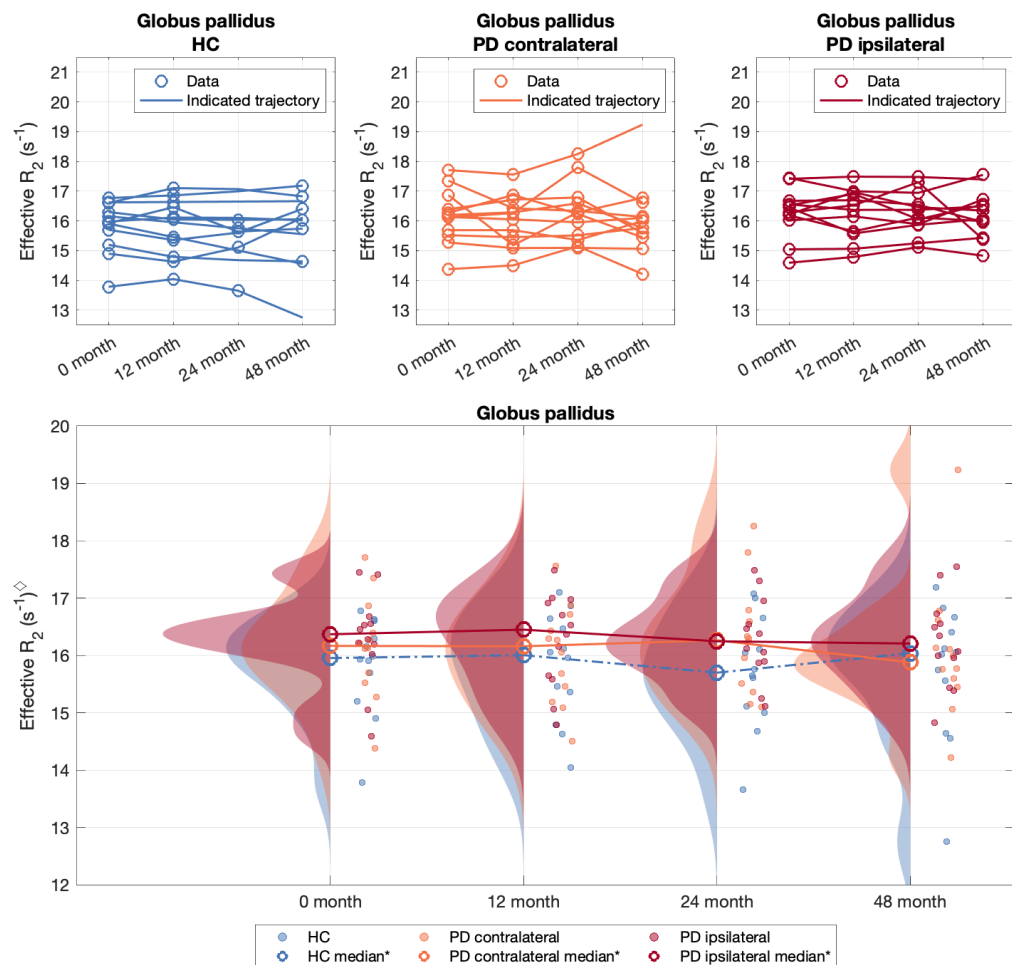


Fig. 5.14 Longitudinal changes of the effective R_2 within globus pallidus.

Upper panel: trajectories of individual; lower panel: group medians and distributions.

◇ plotted with imputed values for missing data, for visualisation (not for hypothesis testing).

With respect to the baseline (0-month) measurements, the median of the effective R_2 change in percentage, and the data distribution, for HC, PD contralateral and

ipsilateral groups, measured at 12-month, 24-month and 48-month studies are summarised in Table 5.6 and Figure 5.15, respectively.

Table 5.6 Median effective R_2 percentage change (%) in the various brain regions.

CN	12-month period	24-month period	48-month period
HC	0.53	1.57	1.12
PD contralateral	0	1.42	2.44
PD ipsilateral	0.21	1.17	0.65
PUT	12-month period	24-month period	48-month period
HC	0.20	0.76	1.61
PD contralateral	1.01	1.71	1.36
PD ipsilateral	-0.47	0.27	0.91
SN	12-month period	24-month period	48-month period
HC	-0.1	0.47	-0.2
PD contralateral	1.7	0.34	1.32
PD ipsilateral	0.32	-1.90	1.23
RN	12-month period	24-month period	48-month period
HC	0.14	-0.77	-1.71
PD contralateral	1.00	-0.52	0.24
PD ipsilateral	1.09	-0.71	1.43
GP	12-month period	24-month period	48-month period
HC	-0.58	-0.78	-0.47
PD contralateral	-0.22	-0.13	-0.82
PD ipsilateral	0.28	-0.61	0.02

Over the 48-month period, the median percentage change of the effective R_2 in HC is small, as the iron-related effective R_2 increase with normal ageing is expected to be nearly negligible, given the duration and the subjects' age at the baseline. In HC, the median effective R_2 percentage changes after the 48-month period are comparable to the expected increasing trends and the magnitude levels in caudate nucleus (1.12% vs. 0.67%), putamen (1.61% vs. 0.95%), but not in globus pallidus (-0.47% vs. 0.15%). The median effective R_2 percentage change of the substantia nigra remain unchanged in HC (-0.2%), in contrast to PD contralateral and ipsilateral hemispheres, where 1.32% and 1.23% increases from baseline are observed, after 48 months. Similarly, a decrease trend in red nucleus is observed in HC after 48 months (-1.71%), but not in

the contralateral or ipsilateral hemispheres of PD. Nevertheless, these trends of groups are largely confounded by individual differences and within-group variations.

The individual differences of the percentage effective R_2 change after 12, 24 and 48 months, with respect to the baseline measurements, are shown as the spread of the distribution in Figure 5.15. Overall, the variation increases with the duration of the time, in all groups (HC, PD contralateral and ipsilateral), especially after 48 months (red patches in Fig. 5.15). In HC, a slight right shift of the distribution on the y-axis is observed in the caudate nucleus, putamen, and globus pallidus, as the time duration increased (blue, yellow and red patches, for 12-, 24- and 48-month time duration from baseline), suggesting an increasing percentage change of the effective R_2 with time. This pattern is less perceptible in the contralateral or ipsilateral PD hemispheres, as the data distribution appeared to deviate from a normal distribution ($p < 0.01$), for the ipsilateral putamen and the contralateral globus pallidus after the 12-month period. In substantia nigra, the percentage change of the effective R_2 in HC is skewed towards the higher values as the time duration increases, indicating the effective R_2 of the substantia nigra increases with time in some subjects, but not the others. Compared with HC, the PD contralateral and ipsilateral substantia nigra show an opposite skewness towards lower and negative percentage change of the effective R_2 values, suggesting that the effective R_2 of the substantia nigra decreases with time in some but not all PD patients. Large variation and deviation from the normal distribution of the data observed in the red nucleus, might be partially contributed by the partial volume effect due to the image resolution limitation and the small segment.

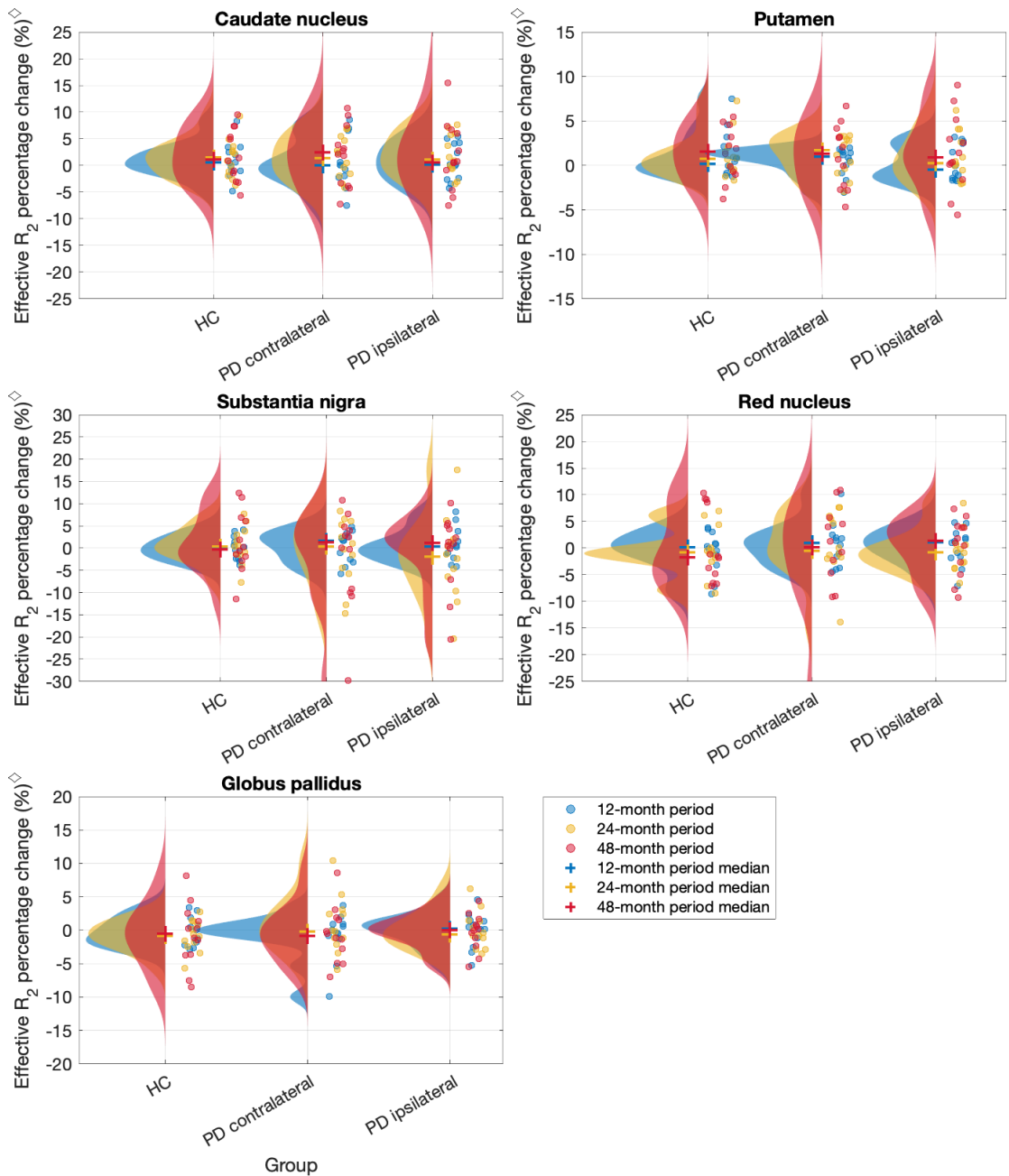


Fig. 5.15 Effective R_2 percentage change in various brain regions after 12, 24, 48 months from baseline.

◇ plotted with imputed values for missing data, for visualisation (not for hypothesis testing).

5.4 Discussion

5.4.1 Effective R_2 is linearly proportional to the iron level across investigated brain regions, can be used as an alternative to conventional R_2

Significantly different ($p < 0.05$) effective R_2 values are found in the different brain regions, corresponding to their distinctive iron levels reported in the literature [13,

46]. Shown in Table 5.3, the baseline effective R_2 values measured in the caudate nucleus, putamen, red nucleus, substantia nigra, and globus pallidus are significantly different (except for red nucleus – substantia nigra), and the rank of the effective R_2 values in these brain regions are found in line with their corresponding age-dependent iron concentrations in the post-mortem study reported by Hallgren and Sourander [11].

The correlation of the effective R_2 with the brain iron concentration, is further supported by the result of regression analysis, between the effective R_2 measurement and the brain iron concentration estimated based on the subject's age [11]. A strong ($R^2 = 0.88$), significant ($p < 0.05$) linear correlation is found for the effective R_2 versus the estimated brain iron. Within HC, the regression analysis shows a linear correlation of the effective R_2 with the age-dependent non-haemin iron concentration, estimated according to previously reported prediction models [11]. Moreover, compared with the theoretical iron-dependent coefficient $k_{estimate}$ for conventional R_2 at 3.0 T field strength [258]:

$$k_{estimate} = 14.1 + 6.2 \times B = 32.7 s^{-1} mg^{-1} / g \approx 0.33 s^{-1} mg^{-1} / 100g$$

Eq. (5.5)

the slope coefficient found in this study, $k = 0.37 s^{-1}/mg/100 g$ in HC group, matches this theoretical value relatively well.

Compared with the conventional R_2 measurements of these brain regions at 3.0 T [13, 186, 191, 316], the effective R_2 derived from the FSE sequence shows an underestimation of the absolute values. It was partially contributed by the long 2nd $T_{E(eff)}$, at 101 ms, by when the signal from the high iron-laden brain tissue have largely decayed. Another reason for the underestimation could be the reduced FA ($5/6\pi$) employed in the PPMI dual-contrast FSE sequence, as a common clinical practice to employed to reduce the SAR. Nevertheless, the well predicted iron-dependent coefficient k (slope) in this study, suggests that the difference between the effective R_2 presented here, and the conventional R_2 in the literature, is mainly caused by the

iron-independent offset (intercept). The latter is also influenced by water diffusion and systematic errors, such as vendors, acquisition parameters and pulse sequences being employed.

When PD patients are included in the observation, variation is introduced to the linearity between the effective R_2 and the estimated iron concentration, but the above findings are overall aligned with published post-mortem results [11], and the correlations found in the current study are generally agreed with reported linear relationships between conventional R_2 obtained from the multi-spin-echoes sequence and the brain iron concentration [11, 48, 50, 176, 186, 191]. It suggests the effective R_2 measurements derived from the dual-contrast FSE sequence reported in the work could be used as an estimator, alternative to the conventional R_2 , to measure the brain iron level in these regions.

5.4.2 Effective R_2 can reveal the asymmetrical disease manifestation in PD brain hemispheres

As the unilaterality of the motor and non-motor symptoms have been clinically recognised in PD [319-321], concordant results are found in this work, when comparing the group medians of effective R_2 between two PD brain hemispheric groups that are separated based on the asymmetrical disease severity at onset. The result shows in the globus pallidus and putamen, the effective R_2 values is found larger in the brain hemisphere ipsilateral to the body side that is predominantly affected by PD at onset, than the contralateral hemisphere (Fig. 5.5). In contrast, a converse trend is suggested in the substantia nigra (Fig. 5.6), where a higher effective R_2 median value is found in the PD contralateral hemisphere, compared with the ipsilateral hemisphere, at baseline, 12-month and 24-month scans. This could be caused by one or combined of the following reasons: 1) the brain regions are on different stages of neurodegeneration caused by the disease, 2) the disease severity progresses in this brain region with a different pattern, and 3) the signal attenuation in the dual-contrast FSE images is dominated by different mechanisms in the substantia nigra comparing to the other brain regions, in PD brains.

The hemispheric difference of brains with PD has been previously reported as neuroimaging results, primarily using SPECT [128, 129] and PET [130, 131, 324], demonstrated as asymmetrically reduced presynaptic striatal tracer uptake by DaT and increased postsynaptic tracer uptake by striatal dopaminergic receptors D₂. Manifested in caudate and putamen, the hemisphere contralateral to the predominantly affected body side showed severer dysfunction of dopamine transportation, compared with the ipsilateral hemisphere. In substantia nigra, a recent PET study suggested reduced striatal dopamine transporter binding in PD brains, correlated with the pigmentation of the ventral nigra tier in the contralateral hemisphere but not the ipsilateral side [324]. The unilateral reduction of the nigrostriatal terminal density, was consistent with the existing post-mortem observation of asymmetrical neuron loss in the substantia nigra in PD [325]. A recent MRI study showed an increase mean diffusivity and decreased fractional anisotropy in the contralateral putamen, while in the substantia nigra the difference was prominent in the transverse relaxation rates R_2 , R_2^* and R_2' , with larger values observed in the nigra contralateral to the symptomatic body side, in 27 PD patients [322].

With the effective R_2 derived from the dual-contrast FSE MRI, our results support the PD hemispheric difference, especially in the putamen, with statistical significance at baseline, 12-month and 24-month scans. Before 48th month, the median effective R_2 values of both PD hemispheric groups (contralateral and ipsilateral) are only marginally larger than the HC group, which might indicate an increased iron level in PD patients. Therefore, the difference of the putamen effective R_2 observed between the contralateral and ipsilateral might be caused by the asymmetrical reduction of the putaminal dopaminergic fibre density [326], predominant in the contralateral hemisphere, resulting in increased diffusivity [322] and decreased effective R_2 in this work. This deduction is consistent with the longitudinal observation of the putamen effective R_2 (Fig. 5.10), that the PD hemispheric difference persists but decreases with time; until after 48 months, when the effective R_2 for contralateral and ipsilateral PD hemispheres both decrease to a similar level as HC. It is in line with the prior-reported

progressive loss of the dopaminergic fibres in dorsal putamen, where virtually depleted putaminal dopaminergic fibres were observed by 4 years post-diagnosis [326]. Hence, the effective R_2 difference between the contralateral and ipsilateral putamen within PD hemispheres become marginal with time.

In contrast, more than 50% loss of dopaminergic neurons in the nigra already takes place at the earliest stage of PD [127, 326, 327], with unilateral depletion [325]. Consequently, the impact of pathological iron accumulation observed in previous reports [43, 138, 328, 329], might be confounded by the overall increased non-compartmentalised water, on the effective R_2 of the substantia nigra. It is demonstrated as a potential trend of larger effective R_2 median in the PD contralateral hemisphere, compared with the ipsilateral PD hemisphere and with HC, but with great individual variation and longitudinal variation (Fig. 5.11), especially within the two PD hemispheric groups. Different effective R_2 of the substantia nigra between the contralateral and ipsilateral PD hemispheres is suggested at 24-month scans ($p < 0.092$), presumably related to the asymmetrical pathological iron elevation, predominantly in the contralateral hemispheres of PD patients. This result is consistent with the existing MRI observation [322]. This observation of the effective R_2 fluctuations in the PD substantia nigra could be partially explained by a recent biophysical model of iron-induced transverse relaxation [330, 331], which demonstrated the iron-induced increase of the transverse relaxation rate in nigrosome 1 primarily originated from iron accumulated in the neuromelanin within dopaminergic neurons, rather than other iron storage complexes such as ferritin. The MRI transverse relaxivity caused by the iron-rich neuromelanin was described by the static dephasing approximation [227], demonstrated as a rather significant R_2^* increasing effect, than R_2 (effective R_2) derived from SE(FSE)-based sequences, whose signal could profoundly rely on the nigrosome integrity.

5.4.3 Putaminal effective R_2 in PD corresponds to the local DaT dysfunction severity at early stage of PD

The positive linear correlation between the putaminal effective R_2 and the corresponding DaT SBR, further suggests that the observed effective R_2 in PD putamen is associated with the disease progress, evaluated by the severity of putaminal DaT dysfunction at baseline (Fig. 5.8) and during the 48-month period (Fig. 5.10). Moreover, in this study, a very strong, positive correlation between the effect of putaminal effective R_2 and SBR, of stable asymmetrical PD, at baseline, is demonstrated by the result (Fig. 5.9), after eliminating the individual variation by calculating and analysed the hemispheric differences of the effective R_2 and SBR. This result also supports the unilateral progress of the putaminal cell loss and dopaminergic fibre density reduction in PD hemispheres [326], suggesting that the hemispheric difference of the local degeneration might be quantified by the effective R_2 , at early stage of PD. Nevertheless, the correlation is not observed in the caudate nucleus (Fig. 5.8-10), which is possibly due to the small variation of effective R_2 found in the region, and the subtle changes of dopaminergic neurodegeneration observed in the caudate nucleus of the PD subjects, compared to HC.

5.4.4 Effective R_2 measurement of individual brain region is limited in distinguishing HC and PD

Previously reported post-mortem results using a variety of techniques, including histochemistry, ICP-MS, AAS and wavelength dispersive X-ray (WDX) spectroscopy [43, 138, 328, 329], suggested an elevation of iron concentration in dopaminergic neurons within the substantia nigra in brains with PD compared to healthy brains. Hence, it was hypothesised an increased effective R_2 could be observed, caused by the enhanced iron-induced proton relaxation as the iron content pathologically accumulated in this brain region.

The absolute difference of the effective R_2 of the substantia nigra, between the HC group and either PD contralateral or ipsilateral group, is comparable to those of the conventional R_2 . In this work, higher group median of effective R_2 measured in the

substantia nigra of both PD hemispheres are observed, compared with HC (effective $R_2 = 12.69 \pm 0.73 \text{ s}^{-1}$), by 0.48 s^{-1} and 0.41 s^{-1} respectively. A similar difference between healthy subjects and PD patients was observed J. H. Barbosa *et al.* [191], using a GRASE sequence, where an elevated R_2 in the substantia nigra by 1 s^{-1} was found in idiopathic PD patients ($N = 20$, $R_2 = 21.7 \pm 1.7 \text{ s}^{-1}$) under 3.0 T, when comparing with healthy subjects ($N = 30$, $R_2 = 20.7 \pm 1.7 \text{ s}^{-1}$). Nevertheless, the difference of the effective R_2 in the substantia nigra, between HC and either PD contralateral or ipsilateral group, is found to be statistically insignificant ($p > 0.1$).

This is possibly because of the variation introduced by the neuron loss-associated change of diffusion coefficient of the tissue, which is a shared limitation by SE(FSE)-based pulse sequences, including the conventional R_2 , and the effective R_2 presented in this work. In particular, the neuron death in the substantia nigra manifests at the early stage of PD [327], which can counteract the T_2 -shortening effect caused by the iron accumulation [332]. In fact, large variation of conventional R_2 among individual PD patients was also reported in the past by Ordidge *et al.* [333]. Using a hybrid SE-GRE sequence, Ordidge showed that 3 out of 7 PD patients had abnormal T_2 measurements within the substantia nigra ($T_2 = 123 \pm 82 \text{ ms}$), and 4 with similar T_2 values ($35.9 \pm 4.1 \text{ ms}$) to those obtained in the healthy participants ($35.1 \pm 4.3 \text{ ms}$, $N = 7$). In our study, derived from an SE-based pulse sequence, the effective R_2 measurement might be also influenced by the neuron death-related change of water diffusion coefficient, decreasing the observed effective R_2 [191]. In contrast, a previous study [334] concluded that the effects of microstructural changes on water diffusion and R_2 were negligible in human subcortical grey matter, but their observation might be confounded by the fixation process of the brain samples [66, 68, 69]. It is also supported by the recent diffusion imaging analysis of the PPMI cohort, which suggested cross-sectional and longitudinal increase of non-compartmentalised water ('free water') within the substantia nigra of PD patients [335-337]. Other factors, such as the B_1 effect, long 2^{nd} $T_{E(\text{eff})}$, partial volume effect, and the sample size, could also contribute to the observed variation.

The increase of the free water in the substantia nigra, could also be supported by the relatively lower effective R_2 of the substantia nigra in PD ipsilateral group, comparing to the PD contralateral group; in contrast with the higher effective R_2 of putamen and globus pallidus in the PD ipsilateral group, comparing to the PD contralateral group. At the early stage of PD progression, neuron-loss takes place primarily in the substantia nigra, while the neurons within the putamen and globus pallidus might be still largely preserved [338, 339]. Therefore, the signal attenuation and effective R_2 difference in the putamen and globus pallidus, observed in this study, are possibly dominated by the iron concentration difference, but the R_2 -reducing effect of the increased water content might compensate for the iron accumulation in the substantia nigra. Recent attempts to manually separating the pixels by the dominant contribution (*i.e.*, iron, free water) of the MRI signal by thresholding or modelling [188, 340] might provide a remedy to the effect of the pathological change of the free water.

5.4.5 Longitudinal change of effective R_2 is overall consistent with the age-dependent non-haemin iron accumulation in HC, but associated with pathological iron alternation and microstructural changes in PD

In line with the previously reported post-mortem observations and MRI results [11, 51, 341, 342], the longitudinal trend of the median effective R_2 of HC group overall reflects the iron accumulation with normal ageing in the brain. Shown in Figure 9, in the caudate nucleus and the putamen, the consistent trend of slow increasing of mean effective R_2 values with time is observed, indicated by a positive effective R_2 change in percentage. This increasing trend is not observed in globus pallidus in this study, possibly because the non-haemin iron concentration in the globus pallidus reached the maximum plateau and the increase slows down at the earlier stage of life, around 30-40 yrs [11], while the age range of the subjects included in this work is between 40 yrs and 60 yrs.

As the overall trend of the effective R_2 values with time is observed as the median of the group measurements, the within-group heterogeneity presented when the

absolute effective R_2 values are examined longitudinally in individuals. This heterogeneity among individuals from the same group is found the most pronounced in the brain regions caudate nucleus, red nucleus, and substantia nigra, which can be partially explained by the partial volume effect, when the relatively small volume being segmented and measured. Nevertheless, compared with the HC group, the large fluctuation of individual subjects along the sampling time in two of the PD hemispheric groups, indicates the presence of factors that do not equally contribute to the observations of each group. Particularly, remarkable alterations of the effective R_2 measurements, with striking rises and falls during the period of 48 months, in the substantia nigra of some individuals from the PD groups, are found.

For PD patients, only a few comparable longitudinal brain MRI studies are found in the literature [180, 343], tracking the transverse relaxation rate R_2^* in the substantia nigra, but controversy results and the individual heterogeneity within PD were also observed. M. Ulla, *et al.* [180] reported the longitudinally increased R_2^* values measured in the substantia nigra of 14 PD patients after 36 months, comparing to those of healthy volunteers ($N = 18$), whose longitudinal changes were not statistically significant. Conversely, an overall unchanged R_2^* in early-stage PD patients ($N = 19$) was reported elsewhere after a 36-month period [343]. The authors suggested different longitudinal trends of the substantia nigra R_2^* among the PD cohort, based on their disease severity, assessed by the UPDRS scores. However, in our work, a correlation between the UPDRS part III scores with measured effective R_2 values of PD substantia nigra was not found ($p > 0.1$), and the longitudinal changes of the effective R_2 in this region was not statistically significant ($p > 0.1$). In comparison with the effective R_2 , R_2^* is obtained using the GRE pulse sequence, which is sensitive to the field inhomogeneity caused by the bulk susceptibility source in the tissue, such as clustering and locally accumulated iron content. Hence, R_2^* is affected by both the concentration and the local distribution of the tissue iron [344]. Therefore, the discrepancy observed in PD patients between the studies might be explained by the forms and the selective accumulation of iron content in certain types of cells [118, 138, 330, 345, 346]. On the other hand, the SE(FSE)-based pulse sequences reflect the

intrinsic molecular and microscopic proton relaxation of the biological tissue, so the observation might indicate the iron content is likely to accumulate in capsulation rather than diffusive distribution in the brain tissue with ageing.

In summary, derived from an SE-based pulse sequence, the effective R_2 can be calculated from the dual-contrast FSE MRI, hereby demonstrated using the PPMI's retrospective MRI data. As a widely employed anatomical MR pulse sequence, the dual-contrast FSE requires much shorter acquisition time than the SE pulse sequences that are used for calculating conventional R_2 , and more prevalent in retrospective MRI data. Compared with the conventional R_2 measurement, the effective R_2 presented here also is linearly correlated with the reported age-dependent brain iron concentration [11], showing an iron-dependent coefficient comparable to that for the conventional R_2 at the same magnetic field strength [258]. Moreover, the effective R_2 shows the capability to indicate the asymmetrical disease progression in PD brain hemispheres. In particular, the effective R_2 of the putamen is able to measure the hemispherical difference of the DaT dysfunction severity in the early stage of PD, with a linear correlation with the hemispherical SPECT SBR difference. UP to 48 months, the longitudinal changes of the effective R_2 in HC are overall in line with the post-mortem and MRI observations of the age-dependent brain iron accumulation in the literature [11, 51, 341, 342].

5.5 Conclusions

A simple, reproducible method to extract quantitative effective R_2 values is demonstrated in this work, using the dual-contrast FSE sequence that have been mainly used for anatomical imaging, as an alternative to the time-consuming conventional R_2 relaxometry. Using the retrospective 3.0 T *in vivo* human brain MR data from the PPMI study, quantitative analysis is performed using the measured effective R_2 within various brain regions of healthy brains and brains with PD. The cross-sectional and longitudinal analyses in this study suggest a novel quantitative use of the commonly assumed qualitative MRI method, and correlated the measurements

with the empirical iron concentration, and with the asymmetrical pathological changes of the brain tissue caused by the PD progression.

5.6 Acknowledgements

Data used in the preparation of this Chapter were obtained from the Parkinson's Progression Markers Initiative (PPMI) database (www.ppmi-info.org/data). For up-to-date information on the study, visit www.ppmi-info.org.

PPMI – a public-private partnership – is funded by the Michael J. Fox Foundation for Parkinson's Research and funding partners, including AbbVie, Allergan, Avid Radiopharmaceuticals, Biogen, BioLegend, Bristol-Myers Squibb, Denali, GE Healthcare, Genentech, GSK GlaxoSmithKline, Eli Lilly and Company, Lundbeck, Merck, Meso Scale Discovery (MSD®), Pfizer Inc, Piramal Imaging, Roche, Sanofi Genzyme, Servier, Takeda, Teva, UCB and Golub Capital.

Chapter 6: Evaluation of QSM contrast and quantitative measurement of iron in phantoms and human brains on 3.0 T MRI: comparison with transverse relaxation.

6.1 Introduction

MRI has been employed as a versatile medical imaging tool in both research and clinical settings. By employing different pulse sequences (see Chapter 2), MRI can generate a spectrum of contrasts and detect various tissue properties. Influenced by the (super)paramagnetic tissue iron, a biological and imaging feature of ageing and pathological changes, enables MRI to be an iron-sensitive technique to study brain iron in living subjects [13, 14] (Chapter 1).

As different MRI parametric methods were previously presented in the literature (Chapter 3), such as R_2 [50, 174, 186, 248, 257] and R_2^* [178, 259-261] mappings, FDRI [251, 264, 265], and R_2' [186, 200, 263], to quantify the iron concentration, QSM emerged in the recent decade as an advanced MRI technique in detecting tissue iron. Utilising the GRE sequence (Section 2.2.2), the QSM technique extracts the information of bulk susceptibility from the MR phase shift (see Sections 3.3 and 4.4.2, and reference [244]), rather than reconstructing the conventional magnitude image from the MR signal. Compared with existing MRI approaches to measuring brain iron, QSM has the advantages of higher sensitivity to tissue iron [51, 191, 260], and faster MR acquisition for clinical settings, which would allow measuring iron concentration in the whole brain within ten minutes.

The susceptibility contrast and the quantitative measurements reconstructed by QSM, rely on both appropriate 3D GRE acquisition and the subsequent image processing. Summarised in Section 4.4.2, the raw phase data received by the MR scanner is first required to be processed to obtain the unaliased local frequency shift caused by the (bulk) susceptibility source within the tissue, by removing the global field inhomogeneity ('background field') [245, 246, 276, 277]. Subsequently, to solve the ill-posed field-to source problem, different approaches have been proposed. Regarded as the current gold standard, the susceptibility source could be solved by

acquiring the above phase information repeatedly from different angles, and resolving the problem using the least square method [279]. However, for human brain MRI, it requires posing and maintaining the patient in multiple orientations within the scanner bore during the acquisitions, as the main magnetic field generated by the MRI scanner is fixed, which is clinically impractical. Consequently, single-orientation methods were proposed [13, 17-19, 280, 347], which often involved regularisation or inverse-filtering the k-space data (see Section 3.1.3), and QSM thereby has shown great potential in measuring tissue iron in clinical settings.

Although the algorithm development for the single-orientation QSM is an active research field [269, 348] by the time of writing, the nMEDI (nonlinear morphology enabled dipole inversion) [17-19] has pioneered in tackling the field-to source problem, and continues demonstrating its influence on this research topic thereafter [273, 305, 307]. Using the magnitude edge information as *a priori* for the L_1 -regularisation, the nMEDI- L_1 (nonlinear morphology enabled dipole inversion with L_1 -regularisation, also see Section 4.4.4.2) algorithm has become publicly available (<http://pre.weill.cornell.edu/mri/pages/qsm.html>). Meanwhile, its accuracy of calculating the susceptibility and superior contrast in human brain MRI to TKD-based methods was also reported [19, 281]. Hence, it provides an opportunity to establish and validate the QSM MRI technique for measuring the iron concentration in phantoms and living tissues.

Moreover, together with complementary prior-published post-mortem data in the literature (reviewed in Section 1.2, as well as in reference [13, 46]), the hallmark study carried out by Hallgren and Sourander [11], has shown the age-dependent iron increase with normal ageing in different brain regions of 81 subjects of age 0-100 yrs, and mathematically demonstrated the correlations between the brain region-specific iron concentration with the age of the subject. It, therefore, has enabled the estimation of brain iron concentration based on the subject's age for current *in vivo* MRI studies [191, 245, 260].

Therefore, this study presented here aimed to set up and validate an MRI pulse sequence, that enables QSM for measuring iron on the GE healthcare 3.0 T MR scanner at the local NHS hospital, UHCW (University Hospital Coventry and Warwickshire), Coventry, United Kingdom. Specifically, the objectives are to develop a protocol of MRI acquisition and image post-processing with nMEDI-L₁ QSM, and to allow the susceptibility contrast and quantification of iron concentration in phantoms and in healthy, living human brains using the measured susceptibility. Subsequently, in comparison with the established transverse relaxation rates, this project also aims to investigate the reliability and reproducibility of the susceptibility, and to identify any potential obstacles for measuring brain iron with QSM of *in vivo*, clinical 3.0 T MRI.

6.2 Methods

6.2.1 MR phantom

To validate the MR acquisition and the post-processing methods, a ferric iron phantom is constructed for this study. As ferric iron (Fe^{3+}) has poor solubility in water at neutral pH, chelators are used to stabilise the iron ions in the phantom and to prevent metal precipitation, by forming soluble coordination complexes. The complexing agents ethylenediaminetetraacetic acid (EDTA) and nitrilotriacetic acid (NTA) are used respectively, to investigate any MR-visible effect of ligands on the iron centre of the coordination compounds. The chelating protocol is adapted from the previous reports [349, 350]: $\text{FeCl}_3 \cdot 6\text{H}_2\text{O}$ is freshly dissolved in a small amount of 0.1 M hydrochloric acid (HCl) to minimise the hydrolysis and polymerisation of the iron ions [351]. The Fe^{3+} chelate solution is then prepared by mixing the dissolved iron solution with the freshly prepared 100 mM PIPES buffer (pH = 7.4, 20 °C) that is doped with NTA and EDTA respectively, in a molar ratio of 1:1.5 for Fe^{3+} :chelator to ensure the entire chelation of Fe^{3+} . The solution is let stirred for an hour to stabilise the pH, and the pH of the solution is re-adjusted to pH = 7.4 if needed, to allow the continuous dissolution of the chelating agent. The final solutions are prepared by stirring the chelated iron solution for an additional hour to ensure complete chelation, and then diluted into a series of concentrations of chelated iron with 100 mM PIPES buffer (pH = 7.4, 20 °C). Already prepared 4 % w/v agarose gel is cooled to

45-55 °C in an ultrasonic bath maintained at 37°C, then carefully mixed with the pre-warmed chelated iron solution in a volume ratio of 1:1 in a cylindrical borosilicate glass container (ID/OD = 18/20 mm) individually. The final concentrations of chelated Fe³⁺ in the 2 % w/v agarose gel were 7.4, 6.17, 4.93, 3.7 2.47, 1.85, 1.23, 0.62, 0 mM. All resulting chelated Fe³⁺ gel samples in the cylinder container are sealed and positioned in a large cylinder polystyrene (PE) container (ID/H = 14/5.5 cm), and the space between samples inside the PE container is filled with 2 % agarose gel to fix the position of individual samples (Fig. 6.1).

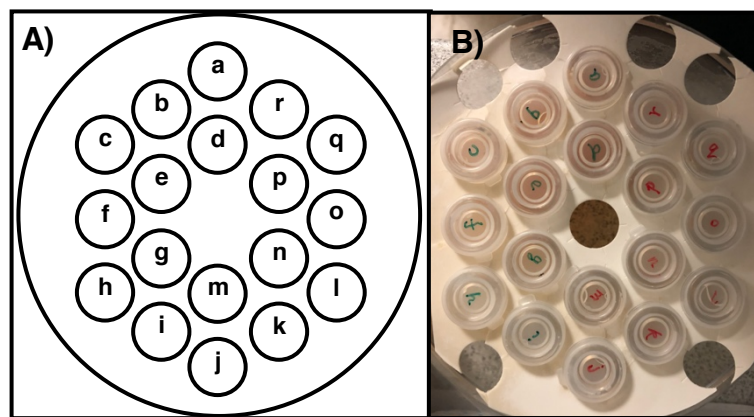


Fig. 6.1 Chelated Fe³⁺ MR phantom construction.

The schematic (A) and the photographic (B) locations of individual samples within the phantom were shown. The Fe³⁺-EDTA samples (a-i) and the Fe³⁺-NTA samples had identical descending gradients for Fe³⁺ concentration: 7.4, 6.17, 4.93, 3.7 2.47, 1.85, 1.23, 0.62, 0 mM.

6.2.2 Healthy volunteers

As the brain iron concentration is known to be a function of age [10, 11, 352], this study aimed to recruit healthy adults with an age span between 20 to 80 yrs, to investigate the potential age-related susceptibility change (see initial study design in Appendix I1: Signed BSREC application form). However, due to the coincidence between the volunteer study and the COVID-19 pandemic, any volunteer aged over 50 yrs was considered to be potentially vulnerable by the GafREC ethical committee, and excluded from the study, and the number of volunteers was reduced. Therefore, eventually, eight healthy adult volunteers (4 females, 4 males) with the age range from 23 to 49 yrs (average age = 33.3 ± 9.3 yrs, matched age between genders) were

recruited from the University of Warwick, United Kingdom, and underwent MRI examination at the University Hospital Coventry and Warwickshire (UHCW), Coventry, United Kingdom, between September and October 2020. Additionally, another volunteer (female, 28 yrs) is scanned twice with two weeks apart during the same period to determine the imaging reproducibility. Informed consent is signed and obtained from all volunteers before the study began. All volunteers are assessed to confirm the absence of neurological disorders or abnormalities before the MR examination, and the resulting MR images are examined by a neurologist after the acquisition for any abnormality.

This study is approved by the Biomedical and Scientific Research Ethics Committee (BSREC, reference: BSREC 74/18-19), and by the Governance arrangements for Research Ethics Committees (GafREC, reference: GF0360), subject to the adjustment for COVID-19 pandemic, in the United Kingdom (see Appendix I).

6.2.3 MR acquisition

6.2.3.1 3D GRE for QSM and R_2^* mapping

To set up an MR pulse sequence that can enable subsequent QSM processing, a 3D GRE sequence is built upon an adapted SWAN (susceptibility weighted angiography, GE Healthcare) on a 3.0 T clinical MR scanner (Discovery MR750w, GE Healthcare) to generate the required complex data. Similar to other SWI sequences, the original SWAN sequence is provided by the manufacturer for clinical angiography, with a 3D GRE backbone, generating combined-echo T_2^* -weighted magnitude images that are masked by weighted phase information. This sequence is modified to acquire multi-echo k-space information with flow compensation, and for this study, short T_E are employed to image brain regions with high iron content.

The acquisition parameters of the 3D GRE pulse sequence are as follows: $T_R = 78$ ms (minimal T_R), $T_E = 3.8, 7.8, 11.8, 15.8, 19.8, 23.8, 27.8, 31.8, 35.8, 39.8, 43.8, 47.8$ ms, ESP = 4 ms, number of echoes = 12 with uni-polar readout gradient, FA = 20°, number of excitation (NEX) = 1, FOV = 256 × 256 × 128 mm, matrix size = 256 × 256 × 64, resolution = 1 × 1 × 2 mm³, BW = 62.5kHz. Parallel imaging using array coil spatial

sensitivity encoding (ASSET) is applied to reduce acquisition time, with an acceleration factor of 2. The acquisition time is 7 min 10 sec. A low spatial resolution 2D fast GRE calibration scan is performed before the SWAN acquisition, to enable the parallel imaging, for calculating the coil sensitivity for the coil combination. The acquisition time for the calibration scan is 6 sec.

6.2.3.2 Axial dual-contrast FSE for anatomical proton density- and T_2 -weighted images, and effective R_2 mapping

To compare the quality and the image contrast of the QSM obtained using the 3D GRE sequence, with clinical routine anatomical MRI, the proton density -weighted and T_2 -weighted images of the individual are acquired by a dual-contrast FSE acquisition during the same scan session. Moreover, the dual-contrast FSE is also set up to investigate the effective R_2 derived from the MR signal of the pulse sequence, in comparison with other quantitative MRI methods for iron measurement, *i.e.*, R_2 , R_2^* and susceptibility. Within the scan time limitation, the T_R is allowed to be long enough for the MR signal relaxation of most of the tissue compartments, and the shortest 1st effective T_E is used to capture the fast-decaying signal within iron-rich regions, which is determined by the minimal ESP allowed by the GE Discovery MR750w system for the dual-contrast FSE. A moderate ETL and a refocus pulse FA smaller than 180° has to be employed to reduce the SAR on the volunteers, and the FOV and the in-plane resolution is set up to match the 3D GRE sequence. The scan parameters are also set up to be comparable to those of PPMI's dual-contrast FSE (see Chapter 5, Method) on the Siemens TrioTim system, to further examine the effective R_2 measurement, compared with R_2 , R_2^* and susceptibility.

Therefore, the 2D dual-contrast FSE sequence is applied with following acquisition parameters: $T_R = 3000$ ms, ESP = 18.5 ms, ETL = 10, effective $T_E = 18.5$ (minimal T_E) and 111.2 ms, FA = 150° , acquisition plane = axial, FOV = 256×256 mm, matrix size = 256×256 , in-plane resolution = 1×1 mm², BW = 20.5 kHz, percent phase FOV = 0.85, slice thickness = 2 mm, number of slices = 62. The acquisition time is 6 min 59 sec.

6.2.3.3 Axial MESE for R_2 mapping

During the same scan session of the volunteer, a 2D CPMG sequence is employed to acquire MESE MRI data (see Section 2.2.1.2) for R_2 mapping, to compare it with effective R_2 , R_2^* and susceptibility for iron measurement. The acquisition parameters used in the pulse sequence are $T_R = 2500$ ms, ESP = 9.5 ms, ETL = 8, $T_E = 9.5, 19, 28.5, 38, 47.5, 57, 66.5, 76$ ms, FA = 90° , acquisition plane = axial, FOV = 256×256 mm, matrix size = 256×256 , in-plane resolution = 1×1 mm², BW = 41.7 kHz, percent phase FOV = 0.75, slice thickness = 2.5 mm, number of slices = 50. The acquisition time is 10 min 40 sec.

6.2.4 Image processing and analysis

6.2.4.1 Reconstruction

Magnitude images are reconstructed first at the scanner after the acquisition to inspect the image quality and to be examined by a neurologist for any abnormality. As no significant distortion or signal drop-out caused by the susceptibility is seen on the magnitude images, near the brain-air and tissue-CFS interfaces, and no motion artifact is observed, the MRI data proceed to be collected and analysed. For the 3D GRE data, the raw MRI data are collected for off-line reconstruction, to avoid any contrast filters and the gradient non-linearity correction, which are automatically performed for the sequence after the acquisition.

Raw 3D GRE data are reconstructed off-line, to preserve the true phase data. For this study, an off-line reconstruction pipeline is built within MATLAB (R2019b, MathWorks) utilising an obtained-access vendor provided software development kit (SDK, Orchestra-sdk-1.9-1, GE Healthcare). The GE MRI raw data are stored in a format of 'P-file' as multi-channel FIDs, containing the entire k-space information of the scans. The complex image data for each channel (channel images) are reconstructed from the 3D k-space data firstly using inverse Fourier transform (IFT) along the slice-direction (2nd PE direction, z-axis), followed by the 2D in-plane (x-y plane) IFT. For the parallel imaging using ASSET, a separate P-file of the calibration scan is acquired to obtain the sensitivity information for each receive coil. Then the receive coil B_1 field is estimated based on the calibration scan signal, using the

function *GERecon('Calibration.Process')*. Using the generated coil sensitivity information, the aliased channel images are combined in the image space by calling the function *GERecon('Asset.Unalias')*. This process is comparable to the SENSE (Sensitivity encoding) technique [233], which generates the unwrapped combined signal matrix (complex MR image) from the aliased intensities of the multi-channel matrix via inversion, with the sensitivity weight of each receive coil. To reverse the effect of phase cycling employed in the acquisition, the un-chopping of RF is carried out along the slice-direction and to the in-plane matrix, which reverses the sign for every other pixel in the image data, generating the final complex MR images.

6.2.4.2 QSM and quantitative parametric mapping

For the further QSM processing of the 3D GRE MRI data, the conceptual pipeline is described in Chapter 4: Research Methodology, following post-processing steps are performed on the complex MR data obtained in this study: 1) region-grow phase unwrapping to resolve the frequency (phase) shift detected by the MR system, which is inherently wrapped within 2π (Δf_{MR} in Eq.(2.25), Section 2.3.2.2), 2) background field removal using PDF [246], to remove the global field inhomogeneity contribution to the detected phase Δf_{MR} (see Eq.(2.26), Section 2.3.2.2), and therefore calculate the local field perturbation caused by the subject and RDF (see Eq.(2.24), Section 2.3.2.2), 3) solving the susceptibility from RDF using MEDI+0 [271] (nMEDI-L₁ [281] with CSF as zero-referencing, see Section 4.4.2) with the empirical selection of the regularisation parameter $\lambda = 100$ for the phantoms, and $\lambda = 1000$ for the human brains, respectively, balancing the susceptibility contrast and the suppression of the streaking artifacts.

To compare the QSM with the quantitative parametric mapping for measuring brain iron, R_2^* , R_2 and the effective R_2 maps of a young adult (male, age 24 yrs) are calculated from the magnitude data of the 3D GRE, MESE and the dual-contrast FSE pulse sequences respectively. All data are pre-processed to achieve a zero-mean background before fitting. The observed signals are then fitted into a mono-exponential decay using the least-squares method, to calculate the transverse relaxation parameters R_2 and the effective R_2 , as described in Section 4.4.1 and

Section 5.2.5. For R_2^* mapping, an algorithm based on the auto-regression on linear operations (ARLO) [353] are used for fitting the mono-exponential decay efficiently, due to the large size of the 3D GRE data (later detailed in Section 7.2.5.2).

Using the identical FOV coverage and corresponding slice thickness among the acquired MR images, the co-registration is minimised to avoid the registration and the interpolation errors, and to equalise the partial volume effects between MRI modalities. An exception is made for the MESE acquisition, where the slice thickness was increased to 2.5 mm due to the long scan time that would have been required otherwise. The acquired MESE images are reconstructed and processed for quantitative MRI parametric mapping, and the resulting R_2 maps are first combined into a 3D volume and then resliced to 2 mm axial slices that have the same coverage and pixel locations as other MR modalities.

6.2.4.3 Segmentation

Circular ROIs within each chelated ferric iron gel sample are delineated for the MR phantom. For the human brain MRI, the ROIs are segmented manually on the reconstructed susceptibility images and measured within ImageJ (Fig. 6.2), based on the human brain atlas [312]. The ROIs include bilateral caudate nucleus head (CN), globus pallidus (GP), putamen (PUT), red nucleus (RN) and substantia nigra (SN). In addition to determining the location and boundaries of the brain regions using the brain atlas reference, segmentation of each ROI also follows the criteria summarised in Table 4.1 in Chapter 4. For repeated measurements in human brains, a set of ROIs for the individual is delineated based on the baseline acquisition, then translated to the follow-up scans, and refined when necessary.

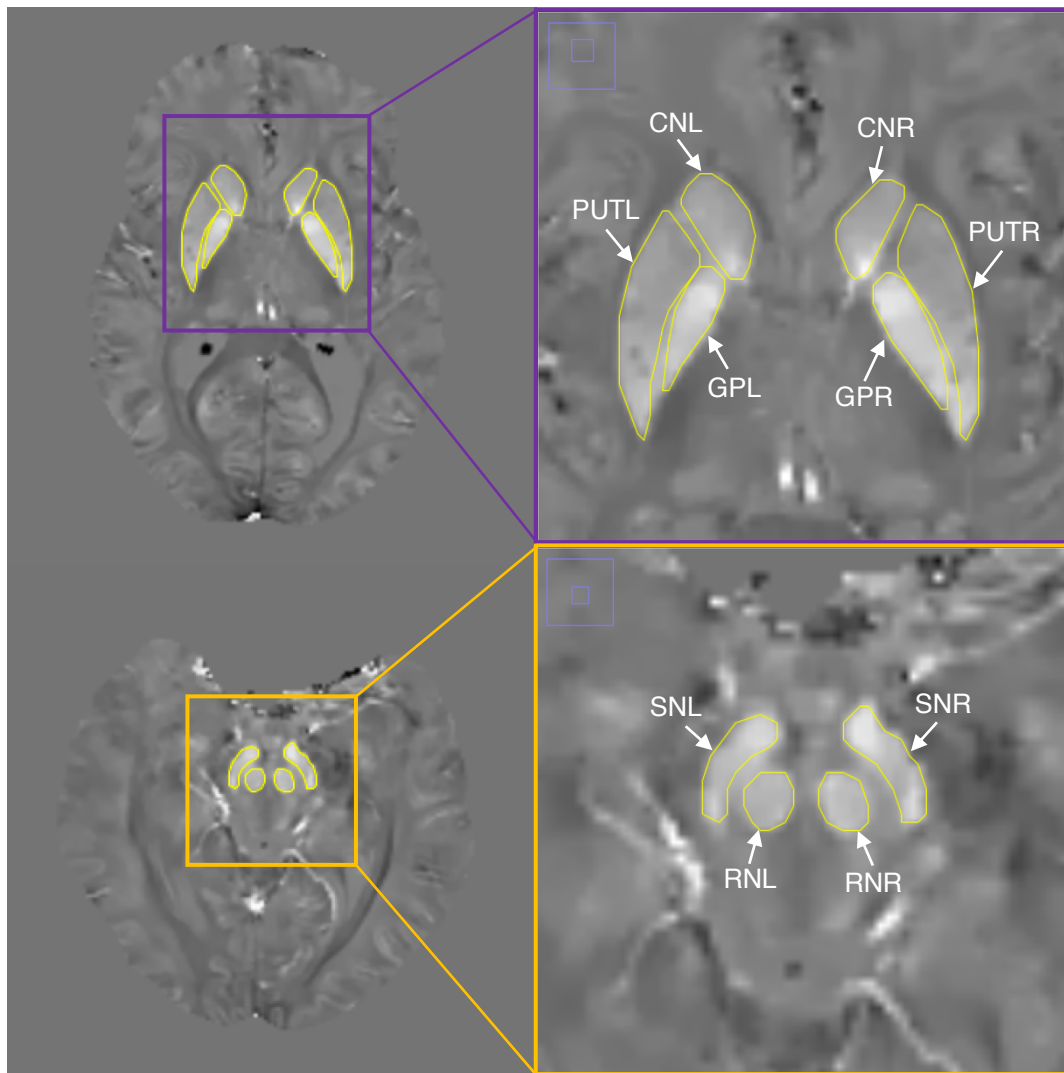


Fig. 6.2 Example segmentation of *in vivo* human brain MRI on QSM.

ROIs overlay on the susceptibility maps (left column). Left (L) and right (R) brain regions on the image included: CN – caudate nucleus, GP – globus pallidus, PUT – putamen, RN – red nucleus, SN – substantia nigra.

6.2.4.4 Contrast comparison

To investigate the susceptibility contrast generated by QSM, the susceptibility images are demonstrated for the phantom and brains, respectively, in comparison with the magnitude images and RDF, derived from the same 3D GRE sequence. Moreover, the anatomical contrast in the brain, generated by QSM, is compared with the clinical routine anatomical scans, proton density-weighted and T₂-weighted images. The neuroanatomy of the subcortical regions (see previous Section 6.2.4.3) is labelled, and the respective line profiles of the signal intensity of the midbrain regions

(substantia nigra and red nucleus), on the susceptibility maps, proton density-weighted and T₂-weighted images are drawn and compared.

6.2.5 Data analysis

6.2.5.1 Theoretical bulk susceptibility of the MR phantom

The theoretical bulk susceptibility of each chelated ferric iron gel sample within the phantom is calculated as:

$$\chi_{theoretical} = \frac{\sum_i \chi_i V_i}{V_{total}} = \chi_{Fe^{3+}} f_{Fe^{3+}} + \chi_{water} f_{water} \quad \text{Eq. (6.1)}$$

where $\chi_{theoretical}$ indicates the theoretical volume susceptibility of each sample, χ_i the volume susceptibility of each component, V_i and V_{total} the individual volume of each component and total volume of the gel sample, and f denotes the volume fraction of each component. $\chi_{Fe^{3+}}$ is calculated from the molar susceptibility of FeCl₃·6H₂O and χ_{water} of H₂O at 20 °C, both according to CRC Handbook of Chemistry and Physics (97th edition, 2017) [354]. All susceptibility is converted into the SI unit.

6.2.5.2 Iron concentration estimation for *in vivo* human brain MRI

For all healthy volunteers, the brain iron concentrations in the caudate nucleus, putamen and globus pallidus are estimated based on the subject's age, using the regression formulas reported by Hallgren and Sourander [11] with the post-mortem results. The prior-reported formulas of the healthy brain iron concentration as a function of age for these brain regions are detailed in Sections 4.2.1. To summarise, the brain iron concentration, measured with the histochemistry method, experiences a region-specific exponential increase during normal ageing. Hence, by adjusting for the age-dependent iron accumulation, the influence of normal ageing on the iron concentration is accounted for, to minimise the estimation error of iron concentration in this work. However, for substantia nigra and red nucleus, the respective average iron concentrations (see Table 1.1 in Chapter 1, averaging from subjects with 30-100 yrs of age) reported from the previous report [11] are used, as the estimated iron concentration in the following analysis of this study, because the prediction model for these two regions was not reported by Hallgren and Sourander.

Recently, concerning the historical post-mortem iron concentration measured by Hallgren and Sourander [11], questions were raised in the research field, regarding the reliability of the historical techniques [53], as the ICP-MS measurement has been used for validation of post-mortem QSM [51]. Nevertheless, the different iron concentration of red nucleus measured utilising ICP-MS, has been reported by Krebs and colleagues [9]. Therefore, the estimated brain iron concentration from the second reference post-mortem study [9] is also demonstrated in this PhD project on a volunteer (male, 24 yrs of age) for comparison, as employed previously [51, 245].

6.2.5.3 Statistical analysis

The mean, median, and standard deviation of each measurement within the ROIs are extracted, and the histograms of the pixel values are examined and tested for normality using Shapiro–Wilk test. The mean values of each ROI are used for the subsequent analysis. For the MR phantom, linear regression analysis is performed between the measured susceptibility and the ferric iron (Fe^{3+}) concentration, in the form of Fe^{3+} -EDTA and Fe^{3+} -NTA, respectively. Linear regression analysis is also performed between the measured susceptibility of each brain region of volunteers, and the corresponding age-dependent iron concentration estimated based on Hallgren and Sourander's work [11]. For the regression analysis of the susceptibility and estimated iron concentrations within human brains, models that employed the measured data from all brain regions, from basal ganglia (caudate nucleus, putamen and globus pallidus) are performed respectively. This is to investigate the impact of the iron estimation with (caudate nucleus, putamen and globus pallidus) and without (substantia nigra, red nucleus) adjustment of the age-dependency (see Section 6.2.5.2). To complete the analysis with data exclusion, subsequent leave-one-region-out regression analysis is carried out, to exclude potential bias introduced by the reduced sample size. The least-squares method is employed for all regression analyses.

To investigate the relationships between different quantitative MRI measurements, correlation analysis is carried out between each two of the measured effective R_2 , R_2 , R_2^* and the susceptibility, within the brain regions of the same individual (male, 24

yrs of age). Moreover, for the same volunteer, the correlation analysis is also performed for each of the above quantitative MRI measurements of the brain regions, with the corresponding iron concentrations estimated using Hallgren and Sourander's model [11], and using Krebs *et al.*'s report [9], respectively. The null hypothesis is rejected at a 5% significance level ($p < 0.05$).

Finally, for the QSM measurement, the reproducibility of the imaging acquisition and processing is estimated within each brain region, calculated by

$$reproducibility = \left(1 - \frac{\sqrt{2} \times \sigma_y}{\sqrt{\bar{y}^2}} \right) \times 100\% \quad \text{Eq.(6.2)}$$

with σ_y denotes within-subject standard deviation, \bar{y} the average between the susceptibility measured from two repeated scans of one individual (female, 28 yrs). All statistical analysis is performed within MATLAB (R2019b, MathWorks).

6.3 Results

6.3.1 Susceptibility contrast in phantoms and human brains

The reconstructed images for the phantom are shown in Fig. 6.3, demonstrating various signal contrasts generated by the iron-loaded gel phantoms. The iron concentration gradient does not show in the magnitude image, because the short T_R and small FA employed in the GRE sequence enables a mixed contrast that more close to a proton density-weighted instead of T_2^* weighted images. Some shading is seen on the magnitude image near the external boundary on the top and the bottom of the phantom, because of the magnetic inhomogeneity possibly caused by the strong susceptibility perturbation of the iron-loaded phantom and the inadequate auto-shimming. The RDF reflects the field disturbance introduced by the individual samples with various susceptibility sources, *i.e.*, chelated ferric iron in different concentrations. In the circular cylinder volume whose axis is perpendicular to the external field B_0 , the susceptibility source demonstrates a location-dependent radial demagnetising field perturbation from the outside of its boundary, known as the blooming effect, and within the boundary, the introduced field perturbation ΔB is proportional to the relative susceptibility $\Delta\chi$ of the sample [239]. This field perturbation is solved as an inversion problem and the resulting susceptibility map

illustrated the contrast that corresponded to the iron concentration in each sample. Figure 6.4 shows an example of a human brain reconstructed via QSM post-processing.

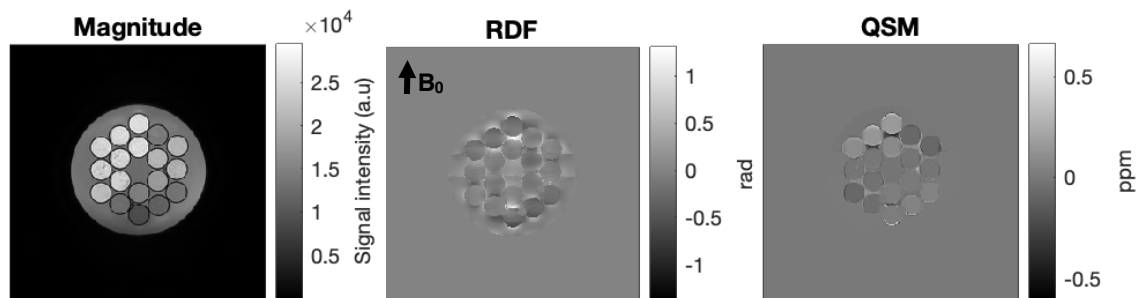


Fig. 6.3 Axial view of the magnitude (left), RDF (middle) and susceptibility map (right) of the iron phantom.

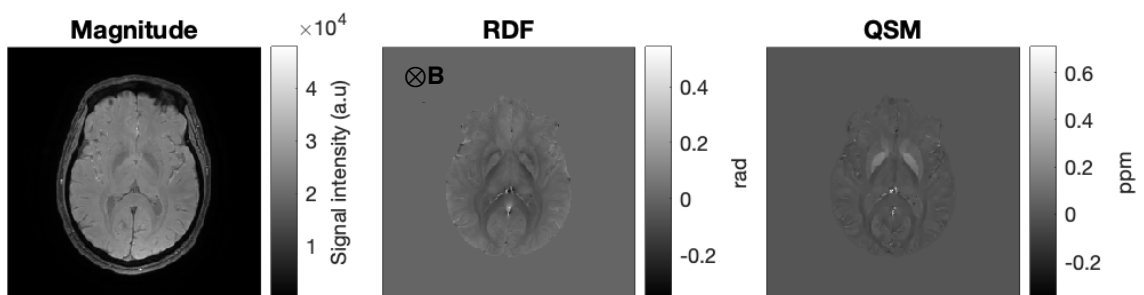


Fig. 6.4 Axial view of the magnitude (left), RDF (middle) and susceptibility map (right) of an example human brain (male, age = 24 yrs).

6.3.2 Anatomical contrast of deep grey matter in proton density-, T_2 -weighted images and QSM

Compared with the proton density- and T_2 -weighted images generated from the dual-contrast FSE, less noise and higher CNR is observed in the susceptibility map (Fig. 6.5 and 6.6). As a variation of the SE sequence, the FSE pulse sequence is not prone to artifacts, compared to GRE sequences, but the enhanced contrast in QSM is contributed by the additional information of the phase and accumulating T_E along the ETL.

6.3.2.1 Basal ganglia

Within the basal ganglia, the regions with high iron content show hyperintensity in QSM, compared to the surrounding tissue, while hypointensity on the proton

density- and T₂-weighted images, caused by the accelerated relaxation due to the paramagnetism of local iron content. Especially for the globus pallidus, the susceptibility contrasts are closely matched the structure in the T₂-weighted images. Better separation of the internal and the external globus pallidus is seen in the QSM, demonstrated as a higher signal intensity of the lateral side of the structure at the level of inferior II in Figure 6.5, and the medullary lamina – a fine line with relatively lower signal intensities (blue arrows in Fig. 6.5 Inferior I and II) that distinguishes the two parts of globus pallidus. The lateral outline of the putamen is clearly shown in the susceptibility map, but not in the proton density- or T₂-weighted images. In fact, this boundary fades into the external capsule and the insula under the current dynamic range. The striatal cell bridge can be seen between the QSM and the proton density-weighted images (orange arrows in Fig. 6.5 Middle I), and signal hyperintensity is observed in QSM around the caudate fundus region (green arrows in Fig. 6.5 Middle II and Superior I). The lateral ventricle is yet diminished in the susceptibility map, compared to its hyperintensity in the proton density- and the T₂-weighted images.

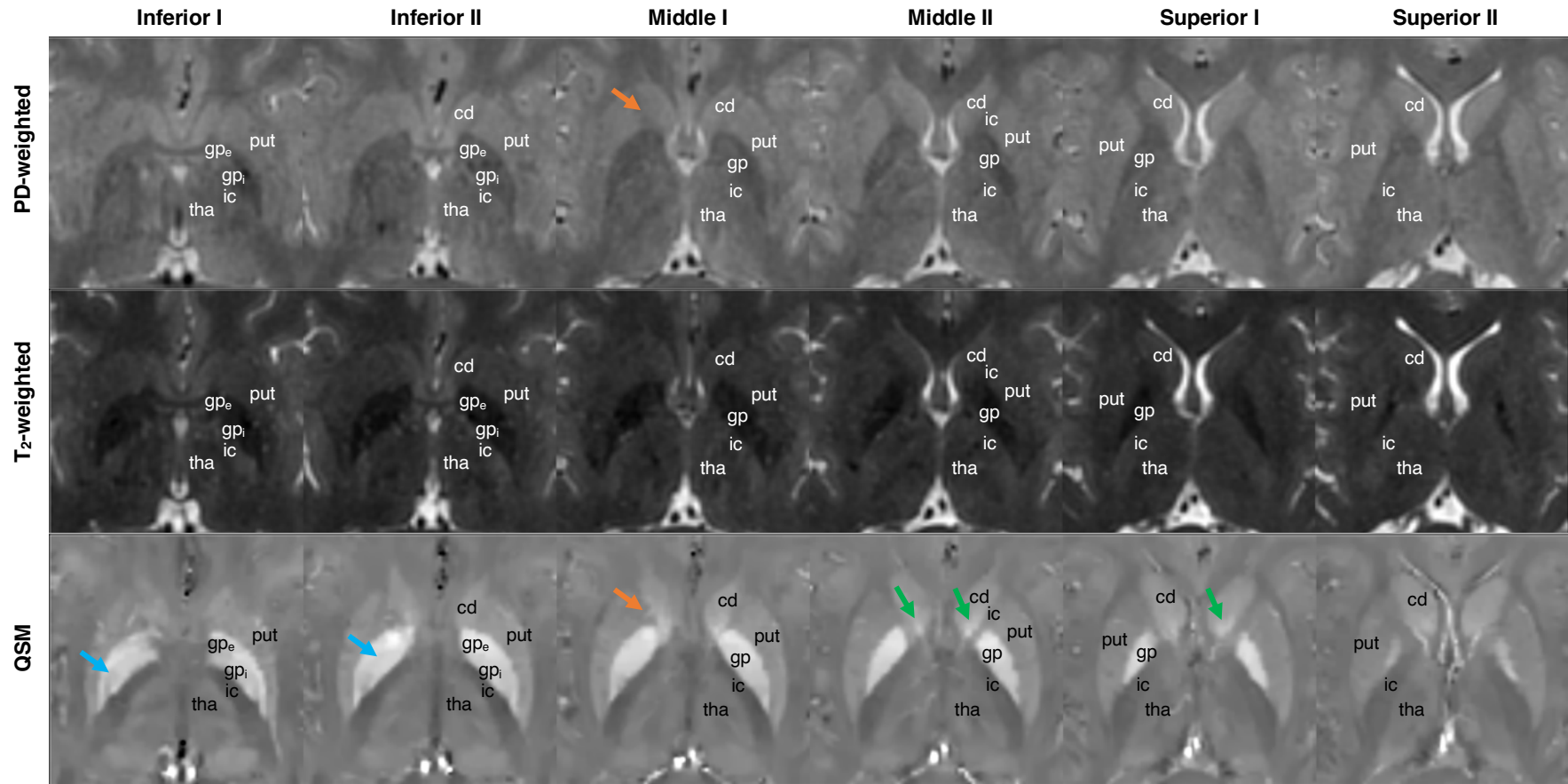


Fig. 6.5 Contrast comparison between proton density(PD)-weighted, T_2 -weighted and susceptibility images in the basal ganglia.

Blue arrows: medullary lamina; orange arrows: striatal cell bridge; green arrows: caudate fundus. cd: caudate nucleus; gp: globus pallidus; gp_e: external globus pallidus; gp_i: internal globus pallidus; ic: internal capsule; put: putamen; tha: thalamic nucleus. Anatomical notations with lower-case letters for image clarity.

6.3.2.2 Midbrain

The signal hyperintensity prolonging the posterior substantia nigra is observed in the susceptibility map (blue arrows in Fig. 6.6), compared to its counterpart in the other weighted images, especially in the inferior midbrain, the CNR of the inferior substantia nigra is greatly enhanced. It possibly corresponds to the substantia nigra pars compacta and its nearby region at the level of inferior I and II, generated by the iron deposit within the region and orientated white matter tracts perpendicular to the axial plane. On the same anatomical level, T₂-weighted images generate the contrast similar to QSM but with much lower CNR, while mainly the approximately circular hyperintense signal can be identified as the superior cerebellar peduncle on the proton density-weighted image. On the level of Middle I and II, where the mamillary body can be seen, the substantia nigra appeared hyperintensity on the susceptibility map, making up the majority of the hypointensity on the T₂-weighted image. Compared to the corresponding contrast on the proton density - and T₂-weighted images, a wider hyperintensity 'tail' (posterior, indicated by blue arrows in Fig. 6.6) and a narrower head (anterior) of the substantia nigra on Middle II is observed, consisting of the reticular and the compacter parts of the substantia nigra, located at the inner (medial) and outer (lateral) sides of the high signal intensity. This broad 'tail' observed in the QSM might correspond to where the nigrosome 1 and 3 within the substantia nigra pars compacta located [355], enriched with iron-loaded dopaminergic neurons. On the other hand, the anterior part of the corresponding hyperintense signal on the proton density- and T₂-weighted images, possibly contains the substantia nigra reticular nigrostriatal fibres and parts of the frontopontine tract. In the susceptibility map, the white matter tracts that reach to the lateral substantia nigra pars reticulata also become more apparent than in the other weighted images, demonstrating as fading signal intensity at the lateral border of the substantia nigra towards both sides of the anterior midbrain, with a woven pattern (green arrows in Fig. 6.6). However, this pattern become less evident in the proton density-weighted and the T₂-weighted images and submerge with the hypointense signal of the anterior substantia nigra pars reticula (white arrows in Fig. 6.6). It is also noticed that the signal contrast is found on the level Middle II on the proton density-weighted image, relatively hyperintense signals of the medial part to its lateral-anterior

neighbour (indicated by a fine yellow dashed line in Fig. 6.6), which possibly delineates the medial-posterior boundary of the iron-rich nigrosome 1 region.

From the mamillary body level and above, a pair of the ball-shaped red nucleus shows hyperintense signal in T₂-weighted image, identified by its main body on the level Middle II and the Superior I, superior to where the substantia nigra pars compacta are located. The hypointense lateral-posterior edge of the red nucleus magnocellular part on the Middle I level (orange arrow in Fig. 6.6, T₂-weighted), and in proton density-weighted image the hyperintense signal also included its surrounding white matter tracts. Showing comparable contrast to the T₂-weighted image, the susceptibility maps delineate the red nucleus as a similar ball shape with hyperintensity.

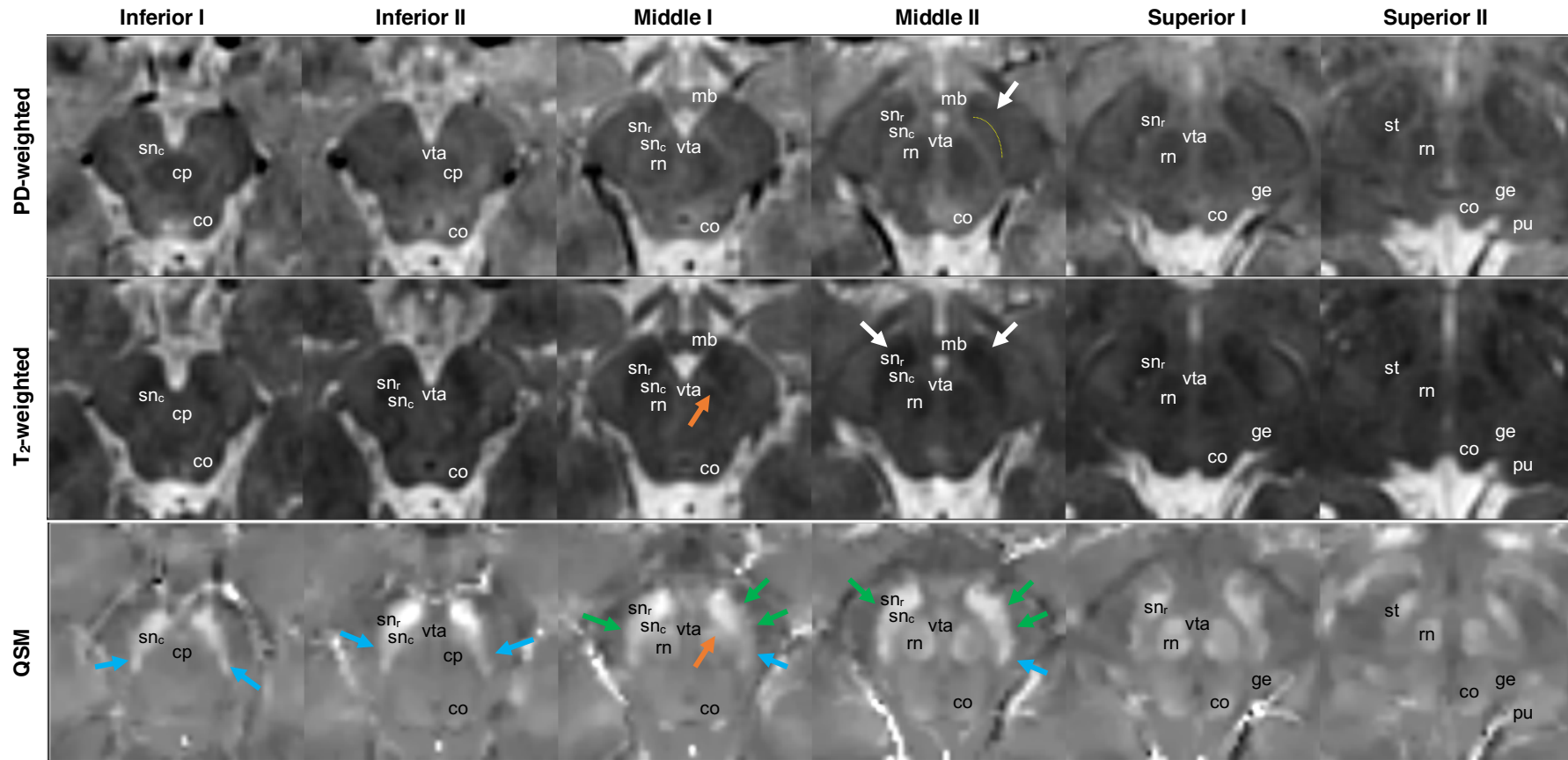


Fig. 6.6 Contrast comparison between proton density(PD)-weighted, T₂-weighted and susceptibility images in the midbrain.

Blue arrows: substantia nigra pars compacta; orange arrows: red nucleus magnocellular part; green arrows: white matter tracts; white arrows: absence of the white matter tracts; yellow dashed line: medial-posterior boundary of the iron-rich nigrosome 1 region. co: colliculus; cp: cerebellar peduncles; ge: geniculate body; mb: mamillary body; pu: pulvinar; rn: red nucleus; sn_c: substantia nigra pars compacta; sn_r: substantia nigra pars reticula; st: subthalamus; vta: ventral tegmental area. Anatomical notations with lower-case letters for image clarity.

The located signal comparison within the anterior midbrain on the inferior-middle level between the proton density-weighted, T₂-weighted and the susceptibility images (Fig. 6.7) is demonstrated by their horizontal line profiles (Fig. 6.8).

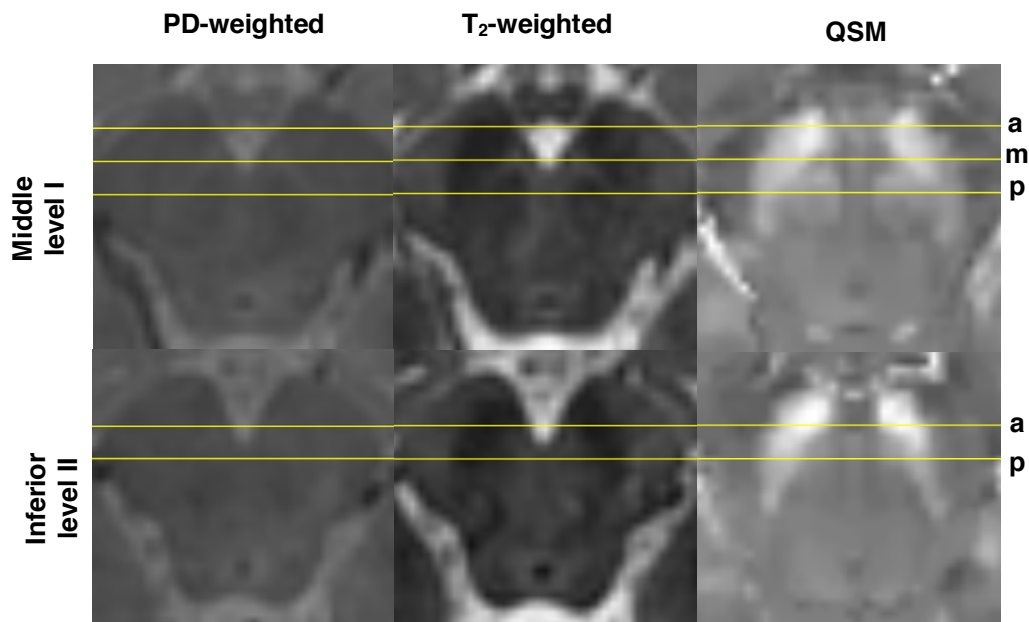


Fig. 6.7 Demonstration of the location of the horizontal line profiles of the midbrain on the inferior-middle level.

The yellow solid line indicated the location of the signal intensity measurement, from left to right. a: anterior, m: middle, p: posterior. PD - proton density.

Consistent with the visual examination of the images, the susceptibility maps generate better CNR among the iron-rich regions in the midbrain, demonstrated as the larger normalised signal intensity measured in the substantia nigra (indicated by yellow arrows in Fig. 6.7) compared to the surrounding tissue. By comparing the signal location, a misalignment is found between the hypointense signal on the T₂-weighted image (orange arrows in Fig. 6.8) and the hyperintensity in the susceptibility map (yellow arrows in Fig. 6.8), especially for the inferior level and the right-side substantia nigra on the images. The hyperintensity peak of the susceptibility is located more adjacent to the central midbrain, compared to its hypointense counterpart on T₂-weighted and proton density-weighted images. Also, this contrast drops out quickly in the susceptibility measurement compared with the slow gradual increase of the signal intensity measured in the proton density-weighted and T₂-weighted images, while moving from the central midbrain towards

the peripheral edge. It is the most pronounced at the anterior area, between 5 mm and 7 mm, and between 29 mm and 33 mm location on the Middle level I (Fig. 6.8a). This finding corresponds to the narrow ‘head’ of substantia nigra observed in the susceptibility maps compared with the other modalities, supporting that the susceptibility map could provide a more straightforward delineation of the nigra structure on the inferior level of the midbrain.

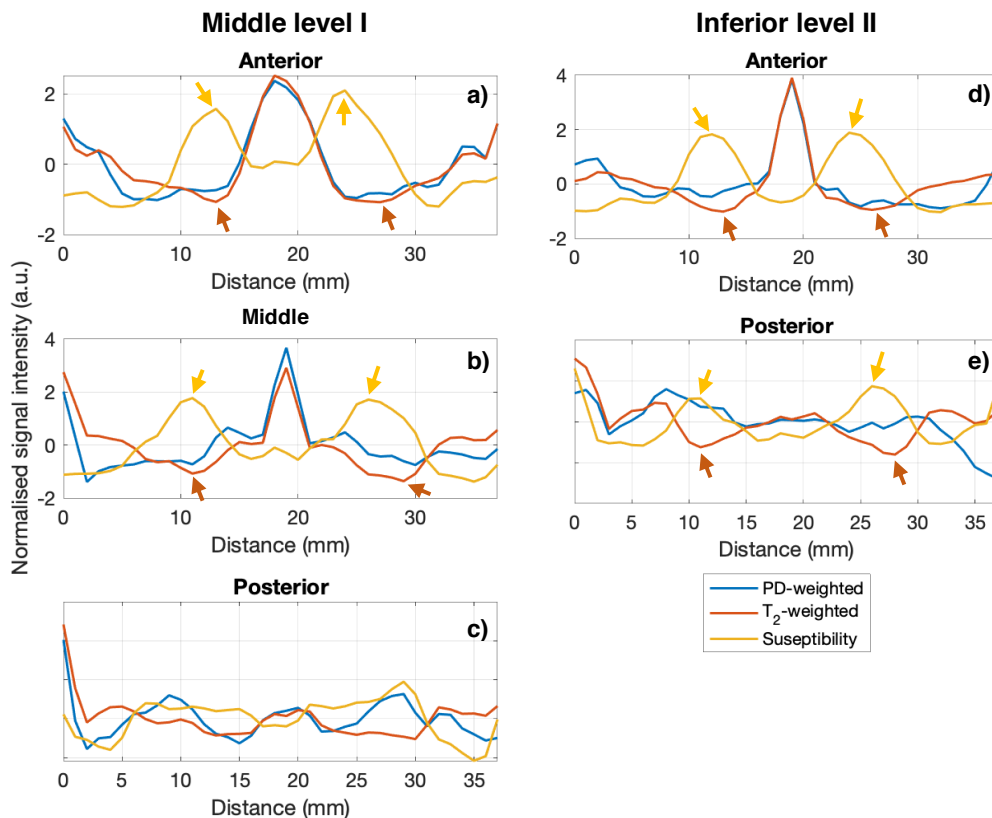


Fig. 6.8 The horizontal line profiles of the signal intensity measured on proton density(PD)-weighted, T₂-weighted images and the susceptibility map of the midbrain on the inferior-middle level.

On the middle level of the midbrain, the signal profiles of anterior (a), middle (b) and posterior (c) were compared; the anterior and posterior profiles of the inferior midbrain was shown in (d) and (e) respectively.

The relative location and the local contrast on the proton density-weighted, T₂-weighted and the susceptibility images (Fig. 6.9), between the substantia nigra and the red nucleus are demonstrated by the crossline profiles (Fig. 6.10).

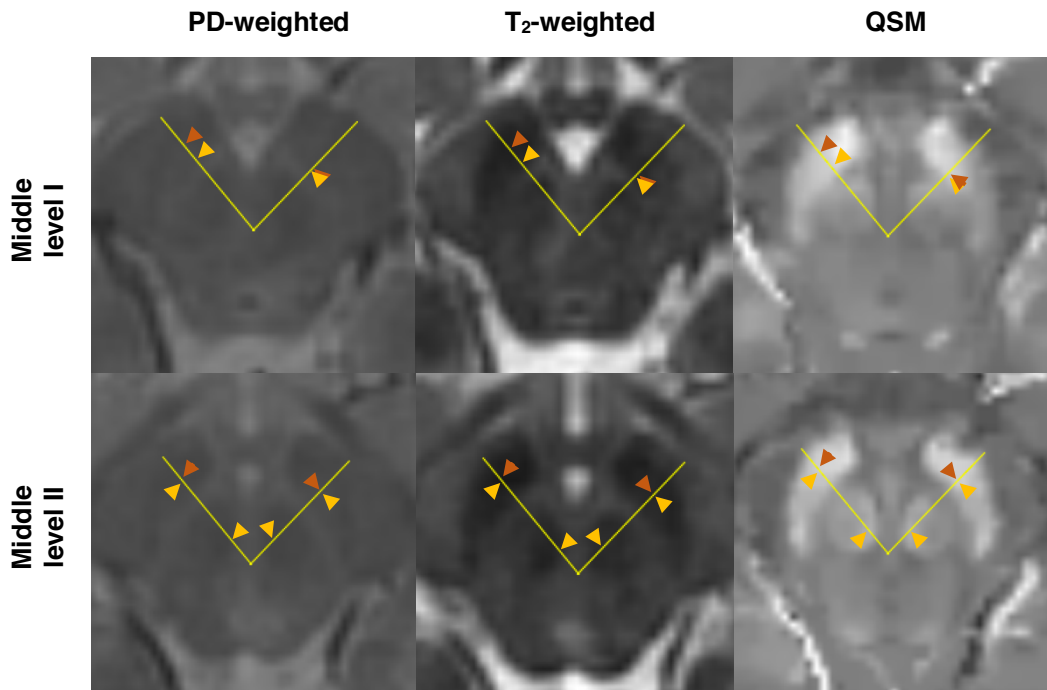


Fig. 6.9 Demonstration of the location of the crossline profiles of the midbrain on the middle level.

The yellow solid line indicated the location of the signal intensity measurement, from left to right. The yellow and orange triangles indicated the located signal used as the landmark in the T_2 -weighted image and the susceptibility map. PD - proton density.

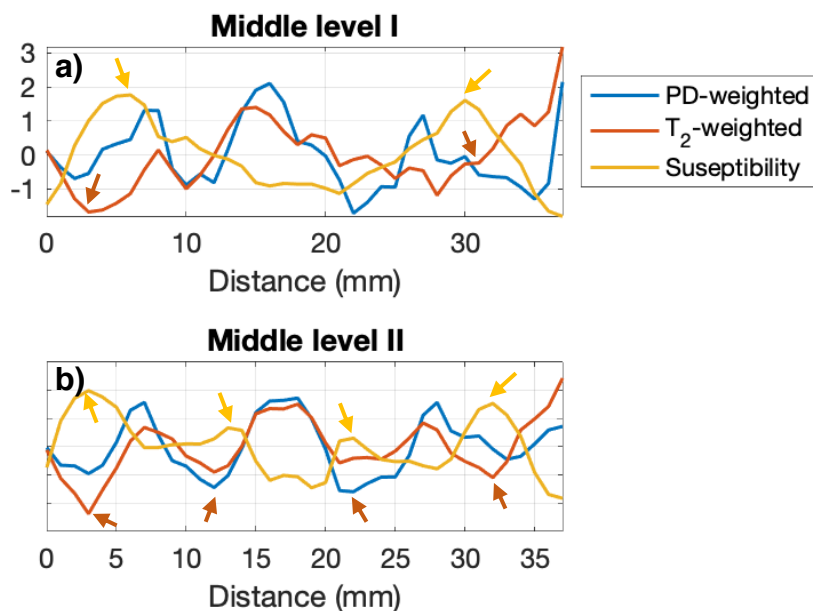


Fig. 6.10 The crossline profiles of the signal intensity measured on proton density(PD)-weighted, T_2 -weighted images and the susceptibility map of the midbrain on the middle level.

The signal line profiles were compared on the Middle level I (a) and II (b) respectively.

As both regions are loaded with iron, the signal intensity peaks and valleys are expected to locate the substantia nigra and the red nucleus on the susceptibility map and the T₂-weighted image respectively. On Middle level I, the largest signal intensity peak in the susceptibility map is located the substantia nigra (Fig. 6.10a, also indicated as the yellow triangles in Fig. 6.9 Middle level I). Compared with the hypointense signal on the proton density-weighted and T₂-weighted images (Fig. 6.10a and indicated as the orange triangles in Fig. 6.9 Middle level I) on the left side, this location is found closer to the magnocellular portion of the lower red nucleus on the left side, which is located at 10 mm distance and appeared as a small peak on the QSM image and a signal drop on the proton density- and T₂-weighted images (Fig. 6.10a). On this anatomical level, the substantia nigra consists of the subregion pars compacta that located at the inner side of the structure and the pars reticular on the lateral peripheral [312, 346, 356, 357], supported by an asymmetrical signal peak skewing towards the measuring centre on the susceptibility line profile as higher iron concentration is expected in the pars compacta [330, 346, 355]. A clear symmetrical observation is not found on the right side of the midbrain, which could be due to the slightly tilted angle of the subject's head during the MR examination or the intrinsic heterogeneity of the brain structure. Towards a higher anatomical level, on the Middle level II, the discrepancy of the signal contrast location and the distance between the centre of the two structures on different image modalities becomes smaller, supported by the matched signal landmarks (indicated orange and yellow triangles on Fig. 6.9, Middle level II, and arrows on Fig. 6.10b) obtained on the T₂-weighted and the susceptibility images.

6.3.3 Correlation of the susceptibility with the Fe³⁺ concentration in phantoms

The regression analysis reveals a significant ($p < 0.001$, $F > 1$), very strong linear (adjusted $R^2 > 0.96$) correlation of the measured susceptibility with the concentration of Fe³⁺-EDTA (Fig.6.11), and of Fe³⁺-NTA (Fig.6.12) respectively, over the range from 0 µg/g to 400 µg/g.

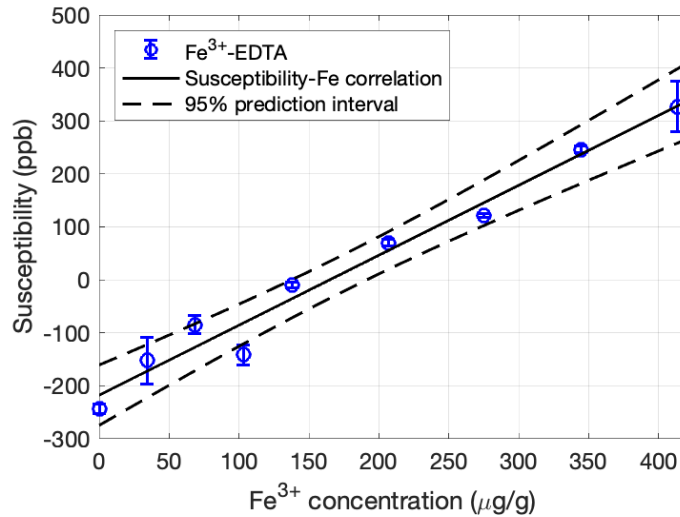


Fig. 6.11 Regression analysis of the observed susceptibility with ferric Fe^{3+} -EDTA. Open blue circle: mean susceptibility of the ROI; error bar: standard deviation.

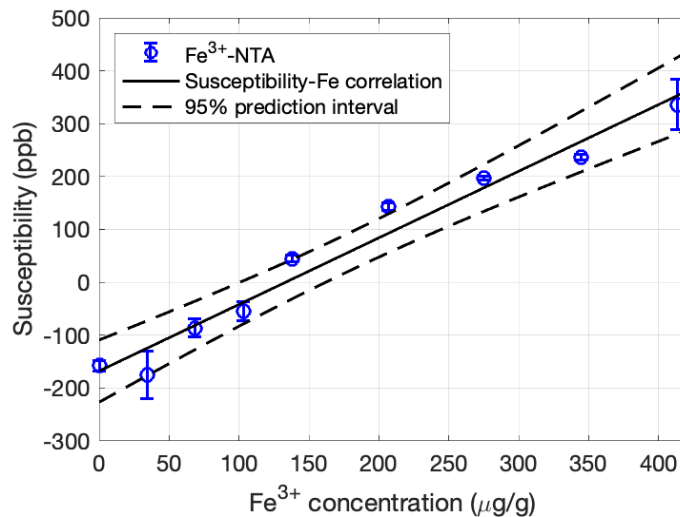


Fig. 6.12 Regression analysis of the observed susceptibility with Fe^{3+} -NTA. Open blue circle: mean susceptibility of the ROI; error bar: standard deviation.

The linear regression model well describes the relationships between the measured susceptibility and the ferric iron in general, and the estimated coefficients for the fitting with the concentration of the ferric iron in two different forms of chelation are relatively close (Table 6.1). The linear regression model for the ferric EDTA is found to have a slope of $1.32 \text{ ppb}/\mu\text{g}\cdot\text{g}^{-1}$ with the intercept at -217.82 ppb , while the one found in ferric NTA is with the slope coefficient of $1.26 \text{ ppb}/\mu\text{g}\cdot\text{g}^{-1}$ and the intercept at -167.99 ppb . The linear regression analysis is summarised in Table 6.1.

Table 6.1 Summary of the regression analysis between susceptibility and iron concentration in phantom.

Correlation [†]	Slope k	C	R^2	Adjusted R^2	RMSE
Susceptibility vs. Fe ³⁺ -EDTA	1.32 ± 0.08	-217.82 ± 18.51	0.973	0.969	33.8
Susceptibility vs. Fe ³⁺ -NTA	1.26 ± 0.09	-167.99 ± 19.13	0.968	0.964	35

[†]Linear model $Susceptibility = k[Fe^{3+}] + C$ was employed for the regression analysis, the units for the susceptibility and the ferric iron concentration $[Fe^{3+}]$ were ppb and $\mu\text{g/g}$, respectively. $N = 9$, F-statistic against the constant model: $F > 1$, $p < 0.001$.

A negative intercept is expected as the water appeared diamagnetic ($\chi_{\text{water}} = -0.727$ ppm at 20 °C, cgs unit) whereas the reference susceptibility of the surrounding (standard air, approximately 21% O₂ and 79% N₂) is estimated $\chi_{\text{Air}} = +0.029$ ppm (cgs unit). The volume susceptibility contribution of the ferric iron is estimated using $\chi_{\text{FeCl}_3 \cdot 6\text{H}_2\text{O}} = 102.68$ ppm (cgs unit, calculated from [354]), a theoretical slope and intercept for the susceptibility-Fe³⁺ solution system are calculated as 1.30 ppb/ $\mu\text{g}\cdot\text{g}^{-1}$ and -9.14 ppm in SI unit. The estimated linear correlation of the measured susceptibility from QSM with the ferric iron concentration suggests the slope coefficient very close to the result given by the theoretical model, 1.32 ppb/ $\mu\text{g}\cdot\text{g}^{-1}$ and 1.26 ppb/ $\mu\text{g}\cdot\text{g}^{-1}$ for Fe³⁺-EDTA and Fe³⁺-NTA respectively. However, the magnitude of the intercept at y-axis estimated from the regression model is one magnitude smaller than the theoretical prediction, when taking the susceptibility of air χ_{Air} (364.4 ppb in SI unit) into account, which gives the intercepts of above linear models -582.22 ppb and -532.39 ppb for Fe³⁺-EDTA and Fe³⁺-NTA respectively. Although the contribution of the agarose gel is not included in the calculation, due to the lack of the absolute measurement of the agarose susceptibility in the literature, the presence of it could possibly be neglected in the estimation, as it was reported to be weakly diamagnetic [358] and the concentration used in the study is low. The different intercepts are not unexpected, as the QSM post-processing only calculated the susceptibility relative to a reference, due to the nature of the dipole kernel singularity at the k-space centre [17, 271, 310]. Nevertheless, the good consistency

between the theoretical and measured slope coefficient, suggests a robust relative susceptibility measurement in the chelated iron phantom using QSM.

6.3.4 Correlation of the susceptibility with the prior-published iron concentration in healthy brains

A linear model is employed for the regression analysis between the susceptibility measured in deep grey matter brain regions, and the estimated iron concentration of the corresponding region by the age of the subject based on the work of Hallgren and Sourander [11], as described in Section 6.2.5.2. The established post-mortem work provided the regression equations between the subject's age and non-haemin iron concentration measured in various brain regions. Therefore, the iron levels of below deep grey matter regions are calculated using those formulas, except the ones for the substantia nigra and the red nucleus, as their iron concentrations as a function of age are not documented in the study. Hence, for these two regions, the respective average iron concentrations reported by Hallgren and Sourander [11] are used for the regression analysis.

A significant ($p < 0.001$, $F > 1$) linear relationship (adjusted $R^2 = 0.576$) is observed in the *in vivo* human brain data (Fig. 6.13A), between the measured susceptibility and the age-dependent iron concentration calculated using Hallgren and Sourander's formulas [11]. The estimated model demonstrates a slope of $0.80 \text{ ppb}/\mu\text{g}\cdot\text{g}^{-1}$ with an intercept at -20.846 ppb , and these values are consistent with the previously reported correlation [14]. The measured susceptibility of the above brain region shows overall positive linearity against the estimated iron concentration, but a large variation is found among the susceptibility measurements in the red nucleus, caused by a few outliers with very low susceptibility. A possibility is considered that the estimated iron concentration is inaccurate in the red nucleus, as the average measurement of the iron concentration of the regions within the midbrain is used, based on the literature [11], where only the mean values are reported for these regions without correlation with the age due to the large variation measured between subjects.

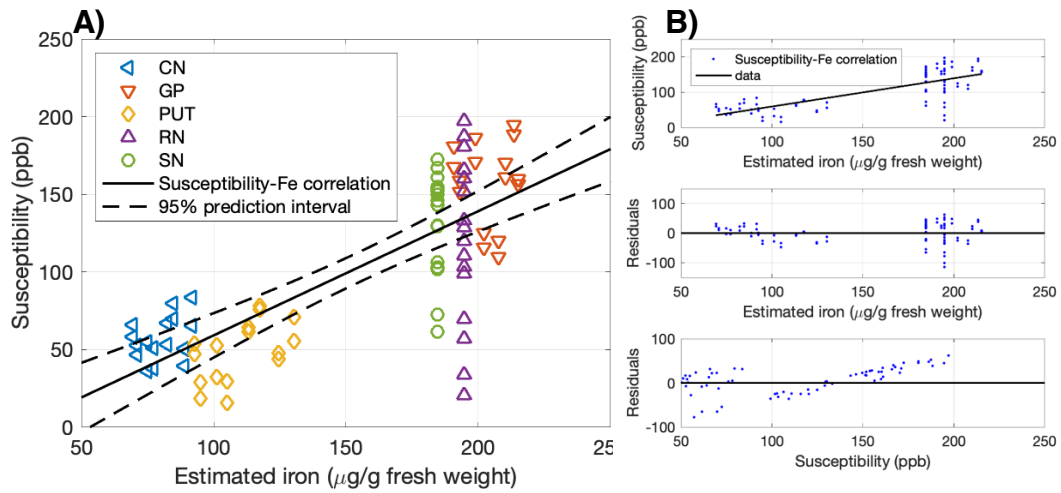


Fig. 6.13 Linear regression (A) and residual (B) analyses between susceptibility and estimated iron concentration in caudate nucleus (CN), globus pallidus (GP), putamen (PUT), red nucleus (RN), and substantia nigra (SN).

Therefore, the linear regression analysis is also performed between the susceptibility measurements and the estimation of iron concentration within the regions where the brain iron concentration as an exact function of age was provided by the post-mortem study [11], including the caudate nucleus, globus pallidus and putamen (Fig. 6.14). As expected, the correlation is found improved in the linear model (adjusted $R^2 = 0.784$), with an estimated slope of $0.88 \text{ ppb}/\mu\text{g}\cdot\text{g}^{-1}$ and the intercept of -28.05 ppb .

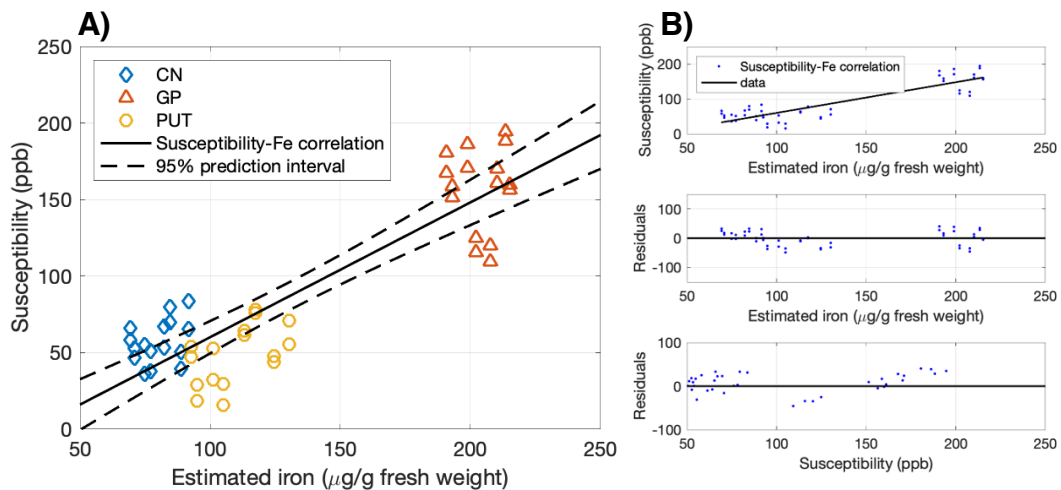


Fig. 6.14 Linear regression (A) and residual (B) analyses between susceptibility and estimated iron concentration in caudate nucleus (CN), globus pallidus (GP), and putamen (PUT).

To avoid the bias, that the improvement might be simply due to the reduction of the data points used in the fitting, the regression analysis is also conducted using the susceptibility values excluding the measurement from the red nucleus, and the putamen respectively (Fig. 6.15).

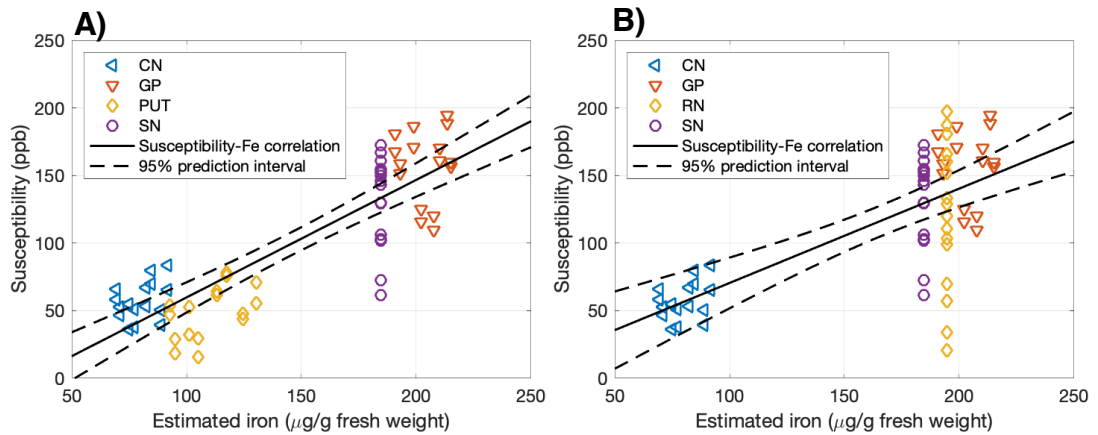


Fig. 6.15 Linear regression analysis of the measured susceptibility in selected brain regions. The linear correlation analysis that excluded (A) red nucleus, and (B) putamen, respectively.

CN – caudate nucleus, GP – globus pallidus, PUT – putamen, RN – red nucleus, SN – substantia nigra.

The regression analysis result shows an improved correlation between the measured susceptibility and the estimated iron concentration only when the region red nucleus is excluded from the model (adjusted $R^2 = 0.737$, Fig. 6.15A) but not when the putamen is excluded (adjusted $R^2 = 0.483$, Fig. 6.15B), comparing to the linear model where all data measured from all brain regions are used adjusted ($R^2 = 0.576$, Fig. 6.13). A summary of the above regression analysis results is shown in Table 6.2.

To summarise, large variation is found in the red nucleus, whose measurements deviate from the linear correlation between the susceptibility and the estimated brain iron concentration (Fig. 6.13). Similar deviation of the susceptibility measured in the red nucleus was also reported in the literature [245, 277], where different QSM processing methods was employed, that SHARP was employed for the background removal, and HEIDI (Homogeneity Enabled Incremental Dipole Inversion) was applied for the dipole inversion [245].

Table 6.2 Summary of the regression analysis between susceptibility and iron concentration in various brain regions.

Correlation ^a with brain regions ^b	N	k	C	R ²	Adjusted R ²	RMSE
Susceptibility vs. Iron in CN, GP, PUT, RN, SN	80	0.80 ± 0.08	-20.85 ± 12.51	0.581	0.576	34.8
Susceptibility vs. Iron in CN, GP, PUT	48	0.88 ± 0.07	-28.05 ± 9.53	0.789	0.784	25
Susceptibility vs. Iron in CN, GP, PUT, SN	64	0.87 ± 0.07	-27.17 ± 10.02	0.741	0.737	27.1
Susceptibility vs. Iron in CN, GP, RN, SN	64	0.70 ± 0.09	0.66 ± 15.64	0.491	0.483	36.4

^a Linear model $Susceptibility = k[Fe] + C$ was employed for the regression analysis, the units for the susceptibility and the ferric iron concentration [Fe] were ppb and µg/g, respectively. N = number of observations, the F-statistic against the constant model in all regression analysis: $F > 1$, $p < 0.001$. CN – caudate nucleus, GP – globus pallidus, PUT – putamen, RN – red nucleus, SN – substantia nigra.

The residual analysis (Fig. 6.14B and Fig. 6.14B) also reveals the deviation of the susceptibility values measured within putamen from the modelled linear correlation, whose measured susceptibility values are close to the observation in the caudate nucleus, even though most of the post-mortem results [7, 9-11, 43, 49, 51, 359] suggested a similar yet slightly higher iron concentration in the putamen, compared with the caudate. Similarly, low susceptibility values measured in putamen were also found in the other studies using various post-processing techniques [245, 277, 360]. Miao *et al.* [360] employed a comparable method with splenium selected as reference, and a similar level of susceptibility in the putamen and the caudate head was observed among subjects with an average age of 26 yrs, in the range of 14-45 yrs. Conversely, in the study where a larger age range was covered or subjects with advanced age took part [51, 361], the separation of the measured susceptibility in the putamen and caudate became evident. Therefore, it might be due to the limited age range of the subject observed in this study, as the iron level in the putamen and caudate are expected to undergo a slow increase until reaching a plateau in a late

stage of life (over 60 yrs and 50 yrs respectively), and the differences between them might be subtle in the age group from 20 to 50, especially when the sample size is small. Even though the age-related iron accumulation is already taken into account in this study by estimating the regional iron concentration based on the individual subject's age, the susceptibility difference between the caudate nucleus and the putamen might be masked by the intra-individual difference of the susceptibility measurement.

The scattering of the susceptibility is also examined, shown in Figure 6.16, against the expected iron level in globus pallidus, putamen and caudate nucleus, using the formulas reported in Hallgren and Sourander's work [11]. When the measurement for each individual is examined, the indifference between the putamen and caudate nucleus is persistent. Hence it is also possible that this difference between these two brain regions, is under the detection limit of QSM, or caused by other effects that are simplified by the physical model employed in the algorithms [268].

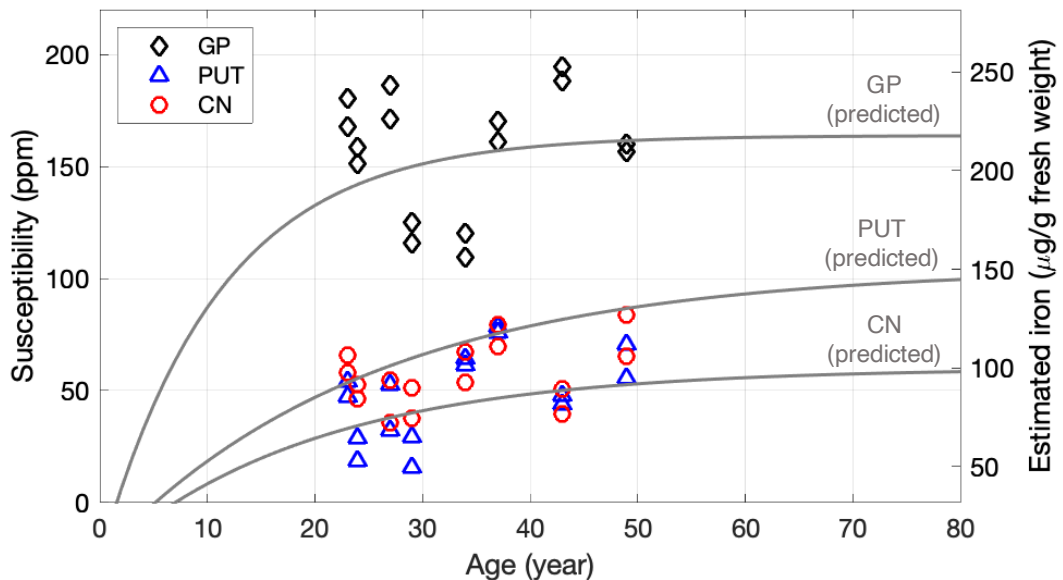


Fig. 6.16 Relationship between the measured susceptibility and the age against expected iron concentration in different brain regions.

6.3.5 Comparison of different quantitative MRI measures of brain iron

The susceptibility, R_2^* , R_2 , and effective R_2 maps (Fig. 6.17) generated from the scans of the same volunteer (male, age 24 yrs), are compared qualitatively and

quantitatively to investigate the relationships between these quantitative measurements for iron content in the healthy brain.

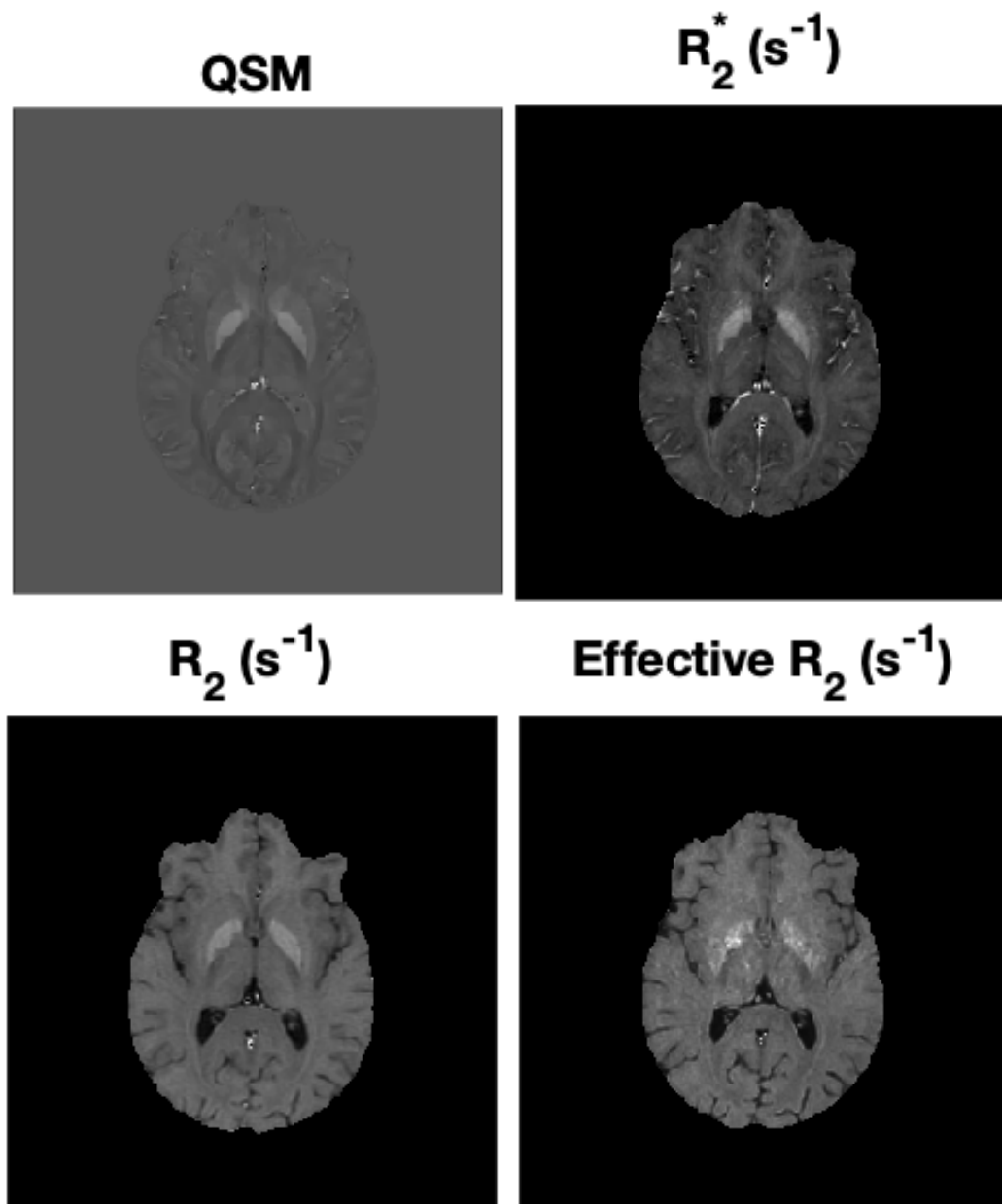


Fig. 6.17 Reconstructed brain images with QSM, R_2^* , R_2 , and effective R_2 .

All reconstructed parametric maps show comparable CNR, except for the effective R_2 derived from the dual-contrast FSE sequence (bottom right image in Fig. 6.17). It is possibly because of the partial contribution of signals from the T_E along the ETL, other than the effective T_E in the segmented k-space (see Section 2.2.1.4), as the price of reduced acquisition time. Additionally, compared with the SE sequence, the FSE pulse sequence is more prone to susceptibility artifacts and the artifacts caused by

the ventricle, due to the reduced FA. Although the proton density-weighted and T₂-weighted images acquired by the FSE sequence are all in the high-SNR regime (SNR > 3), the fitting of two T_E is more sensitive to the background noise compared with other multi-echo methods, which is also shown as a higher standard deviation in the ROI measurements (right-most column in Table 6.3). Conversely, the advantage of full k-space sampling is shown in the R₂ map (see Section 2.2.1.2-3), which is produced by fitting the images acquired by the CPMG sequence with signal acquisition at multiple T_E, to exponential decay. Derived from the same SE family, the multiple SE sequence is robust against susceptibility artifact and macroscopic relaxation caused by the field inhomogeneity. The reconstructed R₂ map (bottom left image in Fig. 6.17) generates a similar contrast to the one of effective R₂ but the image appeared less noisy, and this finding is also supported by the closely matched measured relaxation rates R₂ and effective R₂ shown in Table 6.3.

Table 6.3 Comparison of the prior-published iron concentrations with quantitative MRI measurements[†] within ROIs.

ROI	Iron concentrations ($\mu\text{g/g ww}$) estimated from prior-published data		Susceptibility (ppb)	R_2^* (s^{-1})	R_2 (s^{-1})	Effective R_2 (s^{-1})
	H&S (1958) [11]	Krebs <i>et al.</i> (2014) [9]	mean \pm std	mean \pm std	mean \pm std	mean \pm std
RNL	194.80 \pm 68.6 (N = 44)	77.1 \pm 57.3 (N = 22)	71.80 \pm 22.18	27.75 \pm 3.11	15.88 \pm 1.45	15.03 \pm 1.48
RNR			55.36 \pm 15.56	28.54 \pm 3.44	16.10 \pm 1.21	14.82 \pm 1.17
GPL	193.11	202.7 \pm 37.8 (N = 22)	157.94 \pm 37.05	38.92 \pm 3.46	20.34 \pm 1.13	19.53 \pm 2.89
GPR			157.22 \pm 31.11	39.45 \pm 3.95	20.74 \pm 1.02	18.17 \pm 2.29
SNL	184.60 \pm 65.2 (N = 52)	210.3 \pm 74.6 (N = 15)	125.32 \pm 52.36	30.52 \pm 5.32	16.71 \pm 1.59	15.84 \pm 1.74
SNR			98.37 \pm 54.51	29.68 \pm 5.26	16.22 \pm 1.96	13.65 \pm 2.04
PUTL	94.82	159.3 \pm 36.7 (N = 44)	15.93 \pm 12.47	23.76 \pm 2.25	16.11 \pm 0.76	15.21 \pm 1.29
PUTR			28.50 \pm 9.89	24.48 \pm 1.76	16.59 \pm 0.88	13.63 \pm 1.27
CNL	70.81	106 \pm 26 (N = 43)	45.60 \pm 17.43	22.39 \pm 2.50	15.19 \pm 1.12	12.00 \pm 2.47
CNR			52.55 \pm 11.28	21.88 \pm 1.79	15.31 \pm 0.61	12.59 \pm 0.94

[†] measured from ROIs within the brain of a male volunteer with age 24 yrs. ROIs included the left (L) and right (R) brain regions on the image: CN – caudate nucleus, GP – globus pallidus, PUT – putamen, RN – red nucleus, SN – substantia nigra. N = number of observations, N = 1 if not specified.

Derived from the images acquired from the same 3D GRE sequence, both R_2^* relaxation (top right image in Fig. 6.16) and susceptibility (top left image in Fig. 6.17) reflect the contribution of the local field inhomogeneity caused by the intrinsic tissue electromagnetic properties. Due to the field inhomogeneity, fast relaxation rate R_2^* (third column from the right in Table 6.3) is therefore observed in brain regions compared with corresponding R_2 measurement (second column from the right in Table 6.3) and therefore generates a stronger contrast between iron-rich regions in the grey matter and its surrounding tissues, since the time-independent dephasing caused by the field inhomogeneity is corrected by the refocusing pulse applied in the multiple SE sequence (see Section 2.2.1). Although it is not reflected in the measurements of iron-rich regions included in Table 6.3, the most distinctive difference between the susceptibility map and the R_2^* map is the opposite effect of diamagnetic structure. For instance, both the paramagnetic iron-laden globus pallidus (green arrows in Fig. 6.18) and the diamagnetic calcification in the choroid plexus [362] show hyperintense signals on the R_2^* , but the latter demonstrates hypointensity in the susceptibility image (yellow arrows in Fig. 6.18).

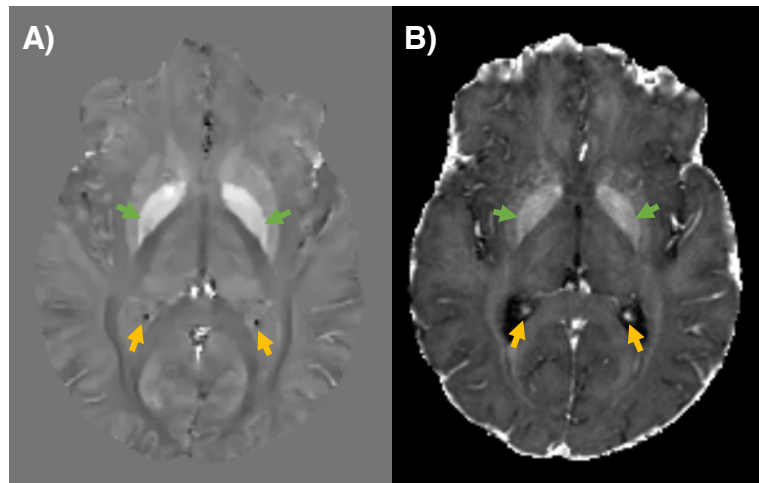


Fig. 6.18 Paramagnetic and diamagnetic structures in the susceptibility map (left) and the R_2^* map (right) of the brain of a subject.

Green arrows: globus pallidus; yellow arrows: choroid plexus.

The comparison between the measured susceptibility, R_2^* , R_2 , and effective R_2 in these brain regions, are further analysed quantitatively. As shown in Figure 6.19, the

correlation analysis suggests significant ($p < 0.05$), strong positive (Pearson's $\rho > 0.75$) linear correlations between each two of the quantitative MRI measurements.

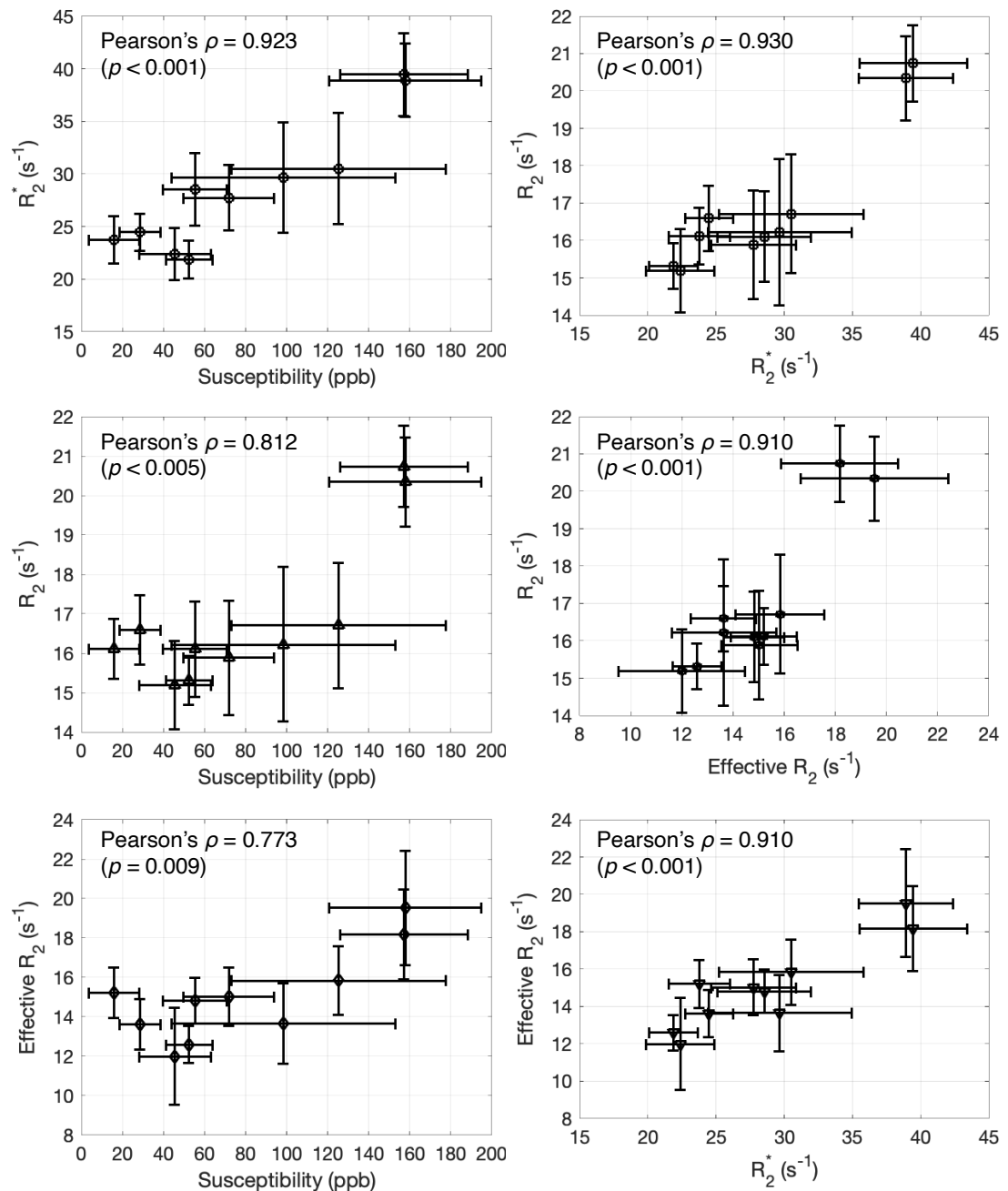


Fig. 6.19 Comparison between quantitative MRI measurements within ROIs.

ROIs covered the bilateral brain regions including the caudate nucleus, globus pallidus, putamen, red nucleus, and substantia nigra. (For pairwise values of each bilateral region, see Table 6.3)

Moreover, the result shows that between every two parameters of R_2^* , R_2 and effective R_2 , the measurements are highly significant ($p < 0.001$) and positively correlated (Pearson's $\rho > 0.9$), as well as between the susceptibility and R_2^* . However, the correlation linearity of the measured susceptibility with R_2 and with effective R_2 is less significant ($p = 0.004$ and 0.009 , respectively), and with weaker positivity (Pearson's $\rho = 0.812$ and 0.773 , respectively). This deviation appeared to be caused by, again, the ordinal difference of the putaminal susceptibility measurements, compared with other quantitative MRI measurements. As shown in Table 6.3, the putaminal susceptibility is found to be the lowest among all brain regions, while the caudate nucleus shows the lowest measurement in R_2^* , R_2 , and effective R_2 . In addition to the discordance of the putamen, the proportional difference observed in the red nucleus, with respect to other brain regions, also varies between different MRI measurements. For instance, the measurement in the red nucleus is lower than those for globus pallidus by about 20~25%, and similar to those for substantia nigra, according to the transverse relaxation rates (R_2^* , R_2 , and effective R_2); however, for the susceptibility measurement, the red nucleus' susceptibility shows more than 50% lower than the globus pallidus', and 30~45% lower than the substantia nigra susceptibilities (estimated from the 4th to 7th column of Table 6.3).

To further investigate the different behaviours of the susceptibility, R_2^* , R_2 , and effective R_2 in measuring the iron concentration within the above brain regions, these measurements are also examined in respect of estimated iron concentrations based on prior-published [9, 11] post-mortem data (Table 6.3). Two of the most widely recognised post-mortem studies are examined against the above quantitative MRI measurements, to investigate any potential bias introduced by the source of the putative brain iron concentration. Detailed in the Method section 6.2.5.2, the age-dependent iron concentrations of the caudate nucleus, putamen, and globus pallidus are estimated from the functions provided by Hallgren and Sourander [11], while the iron concentrations of the red nucleus and substantia nigra (whose age-dependent prediction models were unavailable) are assumed to be the average values ($N = 44$ and 52 respectively, age 30-100 yrs, with median age 65 yrs estimated from the report) reported in the same study. In comparison, Krebs *et al.*'s report [9] of the

average iron concentrations of corresponding brain regions from post-mortem specimens (age 48-81 yrs, median age 61 yrs), without adjustment for age-dependency, is used as a second reference.

As demonstrated in Figure 6.20, between the post-mortem results from two studies, a pronounced difference is found in the iron measurement of the red nucleus, in both the absolute concentration and the relative concentration with respect to the iron level in other grey matter regions. It should be noted that the formalin fixation process in Krebs *et al.*'s study might cause the decrease of measured iron concentration [57, 67], or change of the distribution [64], which may explain the underestimation of the iron concentration in red nucleus. It is also noticed that large standard deviations of the measurements were reported for brain iron concentration of the red nucleus and the substantia nigra, in both post-mortem measurements of when using histochemistry technique [11], as well ICP-MS [9]. In contrast, slightly higher mean iron concentrations of caudate, putamen, and the nigra were reported by Krebs *et al.* (data above the reference line of slope = 1), compared with the reported average concentrations in Hallgren and Sourander's work. It might be caused by the difference in the age range of the subjects included in the two studies, where no subject with age below 48 yrs was included in Krebs *et al.*'s study, as the iron concentration in caudate and putamen was still to increase with normal ageing (see section 1.2.1 in Chapter 1) and below the average [11].

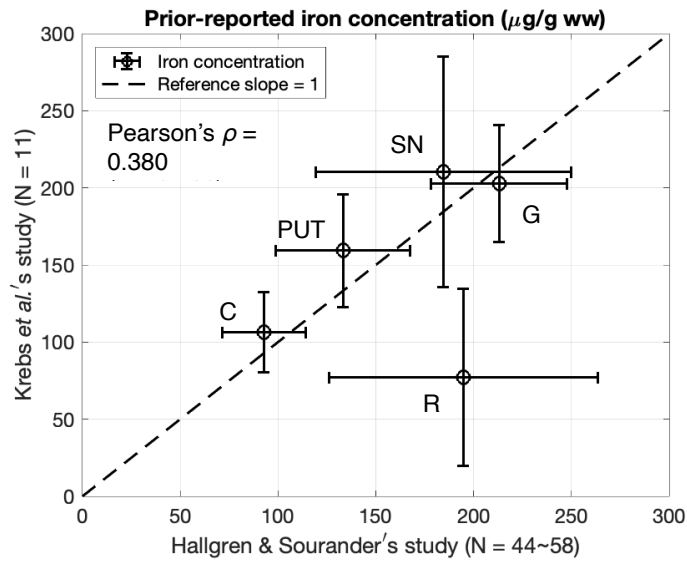


Fig. 6.20 Comparison of the prior-published [9, 11] average iron concentrations in different brain regions.

CN – caudate nucleus, GP – globus pallidus, PUT – putamen, RN – red nucleus, SN – substantia nigra.

Subsequently, in this PhD project, the relationships of the quantitative MRI parameters measured on the same volunteer (see Sections 6.2.5.2-3), including the susceptibility, R_2^* , R_2 , and effective R_2 within the ROIs, with the estimated iron concentrations based on above two prior-published studies [9, 11], are demonstrated in Figure 6.21.

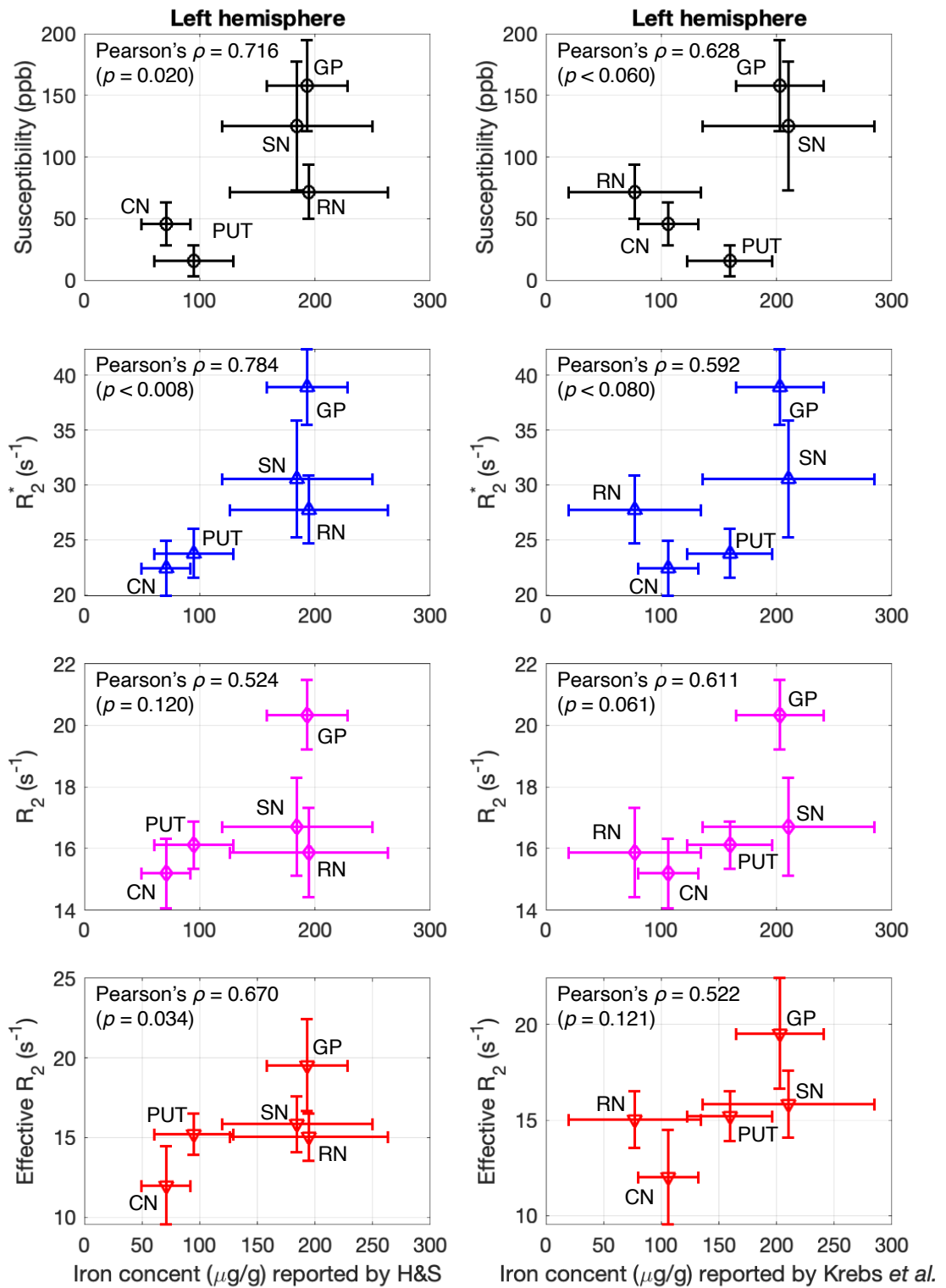


Fig. 6.21 Comparison of quantitative MRI measurements with reported iron concentrations [9, 11].

Pearson correlation was calculated using data from both hemispheres; for clarity, only the left hemisphere's measurements were demonstrated. CN – caudate nucleus, GP – globus pallidus, PUT – putamen, RN – red nucleus, SN – substantia nigra.

Overall, the correlation analysis result shows significant ($p < 0.05$), moderate to strong positive linear correlation (Pearson's $\rho > 0.5$, left column in Fig. 6.21) between each quantitative MRI measurement except for R_2 , with the age-dependent iron concentration, estimated based on Hallgren and Sourander's work [11]. Furthermore, the positive linear correlation of the iron estimation, is the most significant ($p < 0.008$) and strongest (Pearson's $\rho = 0.784$) with the R_2^* measured in this volunteer's brain regions. In comparison, the correlation is slightly weaker (Pearson's $\rho = 0.716$) but significant ($p = 0.020$) with the susceptibility, moderate (Pearson's $\rho = 0.670$), significant ($p = 0.034$) with effective R_2 , insignificant ($p = 0.120$) with R_2 relaxation.

Showed in the left column of Fig 6.21, compared with other brain regions, the substantia nigra and red nucleus deviate from the linear correlations, with the overestimation of the iron content with respect to Hallgren and Sourander's study [11]. As the estimation of these two regions are not adjusted for the age-dependency of the subject, this is possibly because the volunteer in this project is much younger than those included in the Hallgren and Sourander's study [11]. On the contrary, Zecca *et al.* [8] reported an age-dependent increase of total iron concentration of the substantia nigra in healthy brains, where the iron concentration was found to be increasing until about 30 yrs of age. For a young adult with 24 yrs of age, the putative iron concentration of substantia nigra is lower than the average value reported by Hallgren and Sourander ($184.60 \pm 65.2 \mu\text{g/g ww}$) [11], when estimated using the linear model of iron concentration in the substantia nigra, provided by Zecca *et al.* [352] ($150.53 \mu\text{g/g ww}$ for 24 yrs of age). For the red nucleus, however, not enough post-mortem measurement of the iron concentration is found by the time of writing, for the brain region explicitly, except the two studies referred here [9, 11]. Neither of the two studies reported an explicit model (no age-dependency was observed by Krebs *et al.* [9]) to predict the iron concentration of red nucleus, and a large discrepancy is found for the average measurements between these two studies. Nevertheless, a recent *in vivo* MRI work [342] showed an age-dependent susceptibility increase at 1.5 T, using multivariable, structural equation modelling, where the measured susceptibility of red nucleus experienced a quadratic increase with age until 50 yrs of age. Previous *in vivo* MRI studies [245, 342] generally found

good linear correlations of measured susceptibility with the iron concentration estimated based on Hallgren and Sourander's work, when the age range of the subjects was comparable to the post-mortem study [11]. Therefore, in this PhD project, the observed deviation of the substantia nigra and the red nucleus of the young volunteer, from the linear correlation, is probably due to the overestimated iron concentration by using Hallgren and Sourander's data. For the red nucleus, the bias could also be introduced by the partial volume effect on the MRI parametric maps, along the slice-direction in particular, where the 2 mm-slices are acquired, and the averaged signal of the voxel might be contributed by the nearby brain regions.

In contrast, the linear correlation between the quantitative MRI measurements and the iron concentration reported by Krebs *et al.* [9] is found insignificant ($p > 0.05$, right column of Fig. 6.21), but the moderate positive trend (Pearson's $\rho > 0.50$) is observed. As the iron concentrations reported in Krebs *et al.*'s study, are averaged among subjects with an age range from 48 yrs to 81 yrs, these iron concentrations estimated for the volunteer in the PhD project might be overestimated. As the iron concentration experiences a region-specific increase, the deviation from the linear correlation is possibly caused by the age-related bias in the iron estimation. On the other hand, it suggests the necessity of the adjustment for age-dependency when iron concentration should be estimated *in vivo* or *ex vivo* MRI.

6.3.6 Reproducibility of quantitative susceptibility mapping

As shown in Table 6.4, the reproducibility of the QSM is calculated from two scans obtained two weeks apart from the same subject (female, age 28 yrs). The reproducibility is found varied among the brain regions, between 72.01% and 98.29%. The best reproducibility of the susceptibility measurement is found in the globus pallidus (94.13% and 98.29% for bilateral regions), and the reproducibility is generally good in the red nucleus (91.91% and 93.50% bilaterally) and substantia nigra (88.07% and 93.84% bilaterally). However, the result suggests that the susceptibility measurement performed relatively poorly in the caudate nucleus (85.46% and 72.01%) and putamen (81.86% and 82.07%). It is noted that the rank of the susceptibility reproducibility among the brain regions is concordant with the iron

concentration of those regions reported in the literature [10, 11, 13, 14, 43], as well as the myelin content [363] measured as the myelin water fraction (MWF) [364]. This suggests higher susceptibility SNR might be associated with these factors.

Table 6.4 Summary of the susceptibility reproducibility in ROIs.

ROI	Susceptibility	Std	Susceptibility	Std	Reproducibility [†]
CNL	50.13	7.94	57.98	24.64	85.46%
CNR	60.88	16.21	45.93	16.94	72.01%
GPL	169.72	28.56	160.05	27.61	94.13%
GPR	162.37	33.21	165.17	39.45	98.29%
PUTL	64.67	20.39	53.91	15.04	81.86%
PUTR	57.28	19.45	68.56	30.98	82.07%
RNL	123.38	24.98	133.79	35.87	91.91%
RNR	94.81	19.08	101.17	25.82	93.50%
SNL	179.02	51.70	158.86	55.01	88.07%
SNR	122.54	39.56	115.22	60.10	93.84%

[†] measured from ROIs within the brain of a female subject with age 28 yrs. ROIs included the left (L) and right (R) brain regions on the image: CN – caudate nucleus, GP – globus pallidus, PUT – putamen, RN – red nucleus, SN – substantia nigra.

6.4 Discussion

6.4.1 QSM can enhance iron-induced anatomical contrast

Using the QSM technique, the result in Sections 6.3.1-2 demonstrates the novel bulk susceptibility contrast of ferric phantoms and *in vivo* human brains, processed from the 3D GRE MRI data obtained from the local clinical 3.0 T GE scanner. With a focus on the iron-rich brain regions, including the subcortical GM basal ganglia nuclei and the subthalamic nuclei, the human brain susceptibility contrast shows a superior visualisation of these iron-rich brain regions, compared with the clinical routine anatomical proton density-weighted and T₂-weighted images. Principally similar to R₂^{*}, the enhancement of the iron contrast is due to the local field inhomogeneity generated by the iron content [365, 366] agglomerated within these regions, causing the additional phase shift during the GRE acquisition [227, 229, 230]. Compared with the FSE pulse sequence, in GRE acquisition the time-independent proton dephasing is not corrected by the refocusing RF pulse, and therefore the phase shift was

accumulated along the ETL and received by the MR scanner (see Section 2.2.2 and 2.3, Section 3.3). In particular, this difference is most pronounced at inferior and the dorsal-lateral substantia nigra (Fig. 6.6, Fig. 6.7), where the substantia nigra pars compacta and nigrosome 1 located [327, 355]. Dexter *et al.* [43, 367] showed a higher iron deposition within the nigral pars compacta, compared with the neighbouring reticular region, due to the presence of the iron-rich dopaminergic neurons. In contrast to its surrounding tissue, within these regions iron was largely sequestered in the neuromelanin (instead of ferritin) in healthy brains [118, 120, 352], and the heterogeneous microscopic distribution of the iron content dominated the observed susceptibility via the perturbation of the neighbouring proton's Larmor frequency.

6.4.2 QSM can faithfully measure the ferric iron concentration in agarose gel phantoms, with the linear correlation

Evaluated by the customised ferric iron agarose gel phantoms, the susceptibility maps generated by the QSM processing show the capability to measure the ferric iron concentration faithfully, via the linear correlation (Fig. 6.11, Fig. 6.12). Instead of using the previously reported phantom consisting of gadolinium solutions [310, 311], the customised phantom used in the study is constructed with soluble ferric iron in physiological pH, to better simulate the main paramagnetic source of the signal observed in the *in vivo* human brain imaging. The iron oxidative state in the phantom is carefully maintained and stabilised at pH = 7.4 in the soluble ferric form by the coordination with ligands EDTA and NTA, respectively. Good accuracy of iron estimation by the resulting susceptibility measurement of the phantom is found in the chelated iron phantom, without showing a significant difference in the susceptibility between the different coordination ligands. The QSM technique is validated by the statistically significant ($p < 0.05$), strong (adjusted $R^2 > 0.96$) positive linear correlations found between the observed susceptibility and the ferric iron concentration, with the slope coefficient $1.32 \text{ ppb}/\mu\text{g}\cdot\text{g}^{-1}$ and $1.26 \text{ ppb}/\mu\text{g}\cdot\text{g}^{-1}$ for Fe^{3+} -EDTA and Fe^{3+} -NTA respectively, excellently corresponded with the calculated theoretical iron-dependent coefficient in the phantom, $1.30 \text{ ppb}/\mu\text{g}\cdot\text{g}^{-1}$.

6.4.3 *In vivo* brain susceptibility was linearly correlated with the putative iron concentration, and with the transverse relaxation rates (R_2^* , R_2 , effective R_2), but variations existed

Similar to the iron phantom, the results of *in vivo* human brain also show statistically significant ($p < 0.05$), positive linear correlations between the observed susceptibility and the age-dependent brain iron concentration (Table 6.2 in section 6.3.4), estimated from the previous post-mortem study reported by Hallgren and Sourander [11]. Moreover, the coefficients estimated for the linear model are widely agreed with previous reports in the literature [14]. However, compared with the ferric phantom, the strength of the linear correlations between the observed susceptibility and the estimated iron concentrations in the brain are weaker (adjusted $R^2 = 0.48\sim 0.79$ for human brains, versus adjusted $R^2 > 0.96$ for phantoms). Compared with other brain regions, larger inter-subject variation due to the outliers with small susceptibility values, is observed in the red nucleus (Fig. 6.13), which confounds the correlation between the susceptibility and the iron concentration *in vivo*. The deviation of the susceptibility measured in the red nucleus, from the expected level based on the empirical iron concentration [11], is also observed in previous reports [245, 277], but the causes remained unclear by the time of writing.

At the same time, the intra-subject correlation analysis of the susceptibility, R_2^* , R_2 , and effective R_2 (Fig. 6.19), reveals statistically significant ($p < 0.05$) positive linear correlations between these quantitative MRI measurements, indicating the presence of the co-variance (*e.g.*, tissue variables like iron, water diffusion) between these measures [191, 260, 368]. Nevertheless, different values of Pearson's ρ of the intra-subject correlations between the observed susceptibility with R_2^* (0.923), R_2 (0.812), and effective R_2 (0.773), suggest unequal contributions of these tissue variables, to each quantitative MRI measurement. Additionally, the intra-subject analysis of each MRI parameter, with respect to the iron level, show higher sensitivity of R_2^* to the putative tissue iron concentration [11], compared with the susceptibility, R_2 , and effective R_2 (Fig. 6.21).

Taken together, the weaker correlation between the observed susceptibility and the putative brain iron concentration, compared with those for the iron phantoms, is possibly caused by both intra- and inter-subject variation of the tissue properties, such as chemical forms and distributions of iron content [296], as well as the diamagnetic myelin content. For brain iron quantification, myelin is known to be a confounder of the iron-associated susceptibility obtained using QSM techniques, and *vice versa* [4]. The diamagnetic property of myelin reduces the observed tissue susceptibility, and therefore hampers the linear correlation between the apparent susceptibility and the iron concentration in brain tissues. At the same time, the presence of myelin is related to the restricted direction of water diffusion within axons as well as the myelin sheath, therefore increasing the transverse relaxation rate. Recent histological studies [56, 57] quantified the influence of myelin content within human post-mortem brains, on the observed susceptibility using QSM, as well as on the transverse relaxation rate R_2^* , at 7.0 T. Using PIXE together with iron extraction, it was found that myelin contributed to 72% susceptibility contrast in the cortical WM, and 33% in the cortical GM, but for R_2^* , the contribution of myelin decreased to 56% and 19% in WM and GM respectively [56]. The histological staining and biochemistry findings also confirmed the myelin content was the main cause of the observed susceptibility contrast difference of WM, compared with cortical GM and with basal ganglia nuclei [57]. At 3.0 T, the myelin-corrected susceptibility also appeared to improve the linear correlation, between the *in vivo* susceptibility MRI measurement and the putative iron concentration [245]. Using the information of magnetisation transfer saturation to semi-quantify myelin, Schweser *et al.* noted the myelin-corrected susceptibility generated a stronger correlation with the iron concentration estimated from the literature [8, 9, 11], where the iron-associated susceptibility was revealed, especially in WM and heavily myelinated subcortical grey matter like thalamus.

Additional bias might also be introduced by the difference in the cytoarchitectures-associated iron deposition between these brain regions, especially by the cell types, their morphologies, the volume fractions, and the spatial distribution. Demonstrating a brain region-specific cellular distribution, Perls' staining reactive iron was found

largely but not exclusively, in the glia and axons, as well as in the cytoplasm of neuron cell bodies within subcortical nuclei [4, 118, 352]. These cells in the human CNS often appear morphologically distinctive from each other and had region-specific distributions. In the healthy human brain, neurons appear to have median to large soma size (10-30 μm) with round or ovoid nucleus, visible cytoplasm, often elongated dendrite(s) and axon(s); whereas oligodendrocytes and astrocytes are often small (3-10 μm) and round-shaped cells situated in groups (oligodendrocyte) or singularly (astrocyte), whose cytoplasm is usually not visible; and microglia are found in small to medium size, with a thread-like or irregular shape, and with elongated or comma-shaped nucleus [45, 369-372]. At the same time, although various types of neurons, and interneurons (glia as the majority) in rodents and higher vertebrates' CNS are identified and established [372-374], yet a consensus within the research field has not been reached by the time of writing, regarding the absolute number or proportion of each type of cells in human brains [45, 375, 376]. Using the stereological method on the post-mortem brains, Karlsen *et al.* [371] reported the cell count of glia as many as neurons in the neocortex, but a higher glia-to-neuron ratio (GNR) measured in basal ganglia, with the oligodendrocytes double to triple the number of neurons, in healthy female subjects (N = 6, 60 to 80 yrs of age).

Hence, the variation of the cellular distribution might also contribute to the deviation from the linearity (see Section 6.3.4-5) for certain brain regions (such as putamen) in this PhD project, and it might partially explain the indifference in observed susceptibility values between caudate and putamen, even after myelin-correction, in the literature [245]. Nevertheless, within GM of healthy brains, the cellular architecture difference between regions, is not commonly considered to be a confounder for measuring iron using clinical MRI (3.0 T and below), due to the voxel size (1-3 mm). However, the potential bias in MRI-quantified iron concentration, generated by the assumption of the homogeneous intra-/extra-cellular distribution of the iron content, might become detectable under a higher magnetic field, with higher resolution, especially when GRE sequences are employed (see Section 2.2.2).

6.4.4 Potential variation in *in vivo* quantitative MRI correlations may be reduced by using the putative iron concentration in healthy brains with age adjustment

For the MRI study of human brains, there has not been a technique to validate the actual iron concentration *in vivo*, compared with the MRI of iron content in other organs such as the liver [173, 174]. Although measuring the iron concentration in living human brains using MRI is only indirect, relaxation models and post-mortem validation of the parametric MRI measures support the quantitative relationships between the observed imaging parameters (*i.e.*, susceptibility, R_2^* , R_2) and the exact iron concentrations in the literature [50, 51, 170, 173, 174, 330, 331, 366, 368]. However, discrepancies are often observed between studies of living tissues (reviewed in [13, 14]), due to variations in the research methods such as pulse sequences and acquisition parameters, vendors, image processing, as well as subject-related variations such as age and gender.

Relied on the empirical iron concentration in the literature, in this project, the age-dependent estimation of the total iron concentration (of caudate, putamen and globus pallidus), reported by Hallgren and Souranders [11], is used for the linear correlation analysis for the individual (Fig. 6.21) and all healthy volunteers (Fig. 6.14), respectively. The brain regions substantia nigra and the red nucleus, whose putative iron concentrations are not adjusted based on the subject's age (as their age-dependency was not published by [11]), generated the largest variation in the analysis (Fig. 6.13). And the correlation with the observed susceptibility, is weaker when the substantia nigra and the red nucleus are included, compared with when they are not (Table 6.2). Moreover, the results from the intra-subject analysis of a 24-yrs young adult also support the importance of adjusting the putative iron concentration in healthy brains based on the subject's age (Fig. 6.21), especially when the age range of the *in vivo* study could not closely match the age range reported for those post-mortem iron measurements. In this study of the PhD project, the intra-subject analysis results demonstrate a better fit of the *in vivo* MRI measurements (including the susceptibility, R_2^* , R_2 , and effective R_2) with the age-adjusted putative iron concentration in the brain [11, 352], than with prior-reported brain iron concentration that is not age-dependent [9].

Therefore, the observations in this work support the age-related change of brain iron, and it suggests that the age-dependent putative brain iron concentration should be employed to avoid potential bias in *in vivo* MRI studies. Furthermore, it also suggests the urgent need of understanding iron homeostasis, and how iron concentration and other tissue properties (*e.g.*, myelination, cytoarchitecture), would change with brain development and normal ageing, within different brain regions. In particular, the direct, robust measurement of living tissue, or unfixed post-mortem tissue for iron quantification, might fill the gap of knowledge (*e.g.*, red nucleus), and might confirm (or reject) the histological work carried out by Hallgren and Souranders [11] with advanced techniques.

6.4.5 Reproducibility of the susceptibility varies among subcortical nuclei

The results of this study suggest overall good reproducibility of the susceptibility (up to 98.29%) measured in subcortical nuclei (Section 6.3.6). However, using a single-angle acquisition (see Section 3.3), bias is unavoidably introduced in the computed susceptibility [245, 281], when the assumption of the random distribution of the susceptibility sources within brains is violated [308, 377] by the presence of orientated myelin bundles. It was found previously most profound in the susceptibility observed within the WM due to the presence of a large number of myelinated fibres [57, 245].

The subcortical nuclei measured in this PhD project, contain relatively fewer myelinated axons, compared with WM, therefore the influence of myelin on the observed susceptibility is minimised. However, the presence of axon collaterals could still violate the assumption underlying the QSM technique, that the susceptibility source should be randomly and homogeneously distributed within the brain tissue [244, 245, 378]. The medium spiny neurons in the striatum (caudate nucleus and putamen), receive afferents from cortical neurons and dopaminergic neurons originated from the substantia nigra, and projected to the pallidum [379]. In the pallidum (include substantia nigra pars reticula and globus pallidus), a large number of myelinated axons pass through, receiving input from the striatum, *i.e.*, caudate

nucleus and putamen, via medium spiny neurons, and sending output to the superior colliculus in the midbrain, and the motor cortex via thalamus [45, 372]. Those myelinated axon fibres generate an anisotropic demagnetisation field (see Section 2.3.2.1 of Chapter 2), which make the observed susceptibility dependent on the angle between the main magnetic field and the scanned subject (see Section 3.1.3 in Chapter 3, and reference [245, 279]). In contrast, substantia nigra pars compacta consisted of dense cell bodies, and about 40 % of dopaminergic neurons are packed within nigrosomes, which are local regions lacking striatonigral fibres, indicated by previously-reported immunostaining results [355]. Therefore, to quantify brain iron concentration accurately and reproducibly with QSM, even for subcortical nuclei, it would be still preferable to acquire the MR data from multiple directions (see Section 3.1.3, and reference [244, 245, 279]) when possible, suggested by the result of the PhD project.

6.5 Conclusions

To conclude, the QSM technique based on nMEDI-L₁ [271, 281] approach is validated in this study, for measuring iron on the clinical MRI with a local 3.0 T GE scanner, providing the proof-of-concept susceptibility measurement with ferric iron phantoms and in healthy human brains. A dedicated 3D SWAN sequence with ASSET parallel imaging on the Discovery MR750w system is established and reported here for QSM, with in-house image reconstruction and processing. Consistent with the literature, the linear correlation between the computed susceptibility and the putative iron concentration is found in this work, in both ferric iron phantoms and healthy brains. Superior correlation of the iron concentration with the observed susceptibility is found in the phantom, compared with the human brain MRI, due to the inter- and intra-subject variance of the tissue properties. In comparison with the transverse relaxation rates, the sources of bias in *in vivo* QSM MRI are discussed in this work and suggestions for future studies are provided. Finally, the brain region-specific scan-rescan reproducibility is demonstrated, and the remaining challenges are discussed. To summarise, this research has successfully established and evaluated the QSM contrast, as well as the quantitative measurement for the iron

concentration in phantoms and healthy brains, on the local 3.0 T clinical MRI scanner, for accelerated and complementary brain iron quantification.

Chapter 7: Transverse relaxation rate R_2^* and quantitative susceptibility mapping (QSM) of $A\beta(1-42)$ and ferritin-bound iron in MR phantoms for 9.4 T preclinical MRI

7.1 Introduction

$A\beta$ is the primary component of senile plaques, which are commonly found in the extracellular space of the brain tissue with AD [105, 380]. It is a cleavage product of the APP, and its aggregation and extracellular accumulation play the main role in the amyloid cascade hypothesis of the AD [381]. Although the aggregation pathways of $A\beta$ peptide monomers, and the various structures of aggregated oligomers, fibrils, and plaques are still to be elucidated, mounting evidence has established its binding and interactions with transition metal ions [85, 88, 382-386]. As the most abundant transition metal in the brain, tissue iron is primarily stored in the ferric form within the ferritin [22, 23, 387], and could interact with the $A\beta$ peptide and accelerate the peptide aggregation [88, 388, 389]. In AD, iron overload has been found colocalised with the extracellular senile plaques [34, 90] and intercellular NFTs [99], suggesting iron-intermediated pathologies of the disease [390, 391]. Moreover, the association of the $A\beta$ plaque with ferritin was supported by the immunostaining finding, where ferritin was detected in the extracellular senile plaques within AD hippocampus [34, 392]. Although the underlying mechanism remains unclear, the interaction of iron and ferritin with $A\beta$ and APP suggested that the toxicity of the excessive iron may be caused via oxytosis and ferroptosis [114, 385, 389, 393-395].

Meanwhile, increasing interest is drawn to how to detect, image, and quantitative measure tissue iron clinically and preclinically. Exploiting the paramagnetic and superparamagnetic properties of tissue iron, chiefly ferritin-bound iron, MRI has been used to quantify tissue iron *in situ* and *in vivo* in clinical and pre-clinical settings [13, 174, 178, 186, 248, 257, 259-261, 265]. Several approaches to investigate the tissue iron concentration, such R_2 [13, 174, 186, 248, 257], R_2^* [178, 259-261], and FDRI [251, 264], are discussed in Chapter 3. QSM is an advanced MRI technique that has been developed in the recent decade, which can extract the local tissue susceptibility variation from the MR phase information acquired by the gradient echo

sequences [18, 51, 268-273]. It is sensitive to tissue iron, as the abundant paramagnetic iron appears to be the dominant source contributing to the local field shift [14].

In the post-mortem brain [51] and ferritin phantom [53], the empirical linear correlation has been demonstrated and established at 3.0 T, between the susceptibility obtained from QSM and the iron concentration measured by ICP-MS. Analysis of Perl's iron staining with QSM also supported this linear relationship in the subcortical grey matter at 4.7 T [368]. Although QSM appeared to be sensitive to the system and the post-processing [274, 275], as a currently evolving MRI technique [269, 348], its high iron-sensitivity and novel contrast have popularised this technique as a clinical and preclinical tool.

QSM has been employed to investigate iron accumulation [51, 183, 191, 199, 201, 204, 296, 342, 368], demyelination [57, 210], aid diagnosis of neurodegenerative diseases including AD [150, 191, 199, 201, 204, 215, 396-399], and potentially detect iron-laden amyloid plaques and neurofibrillary tangles [109, 150, 215]. As the field strength increases, the susceptibility effect of tissue iron becomes profound, which could produce stronger contrast and higher resolution in QSM. At 7.0 T, the implementation of QSM has been reported for phantoms [311, 400], human brains [57, 109, 151, 221, 260, 398] and animal studies [401-403]. Most recently, QSM studies of living brains and post-mortem tissues were reported in the literature for UHF preclinical MRI systems (9.4 T and above) [210, 214, 215, 311, 404-407]. However, compared with the clinical QSM processing optimisation [273, 399, 408-410], the implementation of QSM has not yet been fully assessed and optimised for the preclinical UHF MRI system.

Nevertheless, this emerging QSM MRI technique provides an opportunity to study iron content and iron-associated pathologies *in vivo*, *ex vivo* and *in vitro*, and especially, with significant effects at UHF MRI. For AD and other neurodegeneration with iron homeostasis disruptions, QSM recently showed potential to detect and image iron-laden A β plaques in the human brain at 7.0 T [109], 9.4 T and 14.1 T [215].

At the time of writing, an ultra-high-resolution QSM study, of the quantitative relationship between the susceptibility and the A β -associated iron, has not yet reported in the literature. Therefore, an attempt to establish an optimised QSM framework for a small-animal-compatible 9.4 T UHF MRI system is presented in this work, to image novel MR phantoms that contained synthetic ferritin-iron-laden A β , in comparison with iron-free A β and dispersed ferritin. It also demonstrates the quantitative relationships for the first time, between the ferritin-bounded iron concentration, the susceptibility, and the R $_2^*$ measurement among those phantoms at 9.4 T.

7.2 Method

7.2.1 Construction of the A β (1-42) + ferritin-bound iron and control phantoms

The preparation and the incubation of the protein suspension are adopted from earlier work by Everett *et al.* [88], described in Appendix E. Horse spleen ferritin (Type I, 57 mg/mL, in saline solution; ref: F4503; Sigma-Aldrich) suspension is freshly prepared in a modified Krebs-Henseleit (KH) buffer (pH 7.4, 37°C), with a concentration of 1.44 mg/mL. Frozen amyloid β -protein (1-42) (A β , ref. 4014447, Bachem) is thawed in 1 mM NaOH at room temperature, to form 2 mg/mL A β suspension. An A β +ferritin protein suspension (A β +Ftn) is made by mixing the prepared A β and ferritin suspension in a volume ratio of 1:5 (to maintain the pH), where the concentrations of A β and ferritin in the mixed suspension are 0.33 mg/mL and 1.2 mg/mL, respectively. The ferritin and A β (1-42) concentrations in the suspension for incubation matches a previous study from our group to investigate aggregation under these conditions [88], and the ferritin concentration is decided accordingly, so that the final ferritin concentration in the agarose gel sample is within the range of physiological levels reported for human brain [7, 13, 43, 411]. The suspension is then incubated at 37 °C for a period of 100 hrs to produce A β +ferritin aggregates. An A β (1-42) control (A β) and a ferritin control (Ftn) are also prepared at the same time by substituting the ferritin suspension and the A β suspension with KH buffer (Fig. 7.1).

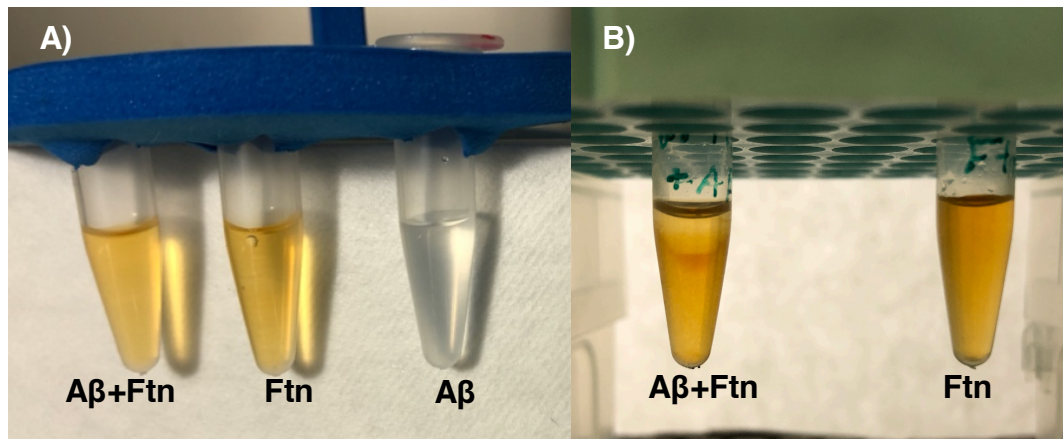


Fig. 7.1 Peptide suspensions (A) and A β (1-42) and ferritin samples after 100 hrs incubation (B).

After the incubation, each suspension is diluted into three different concentrations with the KH buffer to produce separate protein samples. Then in a warm ultrasonic bath (45 °C), each protein suspension sample is carefully mixed with already prepared dispersed 4% w/v agarose stock in a volume ratio of 1:1, to make the final 2 % w/v agarose-protein gel sample. The final 2 % w/v agarose-protein gel samples each has a volume of 120 μ L, and all samples are let set overnight at 4 °C. The final concentrations of the components are summarised in Table 7.1. To cast the final MR phantoms, the already prepared 8 % w/v agarose gel is poured over four 2 % w/v gel samples in a silicone cylinder mould (ID = 20 mm), forming a supporting matrix (Fig. 7.2). The 8 % w/v agarose gel supporting matrix is employed to fill the space between the individual sample volumes to 1) harmonise the B₁ effect over the entire phantom, 2) facilitate global shimming. Each phantom consisted of the sample group of protein gel samples, *i.e.*, A β +ferritin aggregates (A β +Ftn), ferritin control (Ftn), and A β control (A β), with varying concentrations. An internal reference, containing only the modified KH buffer, is included in each phantom and this buffer-only sample is labelled as 'A β +Ftn 0', 'Ftn 0', and 'A β 0' for the respective phantoms (see Table 7.1). The supporting gel of each phantom let set for 2 hrs at 4 °C after casting, and then stored at 4 °C for no longer than 6 hrs before the MR acquisition.

Table 7.1 Summary of final 2 % w/v agarose-protein gel samples[†]

MR phantom	Sample	A β (1-42) (mg/mL)	Horse spleen ferritin (mg/mL)
A β +Ftn phantom	A β +Ftn 3	0.165	0.6
	A β +Ftn 2	0.0825	0.3
	A β +Ftn 1	0.0275	0.1
	A β +Ftn 0 (KH buffer only)	0.0	0.0
Ftn phantom	Ftn 3	0.0	0.6
	Ftn 2	0.0	0.3
	Ftn 1	0.0	0.1
	Ftn 0 (KH buffer only)	0.0	0.0
A β phantom	A β 3	0.165	0.0
	A β 2	0.0825	0.0
	A β 1	0.0275	0.0
	A β 0 (KH buffer only)	0.0	0.0

[†] Prepare phantoms included samples: A β +Ftn – A β +ferritin aggregates samples, A β – A β control samples, and Ftn – ferritin control samples. Note the samples ‘A β +Ftn 0’, ‘Ftn 0’, and ‘A β 0’ only contained KH buffer, served as the identical internal reference.

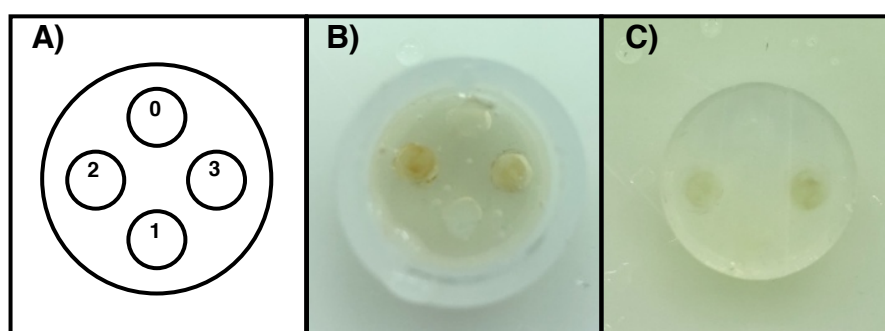


Fig. 7.2 An example of the gel assembly MR phantoms for the small animal coil. Axial views of the schematic drawing (A), gel assembly moulding (B) and the resulting phantom (C) are shown.

7.2.2 Preparation for imaging the phantom in 9.4 T preclinical MRI system

To support and stabilise the sample during the MRI experiment, a dedicated imaging container with sample support is constructed for the phantom, made with MR-invisible materials (Fig. 7.3). Specifically, a polytetrafluoroethylene (PTFE) O-ring (ID/OD = 15/22 mm) is fixed using epoxy inside a 30 mL polystyrene (PS) specimen container (ID/OD \times H = 23/25 \times 94 mm, which could be tightly fitted in the 25-mm RF coil, see following section 7.2.3), parallel to the opening and 4 cm below the sealing screw-in PS cap (OD = 31 mm), to ensure the precise co-localisation of the supported sample with the RF coil sensitive centre during the MR examination (left-side image in Fig. 7.3). To further prevent the motion and the rotation of the phantom, due to the vibration caused by the strong gradient employed for the system, cushioning surrounding the sample is necessary. A flexible, multi-layer nylon mesh is therefore employed to serve this purpose.

Subsequently, the cushioned MR phantom sat on the PTFE O-ring support, and a detachable polypropylene (PP) sample holder is used to prevent motion of the phantom during MR imaging (right-side image in Fig. 7.2). Therefore, the MR phantom is securely fastened within the specimen container, co-localising with the sensitivity centre of the RF coil, allowing vertical (z-direction) geometry offset to be less than ± 2.5 mm, and horizontal offset (x- and y-direction) to be less than ± 0.5 mm.

Susceptibility artifacts are often seen at the sample-air interface, especially at the high magnetic field, due to the large susceptibility differences between the sample (usually weakly diamagnetic, *e.g.*, tissue, gel phantoms, because of the large proportion of diamagnetic water) and the surrounding air (paramagnetic, because of the paramagnetic oxygen O₂) [412, 413]. To minimise the susceptibility effect at the phantom's surface, measures are taken to eliminate the paramagnetic air, by substituting it with a susceptibility-matched (weak diamagnetic) material [54, 221, 414]. Hence, the entire imaging container is filled with a susceptibility-matched perfluorocarbon liquid Fluorinert FC-40, by which the MR phantom to be examined

was surrounded, and any air in the container is carefully eliminated before the MR acquisition.

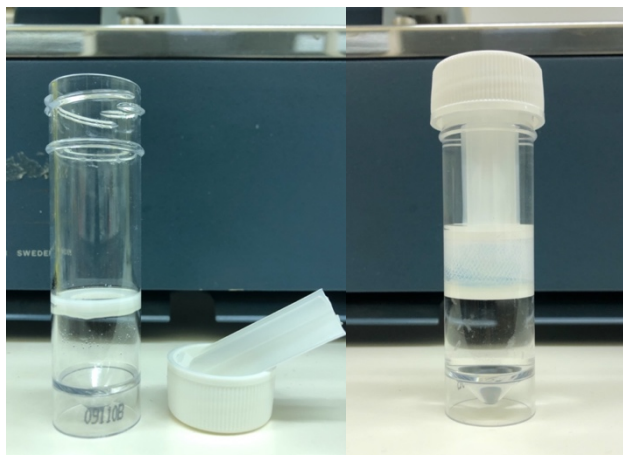


Fig. 7.3 Imaging container and sample installation.

Left: imaging container and its support; Right: a gel assembly MR phantom installed in the dedicated container for MR imaging

7.2.3 Hardware set up for 9.4 T preclinical MRI

The acquisition is carried out on the 400 MHz (9.4 T) spectrometer, using a Bruker's Micro 2.5 gradient system (ID/OD = 40/72 mm), which is compatible with the 89 mm wide-bore magnet (MICWB40), and a (linearly polarised) volume coil tuned to ^1H frequency (Bruker), with the internal diameter of 25 mm. This system is highly flexible in high magnetic field MRI, and suitable for MR microimaging. MRI spatial resolution on the frequency encoding (readout) direction is limited by the gradient strength, and by the digitization rate on the phase encoding direction. Therefore, by using the 3-axis (xyz) gradient MICWB40, which has the gradient linearity of 36 mm (sphere), and a short rise time (gradient rise from 5-95% < 100 μs) and could support the gradient strength of up to 1.5 T/m on each direction (while on clinical 1.5 T and 3.0 T scanners, this value is on the magnitude of tens or hundreds mT/m), it is achievable to obtain high-resolution images using the set-up described [218].

As the temperature of the sample influences its susceptibility and relaxation properties (described by Eq.(2.17) and Eq.(2.18) in Section 2.3.1), the temperature within the RF coil (and of the sample itself) needs to be controlled during the MR acquisition. Although the body temperature (37 °C) would be preferable to imitate

the physiological condition of human brain tissues, the SNR is found to be low at 37 °C, as well as at room temperature 20 °C, generating images with a noisy background. Besides, the SAR is found high due to the repeatedly applied RF pulses. Therefore, to minimise the RF heating deposit on the sample, and to reduce the thermal noise generated by the RF coil's resistance, the temperature of the MR experiment is set to 4°C, as reported previously for unfixed tissue [54, 414]. The temperature control unit EVT (Enhanced Variable Temperature) inserts are installed to monitor and maintain the low sample temperature, and via which the probe is connected to a Ni/air chiller (BCU II, Bruker). The low temperature is employed to maintain the phantom stability. The final hardware set-up for the MRI experiment is shown in Fig. 7.4.



Fig. 7.4 UHF MRI hardware set-up.

Insert: enlarged view of the bottom-loading vertical RF probe/sample insertion point with the temperature control system.

After setting up the hardware, a series of pre-scan adjustments are performed before the acquisition started, to ensure the quality of MR images (Appendix F). This includes: 1) the tuning and matching of the RF pulse, to match the correct power transmission and reception between the preamplifier and the RF coil, crucial to

achieving a high SNR, 2) global shimming to reduce the global field inhomogeneity, also including additional B_0 map shimming for the GRE pulse sequence (see details in Shimming strategy in Appendix F), 3) frequency adjustment to locate the dominant ^1H Larmor frequency ω_0 (see Eq.(2.6) in Section 2.1.1), 4) RF power adjustment and receiver gain adjustment, to calibrate the accurate FA and maximise the signal intensity for the analogue-to-digital converter (ADC), respectively. All adjustments are performed within Paravision 6.0.1 (PV6), after the temperature within the RF coil is stabilised at 277.15 K (4 °C) for at least 30 min, thereby allowing the entire sample to cool to the target temperature.

7.2.4 MR acquisition

7.2.4.1 Localisation scans

A 2D 3-orthogonal planes, proton-weighted fast low angle shot (FLASH) sequence is applied for shim system initialisation and phantom localisation at the beginning of scanning each sample, because of its fast acquisition, with a large FOV coverage and good image contrast. Acquisition parameters: $T_E = 4$ ms, $T_R = 60$ ms, $FA = 30^\circ$, $FOV = 30 \times 30$ mm, matrix size = 128×128 , in-plane resolution = 0.234×0.234 mm, slice thickness = 1 mm. Number of averages (N_A) = 1, scan time = 6 s.

Subsequently, dedicated localising scans are acquired on 3 orthogonal planes using a multi-slice FLASH pulse sequence, the slice location is set to cover the entire outline of the sample volume. Images are acquired with following parameters: $T_E = 3$ ms, $T_R = 15$ ms, $FA = 8^\circ$, $FOV = 30 \times 30$ mm, matrix size = 192×192 , in-plane resolution = 0.156×0.156 mm, slice thickness = 0.8 mm, slice gap = 1 mm (axial plane)/2 mm (sagittal and coronal planes), number of slices = 6/plane. $N_A = 1$, scan time = 2 min 36 s.

7.2.4.2 3D multi-echo GRE pulse sequence for R_2^* mapping and QSM

To investigate the transverse relaxation rate R_2^* and susceptibility of the samples, a high-resolution multi-echo 3D GRE sequence is employed. High isotropic spatial resolution, which is comparable to the routine MR microscopy (≤ 100 μm in at least one direction) [415], is applied to resolve the A β aggregate [215, 218]. As the phase

CNR is maximised at $T_E = T_2^*$ [244], multiple echo times are applied to obtain the varying phase shift caused by components with different susceptibilities. The 1st T_E is minimised, and small ESP is employed to allow the capture of the fast phase shift (dephase) FID caused by the compact iron-laden oligomers and fibrils. For the slow-decaying (dephasing) signals generated by the materials with small-susceptibility (*e.g.*, the KH buffer samples), a long T_E around $T_2^* = 50$ ms is preferable, but the SNR is already too low when $T_E > 40$ ms. Therefore, the long T_E is traded off to shorten the T_R and the scan time, and the last T_E is chosen to be around 25 ms. To further improve the SNR for the small voxel volume (6.36×10^{-4} mm³), a relatively low BW and higher N_A are also applied. To avoid the signal from outside of the FOV, which may cause aliasing along the slice-direction, a sharp, slab-selective Shinnar–Le Roux (SLR) pulse is used to excite the entire 3D FOV volume.

7.2.4.2.1 B_0 map shim for 3D GRE pulse sequence

Before the acquisition, additional shimming steps (B_0 map shim) are required by the GRE sequence, to minimise the global inhomogeneity and any susceptibility artifacts. Detailed in Shimming strategy in Appendix F, it is applied after the 1st- and 2nd-order FID shims (global FID shim). Before the B_0 map shim, a cylinder-shaped shim volume is drawn, entirely within and adjacent to the volume boundary of the MR phantom, covering a total of 4 gel samples. Then the magnetic field within the shim volume is adjusted by the PV6-implemented 'MAPSHIM'. The 'MAPSHIM' algorithm aims to minimise the magnetic field inhomogeneity within the selected shim volume, based on a map of the magnetic field (B_0 map) acquired by a fast two-echoes 3D GRE sequence (described in Shimming strategy in Appendix F) prior to the shimming.

After the 'MAPSHIM' is completed, an updated B_0 map is acquired for inspecting the shim result. An adequate shimming result is determined empirically, as no phase-wrap is observed on the B_0 map within the supporting gel, and the in-plane and z-direction variation of the field shift (a.u., demonstrated as the signal intensity of the B_0 map) within the supporting gel is within $\pm 20\%$, respectively. When the shim result does not satisfy the criteria, the shim sets are reverted to the previous (global) shim result and the B_0 map shim is repeated.

After the shimming, the 3D GRE acquisition is then performed with the following parameters: $T_E = 3.8, 7.8, 11.8, 15.8, 19.8, 23.8$ ms, ESP = 4 ms, number of echoes = 6 with uni-polar (positive) readout gradient, $T_R = 40$ ms, FA = 20° , FOV = $22 \times 22 \times 11$ mm, acquisition matrix size = $256 \times 256 \times 128$, with 2nd PE direction (slice-direction) oversampling = 1.25 to avoid the slice-direction aliasing. Three-dimensional acquisition has isotropic resolution = $0.086 \times 0.086 \times 0.086$ mm, readout direction = L-R, receiver bandwidth = 12.5 kHz, $N_A = 9$, acquisition time = 4 hr 5 min 46 s.

7.2.5 Image processing

7.2.5.1 Reconstruction

The magnitude and phase images are first reconstructed by the vendor's online reconstruction at the console within PV6 (Bruker) to assess the image quality. The magnitude images are first examined by a visual check, for any aliasing, or motion artifact or distortion or signal drop-out that indicated the susceptibility artifact. Subsequently, the SNR, signal homogeneity of the magnitude image, as well as the preliminary T_2^* decay, are examined in PV6, using 'Image Sequence Analysis Tool', as shown in Figure 7.5. The SNR is calculated from the signal intensities of the phantom and the background on the 1st echo image ($T_E = 3.8$ ms), which is accepted when larger than 15. The signal homogeneity within the supporting gel is deemed acceptable, when the variation of the signal intensity measured with a 3-mm diameter circular ROI within the xy-plane and along the z-direction, is within $\pm 5\%$. The preliminary T_2^* decay of the signal magnitude is also inspected, for any deviation from an exponential decay or signal drop-out. As the acquired image satisfied the above criteria, the MR data proceed to be collected for the subsequent image processing.

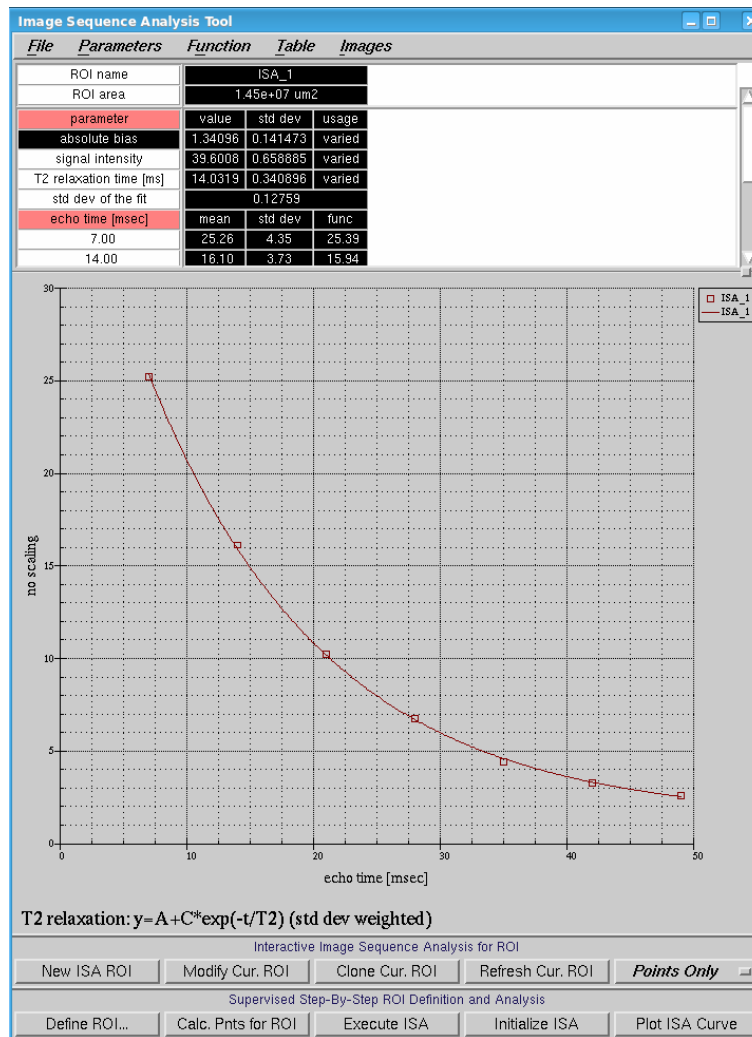


Fig. 7.5 Example examination of the MR signal behaviour within PV6.

The raw 3D GRE MRI data are then exported and reconstructed offline via a user-defined reconstruction in MATLAB (R2019b, MathWorks), which is built using a MATLAB function package 'pvmatlab' from Bruker upon request. The FID data (stored in 'fid' within the Bruker raw data hierarchy) received by the single volume coil is first read into a 4D Cartesian k-space using the *CKDataObject()* class, based on the acquisition parameters (header information) stored in 'Acqp' as a JCAMP file. For each echo (the 4th dimension), 3D- IFT are applied to the k-space data along the slice- and in-plane directions, via the function handle *Bruker_reco()*. To reconstruct the unaltered complex images, the phase correction option ('phase_corr_pi') and the sum-of-squares method ('sumOfSquare') are set to false for the reconstruction. A final step of the RF un-chopping, as described in the previous Chapter 6 (see Section 6.2.4.1), is performed, to calculate the correct complex conjugate by reversing the

sign of every second complex number (image pixel). The complex values (image pixel) are then used to calculate the final magnitude and phase images, shown in Figure 7.6. Averaged over the echo images, the SNR of the reconstructed magnitude images is about 15.

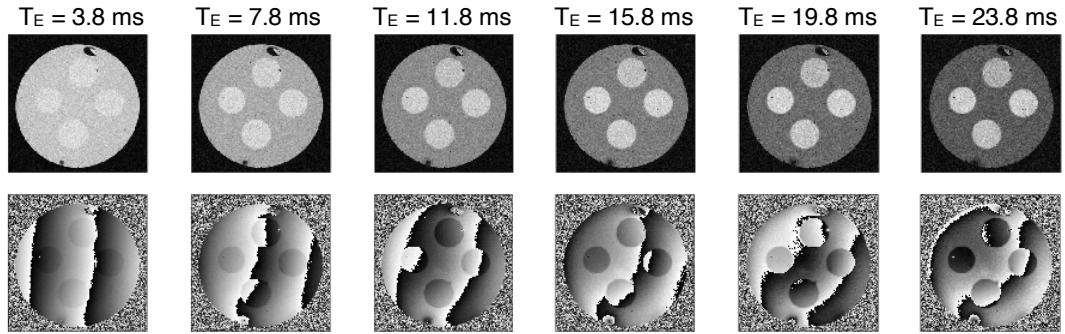


Fig. 7.6 Example reconstructed magnitude (top) and phase (bottom) images of the Ftn phantom acquired by the multi-echo 3D GRE pulse sequence.

7.2.5.2 R_2^* mapping

The transverse relaxation rate R_2^* are calculated pixel-wisely from the magnitude image reconstructed from the 3D GRE pulse sequence. After subtracting the background noise, the signal intensity is fitted into a T_2^* decay, using an algorithm for fast mono-exponential fitting [353]:

$$S(T_E) = S_0 e^{-\frac{T_E}{T_2^*}} \quad \text{Eq. (7.1)}$$

where $S(T_E)$ is the T_E -dependent magnitude MR signal, $S_0 = S(0)$ denotes the signal intensity at $T_E = 0 \text{ ms}$, and $T_2^* = \frac{1}{R_2^*}$ indicates the transverse relaxation time.

The employed algorithm utilised ARLO of the T_2^* signal decay, is capable of fitting the MRI data efficiently with comparable accuracy [353] to the widely used Levenberg-Marquardt method [416], and it has been recently established in the multi-centre study [222]. Compared with the pixel-wise fitting using the conventional least-squares based Levenberg-Marquardt method [249, 417], which took over 40 min for each 3D GRE dataset (with 2.6 GHz 6-Core Intel Core i7, macOS Catalina), ARLO generates the R_2^* maps within seconds.

7.2.5.3 QSM post-processing

7.2.5.3.1 Temporal unwrapping

The reconstructed phase (Fig. 7.7, also see Section 7.2.5.1) is first corrected by removing the echo-to-echo phase inconsistency in the readout direction (see Section 4.4.2.1) with a non-linear least-squares fitting [298], and then the phase images are normalised to the standard deviation of the noise measured in the background. The wrapped phase is observed in the raw phase data (middle row in Fig. 7.7), demonstrated as the fringe lines within the phantom, where the detected phase values jump from positive to negative between two adjacent pixels, forming a $+\pi/-\pi$ boundary. The density of the fringe line pattern also provides visual information of the local field perturbation, which heavily wrapped phase and the fringe lines appeared in a high frequency indicated a rapid magnetic field shift. This is observed near the phantom's surface and within the embedded ferritin gel samples (sagittal and coronal images in the middle row of Fig. 7.7), due to the susceptibility difference between either side of the boundaries. After the temporal unwrapping, the T_E -dependent phase shift is removed, demonstrated as the elimination of the most fringe lines (bottom row of Fig. 7.7).

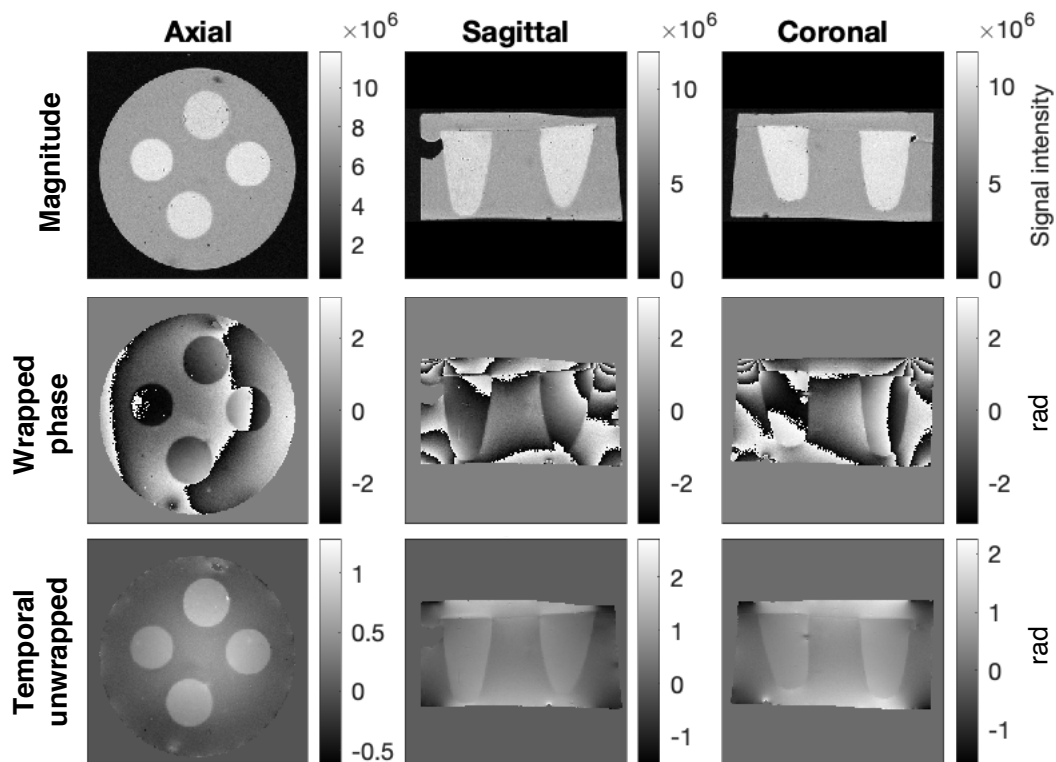


Fig. 7.7 Example temporal unwrapping of Ftn phantom.

7.2.5.3.2 Assessing the phase processing

As discussed in Section 4.4.2, the RDF resulting from the phase processing of QSM, is crucial for the subsequent inversion step. Therefore, various approaches proposed in the literature [245, 246, 276, 299, 300] for the phase processing steps are tested and compared, as a part of the QSM implementation of A β (1-42) and ferritin-bound iron phantoms on the preclinical 9.4 T MRI system. In the initial spatial phase unwrapping steps, the methods based on the region-growing [299], and the continuous Laplacian operator [300] are firstly tested and compared. Each method is applied to the temporally-unwrapped phase image, respectively, and the unwrapped output phase with superior accuracy and consistency across phantoms proceeds to the following background field removal step.

Subsequently, the temporally- and spatially-unwrapped phase is processed to obtain the RDF, via background field removal. Three widely employed methods in the literature are tested and compared here, including PDF [246], SHARP [245] and LBV method [276]. As these methods are already introduced in Section 4.4.2.1-2, thus only how each implementation of them is tested and assessed is summarised here.

In the PDF method, the background field to be removed is fitted into the 0th- and 1st-order spherical harmonic terms in the field expansion and estimated, which is optimised by a CG algorithm [246]. The fitting process is allowed to be controlled by a fitting tolerance noise level and a maximum iteration, to further tune the resulting RDF. A large maximum iteration of 300 is selected imperially to allow sufficient convergence, and the effect of the tolerance level is tested by varying the value from 1×10^{-5} to 1×10^{-1} in log steps of 1×10^{-1} , and from 0.2 to 0.8 in steps of 0.2.

In the LBV approach, a comparable tolerance level parameter is provided as the iteration stopping criteria for the background field removal process [276], and its effect on the RDF is also tested by varying the tolerance level. This tolerance level is the iteration stopping criteria on the coarsest grid of the multigrid algorithm implemented in the LBV method, for solving Poisson's equation with the boundary condition, to enable an efficient computation [276].

For SHARP, the main parameters that controlled the background field removal process include the spherical filter radius and the truncation level. The spherical filter radius in SHARP allows the adjustment of the kernel size of the SMV filter, while the truncated singular value decomposition (SVD) [278], which is employed to regularise the deconvolution [245], is controlled by the truncation level. To investigate the effect of the SMV radius on the resulting RDF, a range of SMV radii, varying from 0.1 to 1 mm in steps of 0.1 mm, as well as radius = 0.05 mm, are tested, at the fixed truncated value = 0.08. At the same time, the effect of the truncation level is investigated by varying the value from 0 to 0.1 in steps of 0.02.

The resulting RDFs are assessed from the following aspects: 1) image quality 2) phase accuracy and consistency, and 3) computational efficiency. In particular, the consequent RDF images of each background field removal method are examined qualitatively for any phase artifacts, and the line profile of x-, y-, and z-direction is examined quantitatively for the varying estimation parameters of each method, as well. After assessing, the generated RDF that best satisfying the above criteria, proceeds to the final step of dipole inversion.

7.2.5.3.3 Selecting the regularisation parameter λ

The RDF (see Section 7.2.5.3.2) is used as the input for the field-to-source inversion, employing nMEDI- L_1 [18], to generate the final susceptibility map. Detailed in Section 4.4.2.3, nMEDI- L_1 provides a sophisticated tool to quantify the bulk susceptibility source from the local field inhomogeneity, by reformulating the inversion problem into a constrained minimisation problem [17, 18, 310]. The susceptibility χ is the optimisation solution to Equation (4.9) in Section 4.4.1, where the difference between the field generated by the pseudo-susceptibility (forward problem) and the RDF (*i.e.*, the observed field) is minimised. As a single-orientation (acquisition) approach, the inversion problem at the magic angle is ill-posed (see Eq. (3.1) in Section 3.1.3), demonstrated as cone-shaped streaking artifacts in the resulting susceptibility maps [17, 244, 245, 418, 419]. Using a regularisation approach to suppress the streaking artifact, the nMEDI- L_1 algorithm [18] could compute a smooth, artifact-minimised, and accurate solution of the susceptibility, when the

regularisation parameter λ is chosen appropriately [419-421]. As demonstrated in Figure 7.8, the regularisation parameter λ determines the smoothness of the output susceptibility images (due to the streaking artifacts), balancing with the susceptibility accuracy [18].

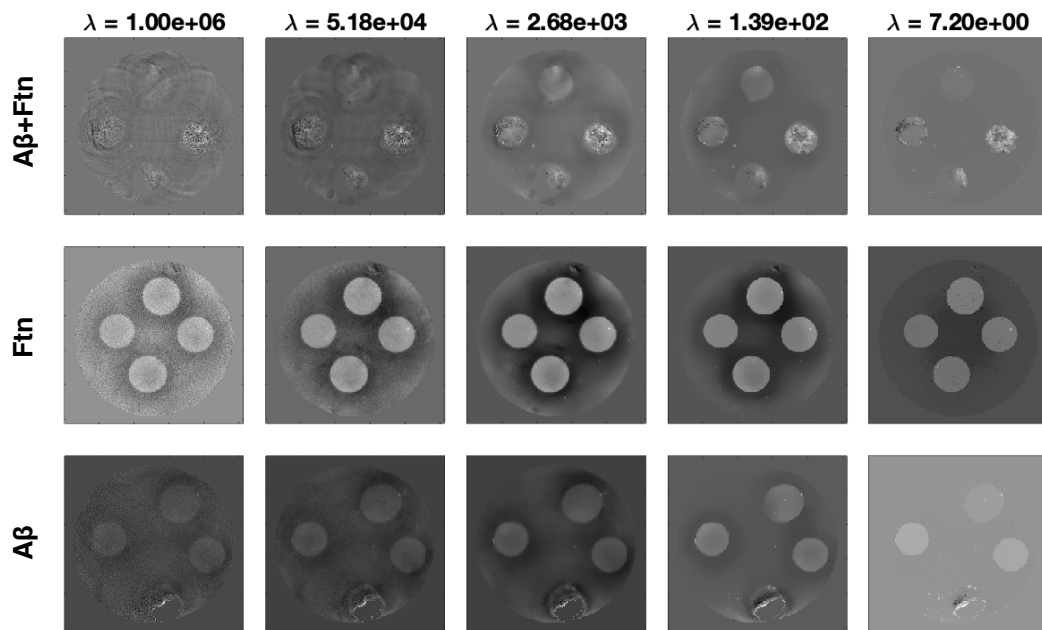


Fig. 7.8 Susceptibility images of phantom A β +Ftn (top row), Ftn (middle row) and A β (bottom row) with varying regularisation parameter λ .

7.2.5.3.3.1 Comparing automatic methods for λ optimisation

Although selecting the regularisation parameter λ empirically with visual examination [399, 407] remains one of the most recognised methods, especially in clinical MRI studies, it is subject to the rater's experience and expertise. In contrast, the discrepancy principle [422] could be employed to find the optimal λ , where the residual in the data fidelity term matched the background noise [18], by sweeping in a large range of λ . Recently, attempts have been made to automatically select λ , demonstrating objective approaches for choosing the λ in human brain QSM [305, 410, 420]. Those methods rely on (and are also mathematically justified by) the properties of the regularisation cost and the data fidelity cost, as functions of λ , and therefore greatly minimise the rater bias. However, those automatic methods have not previously been assessed, for the UHF microimaging MR systems. Hence, to investigate the reliability of the automatic optimisation approaches to choosing

parameter λ , the following methods are investigated and compared here: L-curve heuristic analysis [183, 305, 420], U-curve [305, 410] and rescaled U-curve analysis, and elbow point method [423]. The regularisation parameter λ is swept within the range from 10^6 to 10^0 , decreasing in logarithmical steps of $10^{0.4}$, and the corresponding residuals of the data fidelity term and of the regularisation term are computed for each of the following optimisation approaches.

For the L-curve heuristic analysis, the regularisation cost and the data fidelity cost are examined to create the L-curve [420], and the optimal λ is found at the maximum curvature of the log-log L-curve. The curvature κ is calculated as [305, 420]:

$$\kappa = 2 \frac{\rho' \eta'' - \rho'' \eta'}{((\rho')^2 + (\eta')^2)^{3/2}} \quad \text{Eq. (7.2)}$$

Where ρ and η are the logarithms of the regularisation and the data fidelity cost respectively, and ρ' , η' and ρ'' , η'' are their first and second derivatives to the λ . A spline interpolation is fit to the discretely sampled λ before the differentiation of the parameters ρ , η for calculating the curvature. The U-curve method [305, 410] determines the minimum of the sum of the reciprocates of the two costs:

$$U = \frac{1}{Cost_{data}} + \frac{1}{Cost_{regularisation}} \quad \text{Eq. (7.3)}$$

The resulting value U is then plotted against the parameter λ to determine the minimum. The rescaled U-curved method is based on the same sum-of-reciprocates principle, by normalising the data cost and the regularisation cost to the same scale before calculating the U-curve. In contrast, an elbow (inflection) point search is performed on the linear-linear scale of the curve of the two cost functions. To determine the inflection point of the curve, the bisection method [423] is applied to the curve, and the elbow point is found at the point, where the sum of errors of the fits from both sides is minimised.

Subsequently, determined by each optimisation method, the corresponding resulting susceptibility image quality is assessed in respect of streaking artifacts and blurring (over-smoothing) for each phantom. Then the consistency of the optimal λ

values between the three phantoms ($A\beta$ +Ftn, Ftn, and $A\beta$), computed by each optimisation method, are compared.

7.2.5.3.3.2 Analysing the effect of λ on the susceptibility images

To further quantify the effect of λ on the susceptibility image quality, the standard deviation of the susceptibility is measured within an internal reference ' $A\beta$ +Ftn 0', with the varying λ . Detailed in Method section 7.2.1, the internal reference gel ' $A\beta$ +Ftn 0' (as well as the identical 'Ftn 0' and ' $A\beta$ 0') consisted solely of the homogeneous KH buffer, therefore the susceptibility standard deviation measures the impact of the streaking artifact on the image quality. To investigate the effect of λ on the resulting susceptibility, the average susceptibility measured within the gel samples as a function of λ is demonstrated, for the three phantoms ($A\beta$ +Ftn, Ftn, and $A\beta$) respectively.

7.2.5.3.4 Method for QSM of $A\beta$ (1-42) and ferritin-bound iron with 9.4 T preclinical MRI

After the assessment of the phase processing (Section 7.2.5.3.2) and the λ optimisation (Section 7.2.5.3.3) approaches, an optimised QSM method of $A\beta$ (1-42) and ferritin-bound iron with 9.4 T preclinical MRI is proposed in this work. It is then employed to generate the final susceptibility maps for all three phantoms (see Table 7.1 in Section 7.2.1), from the MR data. To summarise the optimal QSM post-processing, reconstructed from the complex MR data (see Section 7.2.5.1), the raw phase images are first temporally unwrapped using a non-linear least-squares fitting [298], and spatially unwrapped using the Laplacian method [300], to generate the total field map. To produce the RDF, the background field is then efficiently removed from the total field map by solving the LBV [276]. The final susceptibility maps are solved from the RDF, using nMEDI- L_1 [18], with the automatically optimised λ of 1.92×10^2 , by searching the elbow (inflection) point using the bisection method [423], for all three phantoms. All image post-processing is performed in MATLAB (R2019b, MathWorks) on a 16 GB MacBook Pro (macOS, Catalina) with a 2.6 GHz 6-Core processor (Intel Core i7). The final susceptibility maps generated using this optimised QSM method, are used for the following data analysis.

7.2.6 Data analysis

7.2.6.1 ROI analysis

To investigate the susceptibility and R_2^* of $A\beta(1-42)$ and ferritin-bound iron, ROI analysis is performed for each sample within all three phantoms using MATLAB (R2019b, MathWorks). Shown in Figure 7.9, circular ROIs for each gel sample within the phantom are delineated on the consecutive slices of the magnitude images, and the pixels near the sample boundaries and (if any) trapped air bubbles within the gel phantom are avoided. The pixel values within these ROIs are measured.

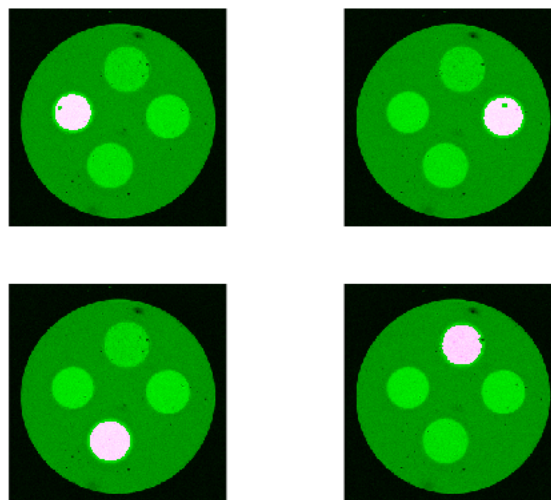


Fig. 7.9 Example ROIs (magenta circles) on the phantom for 9.4 T preclinical MRI.

7.2.6.2 Statistical analysis

The mean, median, and the standard deviation of the susceptibility and R_2^* of each sample are measured, respectively, and the pixel values measured within each ROI are examined with Q-Q plot, and tested for normality using Shapiro–Wilk test. To investigate the distribution of the measurements, the histograms of the pixel values measured within the ROIs are also examined and compared, and the values are fit into the t -location-scale distribution to preserve the shape of the data distribution. To investigate the relationships between the R_2^* and susceptibility of $A\beta$, dispersed ferritin, and aggregated $A\beta$ +ferritin, linear regression analysis is performed for the co-localised R_2^* and susceptibility pixel values measured in $A\beta$, Ftn, and $A\beta$ +Ftn phantoms respectively. To quantify the effects of $A\beta(1-42)$ and ferritin-bound iron on R_2^* and susceptibility, linear regression analysis is also performed between the mean

(median) R_2^* measured within the ROIs, and the ferritin ($A\beta$) concentration, as well as between the mean (median) susceptibility and the ferritin ($A\beta$) concentration. All analyses are carried out in MATLAB (R2019b, MathWorks).

7.3 Results

7.3.1 Assessment of QSM implementation for 9.4 T preclinical MRI

7.3.1.1 Evaluation of spatial unwrapping methods

The region-grow [299] and the Laplacian [300] methods are tested to spatially unwrap any remanent fringe lines (wrapped phase) in the temporally unwrapped phase (Section 7.2.5.3.1, Fig. 7.6). As shown in Fig. 7.10, the phase images generated using both methods have similar results in Ftn phantom (top row, Fig. 7.10) and $A\beta$ +Ftn phantom (middle row, Fig. 7.10). However, the region-grow method [299] is unable to resolve the correct phase for $A\beta$ phantom (bottom right in Fig. 7.10), where the phase of the phantom structure is falsely removed. This unwrapping artifact might be caused by the premature termination of the region-growing, when the growth iteration fails to unwrap any new pixel, and only the regions with high reliability are unwrapped successfully [299]. In contrast, the Laplacian unwrapping technique employs the path-independent Fourier operator [424] to estimate the true phase, and therefore is resistant to the noise and unwrapping artifacts [300]. It also showed robustness, at the presence of the large phase shift caused by the trapped air bubble (bottom left in Fig. 7.10, yellow arrow).

Both methods unwrap the input phase within a few seconds. Nevertheless, compared with the region-grow method [299], the Laplacian operator technique [300] demonstrates a superior spatial unwrapping result for the phantoms. Therefore, the Laplacian technique [300] is employed as the spatial unwrapping step of the QSM presented here, to generate the unwrapped phase images for the subsequent background phase removal.

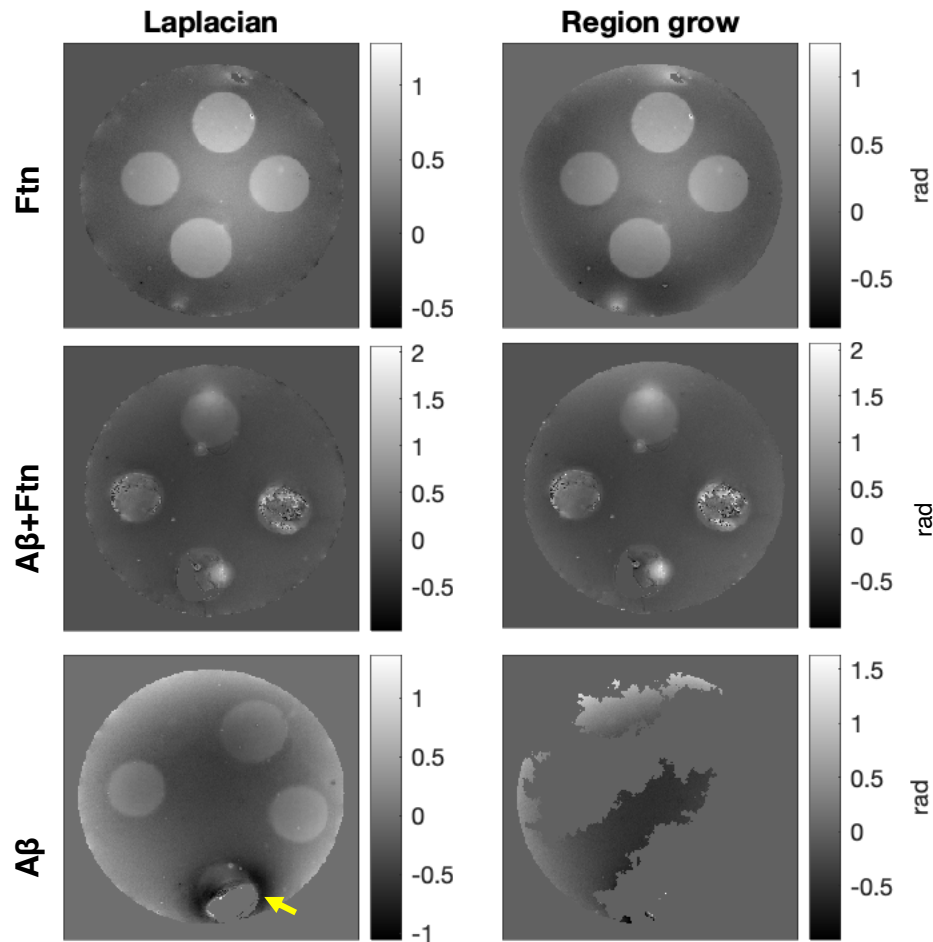


Fig. 7.10 Spatially unwrapped phase of Ftn (top), A β +Ftn (middle) and A β (bottom) phantoms using the Laplacian [300] (left) and region-grow [299] (right) unwrapping. Yellow arrow indicated the void signal caused by a trapped air bubble in the A β gel phantom, adjacent to the sample 'A β 1'.

7.3.1.2 Evaluation of background field removal methods

The results of the background field removal using PDF [246], LBV [276] and SHARP [245] techniques, for the A β +Ftn phantom are shown in Figure 7.11 as an example. Overall, the slowly varying background field, demonstrated as the shadowing in the supporting gel (Fig. 7.11, the unwrapped image), is eliminated after applying the background field removal methods. Similar RDFs are generated by PDF [246] and LBV [276], but the latter performed better near the phantom boundary. On the other hand, the RDF generated by the SHARP technique [245] is prone to the remanent background field and image erosion, and dependent on the parameters SMV radius and the truncation level in the k-space for the deconvolution. For a $256 \times 256 \times 128$

dataset (as shown in Fig. 7.11), the typical processing time of LBV [276], SHARP [245] and PDF [246] is found to be 6 sec, 7 sec, and 10 min 30 sec, respectively.

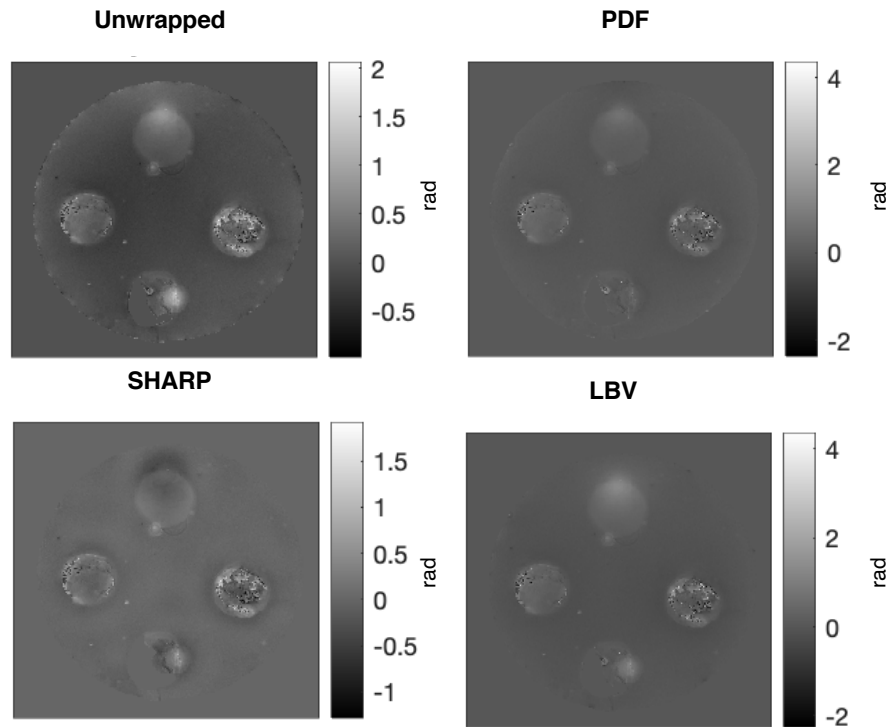


Fig. 7.11 Background field removal of A β +Ftn phantom using PDF [246], LBV [276] and SHARP [245] techniques.

Parameters used to generate the RDFs: maximum iteration = 300 and tolerance = 0.001 for PDF; tolerance = 0.01 for LBV; SMV radius = 0.2 mm, truncation level = 0.002 for SHARP.

For PDF [246], the RDF line profile suggests a more effective elimination of the background field as the tolerance decreased, demonstrated as the removal of the slowly drifting field measured across the supporting gel within the phantom (Fig. G1.1, Appendix G). The resulting RDF appears to be stable at a tolerance of less than 0.01.

For the RDFs generated by the LBV technique [276], the profile also shows effective background field removal, across a large range of the tolerance level (Fig. G1.2, Appendix G). The low-frequency background field is efficiently removed, and it generated the RDF that is visually similar to the result of PDF (Fig. 7.12). The main difference between these results, is near the phantom boundary and the small air

bubbles trapped inside the phantom (white arrows in Fig. 7.12), where the local field is retained better by the LBV method.

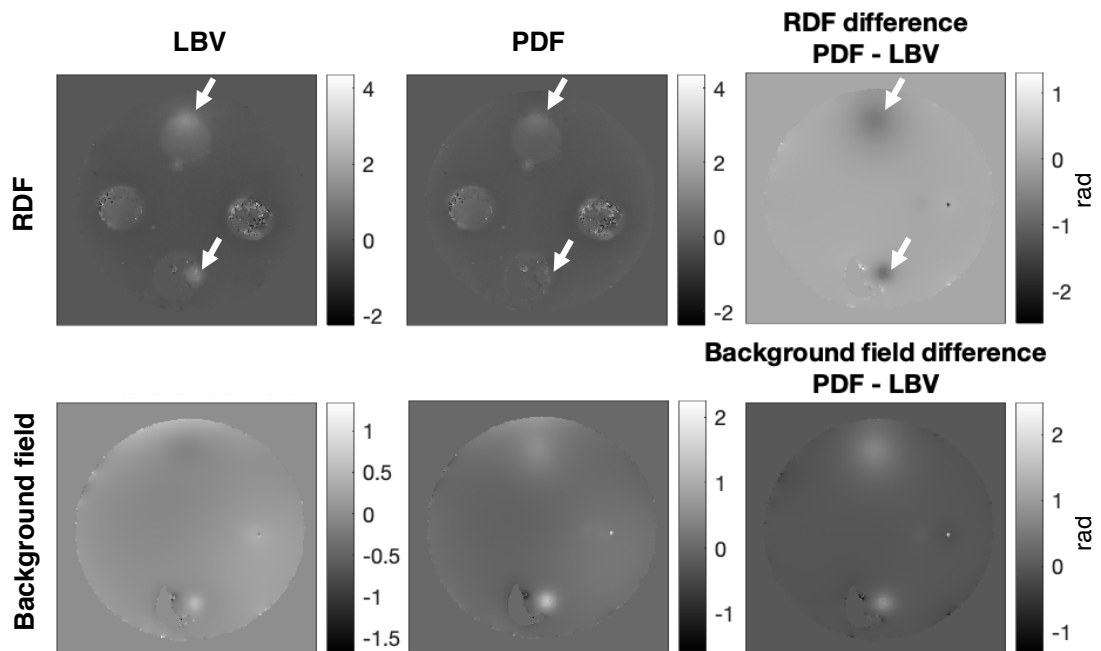


Fig. 7.12 RDFs (top) and background fields (bottom) of the A β +Ftn phantom calculated using LBV [276] (left) and PDF [246] (middle), and the comparison (right).

In contrast, the results demonstrate a strong dependency of the SHARP technique [245] on its parameters, the kernel radius as well as the truncation level. As shown in the RDF profile (Fig. G1.3, Appendix G), a larger kernel size allows a more accurate estimation of the distant field [244], at the cost of the boundary erosion by the SMV filter (orange arrows in Fig. 7.13). Reducing the kernel size minimises the erosion effect, with the penalty of a less accurate susceptibility estimation. When the kernel size is set smaller than the resolution at 0.086 mm (isotropic), the SMV filter become an edge detection function and the local field is also falsely removed (radius = 0.05 mm in Fig. G1.3, Appendix G). In this work, the visually acceptable result is found at kernel radius = 0.2-0.5 mm (about 2 to 5 times the image resolution), but the output RDF is largely dependent on the chosen kernel size (Fig. G1.3, Appendix G).

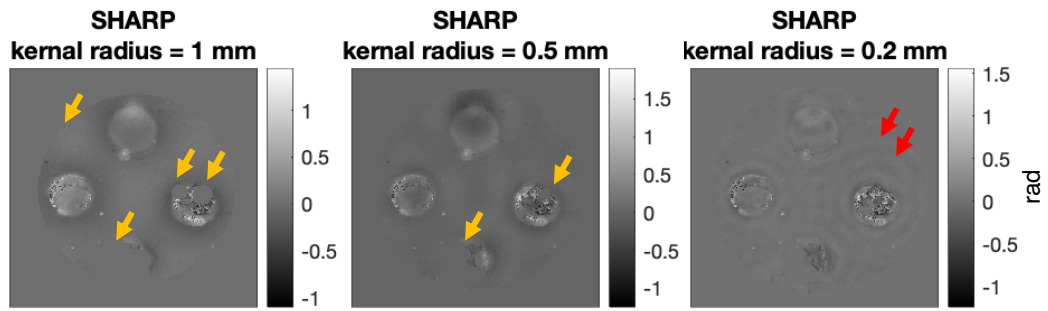


Fig. 7.13 RDFs of A β +Ftn phantom calculated by SHARP [245] with varying SMV filter radius. The k-space truncation value = 0.08 for all results.

Additionally, because the boundary condition has to be relaxed at the ROI boundary, the truncation in the k-space is necessary to solve the background field when using the SHARP technique, to exclude the low-frequency component [245]. The result, therefore, presents a dependency of the selected truncation values (Fig. 7.14), and generates the parameter (truncation level)-dependent artifact in the resulting RDFs due to the following k-space truncation (red arrows in Fig. 7.14).

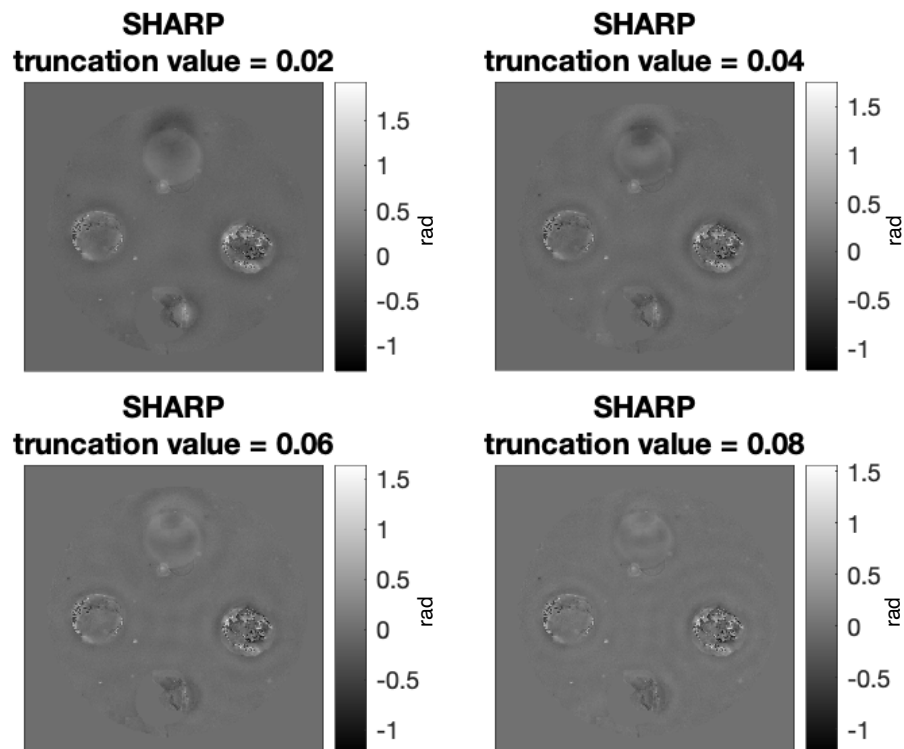


Fig. 7.14 RDFs of A β +Ftn phantom calculated by SHARP [245] with varying truncation value. The SMV filter radius = 0.2 mm.

Taken together, the result suggests that the LBV technique [276] is a robust approach to eliminate the background field and generate the RDF reliably and efficiently, compared with PDF [246], and SHARP [245]. Hence, the LBV method [276] is employed to produce the local field (Fig. 7.15) for the subsequent dipole inversion using nMEDI- L_1 [18].

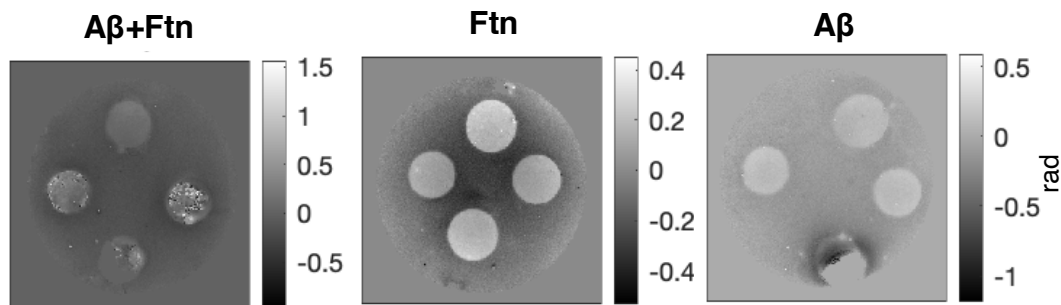


Fig. 7.15 RDFs of the phantoms generated using LBV [276].

7.3.1.3 Evaluation of automatic λ optimisation methods

The L-curve heuristic analysis [183, 305, 420], U-curve [305, 410], scaled U-curve analysis, and the elbow point search [423] are tested and compared in the study, to search for a reliable automatic optimisation approach of the λ selection (see Section 7.2.5.3.3.1) for the nMEDI- L_1 [18] dipole inversion. The result shows a great variation in the λ value suggested by different automatic optimisation methods, in $A\beta$ +Ftn (Fig. 7.16A), Ftn (Fig. 7.16B), and $A\beta$ (Fig. 7.16C) phantoms. Nevertheless, the elbow point search [423], and the U-curve analysis [305, 410] generated the consistent solution across phantoms, at 1.39×10^2 and 7.2 respectively.

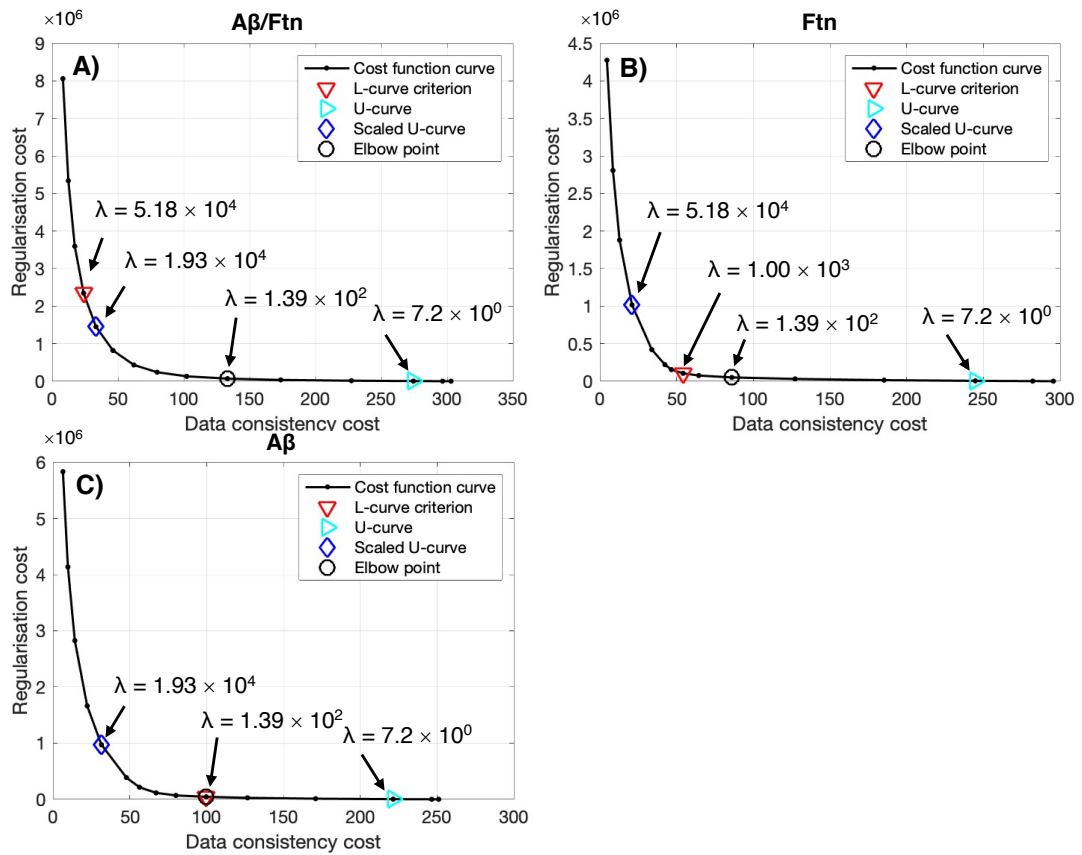


Fig. 7.16 λ values calculated using automatic optimisation methods for A β +Ftn (A), Ftn (B), and A β (C) phantoms.

The corresponding output susceptibility images of each phantom, generated using the λ value suggested by different automatic optimisation methods, are shown in Figure 7.17. The best solution (*i.e.*, the susceptibility map) of nMEDI-L₁ [18] dipole inversion is found when using the regularisation parameter λ optimised by the elbow point search [423], $\lambda = 1.39 \times 10^2$ (first column of Fig. 7.17). The selected λ appears to balance the regularisation cost and the data fidelity cost, generating the susceptibility images of the phantoms without over-smoothing or conspicuous streaking artifacts.

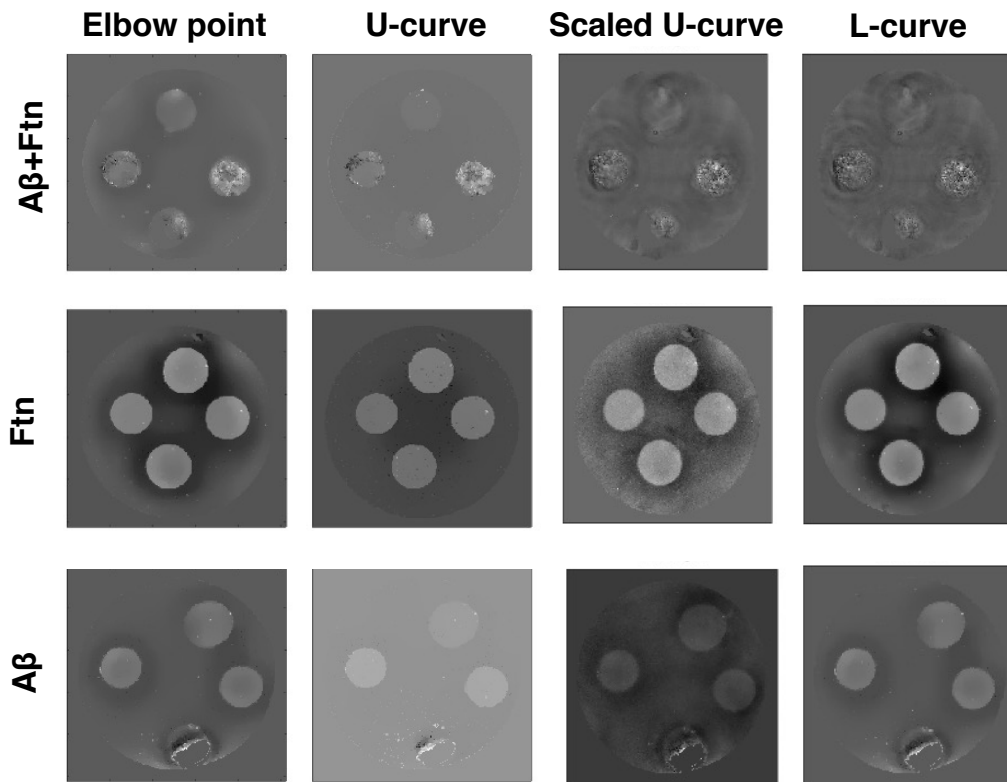


Fig. 7.17 Susceptibility images of each phantom generated with the λ optimised using different methods.

The analysis of each optimisation method suggests a rather distinctive parameter λ , compared with each other (Fig. 7.16, also see Appendix G2). The L-curve analysis [183, 305, 420] and the scale U-curve show the tendency of under-regularisation, while the U-curve method [305, 410] demonstrates a heavily over-regularised result (Fig. 7.17). Recently, similar observations were also reported in the 3.0 T human brain QSM, where neither the conventional L-curve heuristic analysis nor the U-curve analysis was able to generate reliable optimisation result [410]. As both methods rely on the calculation of the curvature of the cost function (Section 7.2.5.3.3.1), the (orders of) magnitude difference between the regularisation cost and the data fidelity cost greatly confounds these approaches, and the optimisation results are dominated by the larger cost, which, in this case, is the regularisation weight. Compared with the standard U-curve optimisation [305, 410], the rescaled U-curve approach retained the information of the data fidelity by minimising the magnitude difference between the two costs, but it is found insufficient in suppressing the streaking artifacts (Appendix G2). In contrast, the elbow (inflection) point search using the bisection

method [423] produces consistent optimisation results of λ for all phantoms, which is concordant with their similarity in the structure and the image SNR.

7.3.1.4 Relationship between the parameter λ and the measured susceptibility

The susceptibility standard deviation of the internal reference 'A β +Ftn 0' is measured at different λ values (Fig. 7.18A), to further examine the effect of the parameter λ on the image quality. As the homogeneous susceptibility is expected (Section 7.2.5.3.3.2) within the ROI (red circle in the inserted image in Fig. 7.18A), the standard deviation of the susceptibility reflects the trade-off between the data accuracy and the presence of the streaking artifacts. When the parameter λ is very small and the solution was over-regularised, the measured mean, median and standard deviation are all near-zero ($\lambda < 10^1$, Fig. 7.18B). As the magnitude of λ increased, the standard deviation measured within the ROI increases almost proportionally (Fig. 7.18A). However, as the λ continues to increase, the solution of the susceptibility becomes under-regularised and the streaking artifacts appear, demonstrated as the spread of the measurement towards negative susceptibility (*i.e.*, (mean-standard deviation) < 0, as $\lambda \geq 10^{2.6}$ in Fig. 7.18B). After the mean (median) susceptibility stops increasing ($\lambda \geq 10^{3.4}$, Fig. 7.18B), the continuously increasing standard deviation demonstrates the heavily over-regularised results, accompanied by prominent streaking artifacts.

This result also supports the elbow (inflection) point search with the bisection method [423] (black arrow in Fig. 7.18B), as the automatic optimisation method for selecting the parameter λ (Sections 7.2.5.3.3.1 and 7.3.1.3), which suggests an ideal trade-off between the data fidelity and the regularisation weight.

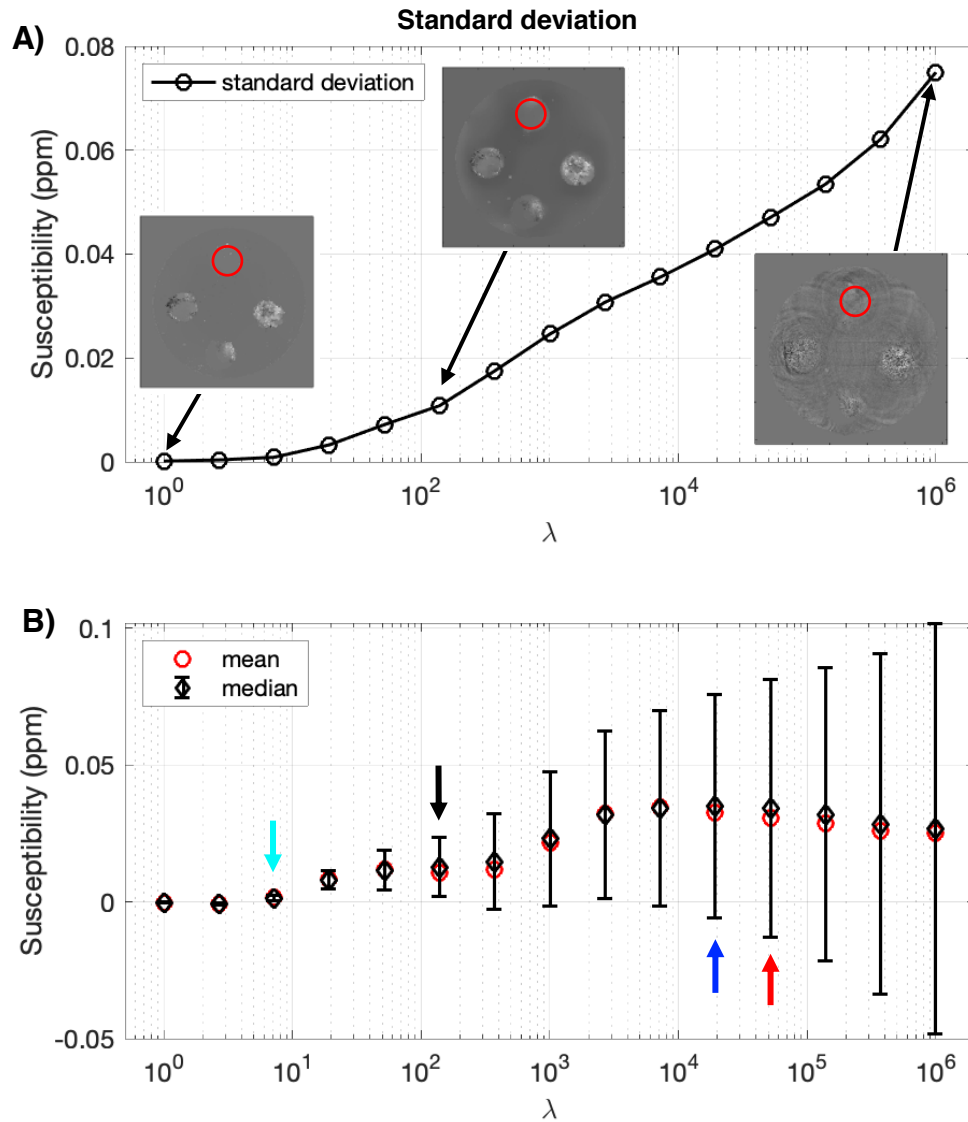


Fig. 7.18 Susceptibility measurements of 'A β +Ftn 0' sample with varying λ .

A: standard deviation of the susceptibility measured within the ROI (red circle); B: mean and median of the susceptibility. Error bar: standard deviation. Red arrows: L-curve criterion; blue arrows: scaled U-curve; black arrows: elbow point; cyan arrows: U-curve.

To further investigate the effect of the parameter λ on the numerical output of the reconstructed susceptibility maps, the average susceptibility of each sample is measured at the varying λ (Fig. 7.19).

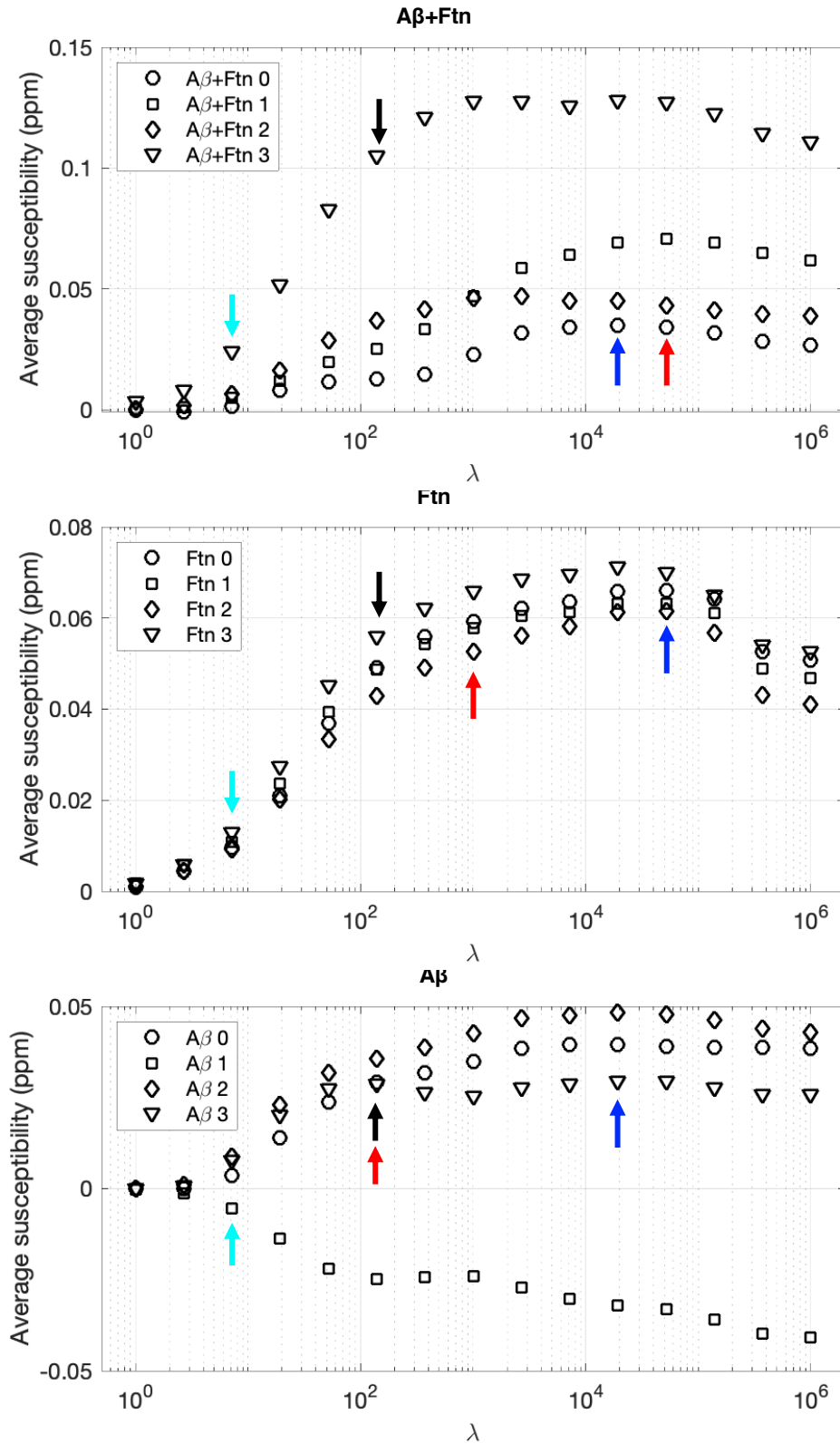


Fig. 7.19 Average susceptibility measured in the samples of A β +Ftn (top), Ftn (middle) and A β (bottom) phantoms with varying λ .

Arrows indicating the optimal λ calculated using different methods: L-curve criterion (red), scaled U-curve (blue), elbow point (black), and standard U-curve (cyan).

Similar to the observation of the internal reference (Fig. 7.19B), when the λ is large, the solution is under-regularised, and the magnitude of the susceptibility remains large and stable in all samples (Fig. 7.19, large λ) because the data fidelity is enforced [278]. As the λ decreases, the contrast of reconstructed susceptibility maps starts to become smoother, at the cost of data fidelity, until the λ becomes so small that the solution is over-regularised, resulting the underestimation of the susceptibility magnitude (Fig. 7.19, small λ). Therefore, the optimal λ is found at which the streaking artifacts are sufficiently suppressed, while the measured susceptibility remains accurate.

In the $A\beta$ +Ftn phantom, the average susceptibility of each sample increases with λ , and the susceptibility measured in each sample increasingly differs from each other as λ become larger (top image in Fig. 7.19). At the optimal λ that is determined by the elbow (inflection) point search (black arrow in Fig. 7.19), the largest susceptibility is found in 'A β +Ftn 3' sample, and the smallest in the internal reference 'A β +Ftn 0'. In the Ftn phantom, a similar trend of the increasing susceptibility with λ is also observed (middle image in Fig. 7.19). However, the λ -associated susceptibility difference between each sample is less significant, compared with the $A\beta$ +Ftn phantom. The sample 'Ftn 3' is found to have the largest average susceptibility at the optimal λ (elbow point method, black arrow in Fig. 7.19), within the Ftn phantom, and the smallest is found in 'Ftn 2'. Nevertheless, in the $A\beta$ phantom (bottom image in Fig. 7.19), similar susceptibility is found in samples 'A β 0', 'A β 2' and 'A β 3' at the optimal λ (elbow point method, black arrow in Fig. 7.19), but the measurement of sample 'A β 1' is driven towards negative susceptibility, due to the artifact caused by the adjacent air bubble trapped inside the phantom (see Fig. 7.10 in Section 7.3.1.1).

7.3.2 Quantitative R_2^* and susceptibility of the A β (1-42) and ferritin-bound iron

The measurements of the R_2^* and susceptibility values of each sample within the MR phantoms are summarised in Table 7.2. Although the ROI carefully excludes the sample boundaries and any trapped air bubbles, the measurements of the sample 'A β 1' is compromised, due to the signal drop-out (susceptibility) artifact caused by an adjacent median-size bubble as demonstrated earlier in Fig. 7.10 (Section 7.3.1.1).

This artifact mainly affects the accuracy of the susceptibility, as the QSM reconstruction is more sensitive to the phase shift caused by the nearby air bubble, compared with R_2^* . For the completeness of the study, the measured values of the sample 'A β 1' are still included here and in the following analysis.

Table 7.2 Summary of R_2^* and susceptibility measurements of phantoms

Sample (ROI)	R_2^* (s^{-1})			Susceptibility (ppm)		
	Median	Mean	Std	Median	Mean	Std
A β +Ftn 0 (KH buffer only)	18.52	18.84	6.55	0.01074	0.01272	0.01082
A β +Ftn 1	27.04	28.61	10.38	0.01079	0.02537	0.04049
A β +Ftn 2	39.64	42.49	24.33	0.03541	0.03668	0.03686
A β +Ftn 3	44.64	54.50	39.78	0.09564	0.10485	0.07060
Ftn 0 (KH buffer only)	15.28	15.42	4.49	0.04836	0.04908	0.00375
Ftn 1	15.57	15.70	4.37	0.04442	0.04878	0.00864
Ftn 2	19.09	19.26	4.76	0.04077	0.04285	0.00941
Ftn 3	23.65	23.99	5.75	0.05514	0.05585	0.00726
A β 0 (KH buffer only)	20.95	21.06	5.33	0.03002	0.02908	0.00640
A β 1 [†]	18.06	18.29	8.05	-0.01464	-0.02486	0.03477
A β 2	19.52	19.63	4.84	0.03368	0.03564	0.00669
A β 3	18.19	18.32	5.07	0.02935	0.02860	0.00562

[†] the susceptibility measurement of sample 'A β 1' was compromised, due to the adjacent susceptibility artifacts.

7.3.2.1 R_2^* distribution

The pixel-wise R_2^* values measured within each ROI from A β +Ftn, Ftn, and A β phantoms are shown in Figures 7.20-22, respectively. The data distribution of the ROI is demonstrated in the violin plot, and any outlier of the measurement is also presented. The distribution of the 8% w/v supporting agarose gel of the phantom (see Section 7.2.1) is also shown in each figure as a reference. The supporting gel

shows a faster transverse relaxation rate R_2^* , compared with the inserted KH-buffer-only reference ('A β +Ftn 0', 'Ftn 0' and 'A β 0', see Section 7.2.1 for details), mainly caused by the restricted proton movement and possibly the MT effect [425] due to the repeatedly applied RF pulses. In the 8% supporting gel, the MR signal from the macromolecule pool (hydrogen bonds formed in the agarose gel) is much attenuated [426, 427], unintentionally by the intensive RF pulses chain, compared with the 2% agarose gel.

Consisting of the aggregated A β and ferritin (see Section 7.2.1), the A β +Ftn phantom shows evidently increased R_2^* with the increasing A β +Ftn concentration (Fig. 7.20, also see Table 7.1 in Section 7.2.1). Moreover, the distribution of the pixelwise R_2^* gradually shifts towards large R_2^* as the aggregated A β +Ftn concentration increases, demonstrated by the increasing number of the high- R_2^* component and outliers in samples 'A β +Ftn 1', 'A β +Ftn 2' and 'A β +Ftn 3'. In particular, the data distributions of samples 'A β +Ftn 2' and 'A β +Ftn 3' are skewed from a normal distribution, and the mean R_2^* of 'A β +Ftn 3' significantly deviates from its median (inserted image in Fig. 7.20). Although all distributions are found to be unimodal, the skewed distributions observed in the samples suggests multiple R_2^* components, possibly caused by the varying forms and clusters of the peptide aggregate [89, 388]. Nevertheless, these measurements are consistent with the *ex vivo* quantitative R_2^* measured in the human brain tissue, at 9.4 T [428].

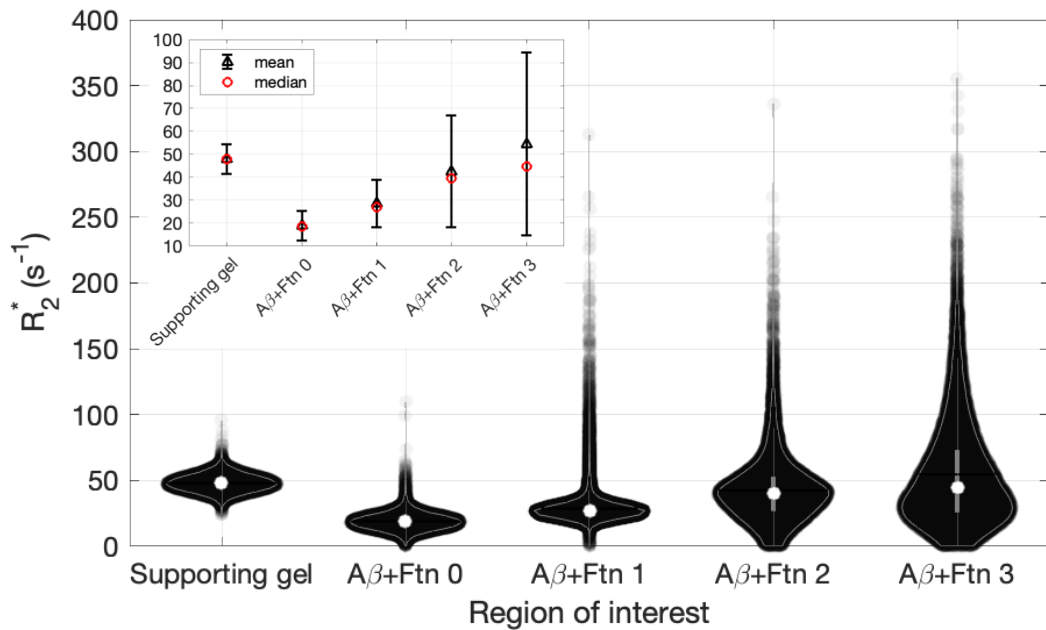


Fig. 7.20 The distribution of R_2^* measured within the ROIs of A β +Ftn phantom.

Insert: the mean, median R_2^* of the ROIs; error bar: standard deviation. The ferritin concentration was 0, 0.1, 0.3, 0.6 mg/mL for 'A β +Ftn 0', 'A β +Ftn 1', 'A β +Ftn 2', 'A β +Ftn 3'.

In contrast, the pixel-wise R_2^* values of samples in the Ftn phantom are found normally distributed (Fig. 7.21), in which the ferritin-bound iron presented in a uniformly dispersed form (see Section 7.2.1). Compared with the KH-buffer-only sample 'Ftn 0', a few high- R_2^* pixels within the samples 'Ftn 2' and 'Ftn 3' are observed, possibly caused by the ferritin clusters as the ferritin concentration increased [171, 285, 366]. Nevertheless, all three ferritin samples ('Ftn 1', 'Ftn 2', and 'Ftn 3') show normal distributions similar to the KH-buffer-only reference ('Ftn 0'), with the concordant mean and median values in each ROI (inserted image in Fig. 7.21), suggesting the ferritin is overall well dispersed during the gel sample preparation.

The observed R_2^* of each sample increases with their ferritin concentration (Fig. 7.21, also summarised in Table 7.1 in Section 7.2.1), in a more moderate manner, compared with the A β +Ftn phantom. Additionally, the result shows an almost indistinct R_2^* difference between the reference sample 'Ftn 0' (contained KH buffer only) and the sample 'Ftn 1' (ferritin concentration of 0.1 mg/mL), suggesting the

measurement is approaching the lower detection limit for the ferritin-bound iron in 'Ftn 1'. House *et al.* [50] reported a lower detection threshold of iron concentration at 55 $\mu\text{g/g}$ wet tissue, using R_2 at 4.7 T, however, this number cannot be compared directly with this PhD project directly, because of the different experiment conditions (*e.g.*, samples, temperature, magnetic field) and quantitative MRI methods (*e.g.*, MR acquisition for R_2 or R_2^* , iron measured in absolute concentration or relative concentration with regard to ferritin). Nevertheless, the ferritin concentration in the sample 'Ftn' (0.1 mg/mL) is found at the lower bound of the human GM reported by Connor *et al.* [411], but one to two magnitude higher than what is found in the WM [7, 13, 43, 411]. In human brain MRI, the GM/WM contrast in T_2 (T_2^*) was found dominated by the (largely, ferritin-bound) iron concentration in healthy brains under clinical field strength (3.0 T and below) [48, 429], and higher magnetic fields [54, 56, 57], and the *in vitro* result presented in this PhD project is agreed with those previous observations.

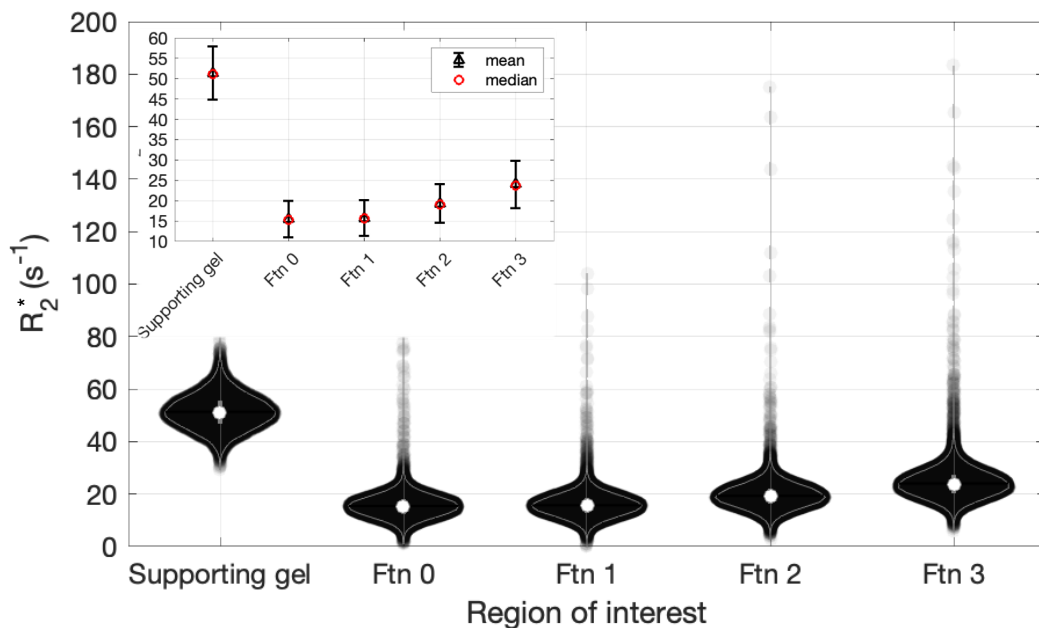


Fig. 7.21 The distribution of R_2^* measured within the ROIs of Ftn phantom.

Insert: the mean, median R_2^* of the ROIs; error bar: standard deviation. The ferritin concentration was 0, 0.1, 0.3, 0.6 mg/mL for 'Ftn 0', 'Ftn 1', 'Ftn 2', 'Ftn 3'.

The normal distributions are also found in the pixel-wise R_2^* in $A\beta$ phantom (Fig. 7.22), and similar mean and median values are measured in samples 'A β 0', 'A β 1', 'A β 2',

and 'A β 3' (inserted image in Fig. 7.22). Except for the sample 'A β 1', whose data spread wider due to the susceptibility artifact caused by the adjacent air bubble (see Section 7.3.1.1 and Fig. 7.10), the distribution of the A β samples ('A β 1', 'A β 2', and 'A β 3') is virtually identical to the reference sample 'A β 0' (contained KH buffer only). In another word, the R_2^* measurement is significantly affected by the A β concentration (Fig. 7.22, also summarised in Table 7.1 in Section 7.2.1).

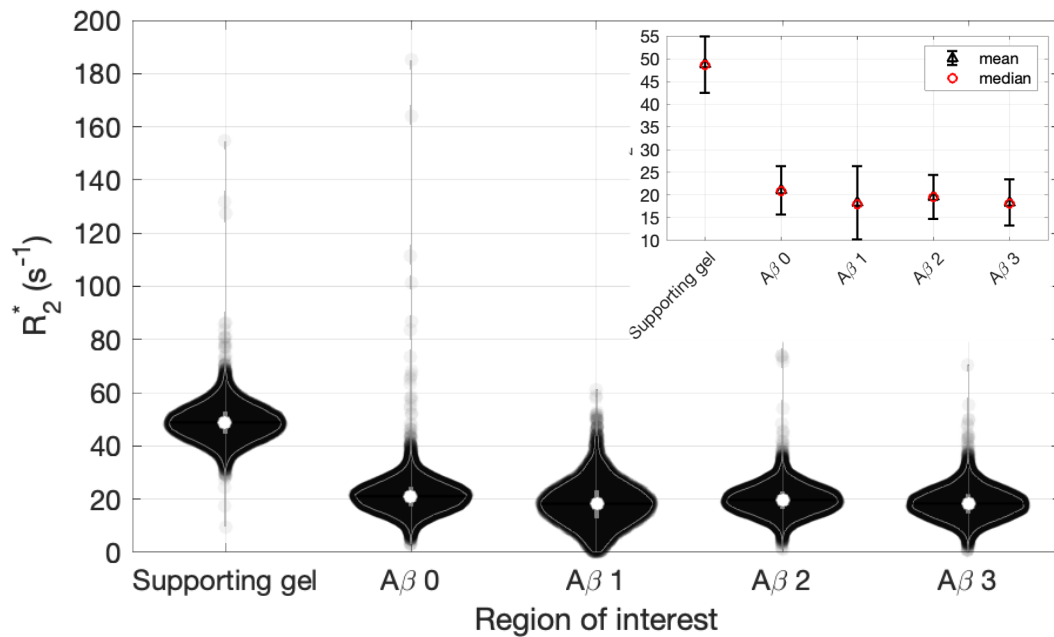


Fig. 7.22 The distribution of R_2^* measured within the ROIs of A β phantom.

Insert: the mean, median R_2^* of the ROIs; error bar: standard deviation. The A β (1-42) concentration was 0, 0.0275, 0.0825, 0.165 mg/mL for 'A β 0', 'A β 1', 'A β 2', 'A β 3'. A wider spread of R_2^* in 'A β 1' was caused by the adjacent susceptibility artifacts.

7.3.2.2 Susceptibility distribution

Compared with the distribution of the R_2^* , the measured susceptibility of the samples displays a pronounced deviation from the normal distribution (Fig. 7.23-25). Multimodal distributions with outliers are observed in the samples, including the A β +Ftn (Fig. 7.23) and Ftn (Fig. 7.24) phantoms, suggesting varied sources of the apparent susceptibility. Inherent in the employed QSM technique, the dipole inversion [18] generated the susceptibility solution from the local field perturbation (*i.e.*, the RDF), which is relative for each acquisition. It is because the inversion step could produce an arbitrary global offset to the solution (susceptibility), as it would not affect the

local field shift numerically in the (source-to-field) forward problem (see Eq.(2.23-24) in Section 2.3.2.1, and Section 3.2). In this PhD project, the scan-to-scan variation is also demonstrated, by the different susceptibility values between the identical reference samples within each phantom ('A β +Ftn 0' in Fig.7.23, 'Ftn 0' in Fig.7.24, and 'A β 0' in Fig.7.25, also see Table 7.1 in Section 7.2.1). The scan-to-scan variation also contributes to the susceptibility variation of the 8 % supporting agarose gel across phantoms ('Supporting gel' in Fig. 7.23-25).

As shown in Figure 7.23, highly homogeneous susceptibility is observed in samples 'Supporting gel' and 'A β +Ftn 0', while the data distribution greatly are skewed towards the high-susceptibility in the A β and ferritin aggregate samples ('A β +Ftn 1', 'A β +Ftn 2', and 'A β +Ftn 3' in Fig. 7.23). As the susceptibility increases with the concentration of the A β and ferritin aggregate (inserted image in Fig. 7.23), multi-modality is also observed in these aggregate samples. A low-susceptibility mode around 7 ppb and varied high-susceptibility modes are found. The low-susceptibility values correspond to the measurement of the KH buffer reference ('A β +Ftn 0' in Fig. 7.23), possibly are contributed by the pixels where the aggregated peptide is not present, due to the highly inhomogeneous distribution of the A β and ferritin aggregate (see Fig. 7.1B in Section 7.2.1, and 'A β +Ftn' in Fig. 7.17 in Section 7.3.1.3). The high-susceptibility pixels are mainly present as outliers when the aggregate concentration is low ('A β +Ftn 1' in Fig. 7.23), but gradually become dominant within the data distribution as the aggregate concentration increased ('A β +Ftn 2' and 'A β +Ftn 3' in Fig. 7.23). This change in the shape of the data distributions also supports that the heterogeneous susceptibility sources co-exist in the samples of the A β and ferritin aggregate, however, other analytical techniques, such as XRF [53, 78], transmission electron microscopy (TEM) [89], and histology [215] would be required to investigate the exact contributors of the observed bulk susceptibility.

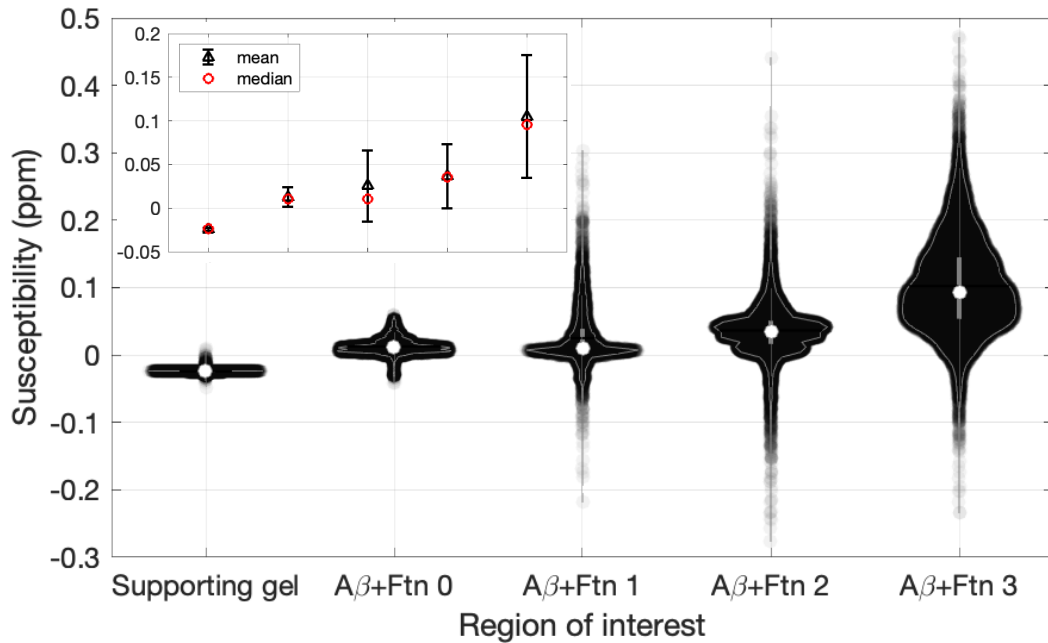


Fig. 7.23 The distribution of susceptibility measured within the ROIs of A β +Ftn phantom. Insert: the mean, median susceptibility of the ROIs; error bar: standard deviation. The ferritin concentration was 0, 0.1, 0.3, 0.6 mg/mL for 'A β +Ftn 0', 'A β +Ftn 1', 'A β +Ftn 2', 'A β +Ftn 3'.

Compared with the A β +Ftn phantom, the susceptibility measured within the Ftn phantom shows much smaller within- and between-samples variations (Fig. 7.24). The homogeneous susceptibility is observed within all samples, generated by the uniformly dispersed ferritin and/or KH buffer in the agarose gel. At the same time, as the ferritin concentration increases, however, significant changes of the susceptibility are not observed (inserted image in Fig. 7.24) among samples 'Ftn 0' (KH buffer, 0 mg/mL ferritin), 'Ftn 1' (0.1 mg/mL ferritin), 'Ftn 2' (0.3 mg/mL ferritin), and 'Ftn 3' (0.6 mg/mL ferritin).

At 3.0 T, Zheng *et al.* [53] measured the susceptibility of the horse spleen ferritin (F4503, Sigma-Aldrich) gelatin samples, using a least-squares forward fitting QSM, and reported a larger susceptibility difference (50-100 ppb) between the comparable samples with varying (ferritin-bound) iron concentrations. Although the ferritin concentration was not specified in the report, the estimated concentrations of their three samples should be \sim 0.7, 0.36, 0.18 mg ferritin/mL according to the reported

serial dilution protocol for their samples 4-6 [53], and therefore should be comparable to the samples 'Ftn 3', 'Ftn 2' and 'Ftn 1' in the current study. Compared with the measurement at the room temperature and 3.0 T field strength [53], a lower temperature (4 °C) is applied in this PhD project, and so a stronger microscopic susceptibility of (super)paramagnetic materials (ferritin) is expected according to Curie's Law (see Section 2.3.1, and references [170, 219, 241]). Nevertheless, the discrepancy is probably caused by the (iron) loading factor (LF) of the ferritin samples used in this study, which might be lower and possess smaller overall susceptibility [167, 430], compared with the previous report [53]. Moreover, higher resolution is employed in this study (0.086 mm), compared with the conventional clinical MRI (~1 mm, including reference [53]), and therefore generated several orders of magnitude difference in the voxel size ($6.36 \times 10^{-4} \text{ mm}^3$ vs. 1 mm^3). As QSM MRI measures the bulk susceptibility generated by each entire voxel, it may be sensitive to the voxel size, demonstrating smaller apparent susceptibility magnitude as the voxel size (volume) decreased, because less macroscopic inhomogeneity is sampled [228, 239, 344, 431-433].

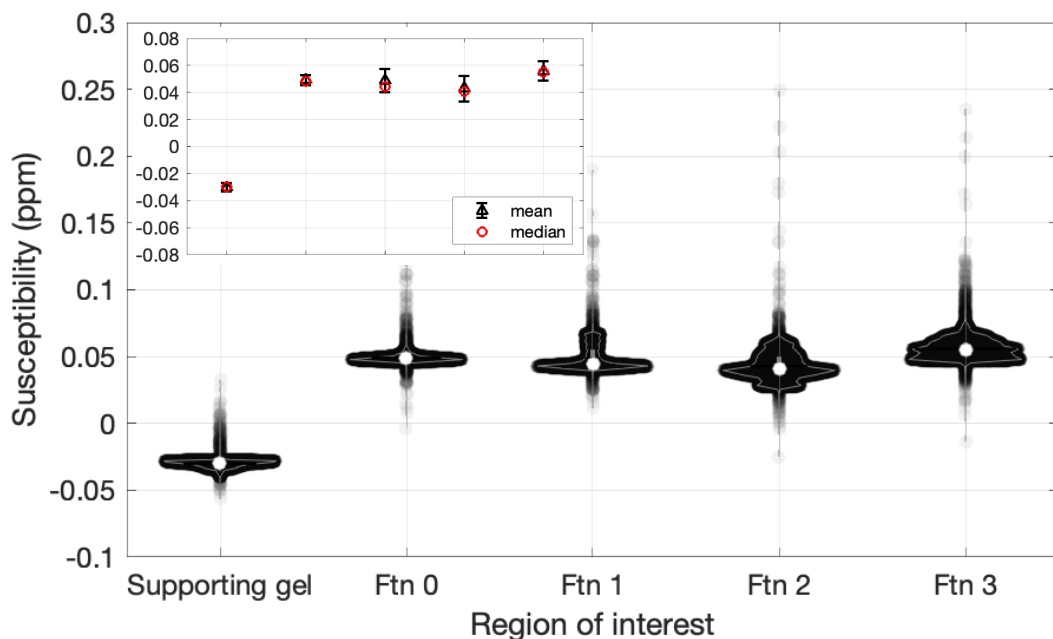


Fig. 7.24 The distribution of susceptibility measured within the ROIs of Ftn phantom. Insert: the mean, median susceptibility of the ROIs; error bar: standard deviation. The ferritin concentration was 0, 0.1, 0.3, 0.6 mg/mL for 'Ftn 0', 'Ftn 1', 'Ftn 2', 'Ftn 3'.

Similar to the Ftn phantom, homogeneous susceptibility is also observed within the samples of A β phantom ('A β 0', 'A β 2', and 'A β 3' in Fig. 7.25), demonstrated as the very narrow spread of the pixel-wise measurement. However, the measurement in the 'A β 1' sample is confounded by the strong susceptibility artifact (see Fig. 7.10 in Section 7.3.1.1, and Table 7.2 and Section 7.3.2), generating a negative susceptibility shift and a great spread of data ('A β 1' in Fig. 7.25). At the same time, in the A β phantom, no significant changes of the mean or median susceptibility are observed with the A β concentration (inserted image in Fig. 7.25, except for 'A β 1'). With the absence of the ferritin-bound iron, the A β peptide itself does not show a strong paramagnetic susceptibility effect in the study.

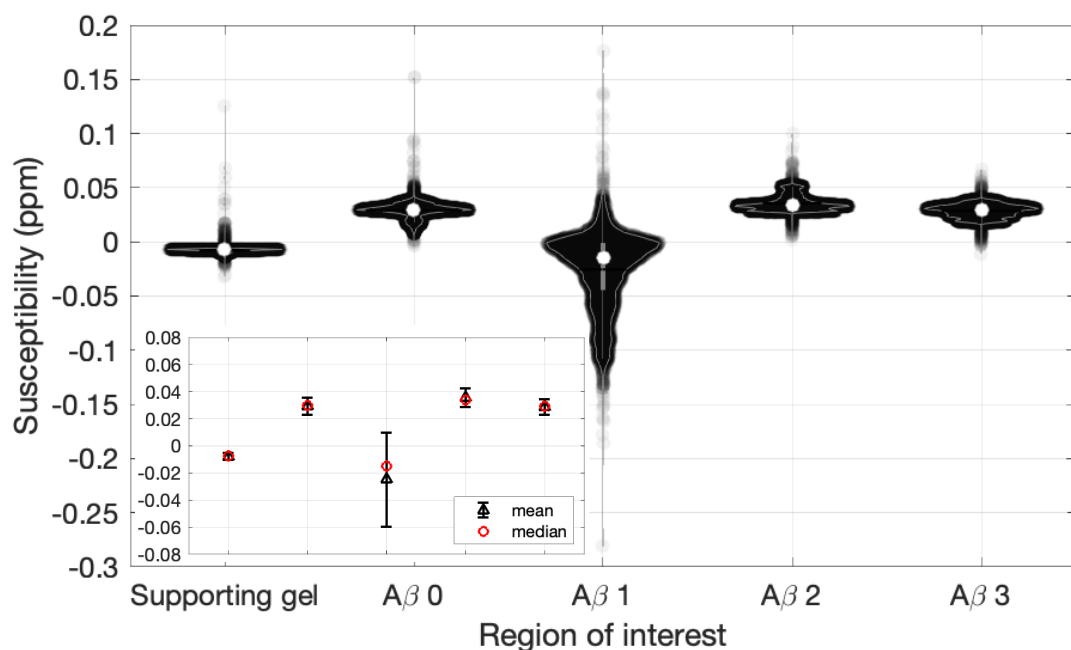


Fig. 7.25 The distribution of susceptibility measured within the ROIs of A β phantom.

Insert: the mean, median susceptibility of the ROIs; error bar: standard deviation. The A β (1-42) concentration was 0, 0.0275, 0.0825, 0.165 mg/mL for 'A β 0', 'A β 1', 'A β 2', 'A β 3'. A negative shift and wider spread of data in 'A β 1' was caused by the adjacent susceptibility artifacts.

7.3.3 Relationship between pixel-wise R_2^* and susceptibility in different phantoms

Figure 7.26 shows the comparison of the fitted distributions of the pixel-wise susceptibility and R_2^* measured in each sample of different phantoms. The main difference is found between the data distributions in A β +Ftn phantom (Fig. 7.26a, d)

and other phantoms (Fig. 7.26b, f and Fig. 7.26c, g). In the A β +Ftn phantom, both R_2^* (Fig.7.26a) and susceptibility (Fig.7.26d) distributions experienced a right shift, but the susceptibility shows a more significant data spreading, as the concentration increases (low-to-high for 'A β +Ftn 0', 'A β +Ftn 1', 'A β +Ftn 2', 'A β +Ftn 3'). In the Ftn phantom, the right shift with the increased concentration (low-to-high for 'Ftn 0', 'Ftn 1', 'Ftn 2', 'Ftn 3') is only observed in the R_2^* distribution (Fig.7.26b), with moderate spreading, but not in the susceptibility distribution (Fig.7.26e). In the A β phantom, the distributions of both R_2^* (Fig.7.26c) and susceptibility (Fig.7.26f) of samples are highly overlapped (except for 'A β 1').

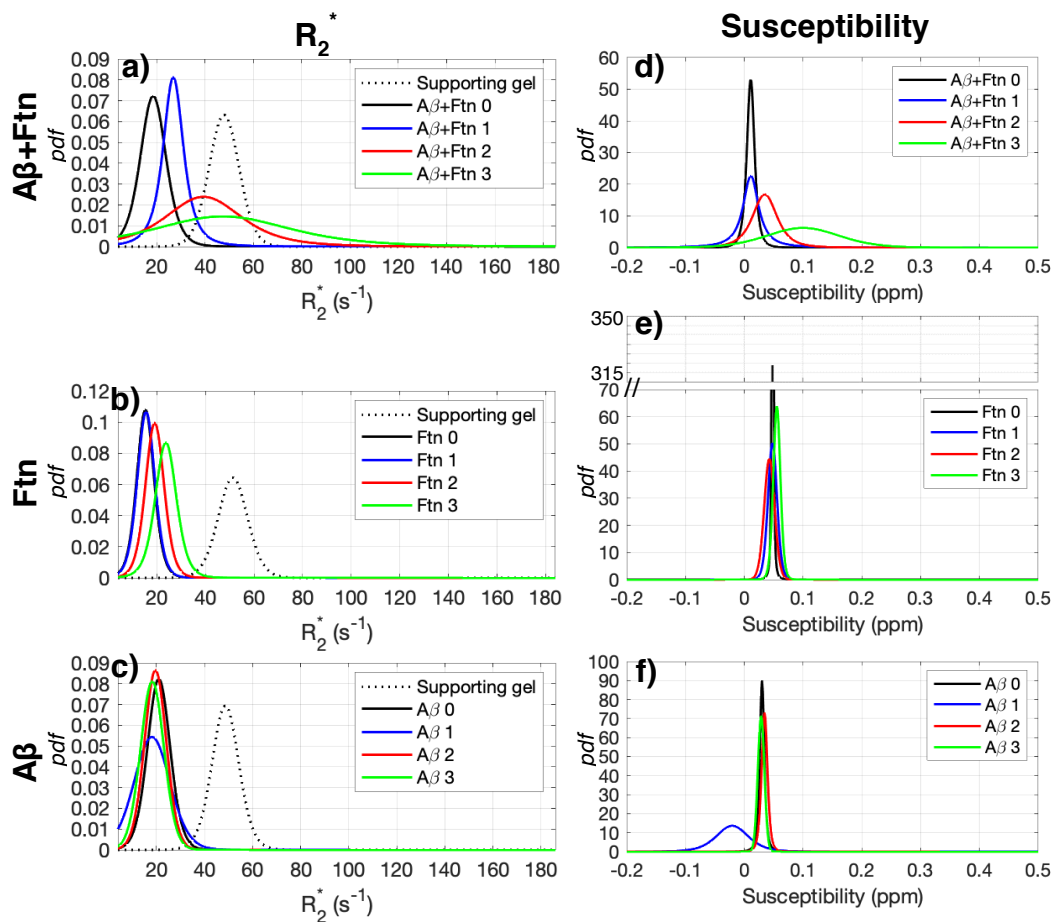


Fig. 7.26 Distributions of R_2^* (left) and susceptibility (right) of samples in each phantom.

The pixel value was fitted to a t-location-scale distribution. The data of 'A β 1' was compromised by the adjacent susceptibility artifacts.

The linear regression analyses between the pixel-wise R_2^* and susceptibility reveal a weak trend ($R^2 = 0.0933$) of positive (slope $k > 0$) correlation, in the A β +Ftn phantom (Fig. 7.27). The weak correlation is possibly caused by the great dispersion of data,

which is observed in the samples with A β and ferritin aggregate (Fig. 7.27B, C), especially within the sample 'A β +Ftn 3' (green data points in Fig. 7.27B, C). This data dispersion, particularly the susceptibility, increases with the concentration of the co-aggregate A β +ferritin (Fig. 7.27C), suggesting the heterogeneous local field inhomogeneity generated by the A β and ferritin aggregate. The positive correlation between the pixel-wise R_2^* and susceptibility, suggests that the observed $T_2(T_2^*)$ -shortening effect is dominantly contributed by the paramagnetic source in the A β +Ftn samples. Although several diamagnetic materials are also presented in the aggregate gel assembly, including water, agarose gel, Ca $^{2+}$ and Mg $^{2+}$ ions in the KH buffer, their effect to the measured susceptibility is negligible due to the concentrations (*e.g.*, $c(\text{Ca}^{2+}) = 1.4 \text{ mM}$, $c(\text{Mg}^{2+}) = 1.2 \text{ mM}$) and molar susceptibility ($\chi_{\text{Ca}^{2+}} = -54.7 \times 10^{-6} \text{ cm}^3/\text{mol}$, $\chi_{\text{Mg}^{2+}} = -47.4 \times 10^{-6} \text{ cm}^3/\text{mol}$), and can be excluded by comparing to the KH-buffer reference sample 'A β +Ftn 0'.

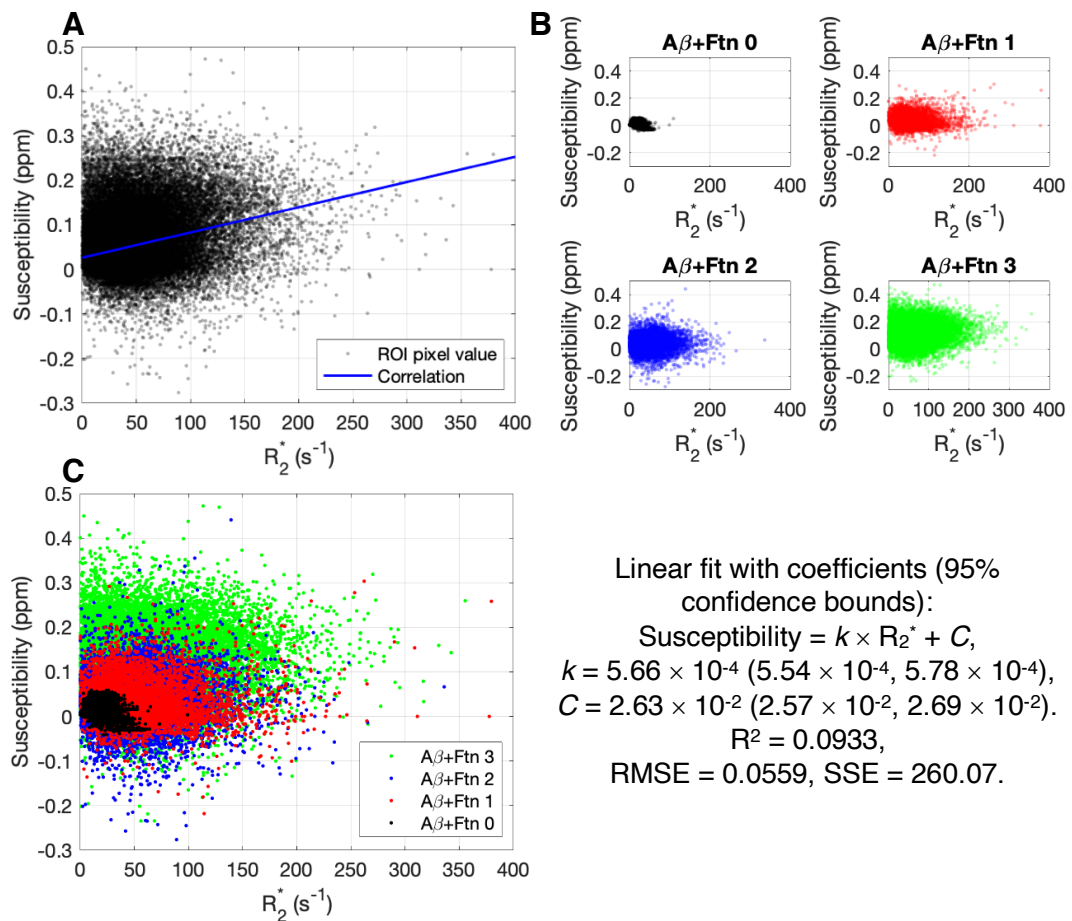


Fig. 7.27 Correlation between pixel-wise R_2^* and susceptibility (A), with the corresponding distribution of each sample (B, C) within A β +Ftn phantom.

Similarly, a positive (slope $k > 0$) correlation is also found between the pixel-wise susceptibility and R_2^* within the Ftn phantom (Fig. 7.28), which might indicate the $T_2(T_2^*)$ -shortening effect induced by the (super)paramagnetic ferritin-bound iron. Compared with the $A\beta$ +Ftn phantom, the data are less scattered in the Ftn phantom, demonstrating a more consistent correlation between the susceptibility and the transverse relaxation among pixels in each sample (Fig. 7.28B). This result suggests that the effect generated by the source materials is microscopic and mesoscopic [228]. At the same time, the data distributions of the sample are overlapped, especially for 'Ftn 0' and 'Ftn 1' (black and red data points in Fig. 7.28C, respectively), indicating the susceptibility-related effect, presumably generated by the ferritin-bound iron, is relatively weak. Nevertheless, pixels with higher susceptibility and R_2^* are observed in 'Ftn 3' (green data points in Fig. 7.28C) when compared with other samples, possibly because of the higher ferritin-bound iron level.

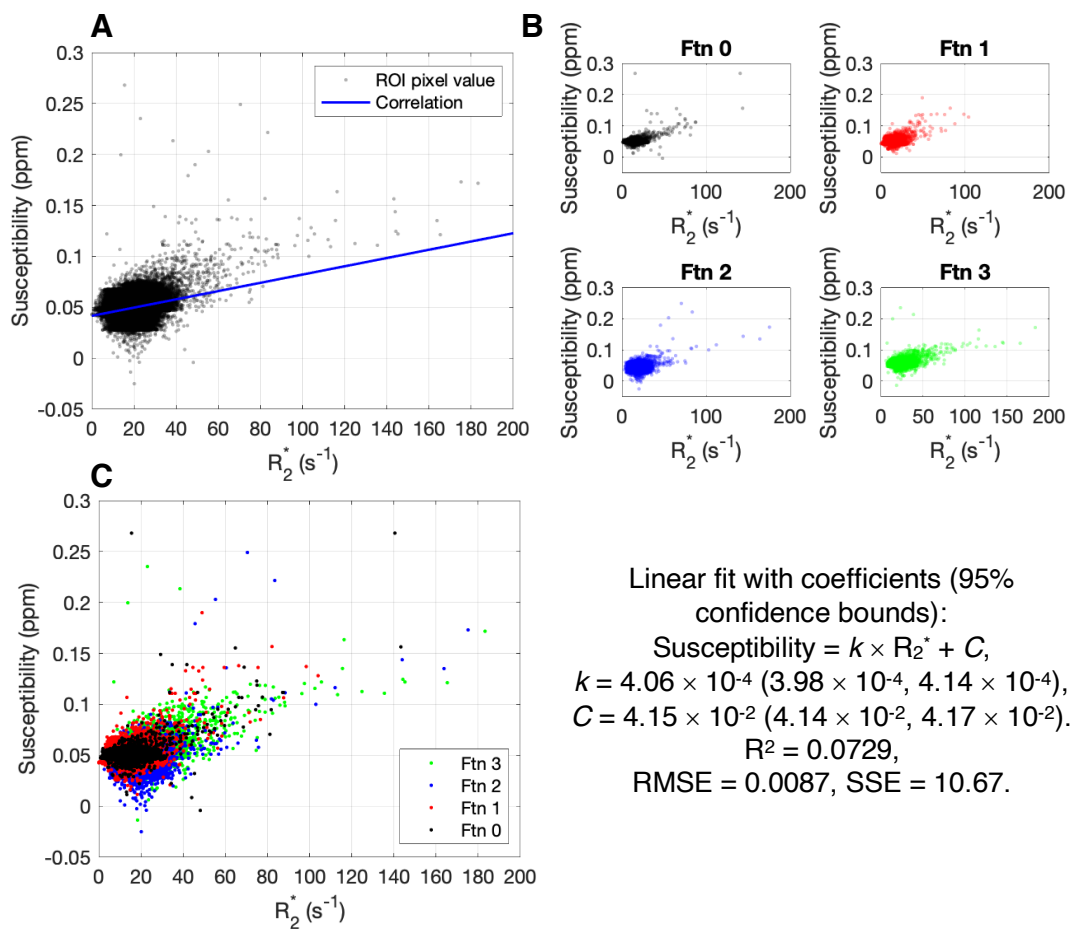


Fig. 7.28 Correlation between pixel-wise R_2^* and susceptibility (A), with the corresponding distribution of each sample (B, C) within Ftn phantom.

In contrast, the linear regression analysis shows a negative (slope $k < 0$) correlation between the pixel-wise R_2^* and susceptibility measured within the A β phantom (Fig. 7.29). The result suggests a weaker linear relationship ($R^2 = 0.0043$) between the R_2^* and susceptibility in this phantom, compared with the A β +Ftn and Ftn phantoms. In the absence of ferritin-bound iron, neither susceptibility-related nor $T_2(T_2^*)$ -shortening effect is observed, therefore generating highly-overlapped data distributions among the A β samples (Fig. 7.29C).

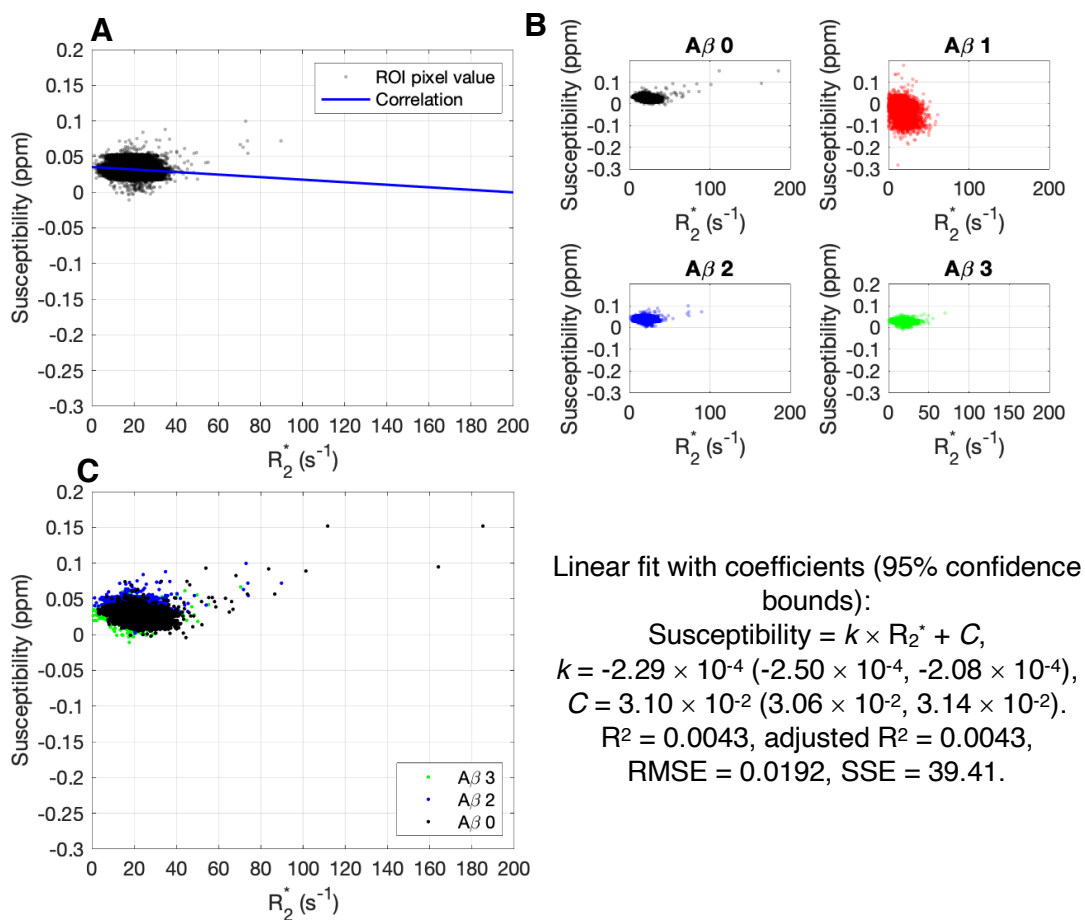


Fig. 7.29 Correlation between pixel-wise R_2^* and susceptibility (A), with the corresponding distribution of each sample (B, C) within A β phantom.

Data from ROI A β 1 was excluded from fitting.

7.3.4 Correlation of R_2^* with the ferritin-bound iron level

The result of the linear regression analysis between the ferritin and A β concentrations of the samples, and the transverse relaxation rate R_2^* mean and median values measured within each phantom, is shown in Figure 7.30, and summarised in Table. F1 in Appendix F. In the A β +Ftn phantom (Fig. 7.30A), a strong

(adjusted $R^2 = 0.949$) positive linear correlation is found between the mean R_2^* and the ferritin concentration. A weaker ($R^2 = 0.842$) linear correlation with the ferritin concentration is observed for the median R_2^* of the samples within the A β +Ftn phantom, suggesting the correlation for the representative data (median R_2^*) is compromised by the high- R_2^* outliers within the distribution (see Fig. 7.20A in Section 7.3.2.1). In the Ftn phantom (Fig. 7.30B), a strong linear correlation with the ferritin concentration are found, for the mean and median R_2^* of the samples (adjusted $R^2 = 0.976$ and 0.977 , respectively). In contrast, the result does not show a linear correlation (adjusted $R^2 < 0.03$) between the A β concentration and the observed R_2^* in the A β samples (Fig. 7.30C).

Moreover, when comparing the A β +Ftn and Ftn phantoms, different correlations between the ferritin concentration and the median R_2^* are found (Fig. 7.30D), where a larger slope (ferritin-dependent) coefficient k is observed in the A β +Ftn phantom ($42.48 \text{ s}^{-1}/\text{mg}\cdot\text{mL}^{-1}$ vs. $14.65 \text{ s}^{-1}/\text{mg}\cdot\text{mL}^{-1}$). This result suggests a higher ferritin sensitivity of R_2^* to the aggregated A β +ferritin content (*i.e.*, A β +Ftn samples), than to the dispersed ferritin (*i.e.*, Ftn samples). A small difference of the intercept coefficient is also observed between the correlations (21.84 s^{-1} vs. 14.73 s^{-1} for aggregated vs. dispersed ferritin), which might be caused by the imperfect shimming, or fitting errors due to the limited data points used for the regression analysis.

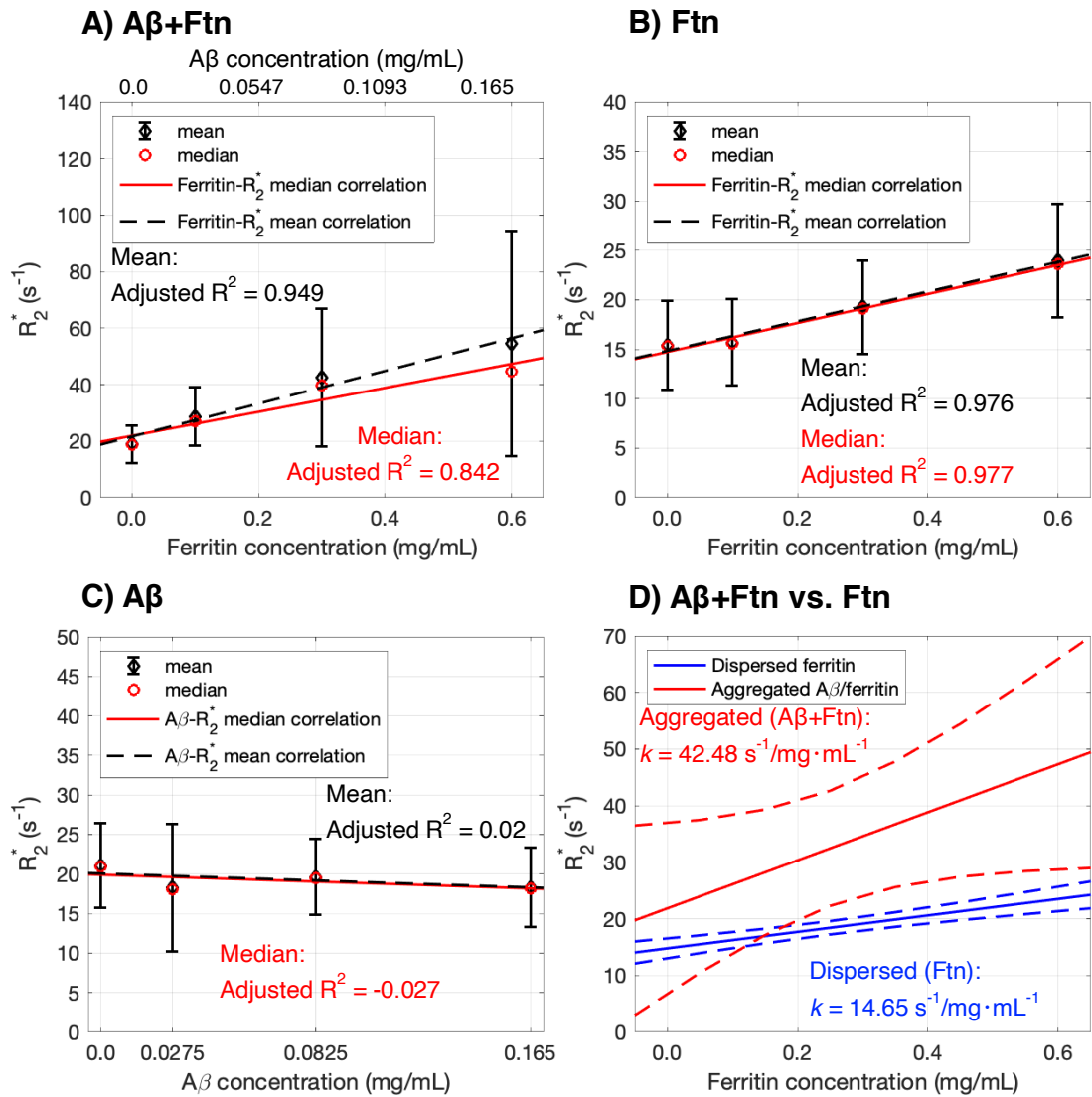


Fig. 7.30 Linear regression analysis of the ferritin (A β) concentration with R_2^* measured in A β +Ftn (A), Ftn (B), and A β (C) phantoms, and the comparison of the correlations (D).

D: the correlations of the ferritin concentration with the median R_2^* observed in A β +Ftn and in Ftn phantoms were compared, the dashed line showed the 95% prediction interval of the correlation.

7.3.5 Correlation of the susceptibility with the ferritin-bound iron level

The regression analysis shows a strong (adjusted $R^2 = 0.921$) positive linear correlation between the ferritin (A β) concentration and the susceptibility observed in the A β +Ftn phantom (Fig. 7.31A), but not in the Ftn (Fig. 7.31B) or A β (Fig. 7.31C) phantoms (adjusted $R^2 < 0$). The linear regression analysis result is summarised in Appendix H.

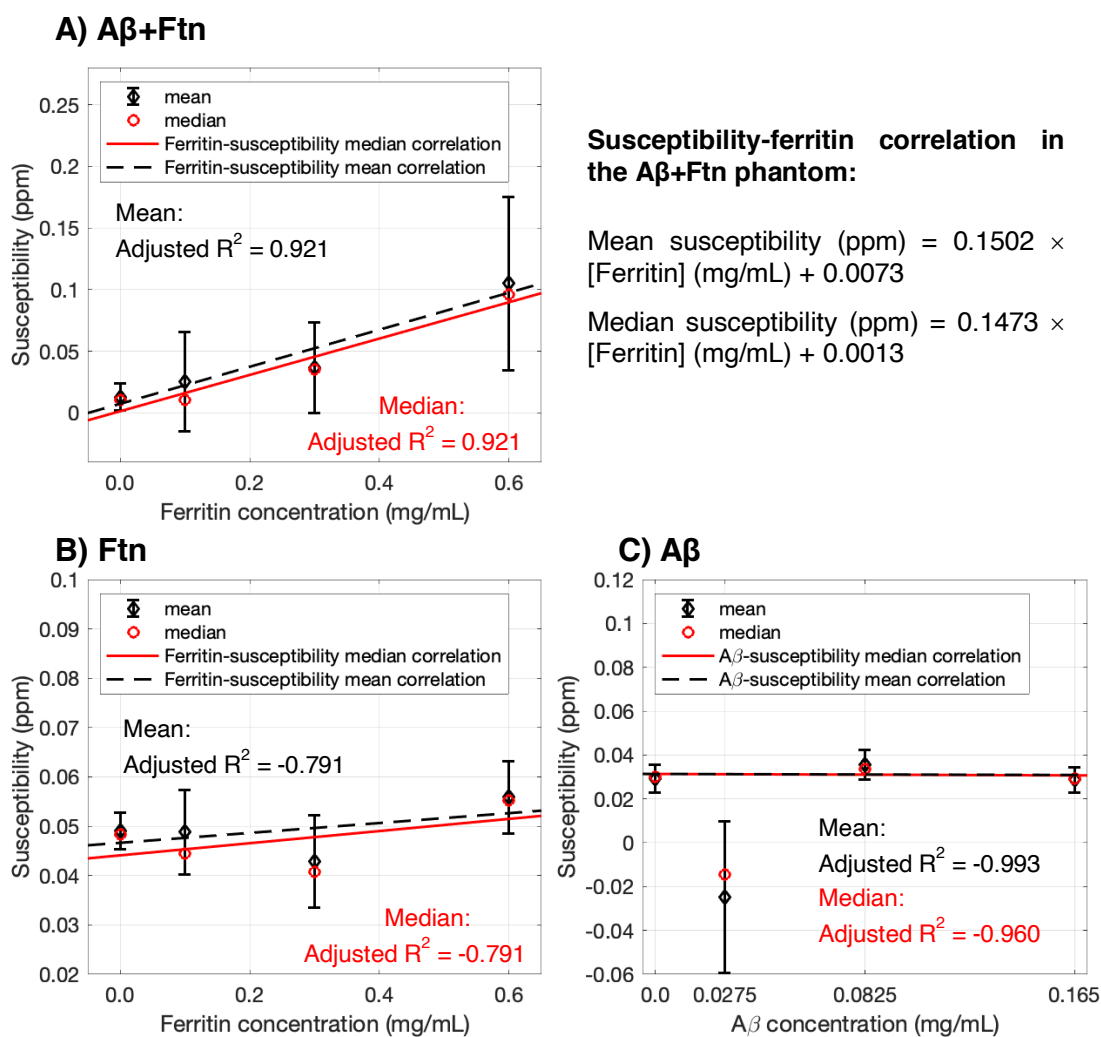


Fig. 7.31 Linear regression analysis of the ferritin (A β) concentration with the susceptibility measured in A β +Ftn (A), Ftn (B), and A β (C) phantoms.

In the A β +Ftn phantom (Fig. 7.31A), the slope (ferritin concentration-dependent) coefficient is found to be $150.2 \text{ ppb/mg}\cdot\text{mL}^{-1}$ for the mean susceptibility, and $147.3 \text{ ppb/mg}\cdot\text{mL}^{-1}$ for the median susceptibility, respectively. In the Ftn phantom (Fig. 7.31B), the linear fit generates the slope coefficient of $12.3 \text{ ppb/mg}\cdot\text{mL}^{-1}$ and $10 \text{ ppb/mg}\cdot\text{mL}^{-1}$ for the median and mean susceptibility. For the A β samples (Fig. 7.31C), these coefficients are found to be $-4 \text{ ppb/mg}\cdot\text{mL}^{-1}$ and $2.9 \text{ ppb/mg}\cdot\text{mL}^{-1}$ for the median and mean susceptibility, respectively.

7.4 Discussion

7.4.1 QSM of A β (1-42) and ferritin-bound iron with 9.4 T small-animal MRI system

Tested and assessed on phantoms, a QSM method optimised for the high-resolution imaging of the A β (1-42) and ferritin-bound iron *in vitro*, with a 9.4 T small-animal MRI system, is presented in this work. The multi-echo 3D GRE pulse sequence is employed to acquire the MR data, with the small voxel volume ($6.36 \times 10^{-4} \text{ mm}^3$, isotropic spatial resolution) to obtain imaging information about the A β aggregate [214, 215, 218] and ferritin-bound iron. A non-linear QSM framework [298] is implemented for the UHF preclinical MRI system, where the frequency map is estimated from the MR phase data using the non-linear least-squares fitting [298] and the Laplacian method [300], followed by the LBV approach [276] to calculate the RDF. The final susceptibility map can be generated using a regularised QSM approach nMEDI-L₁ [18], with automatic optimisation of the regularisation parameter λ , by searching the elbow (inflection) point using the bisection method [423].

The QSM using the UHF small-animal MRI systems to investigate tissue specimens, brains of rodents and monkeys *ex vivo* and *in vivo*, was previously reported in the literature [214, 215, 311, 403-407], but the results were sometimes compromised by pronounced susceptibility artifacts and the fast phase shift caused by the strong paramagnetic source [404, 405]. As the magnetic field strength increased, the B_1 field experienced by the spins varies rapidly with time [239], and the phase evolution with T_E that is estimated using linear fitting might become inappropriate and could cause erroneous results of phase processing [214]. Moreover, the ultra-high-resolution acquisition causes a further reduction of the SNR, and introduces unsuppressed streaking artifacts and low contrast in the susceptibility maps. Previously, a dedicated attempt was made to optimise the QSM method for high-resolution rat brain venography [403], utilising SHARP background field removal [245] with a non-linear regularised approach comparable to nMEDI-L₁ [18] for dipole inversion. In this PhD project, the result suggests the LBV [276] as an improved background removal method for the UHF preclinical MRI and MR microimaging, compared with SHARP [245]. Incorporating the nMEDI-L₁ approach [18], an automatic parameter optimisation scheme, elbow (inflection) point search using the bisection method

[423], is also proposed here for the dipole inversion to improve analysis consistency and comparability between imaging subjects and studies. Tested on A β (1-42) and ferritin-bound iron gel phantoms, this QSM method is found robust against streaking artifacts and small susceptibility fluctuation, but could be confounded by adjacent prominent susceptibility artifacts (*e.g.*, median to large air bubbles, poor shimming). The result of this PhD project also suggests the necessity of finding a suitable reference for QSM based on UHF small-animal MRI and MRM, which could be implemented with MEDI+0 (Section 4.4.2.3) [271] to improve reproducibility [311].

7.4.2 Correlation between R_2^* and susceptibility

Intrinsically, R_2^* and susceptibility are connected via the local field inhomogeneity and the resulting relaxation rate R_2' [227-229], which may be reversed by the refocusing RF pulse of the SE sequence (see Section 2.2.1, and Section 3.1). At 4.7 T [368] and 7.0 T [56, 217, 260] human brain MRI, a positive correlation between the susceptibility and R_2^* has been observed in the iron-laden brain regions, where the susceptibility effect of the (super)paramagnetic iron in tissue was prominent [227]. In this study, such correlation is weaker, demonstrated by the pixel-wise fitting of the susceptibility and the R_2^* measured within samples that contained ferritin. It is because of the high resolution employed in the study, where less field inhomogeneity associated with the ferritin-bound iron is sampled within the small voxel, and therefore, the observed R_2^* might be dominated by the R_2 relaxation. This could partially explain the smaller R_2^* increase with the ferritin iron level in the dispersed ferritin phantom, compared with the phantom consisting of co-aggregated A β +ferritin, whose transverse relaxation is more efficient due to the larger magnetic moment of the clustered ferritin [168, 171, 366], and also generates large local field inhomogeneity [227] even with the ultra-high resolution. On the other hand, QSM reveals the inherent magnetic (bulk) susceptibility property of the sample, directly from the local phase shift and the field inhomogeneity detected by the MRI system and is less affected by the R_2 relaxation or proton diffusion.

7.4.3 R_2^* of A β (1-42) and ferritin-bound iron level

In this PhD project, the ferritin concentration of the sample is within the physiological range for the healthy human brain [13, 43, 411] (0.03-1.54 mg ferritin/mL wet tissue, assumed tissue density of 1 g/mL), as previously reviewed by Haacke *et al.* [13] (Table. 2 of reference [13], data reported by Chen *et al.* [7] was not considered due to magnitudes of difference compared with others). The sample's concentration is comparable to the prior-reported ferritin concentration in several subcortical nuclei such as caudate, putamen, globus pallidus, as well as in substantia nigra [43, 136]. However, the R_2^* of those brain regions reported in the literature, obtained with clinical scanners (3.0 T and below, reviewed in [13]) or at UHF MRI (7.0 T) [260], was larger than the R_2^* of the ferritin samples measured here. Using 9.4 T microimaging MRI, Finnegan *et al.* [54] reported a quantitative relationship between R_2^* and iron concentration measured in the frozen human brain tissue specimen and suggested an iron-dependent coefficient of $0.34 \text{ s}^{-1}/\mu\text{g}\cdot\text{g}^{-1}$ iron for R_2^* prediction. Assuming fully-loaded ferritin (LF = 4500) and 1 g/mL tissue density, the converted ferritin-coefficient $92.9 \text{ s}^{-1}/\text{mg}\cdot\text{mL}^{-1}$ is still larger than the observed $14.65 \text{ s}^{-1}/\text{mg}\cdot\text{mL}^{-1}$ for the dispersed ferritin samples in this PhD project, which might suggest the LF of ferritin used in this project is lower. This is consistent with ferritin in living systems typically being part-full rather than reaching iron storage, and it should also be noted that there will be further differences between the present *in vitro* and previous *in (ex) vivo* observation caused by the different transverse relaxation mechanisms of ferritin in gel (or solution) [169, 434] and in biological tissues [227], whose transverse relaxation was previously found to be more efficient [171, 247].

To investigate the protein pathologies of neurodegenerative diseases, the transverse relaxation rate R_2^* has been employed previously for A β detection in brains and post-mortem tissue [214, 215, 218, 435]. At UHF high-resolution MRI or MRM, often in contrast with the surrounding brain tissue, the A β plaques show hypointensity in T_2^* -weighted images or hyperintense R_2^* on the parametric maps [208, 215, 218, 428]. As some neuritic plaques are known to incorporate with metal ions [34, 90, 382, 384], it is also possible that some highly-condensed, hydrophobic plaques may also demonstrate hypointensity on the weighted images due to the reduced proton

interactions. With a 40- μm in-plane resolution, Nabuurs *et al.* [428] reported a significant $T_2(T_2^*)$ -shortening effect of the post-mortem human brain sample that contained A β plaque, but not the diffused A β , at 9.4 T. In this PhD project, the R_2^* measured from the A β +ferritin aggregate is comparable to the prior-reported *ex vivo* quantitative measurement, between 21.1 s^{-1} (diffused plaques) and 56.5 s^{-1} (A β plaques) [428].

Moreover, the result of this study demonstrates the T_2^* -shortening effect of the ferritin-bound iron *in vitro*, in the form of dispersed ferritin (*i.e.*, Ftn phantom), as well as incorporated into amyloid aggregate structures by A β (1-42) [88] (*i.e.*, A β +Ftn phantom). In contrast, the A β (1-42) aggregate (*i.e.*, A β phantom) does not significantly change the observed R_2^* . The observed $T_2(T_2^*)$ -shortening effect of the ferritin-bound iron in the uniformly dispersed form is comparable to the literature of *in vitro* studies [167, 171, 430], where the transverse relaxation rate showed a linear increase with the ferritin-bound iron level. Although the observed R_2^* is within the previously reported range, the measurements could not be compared directly with the studies of the ferritin aqueous solution, due to the LF variation of the ferritin samples [167, 430]. Nevertheless, the result of the PhD project has confirmed that the R_2^* changes arise from the ferritin-bound iron, and the contribution from the aggregated A β (1-42) fibrils along shows negligible effect in the *in vitro* condition.

7.4.4 Susceptibility of A β (1-42) and ferritin-bound iron level

Based on the magnetometry of ferritin-bound iron (Fe^{3+} , effective magnetic moment $\mu_{\text{eff}} = 3.8$ Bohr Magnetons) and the protein shell [167], Schenck predicted the theoretical susceptibility of a fully-loaded ferritin molecule (LF = 4500) should be 520 ppm at body temperature [436]. This suggests a theoretical correlation between the susceptibility and the ferritin-bound iron concentration, with the iron-dependent coefficient of 1.4 ppb/ μg iron $\cdot\text{g}^{-1}$ [240]. Converted into the ferritin concentration, 340 ppb/mg $\cdot\text{mL}^{-1}$, the theoretical coefficient of the predicted susceptibility is found an order of magnitude larger, than what might be suggested by the observed susceptibility of the dispersed ferritin phantom (12.3 ppb/mg $\cdot\text{mL}^{-1}$) in this PhD project. In the literature, the (ferritin) iron-dependent coefficient estimated from the

experimental data was also found below the theoretical prediction, between 0.55 ppb/ $\mu\text{g iron}\cdot\text{g}^{-1}$ and 1.3 ppb/ $\mu\text{g iron}\cdot\text{g}^{-1}$ (reviewed elsewhere [14]). Given the complexity of the magnetic composition of the biological tissue, a concordance between Schenck's prediction of ferritin's susceptibility and the *in vivo* observation would appear rather coincidental. However, the underestimation observed in the ferritin phantom might also be contributed by the LF, because the overall susceptibility of ferritin is jointly determined by the (super)paramagnetic iron core and the diamagnetic protein shell [167, 430]. Additionally, the discrepancy might be also due to the higher magnetic field applied in this PhD project, which is supported by a recent study of QSM reproducibility. The study [437] showed a slight-to-moderate dependency (with a linear factor of 0.69-0.87) of the measured susceptibility in human brains, using QSM, on the field strength (3.0 T vs. 7.0 T) and the number of echoes (5 vs. 10), where the smaller susceptibility was observed on the higher magnetic field and the larger number of echoes. Interestingly, the field-dependency was not found in the gadolinium phantoms [311], suggesting the QSM might be sensitive to the different magnetic properties between the paramagnetic ions and the ferritin *in vitro* or *in vivo*.

Empirically, the relationship between the susceptibility measured with the clinical QSM MRI, and ferritin-bound iron in gel phantoms has been reported to be linear, and increased with the iron concentration, at 3.0 T [53]. For human brain QSM, as the homogeneously distributed ferritin-bound iron is assumed to be one of the dominant sources (together with myelin) of the observed tissue susceptibility, the linear correlation was also reported [51, 53, 191, 245]. Positive, linear relationships of the susceptibility, with the brain iron concentration that was measured post-mortem [51, 53], or estimated from the literature for *in vivo* data [191, 245], were reported for 3.0 T clinical MRI. At 7.0 T, Wang *et al.* [221] demonstrated a positive, linear correlation (Pearson's $\rho = 0.43$) between the susceptibility and the semi-quantified ferritin concentration in the post-mortem brain with amyotrophic lateral sclerosis. In this PhD project, the linear correlation between the susceptibility and the ferritin level in its dispersed form is not significant, but the quantitative

susceptibility showed a strong dependency of the level of ferritin when it is co-aggregated with A β (1-42).

Under lower resolution ($> 400 \mu\text{m}$), the presence of A β plaques was reported to be associated with elevated susceptibility at 7.0 T [109, 151], while the ultra-high-resolution QSM showed the potential of detecting A β deposit using UHF MRI [215]. In this PhD project, the distribution of the synthetic aggregated peptides is imaged using the ultra-high-resolution susceptibility mapping, and the associated protein concentration could be measured with the QSM signal. The measured mean and median susceptibility of the samples show strong concentration-dependence for the co-aggregated A β +ferritin, with the ferritin concentration coefficients of $150.2 \text{ ppb/mg}\cdot\text{mL}^{-1}$ (mean susceptibility) and $147.3 \text{ ppb/mg}\cdot\text{mL}^{-1}$ (median susceptibility) respectively. In contrast, for the dispersed ferritin, the correlation is not significant between the susceptibility and the ferritin concentration due to the small susceptibility change, compared with the variation; but the data suggest the potential coefficients would be one order of magnitude smaller than the aggregated A β +ferritin. At the same time, the A β (1-42) aggregate on the absence of ferritin does not markedly alter the observed susceptibility. This observation suggests that the susceptibility of the A β +ferritin aggregate, measured *in vitro* using the ultra-high-resolution QSM at 9.4 T, is greatly enhanced by the agglomeration of ferritin by co-aggregating with the A β (1-42) after the incubation [88].

7.4.5 Effect of the mineral form and distribution of the iron, on UHF R_2^* and susceptibility MRI

Compared with the dispersed ferritin sample, the larger slope coefficients of the susceptibility(R_2^*)-ferritin correlation, is found for the aggregated ferritin, which indicated other factors that influenced the observed R_2^* and susceptibility, in addition to the ferritin-bound iron level. It is known that the susceptibility (R_2^*) of the sample is also associated with the oxidation state of the iron ion, which determines the spin energy (see Eq. (2.5) in Section 2.1.1) and the effective magnetic moment [240]. Under normal condition, iron ions stored in the ferritin is in a stable ferric state (Fe^{3+}), mainly in the form of ferrihydrites [438]. However, the magnetite-like

structure of the ferritin core was detected under pathological conditions such as AD [90, 438], or in the presence of aggregating A β (1-42) [86-88], where both Fe³⁺ and Fe²⁺ present. Recently, the impact of the iron oxidation state of the formalin-fixed brain tissue, on quantitative R₂^{*} and susceptibility at 3.0 T clinical MRI, was reported by Birkl *et al.* [296], where the decrease of both measurements was observed in WM and cortex as the iron content was chemically reduced from Fe³⁺ to Fe²⁺. According to the previous observation [88], Fe²⁺ in ferritin was only detected after prolonged incubation of 144-240 hrs with A β (1-42), at 37 °C. In the PhD research, the samples are constructed immediately after 100-hrs incubation, into the MR agarose gel phantoms, and are kept and scanned at 4°C within 24 hrs. Therefore the iron content in the co-aggregated A β (1-42) and ferritin, is less likely to be already chemically reduced by the time of the MR acquisition. However, further experiments are required to confirm the exact mineral form of the ferritin-bound iron in this study.

Moreover, the quantitative R₂^{*} and susceptibility measurements, derived from the GRE pulse sequence, are also sensitive to the magnetic field inhomogeneity (see Section 2.2.2, and Section 3.1). It is concordant with the observation in this study. For the same ferritin-bound iron level, the agglomerated ferritin with A β demonstrates a stronger susceptibility effect and the T₂^{*}-shortening effect, compared with the dispersed ferritin. Compared with the dispersed ferritin, three times larger ferritin-dependent coefficient is found in the aggregated A β +ferritin samples for the median R₂^{*} (42.48 s⁻¹/mg·mL⁻¹ vs. 14.65 s⁻¹/mg·mL⁻¹), and possibly an order of magnitude larger for the median susceptibility (147.3 ppb/mg·mL⁻¹ vs. 12.3 ppb/mg·mL⁻¹). This result suggests that, for the preclinical UHF MRI, the QSM may be more sensitive to the intrinsic magnetic susceptibility effect of the A β +ferritin aggregates, compared with R₂^{*}, with ultra-high resolution. Moreover, it also shows the importance of the chemical form and the spatial distribution of tissue iron, for the accurate interpretation of existing R₂^{*} and QSM results in the literature concerning the A β -associated pathologies and neurodegenerative diseases [14, 150, 204, 439].

7.4.6 Comparison with *in vivo* and *ex vivo* UHF MRI

Using 9.4 T preclinical MRI, this *in vitro* PhD study presented here shows the quantitative R_2^* and QSM have a higher sensitivity to the A β +ferritin aggregate, compared with the dispersed ferritin. Although the agarose gel phantom could not entirely represent the realistic biological tissue, the observation is generally in line with the existing *in (ex) vivo* findings [215, 218, 428]. The stronger $T_2(T_2^*)$ -shortening effect of the tissue that contained A β plaques was observed at UHF MRI [208, 215, 218, 428], and R_2^* was applied to investigate A β -plaque-associated neuropathology in transgenic mice [213, 440]. Compared with R_2^* mapping, QSM also showed the ability to differ the (voxel-averaged) signals of the paramagnetic source from the diamagnetic [51, 245, 441] (see also Chapter 6). At higher field (7.0 T), the human cortex GM susceptibility was dominated by a contribution from the iron-associated (super)paramagnetic source, while the cortex WM was dominated by the diamagnetic myelin content [56, 57] (also see Discussion in Chapter 6). However, for the UHF preclinical MRI (9.4 T and above), the ultra-high-resolution (< 200 μm) mouse brain QSM suggested the whole-brain image contrast might be dominated by the myelination [210, 214]. Although it appeared to pose challenges in detecting iron-associated A β plaques and NTF *in vivo* and *ex vivo*, O'Callaghan *et al.* [214] suggested that QSM could be used to detect the demyelination of the region with less aberrant protein accumulation at the early stage of the disease. On the other hand, the sensitivity of the QSM to the iron-laden tissue or pathological iron accumulation *in (ex) vivo*, could be improved by correcting the myelin content [4, 245]. Nevertheless, the relative susceptibility between mouse brain regions appeared inconsistent among several ultra-high-resolution mouse brain studies [210-212, 214]. This discrepancy might be improved by using multiple T_E to calculate the susceptibility-associated phase shift, as demonstrated here, where the components with different susceptibilities could be sampled.

7.5 Conclusions

For the first time, a comprehensive assessment and comparison of phase processing methods on 9.4 T UHF small-animal MRI system is presented in this work, and a method for QSM of A β (1-42) and ferritin-bound iron *in vitro* is proposed. In this study,

with ultra-high resolution, the quantitative R_2^* and QSM of A β (1-42) and ferritin-bound iron is demonstrated *in vitro*, at 9.4 T. Compared with the dispersed ferritin, both MRI measurements demonstrate a higher sensitivity to the A β +ferritin aggregate, with a potential positive linear correlation with the ferritin-bound iron level. Specifically, R_2^* and QSM are shown to be three and ten times more sensitive to the presence of the A β +ferritin aggregate, respectively, than the dispersed ferritin *in vitro*, indicating they may be useful for non-invasive detection and semi-quantification of the iron-laden A β plaques. This also provides evidence to support the importance of the mineral form and spatial distribution of the iron content, in addition to the concentration, for both R_2^* and susceptibility measurements.

Chapter 8: Conclusions and future work

A range of MRI techniques and applications for measuring brain iron are investigated and assessed in this PhD research, including transverse relaxation rates derived from different pulse sequences, and the current state-of-the-art QSM techniques, in both clinical (3.0 T) and preclinical (9.4 T) systems.

Demonstrated using the retrospective 3.0 T clinical MR data from the PPMI study, the quantitative MRI parameter derived from dual-contrast FSE MRI, effective R_2 , is named in this study (Chapter 5). In contrast to what was commonly believed in the qualitative nature of FSE MRI, at 3.0 T, the dual-contrast FSE-derived effective R_2 , is strongly correlated with the estimated iron concentration of subcortical GM in living human brains. As the linear correlation of the effective R_2 with the estimated iron concentration is reported here for the first time, this quantitative MRI also shows the potential clinical value in evaluating the disease laterality in PD patients. In PD brains, this asymmetry of the putaminal effective R_2 at the early disease stage is associated with the DaT dysfunction, and may share the mechanism with the unilateral reduction of the nigrostriatal terminal density or dopaminergic neuron loss. Hence, it may be concluded here that the proposed effective R_2 could be used to measure brain iron as a fast alternative to the conventional R_2 , in iron-laden brain regions, when the prolonged SE acquisition is impractical at 3.0 T clinical MRI. One limitation in this study is the relatively small sample size, which is practically restricted by the PhD time frame. Although the subjects included in the case-control analysis are matched as rigorously as possible between groups, it might be the source of variation observed in the result. The method of calculating the effective R_2 is straightforward, but the measurement may vary across clinical MRI systems due to the differences in MR acquisition. For the future plan, to compensate for the variance introduced by the acquisition parameters, this quantitative MRI method may benefit from more sophisticated signal modelling, such as adapting the extended-phase-graph [318, 442, 443], or Bloch simulation [444-446], when the aim is to retrieve the 'true' R_2 (T_2) from the FSE MRI sequence.

In phantoms and *in vivo* human brains, the QSM with nMEDI-L₁ dipole inversion is successfully validated and assessed in this PhD project, with 3.0 T clinical MRI (Chapter 6) and 9.4 T preclinical MRI (Chapter 7), respectively. At 3.0 T, the QSM susceptibility is significantly proportional to the Fe³⁺ concentration in the phantom, with a very strong, linear correlation. In the phantoms, the theoretical iron-associated susceptibility increase, 1.30 ppb/μg·g⁻¹, can be accurately measured by the QSM technique using 3.0 T clinical MRI. In the healthy human brain, the QSM method can significantly enhance the anatomical contrast of iron-laden regions, but the correlation of the measured susceptibility with the estimated brain iron is weaker, compared with the phantom. This deviation is caused by the brain region-dependent variations, suggested by the observations in this Chapter (Chapter 6), which may be associated with the myelin content, tissue structure, and iron distribution within a voxel. Good reproducibility can be achieved in subcortical nuclei, especially in iron-laden brain regions. For future research, the myelin correction [245] may be applied to improve the quantitative relationship between the brain iron concentration and bulk susceptibility. Therefore, developing biophysical models and/or MR pulse sequences that may simultaneously measure both tissue components could open new opportunities in this field.

Using 9.4 T preclinical MRI, for the first time, QSM of Aβ(1-42) and ferritin are measured *in vitro*, together with R₂^{*} (Chapter 7). An ultra-high-resolution QSM method, with UHF small-animal MRI, is assessed and optimised here for the first time, to image ferritin-bound iron associated Aβ aggregate *in vitro*. An optimal QSM reconstruction pipeline is devised according to the assessment: 1) the raw MR phase data may be temporally unwrapped with the non-linear least-squares fitting [298], and then spatially unwrapped using the Laplacian operator [300], 2) the background magnetic field of the unwrapped phase can then be removed efficiently and effectively by the LBV approach [276], 3) finally, a regularised approach nMEDI-L₁ [18] may be applied for the field-to-susceptibility dipole inversion, with the regularisation parameter λ automatically optimised by searching the elbow (inflection) point using the bisection method [423]. Using this pipeline, a potential linear correlation is discovered between the observed R₂^{*} and susceptibility, and phantom's ferritin

levels. For the A β +ferritin aggregate, the ferritin-level-associated R_2^* and susceptibility increases are found three times and likely one order of magnitude larger, respectively, than in the dispersed ferritin phantom. The findings suggest that QSM may be a sensitive tool to detect iron-laden A β aggregates at UHF MRI. The observations in this PhD study, on the other hand, also indicate that even with the ultra-high resolution, the R_2^* and susceptibility derived from the 3D GRE pulse sequence may be influenced by the spatial distribution of ferritin under UHF, in addition to its concentration. As the human brain MRI is entering a UHF era, caution may still be taken to quantitatively interpret the iron-associated R_2^* and susceptibility contrast, especially in diseased tissue where aberrant iron-laden plaques and lesions are present. The main limitation in this research is the lack of the measurement of the absolute iron concentration or the LF of the ferritin, which may help to explain the underestimation of the iron-associated R_2^* and susceptibility increase, compared to the theoretical prediction. Therefore, future work may include measuring the exact iron concentration, using analytical techniques such as ICP-MS, together with XRF [53, 78] and TEM [89], to quantitatively incorporate the effect of any different iron species and the spatial distribution on the observed R_2^* and susceptibility.

To summarise, studying the human brains and the synthetic (ferritin-bound) iron-containing MR phantoms, with retrospective 3.0 T clinical FSE MRI data, the new effective R_2 is presented here as a practical alternative quantitative measurement to the conventional R_2 , enabling detection of asymmetrical iron level and DaT dysfunctions in PD hemispheres. Meanwhile, the advanced QSM techniques are originally validated and assessed at 3.0 T clinical MRI and developed for the UHF (9.4 T) small-animal MRI system in this PhD research, to measure brain iron *in vivo* and *in vitro*. The original contributions to research described in this PhD thesis will thereby advance understanding of quantitative MRI techniques and applications for measuring brain iron in both clinical and preclinical settings.

References

- [1] R. J. Ward, F. A. Zucca, J. H. Duyn, R. R. Crichton, and L. Zecca, "The role of iron in brain ageing and neurodegenerative disorders," *The Lancet Neurology*, vol. 13, no. 10, pp. 1045-1060, 2014, doi: 10.1016/s1474-4422(14)70117-6.
- [2] M. W. Hentze, M. U. Muckenthaler, B. Galy, and C. Camaschella, "Two to tango: regulation of Mammalian iron metabolism," *Cell*, vol. 142, no. 1, pp. 24-38, Jul 9 2010, doi: 10.1016/j.cell.2010.06.028.
- [3] K. D. Poss and S. Tonegawa, "Heme oxygenase 1 is required for mammalian iron reutilization," *Proceedings of the National Academy of Sciences*, vol. 94, no. 20, pp. 10919-10924, 1997.
- [4] H. E. Moller *et al.*, "Iron, Myelin, and the Brain: Neuroimaging Meets Neurobiology," *Trends Neurosci*, vol. 42, no. 6, pp. 384-401, Jun 2019, doi: 10.1016/j.tins.2019.03.009.
- [5] R. R. Crichton, D. T. Dexter, and R. J. Ward, "Brain iron metabolism and its perturbation in neurological diseases," *J Neural Transm (Vienna)*, vol. 118, no. 3, pp. 301-14, Mar 2011, doi: 10.1007/s00702-010-0470-z.
- [6] R. R. Crichton, D. T. Dexter, and R. J. Ward, "Metal based neurodegenerative diseases—From molecular mechanisms to therapeutic strategies," *Coordination Chemistry Reviews*, vol. 252, no. 10-11, pp. 1189-1199, 2008, doi: 10.1016/j.ccr.2007.10.019.
- [7] J. C. Chen *et al.*, "T2 values in the human brain: comparison with quantitative assays of iron and ferritin," *Radiology*, vol. 173, no. 2, pp. 521-6, Nov 1989, doi: 10.1148/radiology.173.2.2798884.
- [8] L. Zecca *et al.*, "Iron, neuromelanin and ferritin content in the substantia nigra of normal subjects at different ages: consequences for iron storage and neurodegenerative processes," *Journal of Neurochemistry*, vol. 76, no. 6, pp. 1766-1773, 2001, doi: 10.1046/j.1471-4159.2001.00186.x.
- [9] N. Krebs *et al.*, "Assessment of trace elements in human brain using inductively coupled plasma mass spectrometry," *J Trace Elem Med Biol*, vol. 28, no. 1, pp. 1-7, Jan 2014, doi: 10.1016/j.jtemb.2013.09.006.

- [10] P. Ramos, A. Santos, N. R. Pinto, R. Mendes, T. Magalhaes, and A. Almeida, "Iron levels in the human brain: a post-mortem study of anatomical region differences and age-related changes," *J Trace Elem Med Biol*, vol. 28, no. 1, pp. 13-7, Jan 2014, doi: 10.1016/j.jtemb.2013.08.001.
- [11] B. Hallgren and P. Sourander, "The effect of age on the non-haemin iron in the human brain," *J Neurochem*, vol. 3, no. 1, pp. 41-51, Oct 1958. [Online]. Available: <http://www.ncbi.nlm.nih.gov/pubmed/13611557>.
- [12] M. A. Samuels and S. K. Feske, *Office Practice of Neurology*, 2nd ed. United States: Elsevier Science, 2003.
- [13] E. M. Haacke *et al.*, "Imaging iron stores in the brain using magnetic resonance imaging," (in eng), *Magn Reson Imaging*, vol. 23, no. 1, pp. 1-25, Jan 2005, doi: 10.1016/j.mri.2004.10.001.
- [14] K. Ghassaban, S. Liu, C. Jiang, and E. M. Haacke, "Quantifying iron content in magnetic resonance imaging," *Neuroimage*, vol. 187, pp. 77-92, Feb 15 2019, doi: 10.1016/j.neuroimage.2018.04.047.
- [15] E. M. Haacke, R. W. Brown, M. R. Thompson, and R. Venkatesan, *Magnetic Resonance Imaging: physical principles and sequence design*. John Wiley & Sons, 1999.
- [16] M. A. Bernstein, K. F. King, and X. J. Zhou, *Handbook of MRI pulse sequences*. Elsevier Academic Press, 2004.
- [17] L. de Rochefort, R. Brown, M. R. Prince, and Y. Wang, "Quantitative MR susceptibility mapping using piece-wise constant regularized inversion of the magnetic field," *Magn Reson Med*, vol. 60, no. 4, pp. 1003-9, Oct 2008, doi: 10.1002/mrm.21710.
- [18] J. Liu *et al.*, "Morphology enabled dipole inversion for quantitative susceptibility mapping using structural consistency between the magnitude image and the susceptibility map," *Neuroimage*, vol. 59, no. 3, pp. 2560-8, Feb 1 2012, doi: 10.1016/j.neuroimage.2011.08.082.
- [19] T. Liu, W. Xu, P. Spincemaille, A. S. Avestimehr, and Y. Wang, "Accuracy of the morphology enabled dipole inversion (MEDI) algorithm for quantitative susceptibility mapping in MRI," *IEEE Trans Med Imaging*, vol. 31, no. 3, pp. 816-24, Mar 2012, doi: 10.1109/TMI.2011.2182523.

- [20] M. Perutz, "Regulation of oxygen affinity of hemoglobin: influence of structure of the globin on the heme iron," *Annual review of biochemistry*, vol. 48, no. 1, pp. 327-386, 1979.
- [21] A. H. Koeppen, "The history of iron in the brain," *Journal of the neurological sciences*, vol. 134, pp. 1-9, 1995.
- [22] P. Arosio, R. Ingrassia, and P. Cavadini, "Ferritins: a family of molecules for iron storage, antioxidation and more," *Biochim Biophys Acta*, vol. 1790, no. 7, pp. 589-99, Jul 2009, doi: 10.1016/j.bbagen.2008.09.004.
- [23] N. D. Chasteen and P. M. Harrison, "Mineralization in ferritin: an efficient means of iron storage," *J Struct Biol*, vol. 126, no. 3, pp. 182-94, Jun 30 1999, doi: 10.1006/jsbi.1999.4118.
- [24] P. M. Harrison and P. Arosio, "The ferritins: molecular properties, iron storage function and cellular regulation," *Biochimica et Biophysica Acta (BBA) - Bioenergetics*, vol. 1275, no. 3, pp. 161-203, 1996, doi: 10.1016/0005-2728(96)00022-9.
- [25] H. Svobodová *et al.*, "Deposits of iron oxides in the human globus pallidus," *Open Physics*, vol. 17, no. 1, pp. 291-298, 2019, doi: 10.1515/phys-2019-0030.
- [26] S. Levi *et al.*, "Evidence of H-and L-chains have co-operative roles in the iron-uptake mechanism of human ferritin," *Biochemical Journal*, vol. 288, no. 2, pp. 591-596, 1992.
- [27] S. Levi *et al.*, "Mechanism of ferritin iron uptake: activity of the H-chain and deletion mapping of the ferro-oxidase site. A study of iron uptake and ferro-oxidase activity of human liver, recombinant H-chain ferritins, and of two H-chain deletion mutants," *Journal of Biological Chemistry*, vol. 263, no. 34, pp. 18086-18092, 1988.
- [28] E. C. Theil, "Ferritin: the protein nanocage and iron biomineral in health and in disease," *Inorg Chem*, vol. 52, no. 21, pp. 12223-33, Nov 04 2013, doi: 10.1021/ic400484n.
- [29] P. Arosio and S. Levi, "Cytosolic and mitochondrial ferritins in the regulation of cellular iron homeostasis and oxidative damage," *Biochim Biophys Acta*, vol. 1800, no. 8, pp. 783-92, Aug 2010, doi: 10.1016/j.bbagen.2010.02.005.

- [30] J. R. Connor and S. L. Menzies, "Cellular management of iron in the brain," *Journal of the Neurological Sciences*, vol. 134, pp. 33-44, 1995, doi: 10.1016/0022-510x(95)00206-h.
- [31] J. R. Connor, S. L. Menzies, S. M. St Martin, and E. J. Mufson, "Cellular distribution of transferrin, ferritin, and iron in normal and aged human brains," *J Neurosci Res*, vol. 27, no. 4, pp. 595-611, Dec 1990, doi: 10.1002/jnr.490270421.
- [32] L. Zecca, M. B. Youdim, P. Riederer, J. R. Connor, and R. R. Crichton, "Iron, brain ageing and neurodegenerative disorders," *Nat Rev Neurosci*, vol. 5, no. 11, pp. 863-73, Nov 2004, doi: 10.1038/nrn1537.
- [33] J. F. Collingwood and N. D. Telling, "Iron Oxides in the Human Brain," in *Iron Oxides: From Nature to Applications*, D. Faivre Ed., 2016, ch. 7, pp. 143-176.
- [34] C. Quintana *et al.*, "Study of the localization of iron, ferritin, and hemosiderin in Alzheimer's disease hippocampus by analytical microscopy at the subcellular level," *J Struct Biol*, vol. 153, no. 1, pp. 42-54, Jan 2006, doi: 10.1016/j.jsb.2005.11.001.
- [35] E. M. Taylor, A. Crowe, and E. H. Morgan, "Transferrin and Iron Uptake by the Brain: Effects of Altered Iron Status," *Journal of Neurochemistry*, vol. 57, no. 5, pp. 1584-1592, 1991, doi: 10.1111/j.1471-4159.1991.tb06355.x.
- [36] A. Burkhart *et al.*, "Expression of Iron-Related Proteins at the Neurovascular Unit Supports Reduction and Reoxidation of Iron for Transport Through the Blood-Brain Barrier," *Mol Neurobiol*, vol. 53, no. 10, pp. 7237-7253, Dec 2016, doi: 10.1007/s12035-015-9582-7.
- [37] R. Crichton and J. R. Boelaert, *Inorganic biochemistry of iron metabolism: from molecular mechanisms to clinical consequences*, Second ed. United Kingdom: John Wiley & Sons, 2001.
- [38] R. S. Ohgami, D. R. Campagna, A. McDonald, and M. D. Fleming, "The Steap proteins are metalloredutases," *Blood*, vol. 108, no. 4, pp. 1388-94, Aug 15 2006, doi: 10.1182/blood-2006-02-003681.
- [39] M. U. Muckenthaler, B. Galy, and M. W. Hentze, "Systemic iron homeostasis and the iron-responsive element/iron-regulatory protein (IRE/IRP) regulatory

- network," *Annu Rev Nutr*, vol. 28, pp. 197-213, 2008, doi: 10.1146/annurev.nutr.28.061807.155521.
- [40] L. C. Kuhn, "Iron regulatory proteins and their role in controlling iron metabolism," *Metallomics*, vol. 7, no. 2, pp. 232-43, Feb 2015, doi: 10.1039/c4mt00164h.
- [41] J. L. Beard and J. R. Connor, "Iron status and neural functioning," *Annual review of nutrition*, vol. 23, no. 1, pp. 41-58, 2003.
- [42] J. C. Chen *et al.*, "MR of human postmortem brain tissue: correlative study between T2 and assays of iron and ferritin in Parkinson and Huntington disease," *American journal of neuroradiology*, vol. 14, no. 2, pp. 275-281, 1993.
- [43] D. T. Dexter *et al.*, "Alterations in the levels of iron, ferritin and other trace metals in Parkinson's disease and other neurodegenerative diseases affecting the basal ganglia," *Brain*, vol. 114 (Pt 4), no. 4, pp. 1953-75, Aug 1991, doi: <https://doi.org/10.1093/brain/114.4.1953>.
- [44] P. D. Griffiths and A. R. Crossman, "Distribution of Iron in the Basal Ganglia and Neocortex in Postmortem Tissue in Parkinson's Disease and Alzheimer's Disease," *Dementia and Geriatric Cognitive Disorders*, vol. 4, no. 2, pp. 61-65, 1993, doi: 10.1159/000107298.
- [45] D. Purves, D. Purves *et al.*, Eds. *Neuroscience*, 6th ed. New York: Oxford University Press (in English), 2018.
- [46] P. Ramos, E. Pinto, A. Santos, and A. Almeida, "Reference values for trace element levels in the human brain: A systematic review of the literature," *J Trace Elem Med Biol*, vol. 66, p. 126745, Jul 2021, doi: 10.1016/j.jtemb.2021.126745.
- [47] E. Sofic, W. Paulus, K. Jellinger, P. Riederer, and M. B. H. Youdim, "Selective Increase of Iron in Substantia Nigra Zona Compacta of Parkinsonian Brains," *Journal of Neurochemistry*, vol. 56, no. 3, pp. 978-982, 1991, doi: 10.1111/j.1471-4159.1991.tb02017.x.
- [48] B. Drayer, P. Burger, R. Darwin, S. Riederer, R. Herfkens, and G. A. Johnson, "MRI of brain iron," *AJR Am J Roentgenol*, vol. 147, no. 1, pp. 103-10, Jul 1986, doi: 10.2214/ajr.147.1.103.

- [49] W. W. Harrison, M. G. Netsky, and M. D. Brown, "Trace elements in human brain: Copper, zinc, iron, and magnesium," *Clinica Chimica Acta*, vol. 21, no. 1, pp. 55-60, 1968, doi: 10.1016/0009-8981(68)90010-7.
- [50] M. J. House *et al.*, "Correlation of proton transverse relaxation rates (R2) with iron concentrations in postmortem brain tissue from alzheimer's disease patients," *Magn Reson Med*, vol. 57, no. 1, pp. 172-80, Jan 2007, doi: 10.1002/mrm.21118.
- [51] C. Langkammer *et al.*, "Quantitative susceptibility mapping (QSM) as a means to measure brain iron? A post mortem validation study," *Neuroimage*, vol. 62, no. 3, pp. 1593-9, Sep 2012, doi: 10.1016/j.neuroimage.2012.05.049.
- [52] N. P. Visanji, J. F. Collingwood, M. E. Finnegan, A. Tandon, E. House, and L. N. Hazrati, "Iron deficiency in parkinsonism: region-specific iron dysregulation in Parkinson's disease and multiple system atrophy," *J Parkinsons Dis*, vol. 3, no. 4, pp. 523-37, 2013, doi: 10.3233/JPD-130197.
- [53] W. Zheng, H. Nichol, S. Liu, Y. C. Cheng, and E. M. Haacke, "Measuring iron in the brain using quantitative susceptibility mapping and X-ray fluorescence imaging," *Neuroimage*, vol. 78, pp. 68-74, Sep 2013, doi: 10.1016/j.neuroimage.2013.04.022.
- [54] M. E. Finnegan *et al.*, "Synchrotron XRF imaging of Alzheimer's disease basal ganglia reveals linear dependence of high-field magnetic resonance microscopy on tissue iron concentration," *J Neurosci Methods*, vol. 319, pp. 28-39, May 1 2019, doi: 10.1016/j.jneumeth.2019.03.002.
- [55] A. Reinert, M. Morawski, J. Seeger, T. Arendt, and T. Reinert, "Iron concentrations in neurons and glial cells with estimates on ferritin concentrations," *BMC Neurosci*, vol. 20, no. 1, p. 25, May 29 2019, doi: 10.1186/s12868-019-0507-7.
- [56] C. Stuber *et al.*, "Myelin and iron concentration in the human brain: a quantitative study of MRI contrast," *Neuroimage*, vol. 93 Pt 1, pp. 95-106, Jun 2014, doi: 10.1016/j.neuroimage.2014.02.026.
- [57] S. Hametner *et al.*, "The influence of brain iron and myelin on magnetic susceptibility and effective transverse relaxation - A biochemical and

- histological validation study," *NeuroImage*, vol. 179, pp. 117-133, 2018, doi: 10.1016/j.neuroimage.2018.06.007.
- [58] G. Bartzokis *et al.*, "Brain ferritin iron may influence age- and gender-related risks of neurodegeneration," *Neurobiol Aging*, vol. 28, no. 3, pp. 414-23, Mar 2007, doi: 10.1016/j.neurobiolaging.2006.02.005.
- [59] A. Kwiatkowski *et al.*, "Long-term improvement under deferiprone in a case of neurodegeneration with brain iron accumulation," *Parkinsonism & related disorders*, vol. 18, no. 1, pp. 110-112, 2012.
- [60] J. Liman, A. Wellmer, K. Rostasy, M. Bahr, and P. Kermer, "Transcranial ultrasound in neurodegeneration with brain iron accumulation (NBIA)," *Eur J Paediatr Neurol*, vol. 16, no. 2, pp. 175-8, Mar 2012, doi: 10.1016/j.ejpn.2011.07.009.
- [61] C. Morris and J. Edwardson, "Iron histochemistry of the substantia nigra in Parkinson's disease," *Neurodegeneration*, vol. 3, no. 4, pp. 277-282, 1994.
- [62] Z. M. Qian and X. Shen, "Brain iron transport and neurodegeneration," *Trends in molecular medicine*, vol. 7, no. 3, pp. 103-108, 2001.
- [63] D. A. Loeffler *et al.*, "Transferrin and iron in normal, Alzheimer's disease, and Parkinson's disease brain regions," *J Neurochem*, vol. 65, no. 2, pp. 710-24, Aug 1995, doi: 10.1046/j.1471-4159.1995.65020710.x.
- [64] L. van der Weerd, A. Lefering, A. Webb, R. Egli, and L. Bossoni, "Effects of Alzheimer's disease and formalin fixation on the different mineralised-iron forms in the human brain," *Sci Rep*, vol. 10, no. 1, p. 16440, Oct 5 2020, doi: 10.1038/s41598-020-73324-5.
- [65] K. Schmierer *et al.*, "Quantitative magnetic resonance of postmortem multiple sclerosis brain before and after fixation," *Magn Reson Med*, vol. 59, no. 2, pp. 268-77, Feb 2008, doi: 10.1002/mrm.21487.
- [66] R. J. Dawe, D. A. Bennett, J. A. Schneider, S. K. Vasireddi, and K. Arfanakis, "Postmortem MRI of human brain hemispheres: T2 relaxation times during formaldehyde fixation," *Magn Reson Med*, vol. 61, no. 4, pp. 810-8, Apr 2009, doi: 10.1002/mrm.21909.
- [67] M. Schrag, A. Dickson, A. Jiffry, D. Kirsch, H. V. Vinters, and W. Kirsch, "The effect of formalin fixation on the levels of brain transition metals in archived

- samples," *Biometals*, vol. 23, no. 6, pp. 1123-7, Dec 2010, doi: 10.1007/s10534-010-9359-4.
- [68] C. Birkl *et al.*, "Effects of formalin fixation and temperature on MR relaxation times in the human brain," *NMR Biomed*, vol. 29, no. 4, pp. 458-65, Apr 2016, doi: 10.1002/nbm.3477.
- [69] A. S. Shatil, M. N. Uddin, K. M. Matsuda, and C. R. Figley, "Quantitative Ex Vivo MRI Changes due to Progressive Formalin Fixation in Whole Human Brain Specimens: Longitudinal Characterization of Diffusion, Relaxometry, and Myelin Water Fraction Measurements at 3T," *Front Med (Lausanne)*, vol. 5, p. 31, 2018, doi: 10.3389/fmed.2018.00031.
- [70] H. M. Schipper, "Neurodegeneration with brain iron accumulation - clinical syndromes and neuroimaging," *Biochim Biophys Acta*, vol. 1822, no. 3, pp. 350-60, Mar 2012, doi: 10.1016/j.bbadis.2011.06.016.
- [71] W. A. Cass *et al.*, "Iron accumulation in the striatum predicts aging-related decline in motor function in rhesus monkeys," *Neurobiol Aging*, vol. 28, no. 2, pp. 258-71, Feb 2007, doi: 10.1016/j.neurobiolaging.2005.12.010.
- [72] R. Vidal *et al.*, "Expression of a mutant form of the ferritin light chain gene induces neurodegeneration and iron overload in transgenic mice," *J Neurosci*, vol. 28, no. 1, pp. 60-7, Jan 02 2008, doi: 10.1523/JNEUROSCI.3962-07.2008.
- [73] C. C. Winterbourn, "Toxicity of iron and hydrogen peroxide: the Fenton reaction," *Toxicology Letters*, vol. 82-83, pp. 969-974, 1995, doi: 10.1016/0378-4274(95)03532-x.
- [74] J. R. Hazel and E. E. Williams, "The role of alterations in membrane lipid composition in enabling physiological adaptation of organisms to their physical environment," *Progress in lipid research*, vol. 29, no. 3, pp. 167-227, 1990.
- [75] A. J. Cooper and A. Meister, "Glutathione in the brain: disorders of glutathione metabolism," *The molecular and genetic basis of neurological disease*, vol. 35, 1997.
- [76] T. A. Rouault, "Iron metabolism in the CNS: implications for neurodegenerative diseases," *Nat Rev Neurosci*, vol. 14, no. 8, pp. 551-64, Aug 2013, doi: 10.1038/nrn3453.

- [77] C. Soto, "Unfolding the role of protein misfolding in neurodegenerative diseases," *Nat Rev Neurosci*, vol. 4, no. 1, pp. 49-60, Jan 2003, doi: 10.1038/nrn1007.
- [78] F. Lermyte *et al.*, "Emerging Approaches to Investigate the Influence of Transition Metals in the Proteinopathies," *Cells*, vol. 8, no. 10, Oct 10 2019, doi: 10.3390/cells8101231.
- [79] M. G. Spillantini, M. L. Schmidt, V. M. Lee, J. Q. Trojanowski, R. Jakes, and M. Goedert, "Alpha-synuclein in Lewy bodies," *Nature*, vol. 388, no. 6645, pp. 839-40, Aug 28 1997, doi: 10.1038/42166.
- [80] W. J. Schulz-Schaeffer, "The synaptic pathology of alpha-synuclein aggregation in dementia with Lewy bodies, Parkinson's disease and Parkinson's disease dementia," *Acta Neuropathol*, vol. 120, no. 2, pp. 131-43, Aug 2010, doi: 10.1007/s00401-010-0711-0.
- [81] M. S. Parihar, A. Parihar, M. Fujita, M. Hashimoto, and P. Ghafourifar, "Mitochondrial association of alpha-synuclein causes oxidative stress," *Cell Mol Life Sci*, vol. 65, no. 7-8, pp. 1272-84, Apr 2008, doi: 10.1007/s00018-008-7589-1.
- [82] P. Davies, D. Moualla, and D. R. Brown, "Alpha-synuclein is a cellular ferrireductase," *PLoS One*, vol. 6, no. 1, p. e15814, Jan 10 2011, doi: 10.1371/journal.pone.0015814.
- [83] M. Baba *et al.*, "Aggregation of alpha-synuclein in Lewy bodies of sporadic Parkinson's disease and dementia with Lewy bodies," *American journal of pathology*, vol. 154, no. 4, pp. 879-884, 1998.
- [84] P. R. Angelova *et al.*, "Alpha synuclein aggregation drives ferroptosis: an interplay of iron, calcium and lipid peroxidation," *Cell Death Differ*, vol. 27, no. 10, pp. 2781-2796, Oct 2020, doi: 10.1038/s41418-020-0542-z.
- [85] C. A. Rottkamp *et al.*, "Redox-active iron mediates amyloid- β toxicity," *Free Radical Biology and Medicine*, vol. 30, no. 4, pp. 447-450, 2001, doi: 10.1016/s0891-5849(00)00494-9.
- [86] A. Khan, J. P. Dobson, and C. Exley, "Redox cycling of iron by Abeta42," *Free Radic Biol Med*, vol. 40, no. 4, pp. 557-69, Feb 15 2006, doi: 10.1016/j.freeradbiomed.2005.09.013.

- [87] J. Everett *et al.*, "Evidence of redox-active iron formation following aggregation of ferrihydrite and the Alzheimer's disease peptide beta-amyloid," *Inorg Chem*, vol. 53, no. 6, pp. 2803-9, Mar 17 2014, doi: 10.1021/ic402406g.
- [88] J. Everett *et al.*, "Iron stored in ferritin is chemically reduced in the presence of aggregating Abeta(1-42)," *Sci Rep*, vol. 10, no. 1, p. 10332, Jun 25 2020, doi: 10.1038/s41598-020-67117-z.
- [89] J. Everett, J. Brooks, J. F. Collingwood, and N. D. Telling, "Nanoscale chemical speciation of β -amyloid/iron aggregates using soft X-ray spectromicroscopy," *Inorganic Chemistry Frontiers*, vol. 8, no. 6, pp. 1439-1448, 2021, doi: 10.1039/d0qi01304h.
- [90] J. F. Collingwood *et al.*, "Three-dimensional tomographic imaging and characterization of iron compounds within Alzheimer's plaque core material," *J Alzheimers Dis*, vol. 14, no. 2, pp. 235-45, Jun 2008, doi: 10.3233/jad-2008-14211.
- [91] L. M. Miller, Q. Wang, T. P. Telivala, R. J. Smith, A. Lanzirotti, and J. Miklossy, "Synchrotron-based infrared and X-ray imaging shows focalized accumulation of Cu and Zn co-localized with beta-amyloid deposits in Alzheimer's disease," *J Struct Biol*, vol. 155, no. 1, pp. 30-7, Jul 2006, doi: 10.1016/j.jsb.2005.09.004.
- [92] Y. Peng, C. Wang, H. H. Xu, Y. N. Liu, and F. Zhou, "Binding of alpha-synuclein with Fe(III) and with Fe(II) and biological implications of the resultant complexes," *J Inorg Biochem*, vol. 104, no. 4, pp. 365-70, Apr 2010, doi: 10.1016/j.jinorgbio.2009.11.005.
- [93] M. Goedert, "Alpha-synuclein and neurodegenerative diseases," *Nat Rev Neurosci*, vol. 2, no. 7, pp. 492-501, Jul 2001, doi: 10.1038/35081564.
- [94] M. G. Spillantini, M. L. Schmidt, V. M.-Y. Lee, J. Q. Trojanowski, R. Jakes, and M. Goedert, " α -Synuclein in Lewy bodies," *Nature*, vol. 388, no. 6645, pp. 839-840, 1997.
- [95] A. L. Mahul-Mellier *et al.*, "The process of Lewy body formation, rather than simply alpha-synuclein fibrillization, is one of the major drivers of neurodegeneration," *Proc Natl Acad Sci U S A*, vol. 117, no. 9, pp. 4971-4982, Mar 3 2020, doi: 10.1073/pnas.1913904117.

- [96] F. Febbraro, M. Giorgi, S. Caldarola, F. Loreni, and M. Romero-Ramos, "alpha-Synuclein expression is modulated at the translational level by iron," *Neuroreport*, vol. 23, no. 9, pp. 576-80, Jun 20 2012, doi: 10.1097/WNR.0b013e328354a1f0.
- [97] J. T. Rogers and C. M. Cahill, "Iron-responsive-like elements and neurodegenerative ferroptosis," *Learn Mem*, vol. 27, no. 9, pp. 395-413, Sep 2020, doi: 10.1101/lm.052282.120.
- [98] Y. Xiao *et al.*, "Iron promotes alpha-synuclein aggregation and transmission by inhibiting TFEB-mediated autophagosome-lysosome fusion," *J Neurochem*, vol. 145, no. 1, pp. 34-50, Apr 2018, doi: 10.1111/jnc.14312.
- [99] M. A. Smith, P. L. Harris, L. M. Sayre, and G. Perry, "Iron accumulation in Alzheimer disease is a source of redox-generated free radicals," *Proc Natl Acad Sci U S A*, vol. 94, no. 18, pp. 9866-8, Sep 2 1997, doi: 10.1073/pnas.94.18.9866.
- [100] J. Everett *et al.*, "Nanoscale synchrotron X-ray speciation of iron and calcium compounds in amyloid plaque cores from Alzheimer's disease subjects," *Nanoscale*, vol. 10, no. 25, pp. 11782-11796, Jul 5 2018, doi: 10.1039/c7nr06794a.
- [101] P. Banerjee *et al.*, "Multiple mechanisms of iron-induced amyloid beta-peptide accumulation in SHSY5Y cells: protective action of negletein," *Neuromolecular Med*, vol. 16, no. 4, pp. 787-98, Dec 2014, doi: 10.1007/s12017-014-8328-4.
- [102] K. Joppe, A. E. Roser, F. Maass, and P. Lingor, "The Contribution of Iron to Protein Aggregation Disorders in the Central Nervous System," *Front Neurosci*, vol. 13, p. 15, 2019, doi: 10.3389/fnins.2019.00015.
- [103] S. S. Rao and P. A. Adlard, "Untangling Tau and Iron: Exploring the Interaction Between Iron and Tau in Neurodegeneration," *Front Mol Neurosci*, vol. 11, p. 276, 2018, doi: 10.3389/fnmol.2018.00276.
- [104] M. D. Weingarten, A. H. Lockwood, S. Y. Hwo, and M. W. Kirschner, "A protein factor essential for microtubule assembly," *Proc Natl Acad Sci U S A*, vol. 72, no. 5, pp. 1858-62, May 1975, doi: 10.1073/pnas.72.5.1858.

- [105] G. G. Glenner and C. W. Wong, "Alzheimer's disease: Initial report of the purification and characterization of a novel cerebrovascular amyloid protein," *Biochemical and Biophysical Research Communications*, vol. 120, no. 3, pp. 885-890, 1984, doi: 10.1016/s0006-291x(84)80190-4.
- [106] N. Spotorno *et al.*, "Relationship between cortical iron and tau aggregation in Alzheimer's disease," *Brain*, vol. 143, no. 5, pp. 1341-1349, May 1 2020, doi: 10.1093/brain/awaa089.
- [107] G. M. Halliday *et al.*, "Alpha-synuclein redistributes to neuromelanin lipid in the substantia nigra early in Parkinson's disease," *Brain*, vol. 128, no. Pt 11, pp. 2654-64, Nov 2005, doi: 10.1093/brain/awh584.
- [108] A. Prasad, V. Bharathi, V. Sivalingam, A. Girdhar, and B. K. Patel, "Molecular Mechanisms of TDP-43 Misfolding and Pathology in Amyotrophic Lateral Sclerosis," *Front Mol Neurosci*, vol. 12, p. 25, 2019, doi: 10.3389/fnmol.2019.00025.
- [109] J. M. van Bergen *et al.*, "Colocalization of cerebral iron with Amyloid beta in Mild Cognitive Impairment," *Sci Rep*, vol. 6, p. 35514, Oct 17 2016, doi: 10.1038/srep35514.
- [110] M. Neumann *et al.*, "Ubiquitinated TDP-43 in frontotemporal lobar degeneration and amyotrophic lateral sclerosis," *Science*, vol. 314, no. 5796, pp. 130-3, Oct 6 2006, doi: 10.1126/science.1134108.
- [111] S. M. van Rooden, W. J. Heiser, J. N. Kok, D. Verbaan, J. J. van Hilten, and J. Marinus, "The identification of Parkinson's disease subtypes using cluster analysis: a systematic review," *Mov Disord*, vol. 25, no. 8, pp. 969-78, Jun 15 2010, doi: 10.1002/mds.23116.
- [112] S. M. Fereshtehnejad, Y. Zeighami, A. Dagher, and R. B. Postuma, "Clinical criteria for subtyping Parkinson's disease: biomarkers and longitudinal progression," *Brain*, May 25 2017, doi: 10.1093/brain/awx118.
- [113] P. Lei *et al.*, "Tau deficiency induces parkinsonism with dementia by impairing APP-mediated iron export," *Nat Med*, vol. 18, no. 2, pp. 291-5, Jan 29 2012, doi: 10.1038/nm.2613.

- [114] A. Ashraf and P.-W. So, "Spotlight on Ferroptosis: Iron-Dependent Cell Death in Alzheimer's Disease," (in English), *Frontiers in Aging Neuroscience*, Mini Review vol. 12, no. 196, 2020-July-14 2020, doi: 10.3389/fnagi.2020.00196.
- [115] P. Dusek, S. A. Schneider, and J. Aaseth, "Iron chelation in the treatment of neurodegenerative diseases," *J Trace Elem Med Biol*, vol. 38, pp. 81-92, Dec 2016, doi: 10.1016/j.jtemb.2016.03.010.
- [116] A. A. Belaidi and A. I. Bush, "Iron neurochemistry in Alzheimer's disease and Parkinson's disease: targets for therapeutics," *J Neurochem*, vol. 139 Suppl 1, pp. 179-197, Oct 2016, doi: 10.1111/jnc.13425.
- [117] D. Devos *et al.*, "Targeting chelatable iron as a therapeutic modality in Parkinson's disease," *Antioxid Redox Signal*, vol. 21, no. 2, pp. 195-210, Jul 10 2014, doi: 10.1089/ars.2013.5593.
- [118] F. A. Zucca *et al.*, "Interactions of iron, dopamine and neuromelanin pathways in brain aging and Parkinson's disease," *Prog Neurobiol*, vol. 155, pp. 96-119, Aug 2017, doi: 10.1016/j.pneurobio.2015.09.012.
- [119] L. Zecca, F. A. Zucca, H. Wilms, and D. Sulzer, "Neuromelanin of the substantia nigra: a neuronal black hole with protective and toxic characteristics," *Trends Neurosci*, vol. 26, no. 11, pp. 578-80, Nov 2003, doi: 10.1016/j.tins.2003.08.009.
- [120] L. Zecca, R. Fariello, P. Riederer, D. Sulzer, A. Gatti, and D. Tampellini, "The absolute concentration of nigral neuromelanin, assayed by a new sensitive method, increases throughout the life and is dramatically decreased in Parkinson's disease," *FEBS Letters*, vol. 510, no. 3, pp. 216-220, 2002, doi: 10.1016/s0014-5793(01)03269-0.
- [121] H. Braak, E. Ghebremedhin, U. Rub, H. Bratzke, and K. Del Tredici, "Stages in the development of Parkinson's disease-related pathology," *Cell Tissue Res*, vol. 318, no. 1, pp. 121-34, Oct 2004, doi: 10.1007/s00441-004-0956-9.
- [122] M. M. Hoehn and M. D. Yahr, "Parkinsonism: onset, progression, and mortality," *Neurology*, vol. 50, no. 2, pp. 318-318, 1998.
- [123] D. Movement Disorder Society Task Force on Rating Scales for Parkinson's, "The Unified Parkinson's Disease Rating Scale (UPDRS): status and

- recommendations," *Mov Disord*, vol. 18, no. 7, pp. 738-50, Jul 2003, doi: 10.1002/mds.10473.
- [124] C. G. Goetz *et al.*, "Movement Disorder Society-sponsored revision of the Unified Parkinson's Disease Rating Scale (MDS-UPDRS): scale presentation and clinimetric testing results," *Mov Disord*, vol. 23, no. 15, pp. 2129-70, Nov 15 2008, doi: 10.1002/mds.22340.
- [125] R. L. Doty, P. Shaman, C. P. Kimmelman, and M. S. Dann, "University of Pennsylvania Smell Identification Test: a rapid quantitative olfactory function test for the clinic," *Laryngoscope*, vol. 94, no. 2 Pt 1, pp. 176-8, Feb 1984, doi: 10.1288/00005537-198402000-00004.
- [126] M. M. Hoehn and M. D. Yahr, "Parkinsonism: onset, progression and mortality," *Neurology*, vol. 17, no. 5, pp. 427-42, May 1967, doi: 10.1212/wnl.17.5.427.
- [127] H. Braak, K. D. Tredici, U. Rüb, R. A. I. de Vos, E. N. H. Jansen Steur, and E. Braak, "Staging of brain pathology related to sporadic Parkinson's disease," *Neurobiology of Aging*, vol. 24, no. 2, pp. 197-211, 2003, doi: 10.1016/s0197-4580(02)00065-9.
- [128] F. Sixel-Doring, K. Liepe, B. Mollenhauer, E. Trautmann, and C. Trenkwalder, "The role of 123I-FP-CIT-SPECT in the differential diagnosis of Parkinson and tremor syndromes: a critical assessment of 125 cases," *J Neurol*, vol. 258, no. 12, pp. 2147-54, Dec 2011, doi: 10.1007/s00415-011-6076-z.
- [129] C. C. Verstappen, B. R. Bloem, C. A. Haaxma, W. J. Oyen, and M. W. Horstink, "Diagnostic value of asymmetric striatal D2 receptor upregulation in Parkinson's disease: an [123I]IBZM and [123I]FP-CIT SPECT study," *Eur J Nucl Med Mol Imaging*, vol. 34, no. 4, pp. 502-7, Apr 2007, doi: 10.1007/s00259-006-0258-4.
- [130] A. Kumar *et al.*, "[11C]DTBZ-PET correlates of levodopa responses in asymmetric Parkinson's disease," *Brain*, vol. 126, no. Pt 12, pp. 2648-55, Dec 2003, doi: 10.1093/brain/awg270.
- [131] Y. Kumakura *et al.*, "Elevated [(18)F]FDOPA utilization in the periaqueductal gray and medial nucleus accumbens of patients with early Parkinson's

- disease," *Neuroimage*, vol. 49, no. 4, pp. 2933-9, Feb 15 2010, doi: 10.1016/j.neuroimage.2009.11.035.
- [132] P. K. Morrish, J. S. Rakshi, D. L. Bailey, G. V. Sawle, and D. J. Brooks, "Measuring the rate of progression and estimating the preclinical period of Parkinson's disease with [18F]dopa PET," *Journal of Neurology, Neurosurgery & Psychiatry*, vol. 64, no. 3, pp. 314-319, 1998, doi: 10.1136/jnnp.64.3.314.
- [133] F. Miyoshi *et al.*, "Evaluation of Parkinson disease and Alzheimer disease with the use of neuromelanin MR imaging and (123)I-metaiodobenzylguanidine scintigraphy," *AJNR Am J Neuroradiol*, vol. 34, no. 11, pp. 2113-8, Nov-Dec 2013, doi: 10.3174/ajnr.A3567.
- [134] T. C. Booth, M. Nathan, A. D. Waldman, A. M. Quigley, A. H. Schapira, and J. Buscombe, "The role of functional dopamine-transporter SPECT imaging in parkinsonian syndromes, part 1," *AJNR Am J Neuroradiol*, vol. 36, no. 2, pp. 229-35, Feb 2015, doi: 10.3174/ajnr.A3970.
- [135] T. C. Booth, M. Nathan, A. D. Waldman, A. M. Quigley, A. H. Schapira, and J. Buscombe, "The role of functional dopamine-transporter SPECT imaging in parkinsonian syndromes, part 2," *AJNR Am J Neuroradiol*, vol. 36, no. 2, pp. 236-44, Feb 2015, doi: 10.3174/ajnr.A3971.
- [136] P. Riederer *et al.*, "Transition metals, ferritin, glutathione, and ascorbic acid in parkinsonian brains," *Journal of neurochemistry*, vol. 52, no. 2, pp. 515-520, 1989.
- [137] J. M. Gorell, R. J. Ordidge, G. G. Brown, J. C. Deniau, N. M. Buderer, and J. A. Helpner, "Increased iron-related MRI contrast in the substantia nigra in Parkinson's disease," *Neurology*, vol. 45, no. 6, pp. 1138-43, Jun 1995. [Online]. Available: <http://www.ncbi.nlm.nih.gov/pubmed/7783878>.
- [138] A. E. Oakley *et al.*, "Individual dopaminergic neurons show raised iron levels in Parkinson disease," *Neurology*, vol. 68, no. 21, pp. 1820-5, May 22 2007, doi: 10.1212/01.wnl.0000262033.01945.9a.
- [139] K. Jellinger, W. Paulus, I. Grundke-Iqbal, P. Riederer, and M. B. Youdim, "Brain iron and ferritin in Parkinson's and Alzheimer's diseases," *J Neural Transm Park Dis Dement Sect*, vol. 2, no. 4, pp. 327-40, 1990. [Online]. Available: <http://www.ncbi.nlm.nih.gov/pubmed/2078310>.

- [140] A. Wypijewska *et al.*, "Iron and reactive oxygen species activity in parkinsonian substantia nigra," *Parkinsonism Relat Disord*, vol. 16, no. 5, pp. 329-33, Jun 2010, doi: 10.1016/j.parkreldis.2010.02.007.
- [141] R. J. Uitti, A. H. Rajput, B. Rozdilsky, M. Bickis, T. Wollin, and W. K. Yuen, "Regional metal concentrations in Parkinson's disease, other chronic neurological diseases, and control brains," *Can J Neurol Sci*, vol. 16, no. 3, pp. 310-4, Aug 1989, doi: 10.1017/s0317167100029140.
- [142] J. Galazka-Friedman, E. R. Bauminger, A. Friedman, M. Barcikowska, D. Hechel, and I. Nowik, "Iron in parkinsonian and control substantia nigra--a Mossbauer spectroscopy study," *Mov Disord*, vol. 11, no. 1, pp. 8-16, Jan 1996, doi: 10.1002/mds.870110104.
- [143] "2021 Alzheimer's disease facts and figures," *Alzheimers & Dementia*, vol. 17, no. 3, pp. 327-406, Mar 2021, doi: 10.1002/alz.12328.
- [144] E. Bossy-Wetzel, R. Schwarzenbacher, and S. A. Lipton, "Molecular pathways to neurodegeneration," *Nat Med*, vol. 10 Suppl, pp. S2-9, Jul 2004, doi: 10.1038/nm1067.
- [145] C. R. Jack, Jr. *et al.*, "NIA-AA Research Framework: Toward a biological definition of Alzheimer's disease," *Alzheimers Dement*, vol. 14, no. 4, pp. 535-562, Apr 2018, doi: 10.1016/j.jalz.2018.02.018.
- [146] R. A. Sperling *et al.*, "Toward defining the preclinical stages of Alzheimer's disease: recommendations from the National Institute on Aging-Alzheimer's Association workgroups on diagnostic guidelines for Alzheimer's disease," *Alzheimers Dement*, vol. 7, no. 3, pp. 280-92, May 2011, doi: 10.1016/j.jalz.2011.03.003.
- [147] B. Dubois *et al.*, "Research criteria for the diagnosis of Alzheimer's disease: revising the NINCDS-ADRDA criteria," *The Lancet Neurology*, vol. 6, no. 8, pp. 734-746, 2007, doi: 10.1016/s1474-4422(07)70178-3.
- [148] H. Amieva *et al.*, "Prodromal Alzheimer's disease: successive emergence of the clinical symptoms," *Ann Neurol*, vol. 64, no. 5, pp. 492-8, Nov 2008, doi: 10.1002/ana.21509.

- [149] C. G. Lyketsos *et al.*, "Neuropsychiatric symptoms in Alzheimer's disease," *Alzheimers Dement*, vol. 7, no. 5, pp. 532-9, Sep 2011, doi: 10.1016/j.jalz.2011.05.2410.
- [150] P. M. Cogswell *et al.*, "Associations of quantitative susceptibility mapping with Alzheimer's disease clinical and imaging markers," *Neuroimage*, vol. 224, p. 117433, Jan 1 2021, doi: 10.1016/j.neuroimage.2020.117433.
- [151] S. Tiepolt *et al.*, "Quantitative Susceptibility Mapping of Amyloid-beta Aggregates in Alzheimer's Disease with 7T MR," *J Alzheimers Dis*, vol. 64, no. 2, pp. 393-404, 2018, doi: 10.3233/JAD-180118.
- [152] D. J. Hare *et al.*, "Laser ablation-inductively coupled plasma-mass spectrometry imaging of white and gray matter iron distribution in Alzheimer's disease frontal cortex," *Neuroimage*, vol. 137, pp. 124-131, Aug 15 2016, doi: 10.1016/j.neuroimage.2016.05.057.
- [153] S. van Duijn *et al.*, "Cortical Iron Reflects Severity of Alzheimer's Disease," *J Alzheimers Dis*, vol. 60, no. 4, pp. 1533-1545, 2017, doi: 10.3233/JAD-161143.
- [154] M. J. House, T. G. St Pierre, and C. McLean, "1.4T study of proton magnetic relaxation rates, iron concentrations, and plaque burden in Alzheimer's disease and control postmortem brain tissue," *Magn Reson Med*, vol. 60, no. 1, pp. 41-52, Jul 2008, doi: 10.1002/mrm.21586.
- [155] S. F. Graham *et al.*, "Age-associated changes of brain copper, iron, and zinc in Alzheimer's disease and dementia with Lewy bodies," *J Alzheimers Dis*, vol. 42, no. 4, pp. 1407-13, 2014, doi: 10.3233/JAD-140684.
- [156] N. Bloembergen, E. M. Purcell, and R. V. Pound, "Relaxation Effects in Nuclear Magnetic Resonance Absorption," *Physical Review*, vol. 73, no. 7, pp. 679-712, 1948, doi: 10.1103/PhysRev.73.679.
- [157] H. Y. Carr and E. M. Purcell, "Effects of Diffusion on Free Precession in Nuclear Magnetic Resonance Experiments," *Physical Review*, vol. 94, no. 3, pp. 630-638, 1954, doi: 10.1103/PhysRev.94.630.
- [158] H. M. McConnell, "Reaction Rates by Nuclear Magnetic Resonance," *The Journal of Chemical Physics*, vol. 28, no. 3, pp. 430-431, 1958, doi: 10.1063/1.1744152.

- [159] D. E. Woessner, "Effects of Diffusion in Nuclear Magnetic Resonance Spin-Echo Experiments," *The Journal of Chemical Physics*, vol. 34, no. 6, pp. 2057-2061, 1961, doi: 10.1063/1.1731821.
- [160] J. C. Gore, Y. S. Kang, and R. J. Schulz, "Measurement of radiation dose distributions by nuclear magnetic resonance (NMR) imaging," *Phys Med Biol*, vol. 29, no. 10, pp. 1189-97, Oct 1984. [Online]. Available: <https://www.ncbi.nlm.nih.gov/pubmed/6494247>.
- [161] I. Solomon, "Relaxation Processes in a System of Two Spins," *Physical Review*, vol. 99, no. 2, pp. 559-565, 1955, doi: 10.1103/PhysRev.99.559.
- [162] N. Bloembergen, "Spin Relaxation Processes in a Two-Proton System," *Physical Review*, vol. 104, no. 6, pp. 1542-1547, 1956, doi: 10.1103/PhysRev.104.1542.
- [163] S. Meiboom and D. Gill, "Modified Spin-Echo Method for Measuring Nuclear Relaxation Times," *Review of Scientific Instruments*, vol. 29, no. 8, pp. 688-691, 1958, doi: 10.1063/1.1716296.
- [164] J. H. Simpson and H. Y. Carr, "Diffusion and Nuclear Spin Relaxation in Water," *Physical Review*, vol. 111, no. 5, pp. 1201-1202, 1958, doi: 10.1103/PhysRev.111.1201.
- [165] N. Bloembergen and L. O. Morgan, "Proton Relaxation Times in Paramagnetic Solutions. Effects of Electron Spin Relaxation," *The Journal of Chemical Physics*, vol. 34, no. 3, pp. 842-850, 1961, doi: 10.1063/1.1731684.
- [166] M. H. Levitt, *Spin dynamics: basics of nuclear magnetic resonance*, 2 ed. John Wiley & Sons, 2008.
- [167] R. A. Brooks, J. Vymazal, R. B. Goldfarb, J. W. M. Bulte, and P. Aisen, "Relaxometry and magnetometry of ferritin," *Magnetic Resonance in Medicine*, vol. 40, no. 2, pp. 227-235, 1998, doi: 10.1002/mrm.1910400208.
- [168] Q. L. Vuong, P. Gillis, A. Roch, and Y. Gossuin, "Magnetic resonance relaxation induced by superparamagnetic particles used as contrast agents in magnetic resonance imaging: a theoretical review," *Wiley Interdiscip Rev Nanomed Nanobiotechnol*, vol. 9, no. 6, Nov 2017, doi: 10.1002/wnan.1468.
- [169] Y. Gossuin, A. Roch, R. N. Muller, and P. Gillis, "Relaxation induced by ferritin and ferritin-like magnetic particles: The role of proton exchange," *Magnetic*

- Resonance in Medicine*, vol. 43, no. 2, pp. 237-243, 2000, doi: 10.1002/(sici)1522-2594(200002)43:2<237::Aid-mrm10>3.0.Co;2-5.
- [170] Y. Gossuin, R. N. Muller, and P. Gillis, "Relaxation induced by ferritin: a better understanding for an improved MRI iron quantification," *NMR Biomed*, vol. 17, no. 7, pp. 427-32, Nov 2004, doi: 10.1002/nbm.903.
- [171] Y. Gossuin *et al.*, "Ferritin-induced relaxation in tissues: an in vitro study," *J Magn Reson Imaging*, vol. 20, no. 4, pp. 690-6, Oct 2004, doi: 10.1002/jmri.20152.
- [172] J. F. Schenck and E. A. Zimmerman, "High-field magnetic resonance imaging of brain iron: birth of a biomarker?," *NMR Biomed*, vol. 17, no. 7, pp. 433-45, Nov 2004, doi: 10.1002/nbm.922.
- [173] T. G. St Pierre, G. Jeffrey, J. Olynyk, and P. Pootrakul, "The effect of liver steatosis on non-invasive measurement of liver iron concentration by spin-density projection assisted R2-MRI (FerriScan[®])," *Journal of Hepatology*, vol. 66, no. 1, pp. S675-S676, 2017, doi: 10.1016/s0168-8278(17)31821-4.
- [174] T. G. St Pierre *et al.*, "Noninvasive measurement and imaging of liver iron concentrations using proton magnetic resonance," *Blood*, vol. 105, no. 2, pp. 855-61, Jan 15 2005, doi: 10.1182/blood-2004-01-0177.
- [175] G. Bartzokis *et al.*, "MRI evaluation of brain iron in earlier- and later-onset Parkinson's disease and normal subjects," *Magn Reson Imaging*, vol. 17, no. 2, pp. 213-22, Feb 1999. [Online]. Available: <http://www.ncbi.nlm.nih.gov/pubmed/10215476>.
- [176] G. Bartzokis *et al.*, "In vivo MR evaluation of age-related increases in brain iron," *AJNR Am J Neuroradiol*, vol. 15, no. 6, pp. 1129-38, Jun 1994. [Online]. Available: <http://www.ncbi.nlm.nih.gov/pubmed/8073983>.
- [177] J. P. Carpenter *et al.*, "On T2* magnetic resonance and cardiac iron," *Circulation*, vol. 123, no. 14, pp. 1519-28, Apr 12 2011, doi: 10.1161/CIRCULATIONAHA.110.007641.
- [178] J. S. Hankins *et al.*, "R2* magnetic resonance imaging of the liver in patients with iron overload," *Blood*, vol. 113, no. 20, pp. 4853-5, May 14 2009, doi: 10.1182/blood-2008-12-191643.

- [179] M. J. House, T. G. St Pierre, J. K. Foster, R. N. Martins, and R. Clarnette, "Quantitative MR imaging R2 relaxometry in elderly participants reporting memory loss," *AJNR Am J Neuroradiol*, vol. 27, no. 2, pp. 430-9, Feb 2006. [Online]. Available: <https://www.ncbi.nlm.nih.gov/pubmed/16484425>.
- [180] M. Ulla, J. M. Bonny, L. Ouchchane, I. Rieu, B. Claise, and F. Durif, "Is R2* a new MRI biomarker for the progression of Parkinson's disease? A longitudinal follow-up," *PLoS One*, vol. 8, no. 3, p. e57904, 2013, doi: 10.1371/journal.pone.0057904.
- [181] J. C. Wood and N. Ghugre, "Magnetic resonance imaging assessment of excess iron in thalassemia, sickle cell disease and other iron overload diseases," *Hemoglobin*, vol. 32, no. 1-2, pp. 85-96, 2008, doi: 10.1080/03630260701699912.
- [182] J. C. Wood *et al.*, "MRI R2 and R2* mapping accurately estimates hepatic iron concentration in transfusion-dependent thalassemia and sickle cell disease patients," *Blood*, vol. 106, no. 4, pp. 1460-5, Aug 15 2005, doi: 10.1182/blood-2004-10-3982.
- [183] J. Acosta-Cabronero, M. J. Betts, A. Cardenas-Blanco, S. Yang, and P. J. Nestor, "In Vivo MRI Mapping of Brain Iron Deposition across the Adult Lifespan," *J Neurosci*, vol. 36, no. 2, pp. 364-74, Jan 13 2016, doi: 10.1523/JNEUROSCI.1907-15.2016.
- [184] D. Aquino *et al.*, "Age-related iron deposition in the basal ganglia: quantitative analysis in healthy subjects," *Radiology*, vol. 252, no. 1, pp. 165-72, Jul 2009, doi: 10.1148/radiol.2522081399.
- [185] S. R. Cox *et al.*, "Ageing and brain white matter structure in 3,513 UK Biobank participants," *Nat Commun*, vol. 7, p. 13629, Dec 15 2016, doi: 10.1038/ncomms13629.
- [186] N. Gelman *et al.*, "MR imaging of human brain at 3.0 T: preliminary report on transverse relaxation rates and relation to estimated iron content," *Radiology*, vol. 210, no. 3, pp. 759-67, Mar 1999, doi: 10.1148/radiology.210.3.r99fe41759.
- [187] N. J. Gong, C. S. Wong, E. S. Hui, C. C. Chan, and L. M. Leung, "Hemisphere, gender and age-related effects on iron deposition in deep gray matter

- revealed by quantitative susceptibility mapping," *NMR Biomed*, vol. 28, no. 10, pp. 1267-74, Oct 2015, doi: 10.1002/nbm.3366.
- [188] E. M. Haacke *et al.*, "Correlation of putative iron content as represented by changes in R2* and phase with age in deep gray matter of healthy adults," *J Magn Reson Imaging*, vol. 32, no. 3, pp. 561-76, Sep 2010, doi: 10.1002/jmri.22293.
- [189] R. J. Ogg and R. G. Steen, "Age-related changes in brain T1 are correlated with iron concentration," *Magn Reson Med*, vol. 40, no. 5, pp. 749-53, Nov 1998. [Online]. Available: <http://www.ncbi.nlm.nih.gov/pubmed/9797159>.
- [190] Y. Zhang, I. W. Wu, D. Tosun, E. Foster, N. Schuff, and I. Parkinson's Progression Markers, "Progression of Regional Microstructural Degeneration in Parkinson's Disease: A Multicenter Diffusion Tensor Imaging Study," *PLoS One*, vol. 11, no. 10, p. e0165540, 2016, doi: 10.1371/journal.pone.0165540.
- [191] J. H. Barbosa *et al.*, "Quantifying brain iron deposition in patients with Parkinson's disease using quantitative susceptibility mapping, R2 and R2*," *Magn Reson Imaging*, vol. 33, no. 5, pp. 559-65, Jun 2015, doi: 10.1016/j.mri.2015.02.021.
- [192] D. Berg, B. Merz, K. Reiners, M. Naumann, and G. Becker, "Five-year follow-up study of hyperechogenicity of the substantia nigra in Parkinson's disease," *Mov Disord*, vol. 20, no. 3, pp. 383-5, Mar 2005, doi: 10.1002/mds.20311.
- [193] G. Castellanos *et al.*, "Automated neuromelanin imaging as a diagnostic biomarker for Parkinson's disease," *Mov Disord*, vol. 30, no. 7, pp. 945-52, Jun 2015, doi: 10.1002/mds.26201.
- [194] D. Gupta, J. Saini, C. Kesavadas, P. S. Sarma, and A. Kishore, "Utility of susceptibility-weighted MRI in differentiating Parkinson's disease and atypical parkinsonism," *Neuroradiology*, vol. 52, no. 12, pp. 1087-94, Dec 2010, doi: 10.1007/s00234-010-0677-6.
- [195] C. Ohtsuka *et al.*, "Differentiation of early-stage parkinsonisms using neuromelanin-sensitive magnetic resonance imaging," *Parkinsonism Relat Disord*, vol. 20, no. 7, pp. 755-60, Jul 2014, doi: 10.1016/j.parkreldis.2014.04.005.

- [196] S. Prasad, J. Saini, R. Yadav, and P. K. Pal, "Motor asymmetry and neuromelanin imaging: Concordance in Parkinson's disease," *Parkinsonism Relat Disord*, vol. 53, pp. 28-32, Aug 2018, doi: 10.1016/j.parkreldis.2018.04.022.
- [197] S. T. Schwarz, M. Afzal, P. S. Morgan, N. Bajaj, P. A. Gowland, and D. P. Auer, "The 'swallow tail' appearance of the healthy nigrosome - a new accurate test of Parkinson's disease: a case-control and retrospective cross-sectional MRI study at 3T," *PLoS One*, vol. 9, no. 4, p. e93814, 2014, doi: 10.1371/journal.pone.0093814.
- [198] C. Wang, G. Fan, K. Xu, and S. Wang, "Quantitative assessment of iron deposition in the midbrain using 3D-enhanced T2 star weighted angiography (ESWAN): a preliminary cross-sectional study of 20 Parkinson's disease patients," *Magn Reson Imaging*, vol. 31, no. 7, pp. 1068-73, Sep 2013, doi: 10.1016/j.mri.2013.04.015.
- [199] L. Du *et al.*, "Increased Iron Deposition on Brain Quantitative Susceptibility Mapping Correlates with Decreased Cognitive Function in Alzheimer's Disease," *ACS Chem Neurosci*, vol. 9, no. 7, pp. 1849-1857, Jul 18 2018, doi: 10.1021/acscchemneuro.8b00194.
- [200] Y. Qin *et al.*, "Investigation on positive correlation of increased brain iron deposition with cognitive impairment in Alzheimer disease by using quantitative MR R2' mapping," *J Huazhong Univ Sci Technolog Med Sci*, vol. 31, no. 4, pp. 578-85, Aug 2011, doi: 10.1007/s11596-011-0493-1.
- [201] R. Zivadinov *et al.*, "Brain Iron at Quantitative MRI Is Associated with Disability in Multiple Sclerosis," *Radiology*, vol. 289, no. 2, pp. 487-496, Nov 2018, doi: 10.1148/radiol.2018180136.
- [202] J. P. Armspach, D. Gounot, L. Rumbach, and J. Chambron, "In vivo determination of multiexponential T2 relaxation in the brain of patients with multiple sclerosis," *Magn Reson Imaging*, vol. 9, no. 1, pp. 107-13, 1991, doi: [https://doi.org/10.1016/0730-725X\(91\)90104-T](https://doi.org/10.1016/0730-725X(91)90104-T).
- [203] M. Khalil *et al.*, "Quantitative assessment of brain iron by R(2)* relaxometry in patients with clinically isolated syndrome and relapsing-remitting multiple

- sclerosis," *Mult Scler*, vol. 15, no. 9, pp. 1048-54, Sep 2009, doi: 10.1177/1352458509106609.
- [204] F. Schweser *et al.*, "Decreasing brain iron in multiple sclerosis: The difference between concentration and content in iron MRI," *Hum Brain Mapp*, Dec 30 2020, doi: 10.1002/hbm.25306.
- [205] D. S. Marcus, T. H. Wang, J. Parker, J. G. Csernansky, J. C. Morris, and R. L. Buckner, "Open Access Series of Imaging Studies (OASIS): cross-sectional MRI data in young, middle aged, nondemented, and demented older adults," *J Cogn Neurosci*, vol. 19, no. 9, pp. 1498-507, Sep 2007, doi: 10.1162/jocn.2007.19.9.1498.
- [206] C. R. Jack, Jr. *et al.*, "The Alzheimer's Disease Neuroimaging Initiative (ADNI): MRI methods," *J Magn Reson Imaging*, vol. 27, no. 4, pp. 685-91, Apr 2008, doi: 10.1002/jmri.21049.
- [207] I. Parkinson Progression Marker, "The Parkinson Progression Marker Initiative (PPMI)," *Prog Neurobiol*, vol. 95, no. 4, pp. 629-35, Dec 2011, doi: 10.1016/j.pneurobio.2011.09.005.
- [208] H. Benveniste *et al.*, "Anatomical and functional phenotyping of mice models of Alzheimer's disease by MR microscopy," *Ann N Y Acad Sci*, vol. 1097, pp. 12-29, Feb 2007, doi: 10.1196/annals.1379.006.
- [209] L. Cong *et al.*, "Multimodal MRI Evaluation of the MitoPark Mouse Model of Parkinson's Disease," *PLoS One*, vol. 11, no. 3, p. e0151884, 2016, doi: 10.1371/journal.pone.0151884.
- [210] C. Liu, W. Li, G. A. Johnson, and B. Wu, "High-field (9.4 T) MRI of brain dysmyelination by quantitative mapping of magnetic susceptibility," *Neuroimage*, vol. 56, no. 3, pp. 930-8, Jun 01 2011, doi: 10.1016/j.neuroimage.2011.02.024.
- [211] J. Klohs *et al.*, "Detection of cerebral microbleeds with quantitative susceptibility mapping in the ArcAbeta mouse model of cerebral amyloidosis," *J Cereb Blood Flow Metab*, vol. 31, no. 12, pp. 2282-92, Dec 2011, doi: 10.1038/jcbfm.2011.118.

- [212] J. Klohs *et al.*, "Longitudinal Assessment of Amyloid Pathology in Transgenic ArcAbeta Mice Using Multi-Parametric Magnetic Resonance Imaging," *PLoS One*, vol. 8, no. 6, p. e66097, 2013, doi: 10.1371/journal.pone.0066097.
- [213] M. D. Meadowcroft, J. R. Connor, M. B. Smith, and Q. X. Yang, "MRI and histological analysis of beta-amyloid plaques in both human Alzheimer's disease and APP/PS1 transgenic mice," *J Magn Reson Imaging*, vol. 29, no. 5, pp. 997-1007, May 2009, doi: 10.1002/jmri.21731.
- [214] J. O'Callaghan *et al.*, "Tissue magnetic susceptibility mapping as a marker of tau pathology in Alzheimer's disease," *Neuroimage*, vol. 159, pp. 334-345, Oct 1 2017, doi: 10.1016/j.neuroimage.2017.08.003.
- [215] E. Tuzzi *et al.*, "Ultra-High Field MRI in Alzheimer's Disease: Effective Transverse Relaxation Rate and Quantitative Susceptibility Mapping of Human Brain In Vivo and Ex Vivo compared to Histology," *J Alzheimers Dis*, vol. 73, no. 4, pp. 1481-1499, 2020, doi: 10.3233/JAD-190424.
- [216] R. W. Bowtell *et al.*, "NMR microscopy of single neurons using spin echo and line narrowed 2DFT imaging," *Magn Reson Med*, vol. 33, no. 6, pp. 790-4, Jun 1995, doi: 10.1002/mrm.1910330608.
- [217] K. Shmueli, J. A. de Zwart, P. van Gelderen, T. Q. Li, S. J. Dodd, and J. H. Duyn, "Magnetic susceptibility mapping of brain tissue in vivo using MRI phase data," *Magn Reson Med*, vol. 62, no. 6, pp. 1510-22, Dec 2009, doi: 10.1002/mrm.22135.
- [218] H. Benveniste, G. Einstein, K. R. Kim, C. Hulette, and G. A. Johnson, "Detection of neuritic plaques in Alzheimer's disease by magnetic resonance microscopy," *Proc Natl Acad Sci U S A*, vol. 96, no. 24, pp. 14079-84, Nov 23 1999, doi: 10.1073/pnas.96.24.14079.
- [219] C. Birkl *et al.*, "Iron mapping using the temperature dependency of the magnetic susceptibility," *Magn Reson Med*, vol. 73, no. 3, pp. 1282-8, Mar 2015, doi: 10.1002/mrm.25236.
- [220] C. Birkl *et al.*, "Assessment of ferritin content in multiple sclerosis brains using temperature-induced R*2 changes," *Magn Reson Med*, Jun 15 2017, doi: 10.1002/mrm.26780.

- [221] C. Wang *et al.*, "Methods for quantitative susceptibility and R2* mapping in whole post-mortem brains at 7T applied to amyotrophic lateral sclerosis," *Neuroimage*, vol. 222, p. 117216, Nov 15 2020, doi: 10.1016/j.neuroimage.2020.117216.
- [222] C. Rua *et al.*, "Multi-centre, multi-vendor reproducibility of 7T QSM and R2* in the human brain: Results from the UK7T study," *Neuroimage*, vol. 223, p. 117358, Dec 2020, doi: 10.1016/j.neuroimage.2020.117358.
- [223] S. Lehericy, E. Bardinet, C. Poupon, M. Vidailhet, and C. Francois, "7 Tesla magnetic resonance imaging: a closer look at substantia nigra anatomy in Parkinson's disease," *Mov Disord*, vol. 29, no. 13, pp. 1574-81, Nov 2014, doi: 10.1002/mds.26043.
- [224] S. Wharton and R. Bowtell, "Whole-brain susceptibility mapping at high field: a comparison of multiple- and single-orientation methods," *Neuroimage*, vol. 53, no. 2, pp. 515-25, Nov 1 2010, doi: 10.1016/j.neuroimage.2010.06.070.
- [225] B. C. Tandler and R. Bowtell, "Frequency difference mapping applied to the corpus callosum at 7T," *Magn Reson Med*, vol. 81, no. 5, pp. 3017-3031, May 2019, doi: 10.1002/mrm.27626.
- [226] A. I. Blazejewska *et al.*, "Visualization of nigrosome 1 and its loss in PD: pathoanatomical correlation and in vivo 7 T MRI," *Neurology*, vol. 81, no. 6, pp. 534-40, Aug 06 2013, doi: 10.1212/WNL.0b013e31829e6fd2.
- [227] D. A. Yablonskiy and E. M. Haacke, "Theory of NMR signal behavior in magnetically inhomogeneous tissues: The static dephasing regime," *Magnetic Resonance in Medicine*, vol. 32, no. 6, pp. 749-763, 1994, doi: 10.1002/mrm.1910320610.
- [228] D. A. Yablonskiy, "Quantitation of intrinsic magnetic susceptibility-related effects in a tissue matrix. Phantom study," *Magn Reson Med*, vol. 39, no. 3, pp. 417-28, Mar 1998, doi: 10.1002/mrm.1910390312.
- [229] J. R. Reichenbach, R. Venkatesan, D. A. Yablonskiy, M. R. Thompson, S. Lai, and E. M. Haacke, "Theory and application of static field inhomogeneity effects in gradient-echo imaging," *J Magn Reson Imaging*, vol. 7, no. 2, pp. 266-79, Mar-Apr 1997, doi: 10.1002/jmri.1880070203.

- [230] X. He and D. A. Yablonskiy, "Biophysical mechanisms of phase contrast in gradient echo MRI," *Proc Natl Acad Sci U S A*, vol. 106, no. 32, pp. 13558-63, Aug 11 2009, doi: 10.1073/pnas.0904899106.
- [231] D. W. McRobbie, E. A. Moore, M. J. Graves, and M. R. Prince, *MRI from picture to proton*. Cambridge, United Kingdom: The Press Syndicate of the University of Cambridge, 2003.
- [232] L. G. Hanson, "Is quantum mechanics necessary for understanding magnetic resonance?," *Concepts in Magnetic Resonance Part A*, vol. 32A, no. 5, pp. 329-340, 2008, doi: 10.1002/cmr.a.20123.
- [233] K. P. Pruessmann, M. Weiger, M. B. Scheidegger, and P. Boesiger, "SENSE: sensitivity encoding for fast MRI," *Magn Reson Med*, vol. 42, no. 5, pp. 952-62, Nov 1999. [Online]. Available: <http://www.ncbi.nlm.nih.gov/pubmed/10542355>.
- [234] E. L. Hahn, "Spin Echoes," *Physical Review*, vol. 80, no. 4, pp. 580-594, 1950, doi: 10.1103/PhysRev.80.580.
- [235] J. Hennig, A. Nauerth, and H. Friedburg, "RARE imaging: a fast imaging method for clinical MR," *Magn Reson Med*, vol. 3, no. 6, pp. 823-33, Dec 1986, doi: 10.1002/mrm.1910030602.
- [236] K. M. Jones *et al.*, "Brain hemorrhage: evaluation with fast spin-echo and conventional dual spin-echo images," *Radiology*, vol. 182, no. 1, pp. 53-8, Jan 1992, doi: 10.1148/radiology.182.1.1727309.
- [237] E. G. Kholmovski, A. A. Samsonov, and D. L. Parker, "Motion artifact reduction technique for dual-contrast FSE imaging," *Magnetic Resonance Imaging*, vol. 20, no. 6, pp. 455-462, 2002, doi: 10.1016/s0730-725x(02)00526-x.
- [238] C. J. Durrant, M. P. Hertzberg, and P. W. Kuchel, "Magnetic susceptibility: Further insights into macroscopic and microscopic fields and the sphere of Lorentz," *Concepts in Magnetic Resonance*, vol. 18A, no. 1, pp. 72-95, 2003, doi: 10.1002/cmr.a.10067.
- [239] J. F. Schenck, "The role of magnetic susceptibility in magnetic resonance imaging: MRI magnetic compatibility of the first and second kinds," *Med Phys*, vol. 23, no. 6, pp. 815-50, Jun 1996, doi: 10.1118/1.597854.

- [240] J. H. Duyn and J. Schenck, "Contributions to magnetic susceptibility of brain tissue," *NMR Biomed*, vol. 30, no. 4, Apr 2017, doi: 10.1002/nbm.3546.
- [241] Y. Gossuin, P. Gillis, A. Hocq, Q. L. Vuong, and A. Roch, "Magnetic resonance relaxation properties of superparamagnetic particles," *Wiley Interdiscip Rev Nanomed Nanobiotechnol*, vol. 1, no. 3, pp. 299-310, May-Jun 2009, doi: 10.1002/wnan.36.
- [242] Y. Gossuin *et al.*, "NMR relaxation induced by iron oxide particles: testing theoretical models," *Nanotechnology*, vol. 27, no. 15, p. 155706, Apr 15 2016, doi: 10.1088/0957-4484/27/15/155706.
- [243] R. Salomir, B. D. de Senneville, and C. T. W. Moonen, "A fast calculation method for magnetic field inhomogeneity due to an arbitrary distribution of bulk susceptibility," *Concepts in Magnetic Resonance*, vol. 19B, no. 1, pp. 26-34, 2003, doi: 10.1002/cmr.b.10083.
- [244] F. Schweser, A. Deistung, and J. R. Reichenbach, "Foundations of MRI phase imaging and processing for Quantitative Susceptibility Mapping (QSM)," *Z Med Phys*, vol. 26, no. 1, pp. 6-34, Mar 2016, doi: 10.1016/j.zemedi.2015.10.002.
- [245] F. Schweser, A. Deistung, B. W. Lehr, and J. R. Reichenbach, "Quantitative imaging of intrinsic magnetic tissue properties using MRI signal phase: an approach to in vivo brain iron metabolism?," *Neuroimage*, vol. 54, no. 4, pp. 2789-807, Feb 14 2011, doi: 10.1016/j.neuroimage.2010.10.070.
- [246] T. Liu *et al.*, "A novel background field removal method for MRI using projection onto dipole fields (PDF)," *NMR Biomed*, vol. 24, no. 9, pp. 1129-36, Nov 2011, doi: 10.1002/nbm.1670.
- [247] A. Hocq, M. Luhmer, S. Saussez, S. Louryan, P. Gillis, and Y. Gossuin, "Effect of magnetic field and iron content on NMR proton relaxation of liver, spleen and brain tissues," *Contrast Media Mol Imaging*, vol. 10, no. 2, pp. 144-52, Mar-Apr 2015, doi: 10.1002/cmml.1610.
- [248] P. A. Hardy, D. Gash, R. Yokel, A. Andersen, Y. Ai, and Z. Zhang, "Correlation of R2 with total iron concentration in the brains of rhesus monkeys," *J Magn Reson Imaging*, vol. 21, no. 2, pp. 118-27, Feb 2005, doi: 10.1002/jmri.20244.

- [249] C. Langkammer *et al.*, "Quantitative MR imaging of brain iron: a postmortem validation study," *Radiology*, vol. 257, no. 2, pp. 455-62, Nov 2010, doi: 10.1148/radiol.10100495.
- [250] N. Ben-Eliezer, D. K. Sodickson, and K. T. Block, "Rapid and accurate T2 mapping from multi-spin-echo data using Bloch-simulation-based reconstruction," *Magnetic resonance in medicine*, vol. 73, no. 2, pp. 809-817, 2015.
- [251] G. Bartzokis *et al.*, "In vivo evaluation of brain iron in Alzheimer's disease and normal subjects using MRI," *Biological psychiatry*, vol. 35, no. 7, pp. 480-487, 1994.
- [252] E. M. Haacke, Y. Xu, Y. C. N. Cheng, and J. R. Reichenbach, "Susceptibility weighted imaging (SWI)," *Magnetic resonance in medicine*, vol. 52, no. 3, pp. 612-618, 2004.
- [253] F. Schweser, A. Deistung, B. W. Lehr, and J. R. Reichenbach, "Quantitative imaging of intrinsic magnetic tissue properties using MRI signal phase: an approach to in vivo brain iron metabolism?," *Neuroimage*, vol. 54, no. 4, pp. 2789-2807, 2011.
- [254] J. H. Jensen *et al.*, "Magnetic field correlation as a measure of iron-generated magnetic field inhomogeneities in the brain," *Magnetic resonance in medicine*, vol. 61, no. 2, pp. 481-485, 2009.
- [255] S. H. Koenig and R. D. Brown, 3rd, "Determinants of proton relaxation rates in tissue," *Magn Reson Med*, vol. 1, no. 4, pp. 437-49, Dec 1984, doi: 10.1002/mrm.1910010404.
- [256] R. B. Lauffer, "Paramagnetic metal complexes as water proton relaxation agents for NMR imaging: theory and design," *Chemical Reviews*, vol. 87, no. 5, pp. 901-927, 1987, doi: 10.1021/cr00081a003.
- [257] J. F. Schenck, "Imaging of brain iron by magnetic resonance: T2 relaxation at different field strengths," *Journal of the neurological sciences*, vol. 134, pp. 10-18, 1995.
- [258] J. Vymazal *et al.*, "The relation between brain iron and NMR relaxation times: An invitro study," *Magnetic Resonance in Medicine*, vol. 35, no. 1, pp. 56-61, 1996, doi: 10.1002/mrm.1910350108.

- [259] G. B. Chavhan, P. S. Babyn, B. Thomas, M. M. Shroff, and E. M. Haacke, "Principles, techniques, and applications of T2*-based MR imaging and its special applications," *Radiographics*, vol. 29, no. 5, pp. 1433-49, Sep-Oct 2009, doi: 10.1148/rg.295095034.
- [260] A. Deistung, A. Schafer, F. Schweser, U. Biedermann, R. Turner, and J. R. Reichenbach, "Toward in vivo histology: a comparison of quantitative susceptibility mapping (QSM) with magnitude-, phase-, and R2*-imaging at ultra-high magnetic field strength," *Neuroimage*, vol. 65, pp. 299-314, Jan 15 2013, doi: 10.1016/j.neuroimage.2012.09.055.
- [261] Q. Wang, K. Li, Q. Quan, and G. Zhang, "R2* and R2 mapping for quantifying recruitment of superparamagnetic iron oxide-tagged endothelial progenitor cells to injured liver: tracking in vitro and in vivo," *Int J Nanomedicine*, vol. 9, pp. 1815-22, 2014, doi: 10.2147/IJN.S58269.
- [262] D. A. Yablonskiy, "Quantitative T2 contrast with gradient echoes," in *Proceedings of the International Society for Magnetic Resonance in Medicine*, Denver, CO United States, 2000.
- [263] R. J. Ordidge, J. M. Gorell, J. C. Deniau, R. A. Knight, and J. A. Helpert, "Assessment of relative brain iron concentrations using T2-weighted and T2*-weighted MRI at 3 Tesla," *Magnetic resonance in medicine*, vol. 32, no. 3, pp. 335-341, 1994.
- [264] G. Bartzokis, M. Aravagiri, W. H. Oldendorf, J. Mintz, and S. R. Marder, "Field dependent transverse relaxation rate increase may be a specific measure of tissue iron stores," *Magnetic Resonance in Medicine*, vol. 29, no. 4, pp. 459-464, 1993.
- [265] G. Bartzokis *et al.*, "In vivo MR evaluation of age-related increases in brain iron," *American Journal of Neuroradiology*, vol. 15, no. 6, pp. 1129-1138, 1994.
- [266] E. M. Haacke, Y. Xu, Y. C. Cheng, and J. R. Reichenbach, "Susceptibility weighted imaging (SWI)," *Magn Reson Med*, vol. 52, no. 3, pp. 612-8, Sep 2004, doi: 10.1002/mrm.20198.

- [267] E. M. Haacke, S. Mittal, Z. Wu, J. Neelavalli, and Y. C. Cheng, "Susceptibility-weighted imaging: technical aspects and clinical applications, part 1," *AJNR Am J Neuroradiol*, vol. 30, no. 1, pp. 19-30, Jan 2009, doi: 10.3174/ajnr.A1400.
- [268] F. Schweser and R. Zivadinov, "Quantitative susceptibility mapping (QSM) with an extended physical model for MRI frequency contrast in the brain: a proof-of-concept of quantitative susceptibility and residual (QUASAR) mapping," *NMR Biomed*, vol. 31, no. 12, p. e3999, Dec 2018, doi: 10.1002/nbm.3999.
- [269] C. Langkammer *et al.*, "Quantitative susceptibility mapping: Report from the 2016 reconstruction challenge," *Magn Reson Med*, vol. 79, no. 3, pp. 1661-1673, Mar 2018, doi: 10.1002/mrm.26830.
- [270] X. Lu *et al.*, "Simultaneous quantitative susceptibility mapping (QSM) and R2* for high iron concentration quantification with 3D ultrashort echo time sequences: An echo dependence study," *Magn Reson Med*, vol. 79, no. 4, pp. 2315-2322, Apr 2018, doi: 10.1002/mrm.27062.
- [271] Z. Liu, P. Spincemaille, Y. Yao, Y. Zhang, and Y. Wang, "MEDI+0: Morphology enabled dipole inversion with automatic uniform cerebrospinal fluid zero reference for quantitative susceptibility mapping," *Magn Reson Med*, vol. 79, no. 5, pp. 2795-2803, May 2018, doi: 10.1002/mrm.26946.
- [272] Z. Liu, Y. Kee, D. Zhou, Y. Wang, and P. Spincemaille, "Preconditioned total field inversion (TFI) method for quantitative susceptibility mapping," *Magn Reson Med*, vol. 78, no. 1, pp. 303-315, Jul 2017, doi: 10.1002/mrm.26331.
- [273] J. Acosta-Cabronero, C. Milovic, H. Mattern, C. Tejos, O. Speck, and M. F. Callaghan, "A robust multi-scale approach to quantitative susceptibility mapping," *Neuroimage*, vol. 183, pp. 7-24, Dec 2018, doi: 10.1016/j.neuroimage.2018.07.065.
- [274] S. D. Robinson, K. Bredies, D. Khabipova, B. Dymerska, J. P. Marques, and F. Schweser, "An illustrated comparison of processing methods for MR phase imaging and QSM: combining array coil signals and phase unwrapping," *NMR Biomed*, vol. 30, no. 4, Apr 2017, doi: 10.1002/nbm.3601.
- [275] F. Schweser, S. D. Robinson, L. de Rochefort, W. Li, and K. Bredies, "An illustrated comparison of processing methods for phase MRI and QSM:

- removal of background field contributions from sources outside the region of interest," *NMR Biomed*, vol. 30, no. 4, Apr 2017, doi: 10.1002/nbm.3604.
- [276] D. Zhou, T. Liu, P. Spincemaille, and Y. Wang, "Background field removal by solving the Laplacian boundary value problem," *NMR Biomed*, vol. 27, no. 3, pp. 312-9, Mar 2014, doi: 10.1002/nbm.3064.
- [277] H. Sun and A. H. Wilman, "Background field removal using spherical mean value filtering and Tikhonov regularization," *Magn Reson Med*, vol. 71, no. 3, pp. 1151-7, Mar 2014, doi: 10.1002/mrm.24765.
- [278] M. Bertero and P. Boccacci, *Introduction to Inverse Problems in Imaging*. 2020.
- [279] T. Liu, P. Spincemaille, L. de Rochefort, B. Kressler, and Y. Wang, "Calculation of susceptibility through multiple orientation sampling (COSMOS): a method for conditioning the inverse problem from measured magnetic field map to susceptibility source image in MRI," *Magn Reson Med*, vol. 61, no. 1, pp. 196-204, Jan 2009, doi: 10.1002/mrm.21828.
- [280] C. C. Paige and M. A. Saunders, "LSQR: An Algorithm for Sparse Linear Equations and Sparse Least Squares," *ACM Transactions on Mathematical Software*, vol. 8, no. 1, pp. 43-71, 1982, doi: 10.1145/355984.355989.
- [281] T. Liu *et al.*, "Morphology enabled dipole inversion (MEDI) from a single-angle acquisition: comparison with COSMOS in human brain imaging," *Magn Reson Med*, vol. 66, no. 3, pp. 777-83, Sep 2011, doi: 10.1002/mrm.22816.
- [282] C. Chai *et al.*, "Increased brain iron deposition is a risk factor for brain atrophy in patients with haemodialysis: a combined study of quantitative susceptibility mapping and whole brain volume analysis," *Metab Brain Dis*, vol. 30, no. 4, pp. 1009-16, Aug 2015, doi: 10.1007/s11011-015-9664-2.
- [283] J. H. Jensen *et al.*, "Magnetic field correlation imaging," *Magn Reson Med*, vol. 55, no. 6, pp. 1350-61, Jun 2006, doi: 10.1002/mrm.20907.
- [284] J. H. Jensen *et al.*, "Magnetic field correlation as a measure of iron-generated magnetic field inhomogeneities in the brain," *Magn Reson Med*, vol. 61, no. 2, pp. 481-5, Feb 2009, doi: 10.1002/mrm.21823.
- [285] J. C. Wood, J. D. Fassler, and T. Meade, "Mimicking liver iron overload using liposomal ferritin preparations," *Magn Reson Med*, vol. 51, no. 3, pp. 607-11, Mar 2004, doi: 10.1002/mrm.10735.

- [286] E. Yoshimaru, J. Totenhagen, G. E. Alexander, and T. P. Trouard, "Design, manufacture, and analysis of customized phantoms for enhanced quality control in small animal MRI systems," *Magn Reson Med*, vol. 71, no. 2, pp. 880-4, Feb 2014, doi: 10.1002/mrm.24678.
- [287] Q. Duan *et al.*, "Characterization of a dielectric phantom for high-field magnetic resonance imaging applications," *Med Phys*, vol. 41, no. 10, p. 102303, Oct 2014, doi: 10.1118/1.4895823.
- [288] C. Ianniello *et al.*, "Synthesized tissue-equivalent dielectric phantoms using salt and polyvinylpyrrolidone solutions," *Magn Reson Med*, vol. 80, no. 1, pp. 413-419, Jul 2018, doi: 10.1002/mrm.27005.
- [289] A. Sekowska *et al.*, "Nanodiamond phantoms mimicking human liver: perspective to calibration of T1 relaxation time in magnetic resonance imaging," *Sci Rep*, vol. 10, no. 1, p. 6446, Apr 15 2020, doi: 10.1038/s41598-020-63581-9.
- [290] J. P. Marques *et al.*, "QSM reconstruction challenge 2.0: A realistic in silico head phantom for MRI data simulation and evaluation of susceptibility mapping procedures," *Magn Reson Med*, Feb 26 2021, doi: 10.1002/mrm.28716.
- [291] R. Kuhlperter *et al.*, "R2 and R2* mapping for sensing cell-bound superparamagnetic nanoparticles: in vitro and murine in vivo testing," *Radiology*, vol. 245, no. 2, pp. 449-57, Nov 2007, doi: 10.1148/radiol.2451061345.
- [292] K. M. Bennett, E. M. Shapiro, C. H. Sotak, and A. P. Koretsky, "Controlled aggregation of ferritin to modulate MRI relaxivity," *Biophys J*, vol. 95, no. 1, pp. 342-51, Jul 2008, doi: 10.1529/biophysj.107.116145.
- [293] P. Trujillo *et al.*, "Contrast mechanisms associated with neuromelanin-MRI," *Magn Reson Med*, Dec 26 2016, doi: 10.1002/mrm.26584.
- [294] M. Nilsson *et al.*, "Liquid crystal phantom for validation of microscopic diffusion anisotropy measurements on clinical MRI systems," *Magn Reson Med*, vol. 79, no. 3, pp. 1817-1828, Mar 2018, doi: 10.1002/mrm.26814.

- [295] E. Fieremans and H. H. Lee, "Physical and numerical phantoms for the validation of brain microstructural MRI: A cookbook," *Neuroimage*, vol. 182, pp. 39-61, Nov 15 2018, doi: 10.1016/j.neuroimage.2018.06.046.
- [296] C. Birkl *et al.*, "The influence of iron oxidation state on quantitative MRI parameters in post mortem human brain," *Neuroimage*, p. 117080, Jun 22 2020, doi: 10.1016/j.neuroimage.2020.117080.
- [297] Z. S. Nasreddine *et al.*, "The Montreal Cognitive Assessment, MoCA: a brief screening tool for mild cognitive impairment," *J Am Geriatr Soc*, vol. 53, no. 4, pp. 695-9, Apr 2005, doi: 10.1111/j.1532-5415.2005.53221.x.
- [298] T. Liu, C. Wisnieff, M. Lou, W. Chen, P. Spincemaille, and Y. Wang, "Nonlinear formulation of the magnetic field to source relationship for robust quantitative susceptibility mapping," *Magn Reson Med*, vol. 69, no. 2, pp. 467-76, Feb 2013, doi: 10.1002/mrm.24272.
- [299] X. Wei and I. Cumming, "A region-growing algorithm for InSAR phase unwrapping," *IEEE Transactions on Geoscience and Remote Sensing*, vol. 37, no. 1, pp. 124-134, 1999, doi: 10.1109/36.739143.
- [300] M. A. Schofield and Y. Zhu, "Fast phase unwrapping algorithm for interferometric applications," *Opt. Lett.*, vol. 28, no. 14, pp. 1194-1196, 2003/07/15 2003, doi: 10.1364/OL.28.001194.
- [301] J. P. Marques and R. Bowtell, "Application of a Fourier-based method for rapid calculation of field inhomogeneity due to spatial variation of magnetic susceptibility," *Concepts in Magnetic Resonance Part B: Magnetic Resonance Engineering*, vol. 25B, no. 1, pp. 65-78, 2005, doi: 10.1002/cmr.b.20034.
- [302] W. Li, B. Wu, and C. Liu, "Quantitative susceptibility mapping of human brain reflects spatial variation in tissue composition," *Neuroimage*, vol. 55, no. 4, pp. 1645-56, Apr 15 2011, doi: 10.1016/j.neuroimage.2010.11.088.
- [303] P. S. Ozbay, A. Deistung, X. Feng, D. Nanz, J. R. Reichenbach, and F. Schweser, "A comprehensive numerical analysis of background phase correction with V-SHARP," *NMR Biomed*, vol. 30, no. 4, Apr 2017, doi: 10.1002/nbm.3550.
- [304] J. Fang, L. Bao, X. Li, P. C. M. van Zijl, and Z. Chen, "Background field removal using a region adaptive kernel for quantitative susceptibility mapping of

- human brain," *J Magn Reson*, vol. 281, pp. 130-140, Aug 2017, doi: 10.1016/j.jmr.2017.05.004.
- [305] B. Bilgic *et al.*, "Fast quantitative susceptibility mapping with L1-regularization and automatic parameter selection," *Magn Reson Med*, vol. 72, no. 5, pp. 1444-59, Nov 2014, doi: 10.1002/mrm.25029.
- [306] L. Bao, X. Li, C. Cai, Z. Chen, and P. C. van Zijl, "Quantitative Susceptibility Mapping Using Structural Feature Based Collaborative Reconstruction (SFCR) in the Human Brain," *IEEE Trans Med Imaging*, vol. 35, no. 9, pp. 2040-50, Sep 2016, doi: 10.1109/TMI.2016.2544958.
- [307] C. Milovic, B. Bilgic, B. Zhao, J. Acosta-Cabronero, and C. Tejos, "Fast nonlinear susceptibility inversion with variational regularization," *Magn Reson Med*, vol. 80, no. 2, pp. 814-821, Aug 2018, doi: 10.1002/mrm.27073.
- [308] D. A. Yablonskiy and A. L. Sukstanskii, "Generalized Lorentzian Tensor Approach (GLTA) as a biophysical background for quantitative susceptibility mapping," *Magn Reson Med*, vol. 73, no. 2, pp. 757-64, Feb 2015, doi: 10.1002/mrm.25538.
- [309] Daniel Polak *et al.*, "Nonlinear Dipole Inversion (NDI) enables Quantitative Susceptibility Mapping (QSM) without parameter tuning," *Preprint*, 2021.
- [310] L. de Rochefort *et al.*, "Quantitative susceptibility map reconstruction from MR phase data using bayesian regularization: validation and application to brain imaging," *Magn Reson Med*, vol. 63, no. 1, pp. 194-206, Jan 2010, doi: 10.1002/mrm.22187.
- [311] K. Deh *et al.*, "Multicenter reproducibility of quantitative susceptibility mapping in a gadolinium phantom using MEDI+0 automatic zero referencing," *Magn Reson Med*, vol. 81, no. 2, pp. 1229-1236, Feb 2019, doi: 10.1002/mrm.27410.
- [312] T. P. Naidich, H. M. Duvernoy, B. N. Delman, A. G. Sorensen, S. S. Kollias, and E. M. Haacke, *Duvernoy's atlas of the human brain stem and cerebellum: high-field MRI, surface anatomy, internal structure, vascularization and 3 D sectional anatomy*. Springer Science & Business Media, 2009.
- [313] F. Fellner *et al.*, "True proton density and T2-weighted turbo spin-echo sequences for routine MRI of the brain," *Neuroradiology*, vol. 36, no. 8, pp.

591-7, Nov 1994. [Online]. Available:
<https://www.ncbi.nlm.nih.gov/pubmed/7862271>.

- [314] M. Weigel and J. Hennig, "Contrast behavior and relaxation effects of conventional and hyperecho-turbo spin echo sequences at 1.5 and 3 T," *Magn Reson Med*, vol. 55, no. 4, pp. 826-35, Apr 2006, doi: 10.1002/mrm.20816.
- [315] C. M. Bauer, H. Jara, and R. Killiany, "Whole brain quantitative T2 MRI across multiple scanners with dual echo FSE: Applications to AD, MCI, and normal aging☆," *NeuroImage*, vol. 52, no. 2, pp. 508-514, 2010, doi: 10.1016/j.neuroimage.2010.04.255.
- [316] K. C. McPhee and A. H. Wilman, "T2 quantification from only proton density and T2-weighted MRI by modelling actual refocusing angles," *Neuroimage*, vol. 118, pp. 642-50, Sep 2015, doi: 10.1016/j.neuroimage.2015.05.079.
- [317] M. N. Uddin, K. C. McPhee, G. Blevins, and A. H. Wilman, "Recovery of accurate T2 from historical 1.5 Tesla proton density and T2-weighted images: Application to 7-year T2 changes in multiple sclerosis brain," *Magn Reson Imaging*, vol. 37, pp. 21-26, Apr 2017, doi: 10.1016/j.mri.2016.11.007.
- [318] K. C. McPhee and A. H. Wilman, "Transverse relaxation and flip angle mapping: Evaluation of simultaneous and independent methods using multiple spin echoes," *Magn Reson Med*, vol. 77, no. 5, pp. 2057-2065, May 2017, doi: 10.1002/mrm.26285.
- [319] R. Djaldetti, I. Ziv, and E. Melamed, "The mystery of motor asymmetry in Parkinson's disease," *The Lancet Neurology*, vol. 5, no. 9, pp. 796-802, 2006, doi: 10.1016/s1474-4422(06)70549-x.
- [320] D. E. Hobson, "Asymmetry in parkinsonism, spreading pathogens and the nose," *Parkinsonism Relat Disord*, vol. 18, no. 1, pp. 1-9, Jan 2012, doi: 10.1016/j.parkreldis.2011.06.011.
- [321] M. J. Barrett, S. A. Wylie, M. B. Harrison, and G. F. Wooten, "Handedness and motor symptom asymmetry in Parkinson's disease," *J Neurol Neurosurg Psychiatry*, vol. 82, no. 10, pp. 1122-4, Oct 2011, doi: 10.1136/jnnp.2010.209783.

- [322] J. Wang *et al.*, "MRI evaluation of asymmetry of nigrostriatal damage in the early stage of early-onset Parkinson's disease," *Parkinsonism Relat Disord*, vol. 21, no. 6, pp. 590-6, Jun 2015, doi: 10.1016/j.parkreldis.2015.03.012.
- [323] G. Pagano, N. Ferrara, D. J. Brooks, and N. Pavese, "Age at onset and Parkinson disease phenotype," *Neurology*, vol. 86, no. 15, pp. 1400-7, Apr 12 2016, doi: 10.1212/WNL.0000000000002461.
- [324] A. Martin-Bastida *et al.*, "Relationship between neuromelanin and dopamine terminals within the Parkinson's nigrostriatal system," *Brain*, May 5 2019, doi: 10.1093/brain/awz120.
- [325] P. A. Kempster, W. R. Gibb, G. M. Stern, and A. J. Lees, "Asymmetry of substantia nigra neuronal loss in Parkinson's disease and its relevance to the mechanism of levodopa related motor fluctuations," *J Neurol Neurosurg Psychiatry*, vol. 52, no. 1, pp. 72-6, Jan 1989, doi: 10.1136/jnnp.52.1.72.
- [326] J. H. Kordower *et al.*, "Disease duration and the integrity of the nigrostriatal system in Parkinson's disease," *Brain*, vol. 136, no. Pt 8, pp. 2419-31, Aug 2013, doi: 10.1093/brain/awt192.
- [327] P. Damier, "The substantia nigra of the human brain: II. Patterns of loss of dopamine-containing neurons in Parkinson's disease," *Brain*, vol. 122, no. 8, pp. 1437-1448, 1999, doi: 10.1093/brain/122.8.1437.
- [328] E. Sofic *et al.*, "Increased iron (III) and total iron content in post mortem substantia nigra of parkinsonian brain," *Journal of neural transmission*, vol. 74, no. 3, pp. 199-205, 1988.
- [329] P. D. Griffiths, B. R. Dobson, G. R. Jones, and D. T. Clarke, "Iron in the basal ganglia in Parkinson's disease," *Brain*, vol. 122, no. 4, pp. 667-673, 1999, doi: 10.1093/brain/122.4.667.
- [330] M. Brammerloh *et al.*, "Toward an early diagnostic marker of Parkinson's: measuring iron in dopaminergic neurons with MR relaxometry," *BioRxiv*, 2020, doi: 10.1101/2020.07.01.170563.
- [331] M. Brammerloh *et al.*, "Measuring the iron content of dopaminergic neurons in substantia nigra with MRI relaxometry," *Neuroimage*, vol. 239, p. 118255, Oct 1 2021, doi: 10.1016/j.neuroimage.2021.118255.

- [332] J. Y. Wang *et al.*, "Meta-analysis of brain iron levels of Parkinson's disease patients determined by postmortem and MRI measurements," *Sci Rep*, vol. 6, p. 36669, Nov 9 2016, doi: 10.1038/srep36669.
- [333] R. J. Ordidge, J. M. Gorell, J. C. Deniau, R. A. Knight, and J. A. Helpert, "Assessment of relative brain iron concentrations using T2-weighted and T2*-weighted MRI at 3 Tesla," *Magnetic Resonance in Medicine*, vol. 32, no. 3, pp. 335-341, 1994, doi: 10.1002/mrm.1910320309.
- [334] J. Georgi, R. Metere, C. Jager, M. Morawski, and H. E. Moller, "Influence of the extracellular matrix on water mobility in subcortical gray matter," *Magn Reson Med*, vol. 81, no. 2, pp. 1265-1279, Feb 2019, doi: 10.1002/mrm.27459.
- [335] K. Dzieciol, E. Iordanishvili, Z. Abbas, A. Nahimi, M. Winterdahl, and N. J. Shah, "A robust method for the detection of small changes in relaxation parameters and free water content in the vicinity of the substantia nigra in Parkinson's disease patients," *PLoS One*, vol. 16, no. 2, p. e0247552, 2021, doi: 10.1371/journal.pone.0247552.
- [336] E. Ofori *et al.*, "Increased free water in the substantia nigra of Parkinson's disease: a single-site and multi-site study," *Neurobiol Aging*, vol. 36, no. 2, pp. 1097-1104, Feb 2015, doi: 10.1016/j.neurobiolaging.2014.10.029.
- [337] E. Ofori *et al.*, "Longitudinal changes in free-water within the substantia nigra of Parkinson's disease," *Brain*, vol. 138, no. Pt 8, pp. 2322-31, Aug 2015, doi: 10.1093/brain/awv136.
- [338] G. Halliday, M. Hely, W. Reid, and J. Morris, "The progression of pathology in longitudinally followed patients with Parkinson's disease," *Acta Neuropathol*, vol. 115, no. 4, pp. 409-15, Apr 2008, doi: 10.1007/s00401-008-0344-8.
- [339] R. E. Burke, W. T. Dauer, and J. P. Vonsattel, "A critical evaluation of the Braak staging scheme for Parkinson's disease," *Ann Neurol*, vol. 64, no. 5, pp. 485-91, Nov 2008, doi: 10.1002/ana.21541.
- [340] S. K. Sethi *et al.*, "Iron quantification in Parkinson's disease using an age-based threshold on susceptibility maps: The advantage of local versus entire structure iron content measurements," *Magnetic Resonance Imaging*, 2018, doi: 10.1016/j.mri.2018.10.001.

- [341] L. O. Thomas, O. B. Boyko, D. C. Anthony, and P. C. Burger, "MR detection of brain iron," *AJNR Am J Neuroradiol*, vol. 14, no. 5, pp. 1043-8, Sep-Oct 1993. [Online]. Available: <https://www.ncbi.nlm.nih.gov/pubmed/8237678>.
- [342] N. Persson *et al.*, "Age and sex related differences in subcortical brain iron concentrations among healthy adults," *Neuroimage*, vol. 122, pp. 385-98, Nov 15 2015, doi: 10.1016/j.neuroimage.2015.07.050.
- [343] M. Wieler, M. Gee, and W. R. Martin, "Longitudinal midbrain changes in early Parkinson's disease: iron content estimated from R2*/MRI," *Parkinsonism Relat Disord*, vol. 21, no. 3, pp. 179-83, Mar 2015, doi: 10.1016/j.parkreldis.2014.11.017.
- [344] V. G. Kiselev and D. S. Novikov, "Transverse NMR relaxation in biological tissues," *Neuroimage*, vol. 182, pp. 149-168, Nov 15 2018, doi: 10.1016/j.neuroimage.2018.06.002.
- [345] A. Biesemeier *et al.*, "Elemental mapping of Neuromelanin organelles of human Substantia Nigra: correlative ultrastructural and chemical analysis by analytical transmission electron microscopy and nano-secondary ion mass spectrometry," *J Neurochem*, vol. 138, no. 2, pp. 339-53, Jul 2016, doi: 10.1111/jnc.13648.
- [346] H. Lee, S. Y. Baek, S. Y. Chun, J. H. Lee, and H. Cho, "Specific visualization of neuromelanin-iron complex and ferric iron in the human post-mortem substantia nigra using MR relaxometry at 7T," *Neuroimage*, Nov 21 2017, doi: 10.1016/j.neuroimage.2017.11.035.
- [347] F. Schweser, K. Sommer, A. Deistung, and J. R. Reichenbach, "Quantitative susceptibility mapping for investigating subtle susceptibility variations in the human brain," *Neuroimage*, vol. 62, no. 3, pp. 2083-100, Sep 2012, doi: 10.1016/j.neuroimage.2012.05.067.
- [348] B. Bilgic, C. Langkammer, J. P. Marques, J. Meineke, C. Milovic, and F. Schweser, "QSM Reconstruction Challenge 2.0: Design and Report of Results," 2020, doi: 10.1101/2020.11.25.397695.
- [349] A. De Luca, R. F. Dantas, and S. Esplugas, "Study of Fe(III)-NTA chelates stability for applicability in photo-Fenton at neutral pH," *Applied Catalysis B*:

- Environmental*, vol. 179, pp. 372-379, 2015, doi: 10.1016/j.apcatb.2015.05.025.
- [350] A. De Luca, R. F. Dantas, and S. Esplugas, "Assessment of iron chelates efficiency for photo-Fenton at neutral pH," *Water Res*, vol. 61, pp. 232-42, Sep 15 2014, doi: 10.1016/j.watres.2014.05.033.
- [351] U. Schwertmann, J. Friedl, and H. Stanjek, "From Fe(III) Ions to Ferrihydrite and then to Hematite," *J Colloid Interface Sci*, vol. 209, no. 1, pp. 215-223, Jan 1 1999, doi: 10.1006/jcis.1998.5899.
- [352] L. Zecca *et al.*, "The role of iron and copper molecules in the neuronal vulnerability of locus coeruleus and substantia nigra during aging," *Proc Natl Acad Sci U S A*, vol. 101, no. 26, pp. 9843-8, Jun 29 2004, doi: 10.1073/pnas.0403495101.
- [353] M. Pei *et al.*, "Algorithm for fast monoexponential fitting based on Auto-Regression on Linear Operations (ARLO) of data," *Magn Reson Med*, vol. 73, no. 2, pp. 843-50, Feb 2015, doi: 10.1002/mrm.25137.
- [354] W. M. Haynes, W. M. Haynes and D. R. Lide, Eds. *CRC handbook of chemistry and physics.*, 97 ed. Boca Raton, Florida: CRC Press, 2017.
- [355] P. Damier, "The substantia nigra of the human brain: I. Nigrosomes and the nigral matrix, a compartmental organization based on calbindin D28K immunohistochemistry," *Brain*, vol. 122, no. 8, pp. 1421-1436, 1999, doi: 10.1093/brain/122.8.1421.
- [356] J. Langley, D. E. Huddleston, X. Chen, J. Sedlacik, N. Zachariah, and X. Hu, "A multicontrast approach for comprehensive imaging of substantia nigra," *Neuroimage*, vol. 112, pp. 7-13, May 15 2015, doi: 10.1016/j.neuroimage.2015.02.045.
- [357] W. R. Gibb and A. J. Lees, "Anatomy, pigmentation, ventral and dorsal subpopulations of the substantia nigra, and differential cell death in Parkinson's disease," *Journal of Neurology, Neurosurgery & Psychiatry*, vol. 54, no. 5, pp. 388-396, 1991, doi: 10.1136/jnnp.54.5.388.
- [358] C. J. Bakker and R. de Roos, "Concerning the preparation and use of substances with a magnetic susceptibility equal to the magnetic susceptibility

- of air," *Magn Reson Med*, vol. 56, no. 5, pp. 1107-13, Nov 2006, doi: 10.1002/mrm.21069.
- [359] P. D. Griffiths and A. R. Crossman, "Distribution of iron in the basal ganglia and neocortex in postmortem tissue in Parkinson's disease and Alzheimer's disease," *Dementia*, vol. 4, no. 2, pp. 61-5, Mar-Apr 1993. [Online]. Available: <https://www.ncbi.nlm.nih.gov/pubmed/8358514>.
- [360] X. Miao *et al.*, "Increased brain iron deposition in patients with sickle cell disease: an MRI quantitative susceptibility mapping study," *Blood*, vol. 132, no. 15, pp. 1618-1621, Oct 11 2018, doi: 10.1182/blood-2018-04-840322.
- [361] M. Xuan *et al.*, "Different iron deposition patterns in early- and middle-late-onset Parkinson's disease," *Parkinsonism & Related Disorders*, 2017, doi: 10.1016/j.parkreldis.2017.08.013.
- [362] W. Chen *et al.*, "Intracranial calcifications and hemorrhages: characterization with quantitative susceptibility mapping," *Radiology*, vol. 270, no. 2, pp. 496-505, Feb 2014, doi: 10.1148/radiol.13122640.
- [363] N. Khattar *et al.*, "Investigation of the association between cerebral iron content and myelin content in normative aging using quantitative magnetic resonance neuroimaging," *Neuroimage*, vol. 239, p. 118267, Oct 1 2021, doi: 10.1016/j.neuroimage.2021.118267.
- [364] M. Arshad, J. A. Stanley, and N. Raz, "Adult age differences in subcortical myelin content are consistent with protracted myelination and unrelated to diffusion tensor imaging indices," *Neuroimage*, vol. 143, pp. 26-39, Dec 2016, doi: 10.1016/j.neuroimage.2016.08.047.
- [365] A. Roch, Y. Gossuin, R. N. Muller, and P. Gillis, "Superparamagnetic colloid suspensions: Water magnetic relaxation and clustering," *Journal of Magnetism and Magnetic Materials*, vol. 293, no. 1, pp. 532-539, 2005, doi: 10.1016/j.jmmm.2005.01.070.
- [366] Y. Gossuin, P. Gillis, R. N. Muller, and A. Hocq, "Relaxation by clustered ferritin: a model for ferritin-induced relaxation in vivo," *NMR Biomed*, vol. 20, no. 8, pp. 749-56, Dec 2007, doi: 10.1002/nbm.1140.
- [367] D. T. Dexter *et al.*, "Increased Nigral Iron Content and Alterations in Other Metal Ions Occurring in Brain in Parkinson's Disease," *Journal of*

- Neurochemistry*, vol. 52, no. 6, pp. 1830-1836, 1989, doi: 10.1111/j.1471-4159.1989.tb07264.x.
- [368] H. Sun *et al.*, "Validation of quantitative susceptibility mapping with Perls' iron staining for subcortical gray matter," *Neuroimage*, vol. 105, pp. 486-92, Jan 15 2015, doi: 10.1016/j.neuroimage.2014.11.010.
- [369] D. P. Pelvig, H. Pakkenberg, A. K. Stark, and B. Pakkenberg, "Neocortical glial cell numbers in human brains," *Neurobiol Aging*, vol. 29, no. 11, pp. 1754-62, Nov 2008, doi: 10.1016/j.neurobiolaging.2007.04.013.
- [370] M. A. Garcia-Cabezas, Y. J. John, H. Barbas, and B. Zikopoulos, "Distinction of Neurons, Glia and Endothelial Cells in the Cerebral Cortex: An Algorithm Based on Cytological Features," *Front Neuroanat*, vol. 10, p. 107, 2016, doi: 10.3389/fnana.2016.00107.
- [371] A. S. Karlsen and B. Pakkenberg, "Total numbers of neurons and glial cells in cortex and basal ganglia of aged brains with Down syndrome--a stereological study," *Cereb Cortex*, vol. 21, no. 11, pp. 2519-24, Nov 2011, doi: 10.1093/cercor/bhr033.
- [372] H. Steiner and K. Y. Tseng, *Handbook of basal ganglia structure and function*. Academic Press, 2016.
- [373] S. Darmanis *et al.*, "A survey of human brain transcriptome diversity at the single cell level," *Proc Natl Acad Sci U S A*, vol. 112, no. 23, pp. 7285-90, Jun 9 2015, doi: 10.1073/pnas.1507125112.
- [374] R. D. Hodge *et al.*, "Conserved cell types with divergent features in human versus mouse cortex," *Nature*, vol. 573, no. 7772, pp. 61-68, Sep 2019, doi: 10.1038/s41586-019-1506-7.
- [375] C. S. von Bartheld, J. Bahney, and S. Herculano-Houzel, "The search for true numbers of neurons and glial cells in the human brain: A review of 150 years of cell counting," *J Comp Neurol*, vol. 524, no. 18, pp. 3865-3895, Dec 15 2016, doi: 10.1002/cne.24040.
- [376] S. Herculano-Houzel, C. S. von Bartheld, D. J. Miller, and J. H. Kaas, "How to count cells: the advantages and disadvantages of the isotropic fractionator compared with stereology," *Cell Tissue Res*, vol. 360, no. 1, pp. 29-42, Apr 2015, doi: 10.1007/s00441-015-2127-6.

- [377] D. A. Yablonskiy, X. He, J. Luo, and A. L. Sukstanskii, "Lorentz sphere versus generalized Lorentzian approach: What would Lorentz say about it?," *Magn Reson Med*, vol. 72, no. 1, pp. 4-7, Jul 2014, doi: 10.1002/mrm.25230.
- [378] J. R. Reichenbach, F. Schweser, B. Serres, and A. Deistung, "Quantitative Susceptibility Mapping: Concepts and Applications," *Clin Neuroradiol*, vol. 25 Suppl 2, pp. 225-30, Oct 2015, doi: 10.1007/s00062-015-0432-9.
- [379] D. Milardi *et al.*, "The Cortico-Basal Ganglia-Cerebellar Network: Past, Present and Future Perspectives," *Front Syst Neurosci*, vol. 13, p. 61, 2019, doi: 10.3389/fnsys.2019.00061.
- [380] C. Haass and D. J. Selkoe, "Cellular processing of β -amyloid precursor protein and the genesis of amyloid β -peptide," *Cell*, vol. 75, no. 6, pp. 1039-1042, 1993, doi: 10.1016/0092-8674(93)90312-e.
- [381] G. F. Chen *et al.*, "Amyloid beta: structure, biology and structure-based therapeutic development," *Acta Pharmacol Sin*, vol. 38, no. 9, pp. 1205-1235, Sep 2017, doi: 10.1038/aps.2017.28.
- [382] C. J. Maynard *et al.*, "Overexpression of Alzheimer's disease amyloid-beta opposes the age-dependent elevations of brain copper and iron," *J Biol Chem*, vol. 277, no. 47, pp. 44670-6, Nov 22 2002, doi: 10.1074/jbc.M204379200.
- [383] C. C. Curtain, F. E. Ali, D. G. Smith, A. I. Bush, C. L. Masters, and K. J. Barnham, "Metal ions, pH, and cholesterol regulate the interactions of Alzheimer's disease amyloid-beta peptide with membrane lipid," *J Biol Chem*, vol. 278, no. 5, pp. 2977-82, Jan 31 2003, doi: 10.1074/jbc.M205455200.
- [384] S. Bolognin, L. Messori, D. Drago, C. Gabbiani, L. Cendron, and P. Zatta, "Aluminum, copper, iron and zinc differentially alter amyloid-A β (1-42) aggregation and toxicity," *Int J Biochem Cell Biol*, vol. 43, no. 6, pp. 877-85, Jun 2011, doi: 10.1016/j.biocel.2011.02.009.
- [385] F. Bousejra-ElGarah, C. Bijani, Y. Coppel, P. Faller, and C. Hureau, "Iron(II) binding to amyloid-beta, the Alzheimer's peptide," *Inorg Chem*, vol. 50, no. 18, pp. 9024-30, Sep 19 2011, doi: 10.1021/ic201233b.
- [386] B. Kenkhuis *et al.*, "Iron loading is a prominent feature of activated microglia in Alzheimer's disease patients," *Acta Neuropathol Commun*, vol. 9, no. 1, p. 27, Feb 17 2021, doi: 10.1186/s40478-021-01126-5.

- [387] P. M. Harrison and P. Arosio, "The ferritins: molecular properties, iron storage function and cellular regulation," *Biochim Biophys Acta*, vol. 1275, no. 3, pp. 161-203, Jul 31 1996. [Online]. Available: <http://www.ncbi.nlm.nih.gov/pubmed/8695634>.
- [388] B. Liu *et al.*, "Iron promotes the toxicity of amyloid beta peptide by impeding its ordered aggregation," *J Biol Chem*, vol. 286, no. 6, pp. 4248-56, Feb 11 2011, doi: 10.1074/jbc.M110.158980.
- [389] C. Hureau, "Coordination of redox active metal ions to the amyloid precursor protein and to amyloid- β peptides involved in Alzheimer disease. Part 1: An overview," *Coordination Chemistry Reviews*, vol. 256, no. 19-20, pp. 2164-2174, 2012, doi: 10.1016/j.ccr.2012.03.037.
- [390] M. A. Smith, K. Wehr, P. L. R. Harris, S. L. Siedlak, J. R. Connor, and G. Perry, "Abnormal localization of iron regulatory protein in Alzheimer's disease," *Brain Research*, vol. 788, no. 1-2, pp. 232-236, 1998, doi: 10.1016/s0006-8993(98)00002-x.
- [391] M. A. Smith, P. L. R. Harris, L. M. Sayre, and G. Perry, "Iron accumulation in Alzheimer disease is a source of redox-generated free radicals," *Proceedings of the National Academy of Sciences of the United States of America*, vol. 94, no. 18, pp. 9866-9868, 1997. [Online]. Available: <http://www.jstor.org/stable/43118>.
- [392] I. Grundke-Iqbal, J. Fleming, Y. C. Tung, H. Lassmann, K. Iqbal, and J. G. Joshi, "Ferritin is a component of the neuritic (senile) plaque in Alzheimer dementia," *Acta Neuropathol*, vol. 81, no. 2, pp. 105-110, 1990, doi: 10.1007/BF00334497.
- [393] P. Maher, A. Currais, and D. Schubert, "Using the Oxytosis/Ferroptosis Pathway to Understand and Treat Age-Associated Neurodegenerative Diseases," *Cell Chem Biol*, vol. 27, no. 12, pp. 1456-1471, Dec 17 2020, doi: 10.1016/j.chembiol.2020.10.010.
- [394] R. R. Ratan, "The Chemical Biology of Ferroptosis in the Central Nervous System," *Cell Chem Biol*, vol. 27, no. 5, pp. 479-498, May 21 2020, doi: 10.1016/j.chembiol.2020.03.007.

- [395] J. J. Gallagher, M. E. Finnegan, B. Grehan, J. Dobson, J. F. Collingwood, and M. A. Lynch, "Modest amyloid deposition is associated with iron dysregulation, microglial activation, and oxidative stress," *J Alzheimers Dis*, vol. 28, no. 1, pp. 147-61, 2012, doi: 10.3233/JAD-2011-110614.
- [396] S. Mazzucchi *et al.*, "Quantitative susceptibility mapping in atypical Parkinsonisms," *Neuroimage Clin*, vol. 24, p. 101999, 2019, doi: 10.1016/j.nicl.2019.101999.
- [397] X. Guan *et al.*, "Regionally progressive accumulation of iron in Parkinson's disease as measured by quantitative susceptibility mapping," *NMR Biomed*, vol. 30, no. 4, Apr 2017, doi: 10.1002/nbm.3489.
- [398] A. Alkemade *et al.*, "Comparison of T2*-weighted and QSM contrasts in Parkinson's disease to visualize the STN with MRI," *PLoS One*, vol. 12, no. 4, p. e0176130, 2017, doi: 10.1371/journal.pone.0176130.
- [399] J. Acosta-Cabronero, G. B. Williams, A. Cardenas-Blanco, R. J. Arnold, V. Lupson, and P. J. Nestor, "In vivo quantitative susceptibility mapping (QSM) in Alzheimer's disease," *PLoS One*, vol. 8, no. 11, p. e81093, 2013, doi: 10.1371/journal.pone.0081093.
- [400] L. Xie *et al.*, "Dynamic contrast-enhanced quantitative susceptibility mapping with ultrashort echo time MRI for evaluating renal function," *Am J Physiol Renal Physiol*, vol. 310, no. 2, pp. F174-82, Jan 15 2016, doi: 10.1152/ajprenal.00351.2015.
- [401] K. Deh *et al.*, "Validation of MRI quantitative susceptibility mapping of superparamagnetic iron oxide nanoparticles for hyperthermia applications in live subjects," *Sci Rep*, vol. 10, no. 1, p. 1171, Jan 24 2020, doi: 10.1038/s41598-020-58219-9.
- [402] G. Simchick, Z. Liu, T. Nagy, M. Xiong, and Q. Zhao, "Assessment of MR-based R2* and quantitative susceptibility mapping for the quantification of liver iron concentration in a mouse model at 7T," *Magn Reson Med*, vol. 80, no. 5, pp. 2081-2093, Nov 2018, doi: 10.1002/mrm.27173.
- [403] M. C. Hsieh, C. Y. Tsai, M. C. Liao, J. L. Yang, C. H. Su, and J. H. Chen, "Quantitative Susceptibility Mapping-Based Microscopy of Magnetic Resonance Venography (QSM-mMRV) for In Vivo Morphologically and

- Functionally Assessing Cerebromicrovasculature in Rat Stroke Model," *PLoS One*, vol. 11, no. 3, p. e0149602, 2016, doi: 10.1371/journal.pone.0149602.
- [404] L. Wang *et al.*, "Quantitative susceptibility mapping detects abnormalities in cartilage canals in a goat model of preclinical osteochondritis dissecans," *Magn Reson Med*, vol. 77, no. 3, pp. 1276-1283, Mar 2017, doi: 10.1002/mrm.26214.
- [405] O. Nykanen *et al.*, "T2* and quantitative susceptibility mapping in an equine model of post-traumatic osteoarthritis: assessment of mechanical and structural properties of articular cartilage," *Osteoarthritis Cartilage*, vol. 27, no. 10, pp. 1481-1490, Oct 2019, doi: 10.1016/j.joca.2019.06.009.
- [406] Y. Han *et al.*, "Application of 9.4T MRI in Wilson Disease Model TX Mice With Quantitative Susceptibility Mapping to Assess Copper Distribution," *Front Behav Neurosci*, vol. 14, p. 59, 2020, doi: 10.3389/fnbeh.2020.00059.
- [407] Q. Wen *et al.*, "Ultra-High-Resolution in vitro MRI Study of Age-Related Brain Subcortical Susceptibility Alteration in Rhesus Monkeys at 9.4 T," *Front Aging Neurosci*, vol. 12, p. 259, 2020, doi: 10.3389/fnagi.2020.00259.
- [408] Z. Chen, L. A. Johnston, D. H. Kwon, S. H. Oh, Z. H. Cho, and G. F. Egan, "An optimised framework for reconstructing and processing MR phase images," *Neuroimage*, vol. 49, no. 2, pp. 1289-300, Jan 15 2010, doi: 10.1016/j.neuroimage.2009.09.071.
- [409] V. Fortier and I. R. Levesque, "Phase processing for quantitative susceptibility mapping of regions with large susceptibility and lack of signal," *Magn Reson Med*, vol. 79, no. 6, pp. 3103-3113, Jun 2018, doi: 10.1002/mrm.26989.
- [410] C. Milovic *et al.*, "Comparison of parameter optimization methods for quantitative susceptibility mapping," *Magn Reson Med*, vol. 85, no. 1, pp. 480-494, Jan 2021, doi: 10.1002/mrm.28435.
- [411] J. R. Connor, B. S. Snyder, P. Arosio, D. A. Loeffler, and P. LeWitt, "A quantitative analysis of isoferritins in select regions of aged, parkinsonian, and Alzheimer's diseased brains," *Journal of neurochemistry*, vol. 65, no. 2, pp. 717-724, 1995.
- [412] D. L. Olson, T. L. Peck, A. G. Webb, R. L. Magin, and J. V. Sweedler, "High-Resolution Microcoil 1H-NMR for Mass-Limited, Nanoliter-Volume Samples,"

- Science*, vol. 270, no. 5244, pp. 1967-1970, 1995, doi: 10.1126/science.270.5244.1967.
- [413] A. Haase *et al.*, "NMR probeheads for in vivo applications," *Concepts in Magnetic Resonance*, vol. 12, no. 6, pp. 361-388, 2000, doi: 10.1002/1099-0534(2000)12:6<361::Aid-cmr1>3.0.Co;2-I.
- [414] V. Antharam *et al.*, "High field magnetic resonance microscopy of the human hippocampus in Alzheimer's disease: quantitative imaging and correlation with iron," *Neuroimage*, vol. 59, no. 2, pp. 1249-60, Jan 16 2012, doi: 10.1016/j.neuroimage.2011.08.019.
- [415] H. Benveniste and S. J. Blackband, "Translational neuroscience and magnetic-resonance microscopy," *The Lancet Neurology*, vol. 5, no. 6, pp. 536-544, 2006, doi: 10.1016/s1474-4422(06)70472-0.
- [416] E. J. d'Auvergne and P. R. Gooley, "Optimisation of NMR dynamic models I. Minimisation algorithms and their performance within the model-free and Brownian rotational diffusion spaces," *J Biomol NMR*, vol. 40, no. 2, pp. 107-19, Feb 2008, doi: 10.1007/s10858-007-9214-2.
- [417] T. He, P. D. Gatehouse, G. C. Smith, R. H. Mohiaddin, D. J. Pennell, and D. N. Firmin, "Myocardial T2* measurements in iron-overloaded thalassemia: An in vivo study to investigate optimal methods of quantification," *Magn Reson Med*, vol. 60, no. 5, pp. 1082-9, Nov 2008, doi: 10.1002/mrm.21744.
- [418] L. Zhou, J. K. Choi, Y. Kee, Y. Wang, and J. K. Seo, "Dipole Incompatibility Related Artifacts in Quantitative Susceptibility Mapping," *arXiv*, 2017, doi: arXiv:1701.05457.
- [419] Y. Kee *et al.*, "Quantitative Susceptibility Mapping (QSM) Algorithms: Mathematical Rationale and Computational Implementations," *IEEE Trans Biomed Eng*, vol. 64, no. 11, pp. 2531-2545, Nov 2017, doi: 10.1109/TBME.2017.2749298.
- [420] P. C. Hansen, "Analysis of Discrete Ill-Posed Problems by Means of the L-Curve," *SIAM Review*, vol. 34, no. 4, pp. 561-580, 1992, doi: 10.1137/1034115.
- [421] B. Kressler, L. de Rochefort, T. Liu, P. Spincemaille, Q. Jiang, and Y. Wang, "Nonlinear regularization for per voxel estimation of magnetic susceptibility

- distributions from MRI field maps," *IEEE Trans Med Imaging*, vol. 29, no. 2, pp. 273-81, Feb 2010, doi: 10.1109/TMI.2009.2023787.
- [422] A. G. Ramm, A. Jeffrey, Ed. *Inverse problems: mathematical and analytical techniques with applications to engineering*. Boston: Springer, 2005.
- [423] R. L. Burden and J. D. Faires, *Numerical Analysis*. Brooks/Cole, 2011.
- [424] T. E. Gureyev and K. A. Nugent, "Phase retrieval with the transport-of-intensity equation II Orthogonal series solution for nonuniform illumination," *Journal of the Optical Society of America A*, vol. 13, no. 8, 1996, doi: 10.1364/josaa.13.001670.
- [425] R. M. Henkelman, G. J. Stanisz, and S. J. Graham, "Magnetization transfer in MRI: a review," *NMR Biomed*, vol. 14, no. 2, pp. 57-64, Apr 2001, doi: 10.1002/nbm.683.
- [426] R. M. Henkelman, X. Huang, Q.-S. Xiang, G. J. Stanisz, S. D. Swanson, and M. J. Bronskill, "Quantitative interpretation of magnetization transfer," *Magnetic Resonance in Medicine*, vol. 29, no. 6, pp. 759-766, 1993, doi: 10.1002/mrm.1910290607.
- [427] W. T. Dixon, H. Engels, M. Castillo, and M. Sardashti, "Incidental magnetization transfer contrast in standard multislice imaging," *Magnetic Resonance Imaging*, vol. 8, no. 4, pp. 417-422, 1990, doi: 10.1016/0730-725x(90)90050-c.
- [428] R. J. Nabuurs *et al.*, "MR microscopy of human amyloid-beta deposits: characterization of parenchymal amyloid, diffuse plaques, and vascular amyloid," *J Alzheimers Dis*, vol. 34, no. 4, pp. 1037-49, 2013, doi: 10.3233/JAD-122215.
- [429] B. P. Drayer, "Imaging of the aging brain. Part I. Normal findings," *Radiology*, vol. 166, no. 3, pp. 785-96, Mar 1988, doi: 10.1148/radiology.166.3.3277247.
- [430] J. Vymazal, O. Zak, J. W. M. Bulte, P. Aisen, and R. A. Brooks, "T1 and T2 of ferritin solutions: Effect of loading factor," *Magnetic Resonance in Medicine*, vol. 36, no. 1, pp. 61-65, 1996, doi: 10.1002/mrm.1910360111.
- [431] R. Fleysher, L. Fleysher, S. Liu, and O. Gonen, "On the voxel size and magnetic field strength dependence of spectral resolution in magnetic resonance

- spectroscopy," *Magn Reson Imaging*, vol. 27, no. 2, pp. 222-32, Feb 2009, doi: 10.1016/j.mri.2008.06.009.
- [432] B. S. Li, J. Regal, and O. Gonen, "SNR versus resolution in 3D 1H MRS of the human brain at high magnetic fields," *Magn Reson Med*, vol. 46, no. 6, pp. 1049-53, Dec 2001, doi: 10.1002/mrm.1297.
- [433] A. Ruh, H. Scherer, and V. G. Kiselev, "The Larmor frequency shift in magnetically heterogeneous media depends on their mesoscopic structure," *Magn Reson Med*, vol. 79, no. 2, pp. 1101-1110, Feb 2018, doi: 10.1002/mrm.26753.
- [434] Y. Gossuin, A. Roch, R. N. Muller, P. Gillis, and F. Lo Bue, "Anomalous nuclear magnetic relaxation of aqueous solutions of ferritin: an unprecedented first-order mechanism," *Magn Reson Med*, vol. 48, no. 6, pp. 959-64, Dec 2002, doi: 10.1002/mrm.10316.
- [435] M. Dhenain, B. Delatour, C. Walczak, and A. Volk, "Passive staining: a novel ex vivo MRI protocol to detect amyloid deposits in mouse models of Alzheimer's disease," *Magn Reson Med*, vol. 55, no. 3, pp. 687-93, Mar 2006, doi: 10.1002/mrm.20810.
- [436] J. F. Schenck, "Health and physiological effects of human exposure to whole-body four-Tesla magnetic fields during MRI," *Ann N Y Acad Sci*, vol. 649, pp. 285-301, Mar 31 1992, doi: 10.1111/j.1749-6632.1992.tb49617.x.
- [437] P. Spincemaille *et al.*, "Quantitative Susceptibility Mapping: MRI at 7T versus 3T," *J Neuroimaging*, vol. 30, no. 1, pp. 65-75, Jan 2020, doi: 10.1111/jon.12669.
- [438] C. Quintana, J. M. Cowley, and C. Marhic, "Electron nanodiffraction and high-resolution electron microscopy studies of the structure and composition of physiological and pathological ferritin," *J Struct Biol*, vol. 147, no. 2, pp. 166-78, Aug 2004, doi: 10.1016/j.jsb.2004.03.001.
- [439] C. Langkammer, S. Ropele, L. Pirpamer, F. Fazekas, and R. Schmidt, "MRI for iron mapping in Alzheimer's disease," *Neurodegener Dis*, vol. 13, no. 2-3, pp. 189-91, 2014, doi: 10.1159/000353756.

- [440] C. Duffeffant *et al.*, "Contrast-enhanced MR microscopy of amyloid plaques in five mouse models of amyloidosis and in human Alzheimer's disease brains," *Sci Rep*, vol. 7, no. 1, p. 4955, Jul 10 2017, doi: 10.1038/s41598-017-05285-1.
- [441] F. Schweser, A. Deistung, B. W. Lehr, and J. R. Reichenbach, "Differentiation between diamagnetic and paramagnetic cerebral lesions based on magnetic susceptibility mapping," *Med Phys*, vol. 37, no. 10, pp. 5165-78, Oct 2010, doi: 10.1118/1.3481505.
- [442] M. Weigel, "Extended phase graphs: dephasing, RF pulses, and echoes - pure and simple," *J Magn Reson Imaging*, vol. 41, no. 2, pp. 266-95, Feb 2015, doi: 10.1002/jmri.24619.
- [443] S. J. Malik, R. Teixeira, and J. V. Hajnal, "Extended phase graph formalism for systems with magnetization transfer and exchange," *Magn Reson Med*, vol. 80, no. 2, pp. 767-779, Aug 2018, doi: 10.1002/mrm.27040.
- [444] A. D. Bain, C. K. Anand, and Z. Nie, "Exact solution to the Bloch equations and application to the Hahn echo," *J Magn Reson*, vol. 206, no. 2, pp. 227-40, Oct 2010, doi: 10.1016/j.jmr.2010.07.012.
- [445] K. Murase and N. Tanki, "Numerical solutions to the time-dependent Bloch equations revisited," *Magn Reson Imaging*, vol. 29, no. 1, pp. 126-31, Jan 2011, doi: 10.1016/j.mri.2010.07.003.
- [446] N. Ben-Eliezer, D. K. Sodickson, and K. T. Block, "Rapid and accurate T2 mapping from multi-spin-echo data using Bloch-simulation-based reconstruction," *Magn Reson Med*, vol. 73, no. 2, pp. 809-17, Feb 2015, doi: 10.1002/mrm.25156.

Appendix A Empirical prediction of iron concentrations of brain regions by Hallgren and Sourander

Frontal white matter:	$y = 39.5 \times (1 - e^{-0.10x}) + 3.1$
Globus pallidus:	$y = 214.1 \times (1 - e^{-0.09x}) + 3.7$
Cerebellar cortex:	$y = 27 \times (1 - e^{-0.085x}) + 6.8$
Prefrontal cortex:	$y = 24.3 \times (1 - e^{-0.07x}) + 5.8$
Temporal cortex:	$y = 27 \times (1 - e^{-0.07x}) + 5.5$
Sensory cortex:	$y = 39.7 \times (1 - e^{-0.07x}) + 4.9$
Parietal cortex:	$y = 33.1 \times (1 - e^{-0.06x}) + 6.0$
Occipital cortex:	$y = 40.3 \times (1 - e^{-0.06x}) + 7.2$
Motor cortex:	$y = 47.9 \times (1 - e^{-0.05x}) + 4.0$
Caudate nucleus:	$y = 96.6 \times (1 - e^{-0.05x}) + 3.3$
Putamen:	$y = 146.2 \times (1 - e^{-0.04x}) + 4.6$

with y denoted the non-haemin iron in $\mu\text{g/g}$ wet weight (ww), x the age in years.

Appendix B Effective R_2 measurements in reported PPMI subjects

Table B1. Caudate nucleus

Gender	Group	Region	Age @ 0 month	Effective R_2 (s^{-1})				Effective R_2 percentage change (%)		
				0 month	12 month	24 month	48 month	0-12 month	0-24 month	0-48 month
Male	HC	CN	44	9.96952	10.79346		10.92203	8.26459		9.554221
Male	HC	CN	44	10.50505	10.00427		11.07133	-4.76704		5.39055
Male	HC	CN	45.8	10.8332	10.89931		10.6776	0.610254		-1.43633
Male	HC	CN	46.8	10.59513		11.11357			4.893191	
Male	HC	CN	52.4	10.40112	10.75883	10.65757	10.49292	3.439149	2.4656	0.882597
Male	HC	CN	54.1	10.77844	11.15083		10.66625	3.454953		-1.04087
Male	HC	CN	60.1	10.4322	10.40842		10.11873	-0.22795		-3.00483
Female	HC	CN	40.6	10.06181	10.25496	10.42221		1.919635	3.581861	
Female	HC	CN	48.8	10.23738	10.13643	10.02848		-0.98609	-2.04056	
Female	HC	CN	50.3	10.95358	10.74672			-1.88851		
Female	HC	CN	52.7	10.58046	10.62798			0.44913		
Female	HC	CN	54.1	10.3924	10.29155	10.62593		-0.97042	2.247123	
Male	PD contralateral	CN	40.8	10.29213	10.29112	10.34259	10.48465	-0.00981	0.490278	1.870555
Male	PD contralateral	CN	45.2	10.56837	9.77448	10.35481	10.16486	-7.51194	-2.02075	-3.81809
Male	PD contralateral	CN	46	10.61708	10.61801	11.11476		0.008759	4.687541	
Male	PD contralateral	CN	49	10.18244	11.05785	10.89468	11.27537	8.597252	6.994787	10.73348
Male	PD contralateral	CN	51.9	11.90846	11.82229	11.49647	11.51175	-0.7236	-3.45964	-3.33133

Male	PD contralateral	CN	56	10.10652	9.90684	9.95239	10.38235	-1.97575	-1.52506	2.729228
Male	PD contralateral	CN	60.3	10.06367	9.83789	10.29967	10.81782	-2.24352	2.345069	7.493787
Female	PD contralateral	CN	39.2	10.54934	10.7966	11.12395	10.77596	2.343843	5.446881	2.148191
Female	PD contralateral	CN	49.8	9.89197	9.94746	9.85783	10.26883	0.56096	-0.34513	3.809757
Female	PD contralateral	CN	50.6	10.61864	11.31104	10.91095	9.84887	6.520609	2.752801	-7.24923
Female	PD contralateral	CN	52.9	10.14803	10.84812	10.84145	10.46753	6.898777	6.83305	3.148394
Female	PD contralateral	CN	54.1	11.84408	11.33045	11.35069	11.33499	-4.3366	-4.16571	-4.29827
Male	PD ipsilateral	CN	40.8	10.41052	10.4316	10.49638	10.45675	0.202487	0.824743	0.44407
Male	PD ipsilateral	CN	45.2	10.66972	10.30745	10.65859	9.87413	-3.39531	-0.10431	-7.45652
Male	PD ipsilateral	CN	46	10.78513	10.80935	11.61073		0.224568	7.654984	
Male	PD ipsilateral	CN	49	10.61471	11.19495	11.36123	9.97664	5.466376	7.032882	-6.01119
Male	PD ipsilateral	CN	51.9	11.47872	11.19843	11.40748	11.79452	-2.44182	-0.62063	2.751178
Male	PD ipsilateral	CN	56	9.53488	9.52485	9.49418	9.59103	-0.10519	-0.42685	0.58889
Male	PD ipsilateral	CN	60.3	10.32488	9.88332	10.00386	10.23253	-4.27666	-3.10919	-0.89444
Female	PD ipsilateral	CN	39.2	10.35598	10.87464	10.98044	11.12284	5.008314	6.029946	7.404997
Female	PD ipsilateral	CN	49.8	9.75292	9.98304	9.90116	10.34467	2.359498	1.519955	6.067414
Female	PD ipsilateral	CN	50.6	9.87102	10.27477	10.43747	9.41052	4.090256	5.738515	-4.66517
Female	PD ipsilateral	CN	52.9	10.57279	11.02611	10.96864	11.27402	4.28761	3.744045	6.632403
Female	PD ipsilateral	CN	54.1	11.36699	11.06981	10.97685	11.44771	-2.61441	-3.43222	0.710126

Table B2. Putamen

Gender	Group	Region	Age @ 0 month	Effective R ₂ (s ⁻¹)				Effective R ₂ percentage change (%)		
				0 month	12 month	24 month	48 month	0-12 month	0-24 month	0-48 month
Male	HC	PUT	44	12.11453	12.66974		12.71207	4.582968		4.93242
Male	HC	PUT	44	12.15158	12.14061		12.53785	-0.09029		3.178787
Male	HC	PUT	45.8	12.50174	12.3425		12.37272	-1.27379		-1.03207
Male	HC	PUT	46.8	13.53829		13.65826			0.886129	
Male	HC	PUT	52.4	13.74504	14.18229	13.96127	14.05252	3.181157	1.573174	2.23706
Male	HC	PUT	54.1	13.7121	14.74349		14.46479	7.521733		5.489222
Male	HC	PUT	60.1	12.2513	12.34194		11.79213	0.739837		-3.7479
Female	HC	PUT	40.6	12.3617	12.62461	12.62087		2.126839	2.09656	
Female	HC	PUT	48.8	13.23656	13.18746	13.15597		-0.37096	-0.60885	
Female	HC	PUT	50.3	13.18663	13.18208			-0.03451		
Female	HC	PUT	52.7	12.80613	12.69906			-0.83613		
Female	HC	PUT	54.1	11.7726	11.64606	11.85179		-1.07493	0.672638	
Male	PD contralateral	PUT	40.8	12.94535	13.14017	13.32637	13.20768	1.504912	2.943254	2.026429
Male	PD contralateral	PUT	45.2	12.03312	12.20539	12.07688	11.76501	1.431617	0.363671	-2.22809
Male	PD contralateral	PUT	46	12.52283	12.63097	12.94468		0.863573	3.36863	
Male	PD contralateral	PUT	49	11.64379	11.87807	12.02893	12.12937	2.012102	3.307749	4.170281
Male	PD contralateral	PUT	51.9	13.39845	13.17372	13.12959	13.02462	-1.67727	-2.00664	-2.79006

Male	PD contralateral	PUT	56	10.54912	10.45616	10.45801	10.62322	-0.88124	-0.86373	0.70237
Male	PD contralateral	PUT	60.3	11.73677	11.79688	11.87053	11.7356	0.512177	1.139723	-0.00992
Female	PD contralateral	PUT	39.2	13.15497	13.30814	13.58752	13.57621	1.16432	3.288095	3.202146
Female	PD contralateral	PUT	49.8	11.85956	12.07114	11.81147	12.45106	1.784032	-0.40552	4.987507
Female	PD contralateral	PUT	50.6	12.88514	13.09697	13.17804	12.28077	1.644056	2.273215	-4.69038
Female	PD contralateral	PUT	52.9	12.95561	12.9622	13.31478	13.35677	0.050861	2.772283	3.096423
Female	PD contralateral	PUT	54.1	13.51459	13.09854	13.11138	13.14489	-3.07855	-2.98353	-2.73561
Male	PD ipsilateral	PUT	40.8	13.38438	13.58454	13.50951	13.72577	1.495518	0.934904	2.550675
Male	PD ipsilateral	PUT	45.2	12.14476	11.97196	11.89528	11.47057	-1.4228	-2.05419	-5.55128
Male	PD ipsilateral	PUT	46	13.03583	13.45184	13.84553		3.191244	6.211304	
Male	PD ipsilateral	PUT	49	11.79697	12.08507	12.10344	12.65338	2.442168	2.597811	7.259533
Male	PD ipsilateral	PUT	51.9	13.32994	13.09354	13.06558	12.75383	-1.77349	-1.98321	-4.32198
Male	PD ipsilateral	PUT	56	10.55716	10.55309	10.57077	10.59825	-0.03856	0.128907	0.38924
Male	PD ipsilateral	PUT	60.3	12.61973	12.41054	12.61623	12.65819	-1.6576	-0.02774	0.304797
Female	PD ipsilateral	PUT	39.2	13.45437	13.82162	14.00294	14.14764	2.729631	4.077312	5.152771
Female	PD ipsilateral	PUT	49.8	12.29134	12.18166	12.22603	12.65327	-0.89236	-0.53138	2.944559
Female	PD ipsilateral	PUT	50.6	12.93225	13.31132	13.46476	12.72595	2.931164	4.117715	-1.59527
Female	PD ipsilateral	PUT	52.9	13.13297	12.99324	13.18694	13.3221	-1.06397	0.410908	1.440074
Female	PD ipsilateral	PUT	54.1	13.55005	13.32935	13.30755	13.56814	-1.62881	-1.78966	0.133503

Table B3. Globus pallidus

Gender	Group	Region	Age @ 0 month	Effective R ₂ (s ⁻¹)				Effective R ₂ percentage change (%)		
				0 month	12 month	24 month	48 month	0-12 month	0-24 month	0-48 month
Male	HC	GP	44	16.60637	17.10597		16.82664	3.008476		1.326405
Male	HC	GP	44	15.70205	15.35727		16.40937	-2.19578		4.504664
Male	HC	GP	45.8	15.98131	16.11558		16.02169	0.840176		0.252649
Male	HC	GP	46.8	16.15652		15.75549			-2.4822	
Male	HC	GP	52.4	15.92761	16.46213	15.64295	15.74065	3.355899	-1.78723	-1.17384
Male	HC	GP	54.1	16.77154	16.85943		17.18725	0.524042		2.47865
Male	HC	GP	60.1	15.19773	14.79271		14.64043	-2.665		-3.66697
Female	HC	GP	40.6	16.29753	16.05182	16.03991		-1.50762	-1.58071	
Female	HC	GP	48.8	14.89904	14.6327	15.10723		-1.78762	1.397384	
Female	HC	GP	50.3	16.62461	16.638			0.080564		
Female	HC	GP	52.7	15.90803	15.45767			-2.83103		
Female	HC	GP	54.1	13.7864	14.04506	13.65629		1.876155	-0.94375	
Male	PD contralateral	GP	40.8	15.27478	15.08842	15.09544	15.06337	-1.22003	-1.17406	-1.38401
Male	PD contralateral	GP	45.2	16.27277	16.87378	16.23609	15.44792	3.693385	-0.22538	-5.06886
Male	PD contralateral	GP	46	17.70944	17.56145	18.25248		-0.83564	3.066405	
Male	PD contralateral	GP	49	16.86308	15.18279	16.29025	16.7763	-9.96431	-3.3969	-0.51462
Male	PD contralateral	GP	51.9	16.13173	16.05455	15.95375	16.1043	-0.47841	-1.10323	-0.16998

Male	PD contralateral	GP	56	15.69077	15.68994	15.35812	15.99322	-0.00532	-2.12008	1.927525
Male	PD contralateral	GP	60.3	14.37829	14.50637	15.15015	14.21653	0.890768	5.368223	-1.12508
Female	PD contralateral	GP	39.2	16.20099	16.29006	16.59423	15.75917	0.549738	2.427262	-2.72715
Female	PD contralateral	GP	49.8	15.52131	15.45519	15.51581	15.76556	-0.42596	-0.03544	1.573681
Female	PD contralateral	GP	50.6	16.39376	16.71739	16.79054	15.59334	1.974056	2.420259	-4.88248
Female	PD contralateral	GP	52.9	16.11822	16.26505	17.79494	16.61898	0.910956	10.40257	3.106737
Female	PD contralateral	GP	54.1	17.35226	16.42756	16.33598	16.13716	-5.32897	-5.85677	-7.00253
Male	PD ipsilateral	GP	40.8	15.046	15.06569	15.25127	15.43432	0.13089	1.364302	2.580923
Male	PD ipsilateral	GP	45.2	16.21772	16.97025	16.4609	16.34854	4.640175	1.49946	0.806655
Male	PD ipsilateral	GP	46	17.41464	17.49069	17.47893		0.436739	0.369184	
Male	PD ipsilateral	GP	49	16.67692	16.69739	16.54423	15.96296	0.12274	-0.79563	-4.28114
Male	PD ipsilateral	GP	51.9	16.55944	16.37111	16.37452	16.49099	-1.13728	-1.11669	-0.41337
Male	PD ipsilateral	GP	56	16.52544	16.90975	16.0555	16.54808	2.325541	-2.84373	0.137009
Male	PD ipsilateral	GP	60.3	14.5942	14.79069	15.11818	14.83253	1.346349	3.590309	1.63307
Female	PD ipsilateral	GP	39.2	16.02014	16.15412	15.89096	16.72362	0.836309	-0.80641	4.391194
Female	PD ipsilateral	GP	49.8	16.4526	15.58072	15.86882	16.06506	-5.2993	-3.5482	-2.35548
Female	PD ipsilateral	GP	50.6	16.28501	16.52671	17.30282	15.38634	1.484214	6.250023	-5.51839
Female	PD ipsilateral	GP	52.9	17.44616	16.99878	16.94618	17.55077	-2.56432	-2.86581	0.599649
Female	PD ipsilateral	GP	54.1	16.18793	15.65161	16.11807	15.99383	-3.31309	-0.43156	-1.19904

Table B4. Red nucleus

Gender	Group	Region	Age @ 0 month	Effective R ₂ (s ⁻¹)				Effective R ₂ percentage change(%)		
				0 month	12 month	24 month	48 month	0-12 month	0-24 month	0-48 month
Male	HC	RN	44	14.81094	14.94241		13.82837	0.88768		-6.63407
Male	HC	RN	44	14.34354	13.3032		13.38826	-7.25301		-6.66005
Male	HC	RN	45.8	15.65028	15.75647		15.35413	0.678552		-1.89224
Male	HC	RN	46.8	15.23241		15.07795			-1.01399	
Male	HC	RN	52.4	14.41725	14.96682	14.34114	14.25888	3.811889	-0.52794	-1.09851
Male	HC	RN	54.1	13.86952	14.3599		15.30643	3.53565		10.36021
Male	HC	RN	60.1	14.6517	13.38433		13.60425	-8.64993		-7.14899
Female	HC	RN	40.6	13.40433	13.39341	13.99798		-0.08148	4.428782	
Female	HC	RN	48.8	13.93471	13.48977	13.86595		-3.19304	-0.4935	
Female	HC	RN	50.3	14.66252	14.47832			-1.25627		
Female	HC	RN	52.7	13.30178	13.71369			3.096655		
Female	HC	RN	54.1	13.18967	13.23728	12.94478		0.361017	-1.85666	
Male	PD contralateral	RN	40.8	14.83426	14.68509	14.84575	14.14686	-1.0056	0.077456	-4.63385
Male	PD contralateral	RN	45.2	13.87174	14.06202	14.69911	12.60538	1.371718	5.964407	-9.12907
Male	PD contralateral	RN	46	15.15167	14.48143	13.05104		-4.42352	-13.864	
Male	PD contralateral	RN	49	13.27479	13.35801	13.01289	13.17499	0.626952	-1.97291	-0.75174
Male	PD contralateral	RN	51.9	14.56786	14.84455	14.20631	15.15381	1.899286	-2.48184	4.022203

Male	PD contralateral	RN	56	12.81362	13.04628	13.79769	14.1484	1.815766	7.679907	10.41689
Male	PD contralateral	RN	60.3	14.50689	15.97795	15.61011	15.33788	10.1404	7.604812	5.728219
Female	PD contralateral	RN	39.2	14.54419	15.16121	15.21531	16.12064	4.2424	4.614357	10.83901
Female	PD contralateral	RN	49.8	13.57614	13.03118	13.42391	13.74261	-4.01411	-1.12133	1.226145
Female	PD contralateral	RN	50.6	13.83851	14.17447	13.59385	12.58328	2.427714	-1.76796	-9.07053
Female	PD contralateral	RN	52.9	14.23457	14.00976	15.01119	14.87954	-1.57936	5.455893	4.530983
Female	PD contralateral	RN	54.1	13.38111	12.88665	13.20745	13.08094	-3.69519	-1.29781	-2.24322
Male	PD ipsilateral	RN	40.8	14.27032	14.40808	14.84663	14.41584	0.965375	4.038511	1.019777
Male	PD ipsilateral	RN	45.2	13.03015	13.655	12.53955	13.56946	4.795429	-3.76513	4.138981
Male	PD ipsilateral	RN	46	14.85733	14.72449	14.94703		-0.89416	0.603704	
Male	PD ipsilateral	RN	49	12.90136	13.26005	12.5466	12.5608	2.780294	-2.74979	-2.63973
Male	PD ipsilateral	RN	51.9	14.12997	14.30081	14.00687	14.98121	1.208994	-0.8712	6.024317
Male	PD ipsilateral	RN	56	12.86369	13.10741	12.01106	13.80203	1.894645	-6.62817	7.294529
Male	PD ipsilateral	RN	60.3	14.90927	14.30496	16.1621	14.977	-4.05326	8.403013	0.454277
Female	PD ipsilateral	RN	39.2	14.8103	15.50632	14.92242	15.37576	4.699581	0.757016	3.817993
Female	PD ipsilateral	RN	49.8	14.09197	13.09042	13.54301	12.99946	-7.10721	-3.89552	-7.75273
Female	PD ipsilateral	RN	50.6	13.99198	14.228	13.9152	12.68788	1.686816	-0.54877	-9.32037
Female	PD ipsilateral	RN	52.9	15.06344	14.79333	15.03491	15.34206	-1.79312	-0.1894	1.849641
Female	PD ipsilateral	RN	54.1	13.38332	13.17422	13.02031	12.72177	-1.56244	-2.71246	-4.9431

Table B5. Substantia nigra

Gender	Group	Region	Age @ 0 month	Effective R ₂ (s ⁻¹)				Effective R ₂ percentage change (%)		
				0 month	12 month	24 month	48 month	0-12 month	0-24 month	0-48 month
Male	HC	SN	44	15.38105	15.47776		15.29475	0.628773		-0.56108
Male	HC	SN	44	13.88179	13.56211		13.22858	-2.3029		-4.70553
Male	HC	SN	45.8	14.88613	14.78042		14.59948	-0.71009		-1.9256
Male	HC	SN	46.8	16.32024		16.16374			-0.9589	
Male	HC	SN	52.4	13.2879	13.64532	13.79538	13.30881	2.689779	3.819119	0.157335
Male	HC	SN	54.1	14.78367	15.38635		15.80324	4.076698		6.89666
Male	HC	SN	60.1	14.11654	13.78599		14.37724	-2.34157		1.846777
Female	HC	SN	40.6	14.23919	14.28033	14.65801		0.288909	2.941357	
Female	HC	SN	48.8	13.25507	12.85809	13.48345		-2.99497	1.722974	
Female	HC	SN	50.3	14.6331	14.07179			-3.83586		
Female	HC	SN	52.7	13.17549	13.67766			3.811361		
Female	HC	SN	54.1	12.56421	12.73319	12.63321		1.344932	0.549221	
Male	PD contralateral	SN	40.8	14.08304	14.31954	14.99603	14.44076	1.679278	6.482898	2.540073
Male	PD contralateral	SN	45.2	14.99275	14.62393	14.31435	13.60835	-2.45999	-4.52489	-9.23378
Male	PD contralateral	SN	46	17.3188	16.76819	14.77863		-3.17927	-14.6671	
Male	PD contralateral	SN	49	16.20959	16.84926	16.37188	14.4477	3.946197	1.001156	-10.8694
Male	PD contralateral	SN	51.9	13.40329	13.69938	14.09807	14.83999	2.209126	5.183652	10.71905

Male	PD contralateral	SN	56	13.41169	13.64343	11.70928	13.93201	1.727884	-12.6935	3.879608
Male	PD contralateral	SN	60.3	13.62384	13.47572	14.44758	14.27864	-1.08717	6.046313	4.806295
Female	PD contralateral	SN	39.2	14.432	14.79249	15.63881	14.84578	2.497882	8.362066	2.867141
Female	PD contralateral	SN	49.8	15.00019	14.14266	14.13319	15.01487	-5.7168	-5.77991	0.097847
Female	PD contralateral	SN	50.6	14.69288	14.05056	14.46631	13.21558	-4.37166	-1.54206	-10.0545
Female	PD contralateral	SN	52.9	14.62418	15.31482	14.57626	15.75103	4.722583	-0.32771	7.705388
Female	PD contralateral	SN	54.1	13.451	13.89947	13.79514	13.40579	3.334114	2.558462	-0.33612
Male	PD ipsilateral	SN	40.8	14.1401	14.16184	13.79509	14.74425	0.153745	-2.43997	4.272585
Male	PD ipsilateral	SN	45.2	15.16026	14.9417	12.05906	15.14281	-1.44164	-20.4561	-0.11512
Male	PD ipsilateral	SN	46	14.9287	15.48748	14.2389		3.742954	-4.62062	
Male	PD ipsilateral	SN	49	15.68933	15.76579	13.77798	14.5816	0.487305	-12.1825	-7.0604
Male	PD ipsilateral	SN	51.9	13.82724	14.95947	13.64006	15.22446	8.18841	-1.3537	10.10479
Male	PD ipsilateral	SN	56	13.23918	14.09054	15.57805	13.38733	6.430605	17.66628	1.119013
Male	PD ipsilateral	SN	60.3	13.95536	13.37045	14.13931	14.03678	-4.19127	1.31811	0.583435
Female	PD ipsilateral	SN	39.2	13.55795	13.40803	14.40674	14.30506	-1.10576	6.260514	5.510556
Female	PD ipsilateral	SN	49.8	14.01106	13.48401	12.6526	14.73477	-3.76163	-9.69564	5.16533
Female	PD ipsilateral	SN	50.6	14.13869	13.82144	13.22318	12.27418	-2.24382	-6.47523	-13.1873
Female	PD ipsilateral	SN	52.9	15.14972	15.36886	15.20504	15.50581	1.446487	0.365162	2.350502
Female	PD ipsilateral	SN	54.1	12.96592	13.03366	13.21931	13.14023	0.522442	1.95424	1.34432

Appendix C DaT SBR results of reported PPMI subjects

Table C1. Healthy controls

HC		SBR				SBR L-R difference		Effective R ₂ (s ⁻¹)				Effective R ₂ L-R difference (s ⁻¹)	
Patient Number	Visit*	right caudate	left caudate	right putamen	left putamen	caudate	putamen	right caudate	left caudate	right putamen	left putamen	caudate	putamen
3301	SC	2.64	2.94	1.93	1.46	0.3	-0.5	10.58	10.22	14.02	13.47	-0.36	-0.5
3357	U01	3.42	3.5	2.37	2.6	0.08	0.23	10.55	10.46	12.06	12.25	-0.09	0.19
3369	SC	3.08	3.95	2.63	2.7	0.87	0.07	9.979	9.96	11.99	12.24	-0.02	0.25
3563	U01	1.98	2.15	1.68	1.38	0.17	-0.3	10.4	10.47	12.26	12.24	0.07	-0
3565	SC	2.21	2.36	1.83	1.59	0.15	-0.2	10.6	10.96	13.67	13.75	0.36	0.07
3571	SC	3.01	2.69	2.18	1.89	-0.3	-0.3	10.83	10.84	12.56	12.44	0.01	-0.1
3853	SC	3.21	3.67	2.97	2.62	0.46	-0.4	10.69	10.47	12.63	12.98	-0.22	0.34
3857	SC	3.53	3.6	2.73	2.81	0.07	0.08	10.68	11.23	13.15	13.22	0.55	0.06
3855	SC	2.79	3.25	2.47	2.19	0.46	-0.3	10.24	10.55	11.88	11.66	0.31	-0.2
3850	SC	3.31	3.14	2.62	2.32	-0.2	-0.3	10.35	10.84	13.36	13.71	0.48	0.35
3767	SC	2.64	2.62	2.28	1.98	-0	-0.3	10.36	10.12	13.28	13.19	-0.24	-0.1
3851	SC	2.48	2.86	2.13	2.25	0.38	0.12	10	10.12	12.45	12.27	0.12	-0.2

*Visit code: SC/U01 = 0 month, V04 = 12 month, V06 = 24 month, V10 = 48 month.

Table C2. PD patients

Patient Number	Visit*	SBR				SBR L-R difference		Effective R ₂ (s ⁻¹)				Effective R ₂ L-R difference (s ⁻¹)	
		right caudate	left caudate	right putamen	left putamen	caudate	putamen	right caudate	left caudate	right putamen	left putamen	caudate	putamen
3352	SC	1.9	1.77	0.7	0.55	-0.1	-0.2	11.48	11.91	13.33	13.4	0.43	0.07
3352	V04	1.71	1.62	0.69	0.62	-0.1	-0.1	11.2	11.82	13.09	13.17	0.62	0.08
3352	V06	1.37	1.33	0.6	0.33	-0	-0.3	11.41	11.5	13.07	13.13	0.09	0.06
3352	V10	1.33	1.37	0.74	0.46	0.04	-0.3	11.79	11.51	12.75	13.02	-0.28	0.27
3367	SC	2.01	1.23	0.51	0.34	-0.8	-0.2	10.67	10.57	12.14	12.03	-0.1	-0.1
3367	V04	1.83	1.5	0.7	0.59	-0.3	-0.1	10.31	9.774	11.97	12.21	-0.53	0.23
3367	V06	1.88	1.15	0.38	0.53	-0.7	0.15	10.66	10.35	11.9	12.08	-0.3	0.18
3367	V10	1.62	1.26	0.33	0.11	-0.4	-0.2	9.874	10.16	11.47	11.77	0.29	0.29
3800	SC	2.59	2.25	1.36	0.85	-0.3	-0.5	10.41	10.29	13.38	12.95	-0.12	-0.4
3118	SC	1.5	1.9	0.76	0.56	0.4	-0.2	10.06	10.32	11.74	12.62	0.26	0.88
3118	V04	1.59	1.72	0.51	0.68	0.13	0.17	9.838	9.883	11.8	12.41	0.05	0.61
3118	V06	1.28	1.44	0.44	0.52	0.16	0.08	10.3	10	11.87	12.62	-0.3	0.75
3118	V10	1	1.14	0.42	0.29	0.14	-0.1	10.82	10.23	11.74	12.66	-0.59	0.92
3822	SC	1.83	1.47	0.59	0.52	-0.4	-0.1	9.535	10.11	10.56	10.55	0.57	-0
3822	V04	1.74	1.24	0.55	0.54	-0.5	-0	9.525	9.907	10.55	10.46	0.38	-0.1
3822	V06	1.67	1.25	0.56	0.42	-0.4	-0.1	9.494	9.952	10.57	10.46	0.46	-0.1
3822	V10	1.44	1.36	0.52	0.3	-0.1	-0.2	9.591	10.38	10.6	10.62	0.79	0.02
3125	SC	2.05	2.79	0.59	1.12	0.74	0.53	10.62	10.79	12.52	13.04	0.17	0.51
3125	V04	1.88	2.15	0.66	0.99	0.27	0.33	10.62	10.81	12.63	13.45	0.19	0.82
3125	V06	1.63	2.2	0.85	0.83	0.57	-0	11.11	11.61	12.94	13.85	0.5	0.9
3125	V10	1.69	2.02	0.75	0.74	0.33	-0						

3365	SC	2.34	3.41	0.76	1.02	1.07	0.26	10.18	10.61	11.64	11.8	0.43	0.15
3365	V04	1.68	2.56	0.6	0.78	0.88	0.18	11.06	11.19	11.88	12.09	0.14	0.21
3365	V06	1.64	2.53	0.67	0.95	0.89	0.28	10.89	11.36	12.03	12.1	0.47	0.07
3365	V10	1.43	1.9	0.65	0.81	0.47	0.16	11.28	9.977	12.13	12.65	-1.3	0.52
3364	U01	2.6	2.98	0.96	1.37	0.38	0.41	10.55	10.36	13.15	13.45	-0.19	0.3
3364	V04	1.98	2.63	0.56	0.97	0.65	0.41	10.8	10.87	13.31	13.82	0.08	0.51
3364	V06	1.63	2.44	0.5	0.75	0.81	0.25	11.12	10.98	13.59	14	-0.14	0.42
3364	V10	1.09	1.51	0.59	0.43	0.42	-0.2	10.78	11.12	13.58	14.15	0.35	0.57
3108	SC	2.36	3.09	0.8	1.2	0.73	0.4	9.892	9.753	11.86	12.29	-0.14	0.43
3108	V04	2.36	2.81	0.76	0.95	0.45	0.19	9.947	9.983	12.07	12.18	0.04	0.11
3108	V06	2.44	3.1	0.65	1.28	0.66	0.63	9.858	9.901	11.81	12.23	0.04	0.41
3108	V10	2.03	2.42	0.64	0.82	0.39	0.18	10.27	10.34	12.45	12.65	0.08	0.2
4012	SC	2.16	2.48	0.81	1.08	0.32	0.27	10.62	9.871	12.89	12.93	-0.75	0.05
4012	V04	1.76	2.16	0.66	0.94	0.4	0.28	11.31	10.27	13.1	13.31	-1.04	0.21
4012	V10	1.34	1.74	0.68	0.96	0.4	0.28	9.849	9.411	12.28	12.73	-0.44	0.45
4012	V06	1.74	1.81	0.68	0.81	0.07	0.13	10.91	10.44	13.18	13.46	-0.47	0.29
3819	SC	2.33	1.68	0.97	0.6	-0.7	-0.4	10.57	10.15	13.13	12.96	-0.42	-0.2
3819	V04	2.37	1.96	0.98	0.56	-0.4	-0.4	11.03	10.85	12.99	12.96	-0.18	-0
3819	V06	1.88	1.67	0.68	0.51	-0.2	-0.2	10.97	10.84	13.19	13.31	-0.13	0.13
3819	V10	2.03	1.66	0.64	0.54	-0.4	-0.1	11.27	10.47	13.32	13.36	-0.81	0.03
3309	SC	1.83	2.38	0.94	1.04	0.55	0.1	11.84	11.37	13.51	13.55	-0.48	0.04
3309	V04	1.97	2.24	0.61	1.05	0.27	0.44	11.33	11.07	13.1	13.33	-0.26	0.23
3309	V06	1.96	2.24	0.81	0.94	0.28	0.13	11.35	10.98	13.11	13.31	-0.37	0.2
3309	V10	1.87	2.21	0.61	0.8	0.34	0.19	11.33	11.45	13.14	13.57	0.11	0.42

*Visit code: SC/U01 = 0 month, V04 = 12 month, V06 = 24 month, V10 = 48 month.

Appendix D Magnitude signal decays in 3D GRE, MESE and dual-contrast FSE sequences for 3.0 T clinical study at UHCW, Coventry

MR signal decays of the magnitude images acquired by the 3D GRE, MESE and dual-contrast FSE sequence, at 3.0 T clinical MRI study at UHCW, Coventry were initially checked as part of MR pulse sequence set-up and quality reassurance.

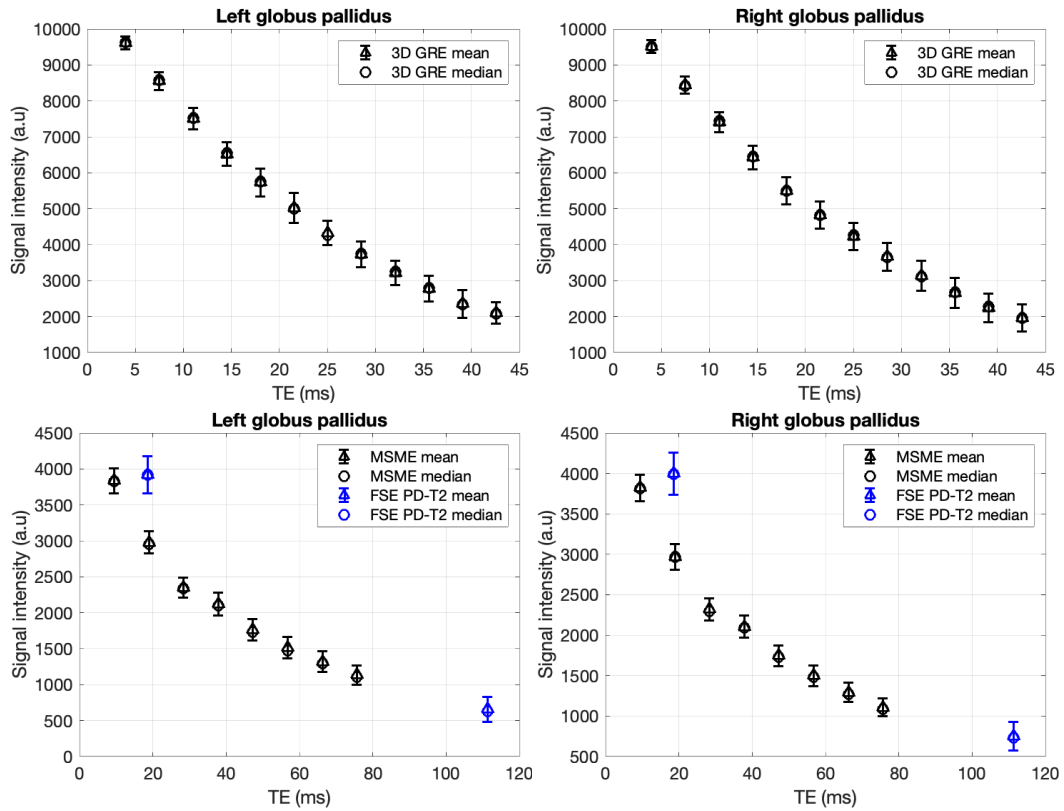


Fig. D.1 Magnitude signal decays for various sequences.

Iron-rich brain region globus pallidus was measured.

Appendix E Agarose gel preparation, protein aggregation and gelation

E1. Agarose gel preparation

Preparation of 4 % w/v agarose gel stock

A 4 % w/v agarose gel stock was prepared by melting the agarose (A9539, Sigma-Aldrich) in the prepared minimum KH buffer (pH 7.4) using a hot plate instead of a water bath method due to the moderate concentration. To minimise extended heating, the agarose suspension was placed in a beaker that can contain 3-4 times the volume of the suspension and was gently stirred at room temperature for 20 min to prevent clumping. To avoid charring during the gel dispersion, while stirring moderately, the suspension was covered and first allowed to stand at the 110°C-hot plate for 1 hr, and the temperature was lowered to 95°C to prevent boiling/charring. The gel solution was then heated at 95°C for another hour meanwhile continued stirring gently, to ensure complete dispersion of the gel and let the air bubbles escape. The agarose gel mixture was weighed before and after heating, and deionised water was added to the mixture and dispersed completely to compensate for the mass loss via evaporation during heating. The hot 4 % w/v agarose gel was allowed to cool to 50-55°C before the following gelation with protein samples.

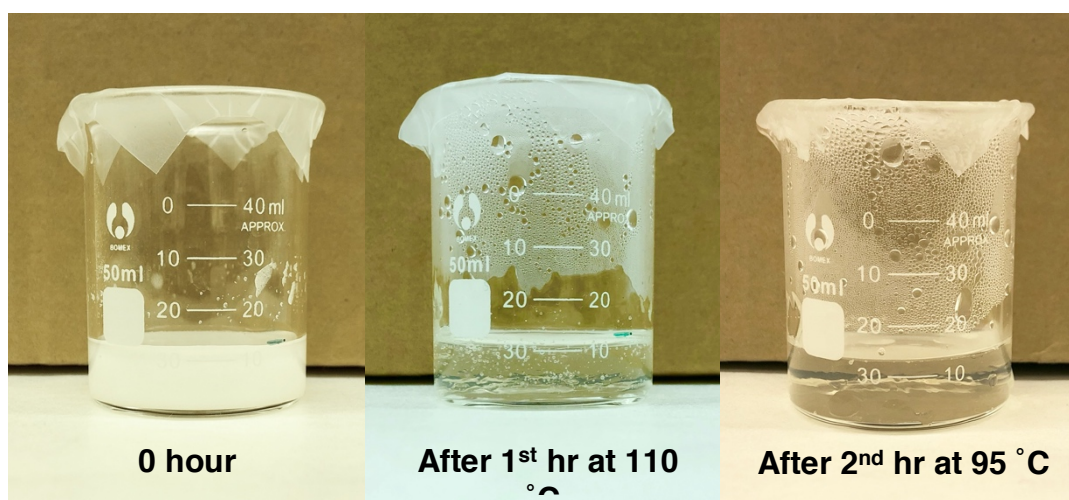


Fig. E1.1 Preparation of 4 % w/v agarose gel stock

Preparation of 8 % w/v agarose gel

A very high concentration of 8 % w/v agarose gel was prepared to serve as a supporting matrix for the 2 % w/v agarose-protein gel sample during the MRI examination. Because of the high concentration of the gel, boiling water bath was

not sufficient anymore to disperse the agarose gel without extremely extending the reacting time; and the direct hot plate method was challenged in evenly heating up the agarose suspension without charring the agarose mixture near the direct contact point, due to the swelling of agarose in the confined volume that largely disabled stirring during heating. Therefore, the 8 % w/v agarose gel solution was prepared by melting agarose using a modified microwave-ultrasonic bath combined method.

The appropriate amount of agarose (A9539, Sigma-Aldrich) powder was weighed and slowly sprinkled into 50 mL deionised water. After gently stirring to remove clumps, the stirrer was removed, and the high agarose content suspension was let stand at room temperature for 30 min to allow the agarose to be hydrated and swelled. Then the gel mixture was covered and transferred to the centre of a microwave oven to be heated, a beaker with 4-5 times the volume of the agarose suspension was used to give enough space for the solution to foam and boil during heating. The agarose suspension was heated on medium power for 15-10-10 s, with an interval of a few seconds to prevent foaming when the agarose mixture was swirled gently to re-collect evaporated solution from the cover and wall of the beaker, and to re-suspend undissolved agarose particles each time; then the suspension was heated for another 10 s to come to boil. After boiling, the agarose solution was re-heated in the microwave oven for 30 s to allow continue boiling, with a pulse every 5 s to avoid overboiling/overheating; and this re-heating process was repeated once to ensure the complete dissolution of agarose and to form a clear, colourless to light yellow agarose solution.

After boiling and completely dispersing the agarose, the resulting hot agarose solution was transferred to a pre-heated 65 °C ultrasonic bath to sit for 2 hrs, to remove bubbles generated from the previous microwave heating/re-heating process. Every 30 min, the gel solution was gently swirled to re-collect and disperse droplets formed by evaporated solution. The agarose gel mixture was weighed before and after heating, and deionised water was added to the mixture and dispersed completely to compensate for the mass loss via evaporation during heating. The 8 % w/v gel solution was allowed to cool to 55 °C before casting.

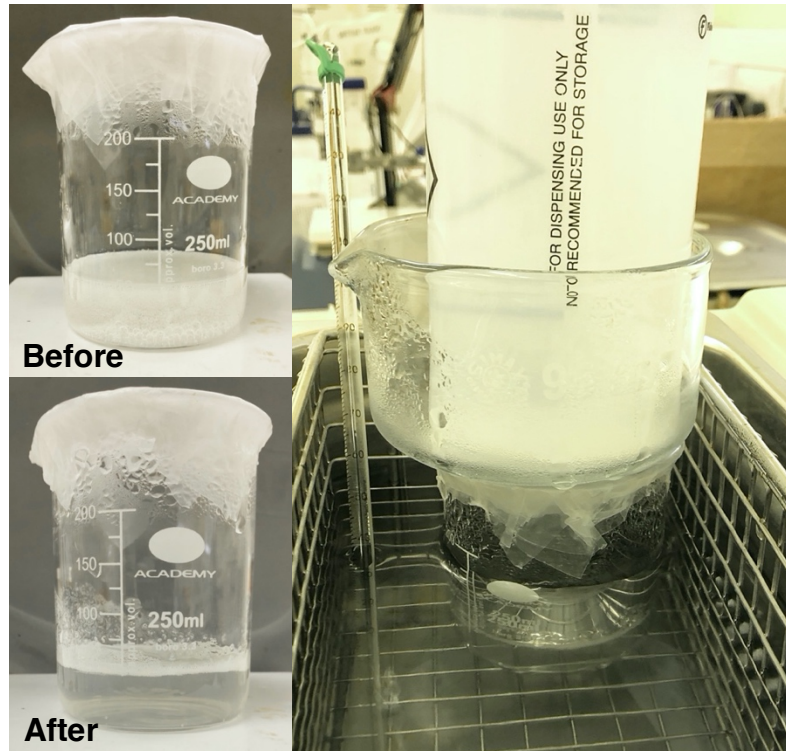


Fig. E1.2 Preparation of 8 % w/v agarose gel using the ultrasonic bath. The agarose gel before (top left), during (right) and after (bottom left) 2-hour 65 °C ultrasonic bath.

E2. Protein aggregation and gelation for phantom construction

Preparation of modified Krebs-Henseleit (KH) buffer and protein suspensions

The suspension preparation and the incubation methods were adopted from the work of Everett *et al* [88]. A modified Krebs-Henseleit (KH) buffer was prepared before the experiment. In 100 mL deionised water, 3.02 g piperazine-N,N'-bis(2-ethanesulfonic acid) (PIPES), 0.70 g NaCl, 0.036 g KCl, 0.030 g MgSO₄, 0.021 g CaCl₂, 0.2 g glucose were weighed and carefully dissolved. While stirring, the solution was first neutralised by adding 1 M NaCl to allow the complete dissolution of the remaining PIPES. At 37 °C, the pH of the buffer was adjusted to 7.4, and then continually stirred for another hour to ensure a stable pH. This modified KH buffer contained 100 mM PIPES, 118.5 mM NaCl, 4.8 mM KCl, 1.2 mM MgSO₄, 1.4 mM CaCl₂, 11 mM glucose. A minimum KH buffer (pH 7.4, 37°C) was also made using the above method, but only consisted of 100 mM PIPES and 118.5 mM NaCl. All reagents used were analytical grade. All buffers were stored at 4 °C until use.

Horse spleen ferritin (Type I, 57 mg/mL, in saline solution; ref: F4503) was obtained from Sigma-Aldrich (Gillingham, United Kingdom). A total of 0.5 mL ferritin stock with the concentration of 1.44 mg/mL horse spleen ferritin was made by diluting 12.6 µL 57 mg/mL ferritin with 487.4 µL modified KH buffer (pH 7.4). The 1.44 mg/mL ferritin stock solution was then divided into two 250 µL ferritin solutions.

Amyloid β-protein (1-42) (ref. 4014447) was purchased from Bachem (Bubendorf, Switzerland) and stored at -80 °C before use. The entire 1 mg peptide was freshly dissolved into 0.5 mL 1 mM NaOH to make a 2 mg/mL Aβ(1-42) solution on the day of use to prevent aggregation. The peptide solution was let stand for 30 min at room temperature before use to allow complete dissolution.

Incubation of Aβ(1-42) with Horse Spleen Ferritin

Three protein/peptide suspensions were prepared for the following incubation. From the 2 mg/mL Aβ(1-42) stock, 50 µL peptide solution was added to 250 µL 1.44 mg/mL ferritin stock to create an Aβ+ferritin suspension (Aβ+Ftn), where the concentrations of Aβ and ferritin were 0.33 mg/mL and 1.2 mg/mL respectively. At the same time, a

ferritin reference (Ftn) was prepared as above but substituting the A β solution with 1 mM NaOH. Similarly, an A β control (A β) was also made by adding the corresponding A β stock solution to 250 μ L modified KH buffer. All three suspensions were kept in tightly closed microcentrifuge tubes and incubated at 37 °C for a consecutive period of 100 hrs before gelation.

Gelation of incubated protein suspensions

The incubated protein suspensions A β +Ftn, A β , and Ftn were distributed into individual microcentrifuge tubes after incubation and diluted with modified KH buffer (pH 7.4) to a concentration gradient series according to Table SB.1.

Table E2.1 Dilution gradient series of 3 incubated protein suspensions.

	A β +Ftn suspension	Ftn suspension	A β suspension	Modified KH buffer (pH 7.4)
A β +Ftn 3	60 μ L	-	-	-
A β +Ftn 2	30 μ L	-	-	30 μ L
A β +Ftn 1	10 μ L	-	-	50 μ L
A β +Ftn 0	-	-	-	60 μ L
Ftn 3	-	60 μ L	-	-
Ftn 2	-	30 μ L	-	30 μ L
Ftn 1	-	10 μ L	-	50 μ L
Ftn 0	-	0 μ L	-	60 μ L
A β 3	-	-	60 μ L	-
A β 2	-	-	30 μ L	30 μ L
A β 1	-	-	10 μ L	50 μ L
A β 0	-	-	0 μ L	60 μ L

Each diluted sample was allowed to sit in a heated ultrasonic bath for 5 min to remove air bubbles and to disperse any moderate protein clumps, at the same time the heated ultrasonic treatment pre-warmed the microcentrifuge tube and the contained sample suspension individually to 45 °C.

Then the prepared 4 % w/v agarose gel stock that was cooled to 50-55 °C was gently pipetted and mixed with the ultrasonic treated, pre-warmed protein suspension in a volume ratio of 1:1, to create the 2 % w/v agarose-protein gel mixture. Care was taken in handling the mixture to well distribute the solution/suspension at the bottom of the microcentrifuge tube, while not generating air bubbles in the mixture during pipetting. After mixing, the 2 % w/v agarose-protein gel mixture was immediately returned to the 45 °C ultrasonic bath for another 10 min to remove any remaining bubbles and to reduce protein/gel clumping. The 2 % w/v agarose-protein gel was transferred to a 37°C ultrasonic bath for 30 min to allow gelation to start, then the protein gel sample was let sit at room temperature overnight to complete the gelation process. All 2 % w/v agarose-protein gel samples were stored at 4 °C for no more than one week until use.

Supporting gel casting and phantom construction

The set 2 % w/v agarose-protein gel sample was carefully removed from the microcentrifuge tube while keeping its shape intact, providing a near cone-shaped gel with around 7-mm height and 5-mm diameter at its base. The gel was then rinsed using deionised water and the solution remaining on the gel surface was removed using filter papers.

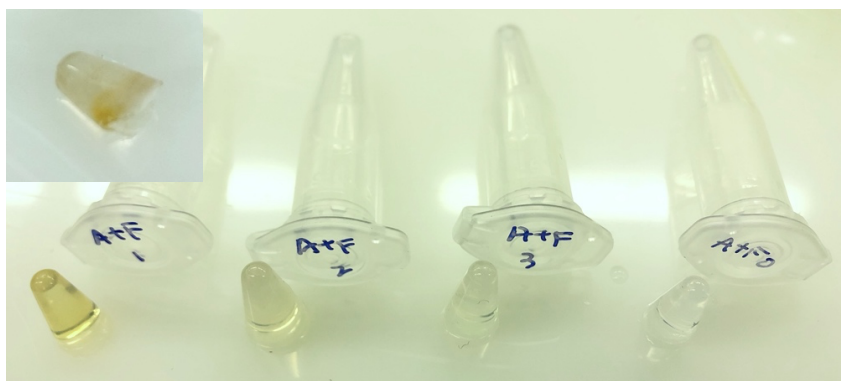


Fig. E2.1 Removed 2 % w/v agarose-protein gel samples.

Insert: side-view of a protein gel sample.

The protein gel sample was then placed on the bottom of a 20 × 20 mm (ID × H) soft silicone cylinder mould, standing on its base and its round end pointing upwards. The

8 % w/v agarose gel solution was then cast into the cylinder mould to about 1.5 cm height, covering the 2 % w/v agarose-protein gel sample. Some small air bubbles floating on the surface of the 8 % w/v gel solution was carefully removed before pouring, and those remaining in the gel solution tended to float to the surface of the gel assembly that was just cast. The gel assembly was allowed to stand for 5-10 min until it set and can be removed from the cylinder mould, then was slid back into the mould with the topside first to expose the base of the gel block. More supporting agarose gel solution was then cast until the entire cylinder mould was filled. The complete 20 × 20 mm (ID × H) gel assembly was let sit for another 10 min until the whole block can be removed from the mould, then the excessive top and bottom of the gel cylinder was removed with a sharp blade to form the final gel assembly MR phantom with an approximate dimension of 20 × 10 mm (D × H), in which the 2 % w/v agarose-protein gel sample was sitting at the centre of an 8 % w/v agarose supporting matrix. The final gel assembly MR phantom was transferred to 4 °C to continue gelation for another 2 hrs. The gel assemblies were stored at 4 °C for no more than 48 hrs before MR examinations.

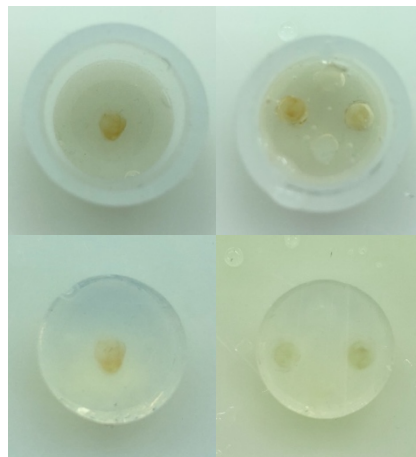


Fig. E2.2 Moulding and the resulting gel assembly MR phantoms. Left column: single protein gel sample embedded; Right column: four protein gel samples embedded.

Appendix F Pre-scan adjustments and shimming strategies for 9.4 T preclinical MRI

F1. Pre-scan adjustments

Tuning and matching

The MR signal-to-noise ratio (SNR) is highly dependent on the efficiency of the RF power transmission and reception. The power is transported between the preamplifier and the RF coil via a coaxial cable. To reach its maximum, the transmitter, the cable, and the RF coil needed to achieve the same impedance. This was achieved by manually adjusting the matching capacitor of the RF coil/probe, until all the power was transferred to the coil with zero power reflected back to the transmitter. It is referred to as a power match situation.

On the other hand, the sensitivity of the probe required adjustment so that the transmission frequency of the RF coil was near the observed nucleus' frequency (^1H). Although the probe had been initially tuned for the 400 MHz spectrometer during installation, slight variations in the transmission frequency (< 100 kHz) were adjusted within a specified range using the tuning capacitor built into the probe circuitry. The tuning and matching result was examined on the wobble curve (Fig. F1.1) of the RF coil after the sample was inserted and stabilised. The 'dip' in the wobble curve should reach the bottom (matched) and align with the frequency centre (tuned).

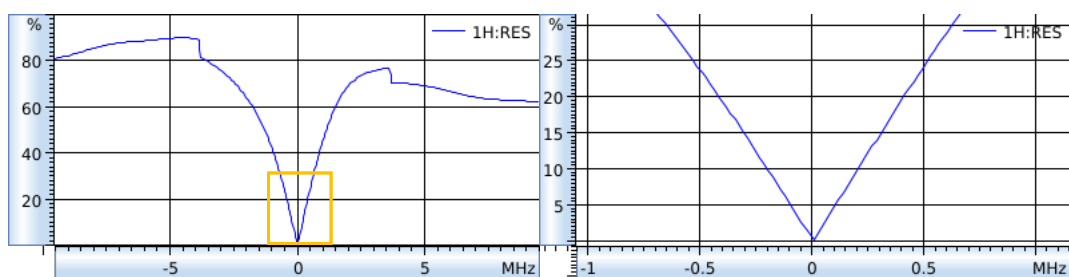


Fig. F1.1 An example wobble curve of a phantom after the tuning and matching adjustment. Left: the entire wobble curve of the phantom; Right: zoom area of the selected yellow box.

Shimming

Shimming describes the process of correcting the magnetic field inhomogeneity caused by the hardware (e.g., coils materials and electric currents) and the sample's

location and magnetic properties. The GRE sequence is highly sensitive to the magnetic field inhomogeneity, which is generally present near the sample-air interface. On the other hand, in sequences where multiple, repetitive RF pulses are used to generate MR signals, i.e., MESE, FSE, EPI sequences, the phase error caused by the field inhomogeneity tends to propagate along the echo train length via phase accumulation.

Within the sample space of the RF coil, the total magnetic field (B_0') experienced by each location (x,y,z) is the summation of the desired constant or homogeneous magnetic field B_0 and the field inhomogeneity at that point. Shimming is a process of finding a set of spatial functions $S_i(x, y, z)$ that satisfy

$$B_0 = B_0'(x, y, z) + \sum_i c_i S_i(x, y, z) \quad \text{Eq.(F1.1)}$$

Ideally, shimming therefore counteracts the field inhomogeneity caused by the hardware design and the inserted sample, by manipulating the current in the shim coils so that it generates the desired field profile $S_i(x, y, z)$.

Before starting the shimming, the sample tube was placed in the centre of the RF coil, then the RF coil/probe was carefully moved into the gradient coil and fixed at the vertical shim centre, which is also the 3-axis gradient centre.

Shimming strategy

To achieve high quality of the image data, a systematic, multi-step shimming strategy was developed for the MR examination of sample with large susceptibility variation, on a total of 18 shim sets (up to 4th order shim). It included three steps of FID shimming, with increased shim order at each step to achieve maximum FID signal globally and followed by an additional localised shimming based on the field map to minimise the B_0 inhomogeneity within the sample. With this shimming strategy, the MR acquisition minimised the field inhomogeneity caused by the susceptibility variation within the sample, whilst maintaining a good field homogeneity within the RF coil by compensating for the field distortion caused by the insertion of sample. The details of the shimming step are described in the following section F2.

Frequency adjustment

This adjustment was performed automatically at the beginning of scanning each sample, and manually re-adjusted after alternation of higher-order (3rd and 4th order) shim sets. The algorithm searched the dominant ¹H resonance frequency of the sample by sweeping the central frequency around 398.2 MHz (Fig. F1.2), the configuration frequency for water considering the main field B₀ drift of the magnet and set it to the frequency of the spectrometer.

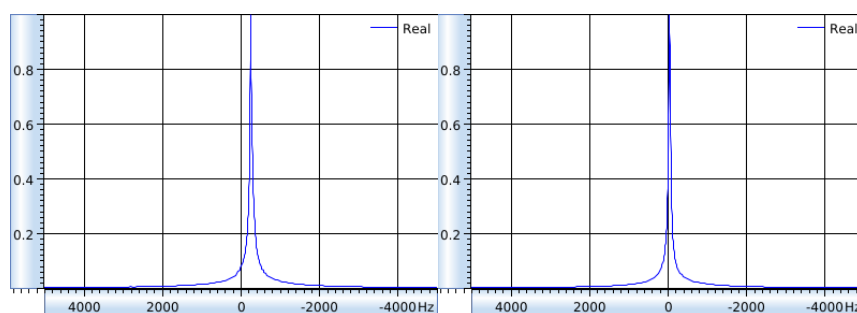


Fig. F1.2 Frequency shift of the dominant resonance frequency of a sample before (left) and after (right) the frequency adjustment.

Reference RF power and receiver gain

After the completion of all the above adjustments, reference power and receiver gain adjustments were carried out to calculate the transmitter and receiver attenuation/gain. As the RF adjustment depends on the coil loading and sample location, when the RF coil was fastened at the magnet centre, the construction of the phantom holder allowed the sample to be placed within the sensitivity centre of the coil, around $z = 0$ and occupied at least $z = \pm 2.5$ mm coil space, therefore a standard Paravision method (PVM) can be reliably used to adjust the reference power. In this method, a 3-pulses stimulated echo (STE) sequence was employed, where an α - 2α - α pulse train with a consistent pulse amplitude was applied to the selective 5-mm slice located at the imaging centre ($z=0$). The algorithm varied the pulse angle α by gradually increasing the RF pulse amplitude, until the signal amplitude at the slice profile's centre of the STE was minimised, which was generated after the last α excitation pulse. The peak power reached for the α pulse at this point was set to be the reference power of a 1-ms 90° RF pulse.

As the last step of the pre-scan adjustment, the receiver gain was adjusted individually for each pulse sequence of the following MR acquisition, according to their scan parameters, to obtain appropriate signal intensity for the analogue-to-digital converter (ADC). The adjustment result was confirmed once the maximum signal intensity received was adjusted to 1 (Fig. F1.3).

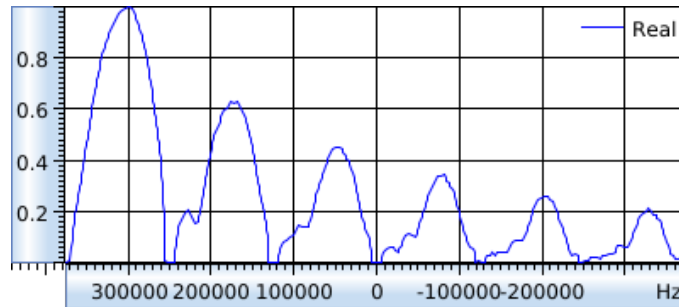


Fig. F1.3 Adjusted receiver gain of a multi-echo gradient echo sequence.

F2. Shimming strategies

To minimise the susceptibility artefact and optimise SNR, a consistent multi-step shimming was employed in this work, with details described here.

a) Global FID shim

An iterative global linear shim adjustment of 1st order shim sets based on the non-localised FID integral was initially ran at the beginning of scanning each sample. A non-selective hard pulse was sent by the RF coil to generate an FID signal for each shim setting, and the area under the FID in the time domain (showed as GS_normalised area) was maximised, by fitting the FID area as a function of shim sets to a Gaussian curve, and setting the shim values corresponding to the FID area at the centre of the curve the optimised results.

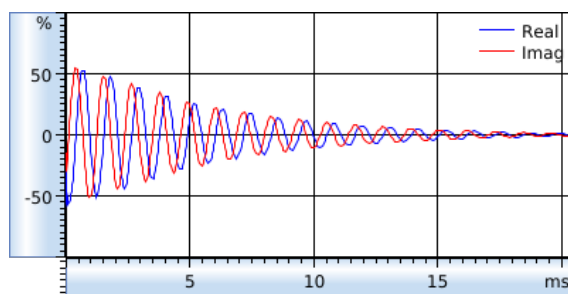


Fig. F2.1 An example global FID of a phantom after the 1st order shim adjustment

The resonance frequency was adjusted to the frequency where the maximum peak of the Fourier Transform of the FID signal was located. This process was done automatically at the beginning of each study (sample) within PV6.

b) 1st order and z² shim

Similar to the 1st order shimming, a series of gradient sweeping was performed on Z2-X-Y-Z shims to locate the maximum FID area. It was based on an algorithm, which allowed repetitive sweeping of above shims on both sides of the established shim setting, back-and-forward for 3 times. The sensitivity of the sweeping was increased for each repetition, with 200 Hz, 100 Hz and 50 Hz respectively.

c) 1st and 2nd order shim

An iterative shimming was then performed on X-Y-Z shims and Z²-XZ-YZ-XY-X²-Y² shims. For each shim set, 3 iterative were carried out with a decreasing step length that started from 200 Hz. Every time when completing a 2nd order shim, 1st order shims X-Y-Z were readjusted afterwards.

d) B₀ map shim

To minimise the high-order gradients that generated at the sample surface, higher-order shims and localised signal examination were performed using B₀ map shim. A corresponding B₀ map (field map) was acquired before shimming, using a temporary phase-difference technique, within a cubic 22mm-FOV that covered the whole sample and the region-of-interest (ROI) to be imaged later at the centre of the geometry. The acquisition was carried out using a 3D GRE pulse sequence with a non-selective hard pulse, and with two echo times (T_E) at T_{E1}=1.63 ms (minimum echo allowed) and T_{E2}=3.58 ms. The field map was calculated from the spatially varied phase evolution $\phi(x,y,z,t)$ during the echo spacing ΔTE .

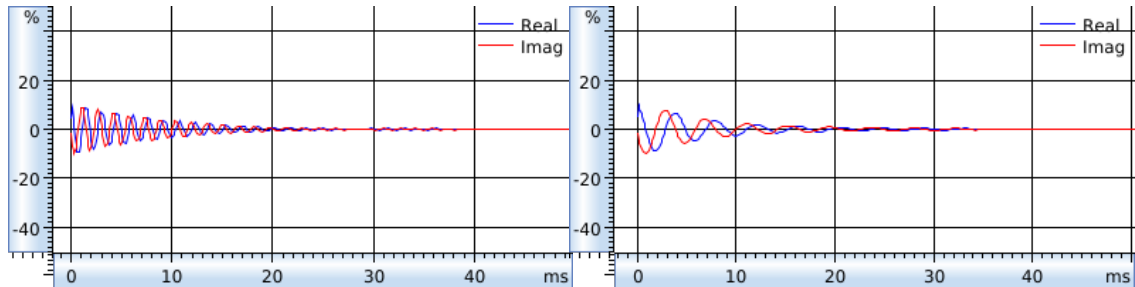


Fig. F2.2 Comparison of FIDs within the selected shim volume from two sets of shims calculated using different shimming methods.

Left: 1st and 2nd order shimming; Right: B₀ map shimming

The field profile was calculated pixel-wisely within a 128*128*128 matrix, then the mapshim algorithm can calculate the optimal shim sets that satisfy Eq(F1.1), using the least-squares method to minimise the residual field across the chosen shim volume. The shim volume was selected to cover the entire inserted gel sample. After this step, sometimes the time-domain FID area was slightly compromised compared with lower-order shimming results, but the local field homogeneity within the sample

was generally improved, by visual examination of B_0 maps and the image quality of the anatomical scans (localiser) before and after the shimming.

Appendix G Assessment of QSM reconstruction on 9.4 T preclinical MRI

G1. Background field removal

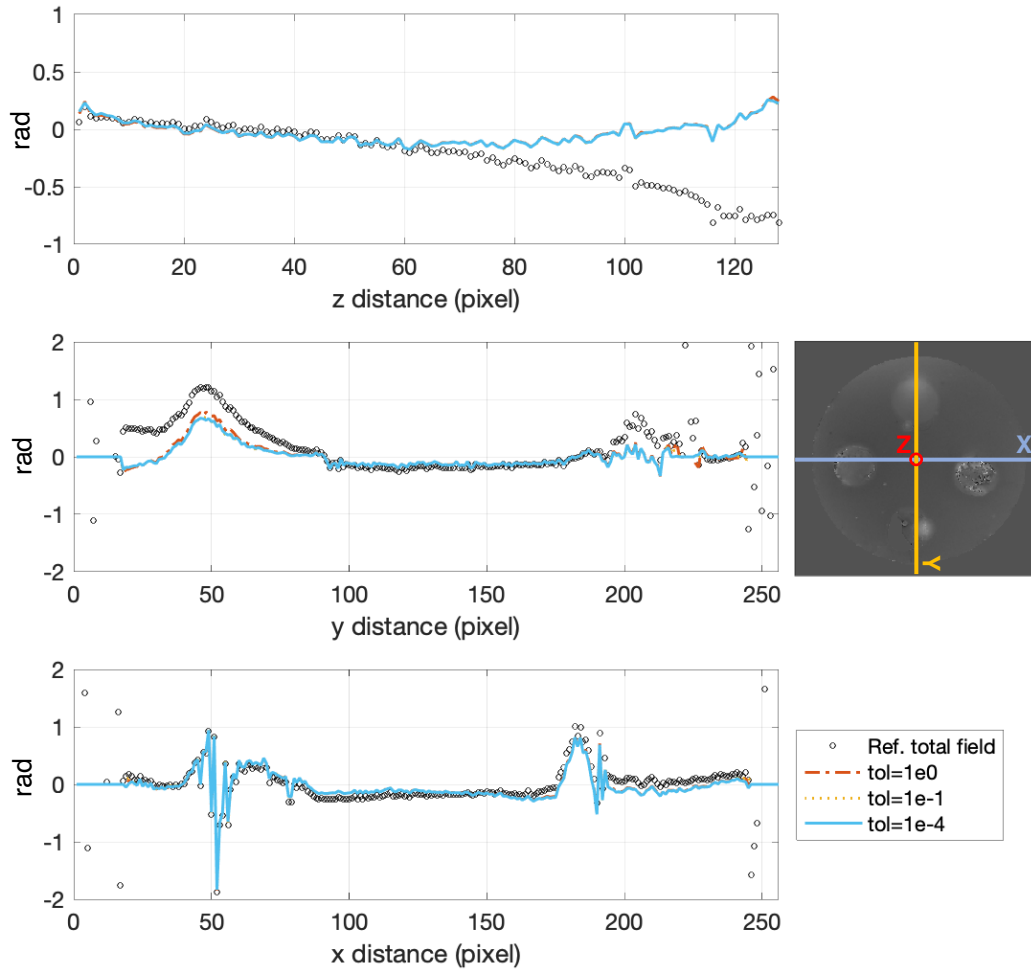


Fig. G1.1 An example line-profile of the RDF for A β +Ftn phantom estimated using PDF method with different tolerance (tol) at maximum iteration = 300.

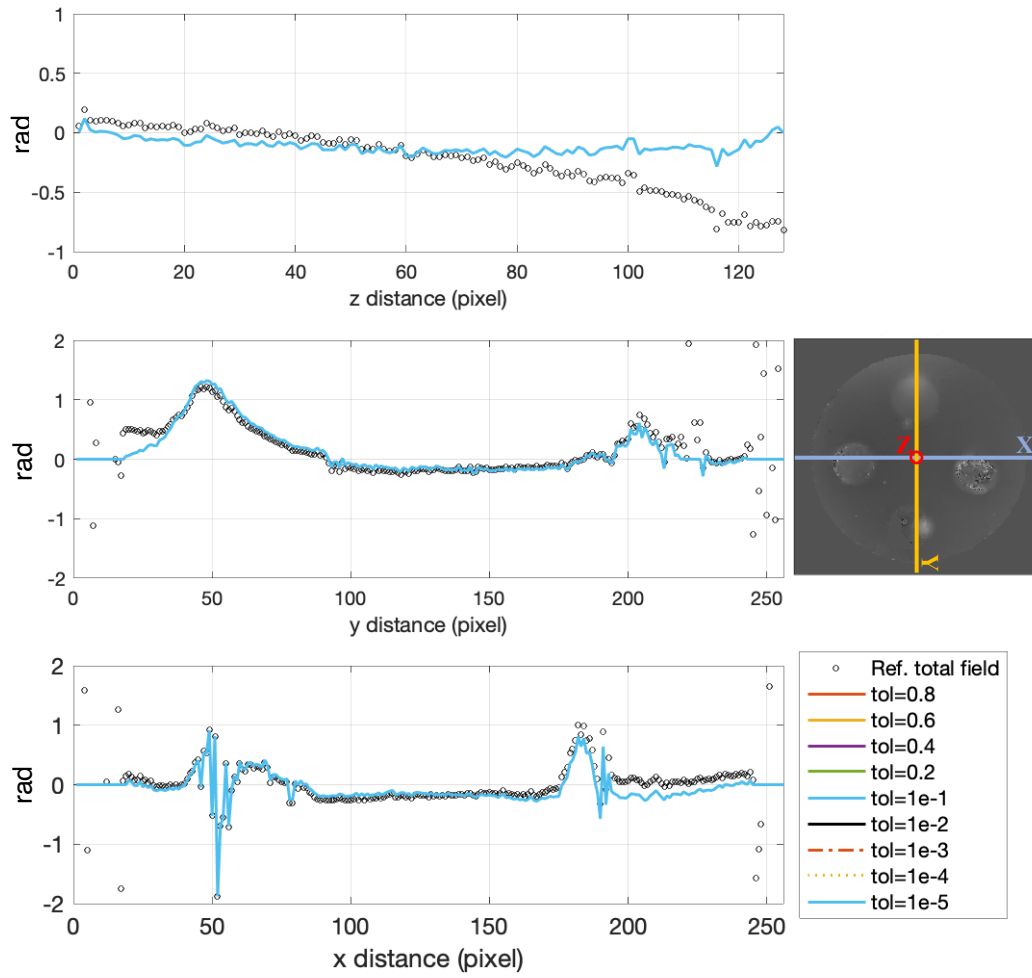


Fig. G1.2 An example line-profile of the RDF for $A\beta$ +Ftn phantom estimated using LBV method with varied tolerance (tol).

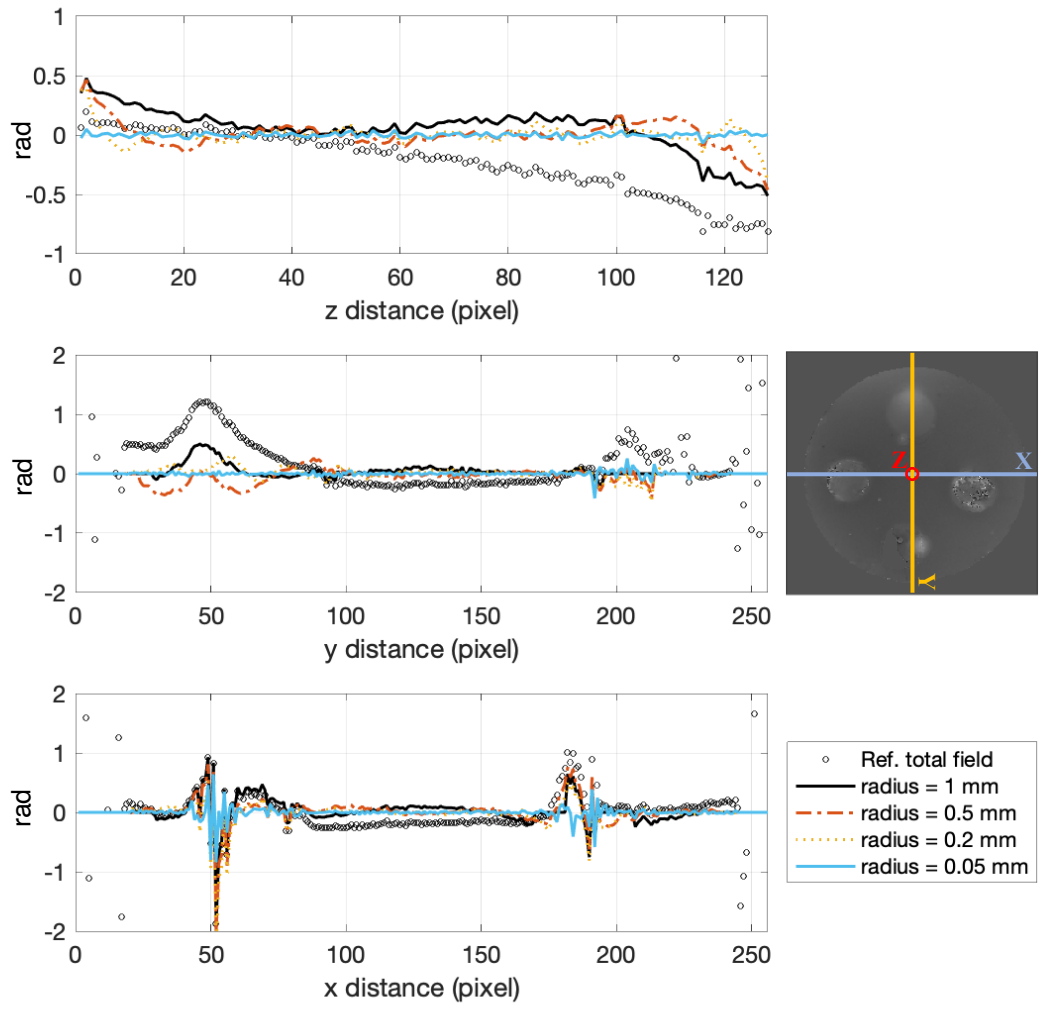


Fig. G1.3 An example line-profile of the RDF for $A\beta$ +Ftn phantom estimated using SHARP method with various SMV kernel radius. The k-space truncation values = 0.08.

G2.L-curve analysis

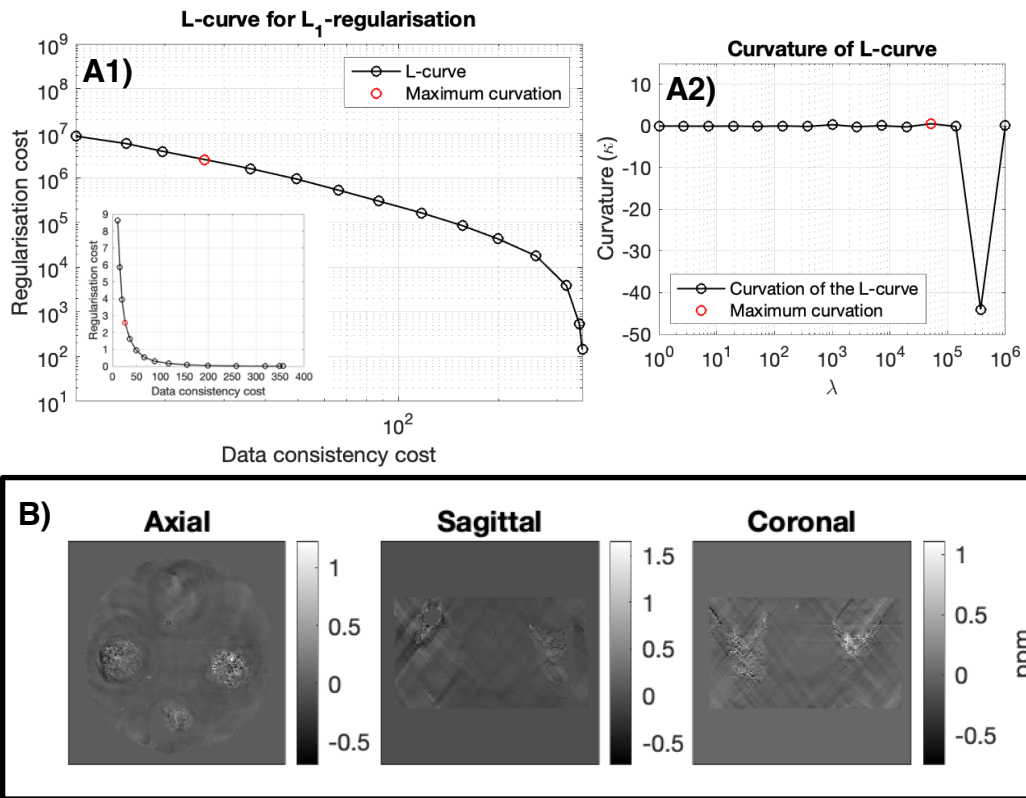


Fig. G2.1 L-curve analysis and the susceptibility images of $A\beta$ +Ftn phantom reconstructed with λ selected using the L-curve criterion.

A1: Log-log L-curve of the regularisation cost and the data fidelity cost; inserted image: plotting in a linear axis; A2: calculated curvature derived from λ spanning across a large logarithm scale. B: reconstructed susceptibility images with $\lambda = 5.18 \times 10^4$.

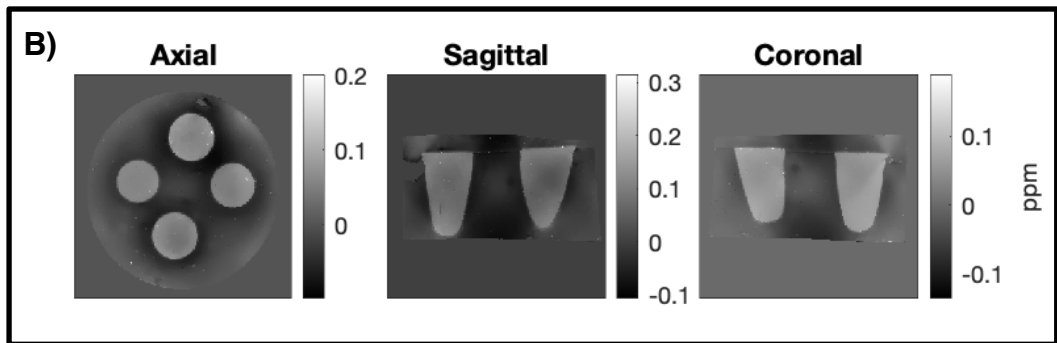
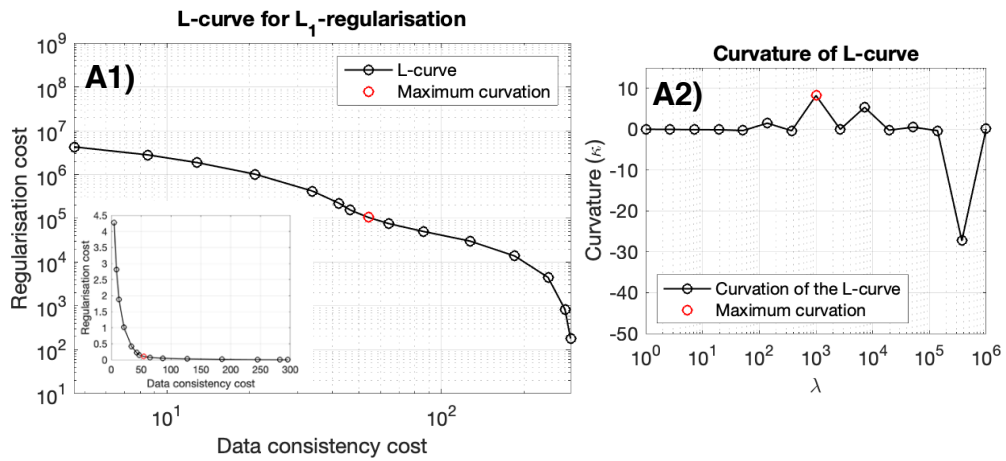


Fig. G2.2 L-curve analysis and the susceptibility images of Ftn phantom reconstructed with λ selected using the L-curve criterion.

A1: Log-log L-curve of the regularisation cost and the data fidelity cost; inserted image: plotting in a linear axis; A2: calculated curvature derived from λ spanning across a large logarithm scale. B: reconstructed susceptibility images with $\lambda = 1 \times 10^3$.

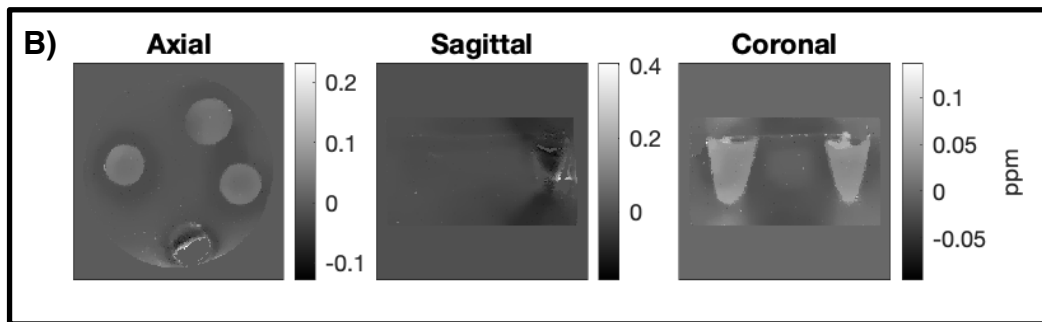
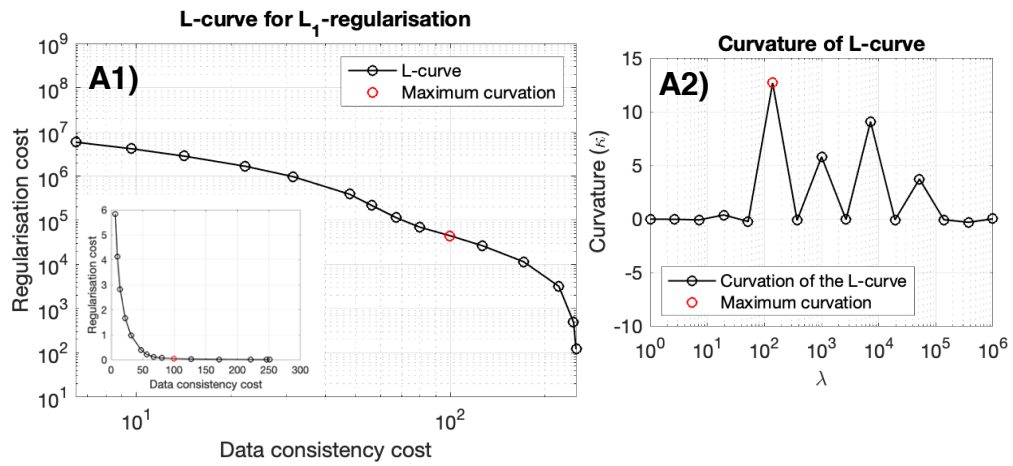


Fig. G2.3 Fig.11 L-curve analysis and the susceptibility images of A β phantom reconstructed with λ selected using the L-curve criterion.

A1: Log-log L-curve of the regularisation cost and the data fidelity cost; inserted image: plotting in a linear axis; A2: calculated curvature derived from λ spanning across a large logarithm scale. B: reconstructed susceptibility images with $\lambda = 1.39 \times 10^2$.

G3.U-curve analysis

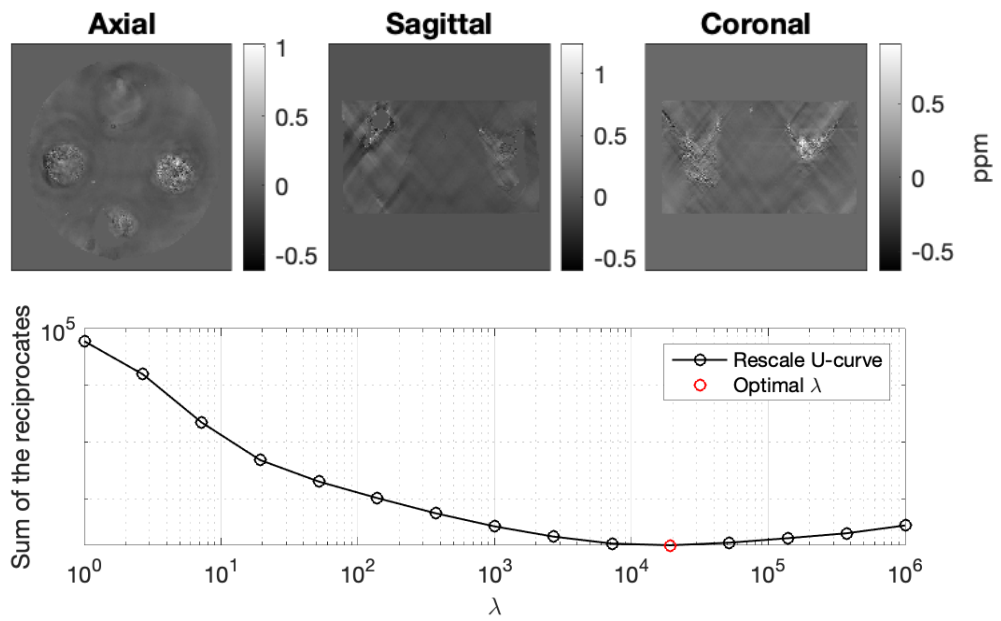


Fig. G3.1 Reconstructed susceptibility images (upper) of $A\beta$ +Ftn phantom and its U-curve (bottom). Optimal regularisation parameter $\lambda = 1.93 \times 10^4$.

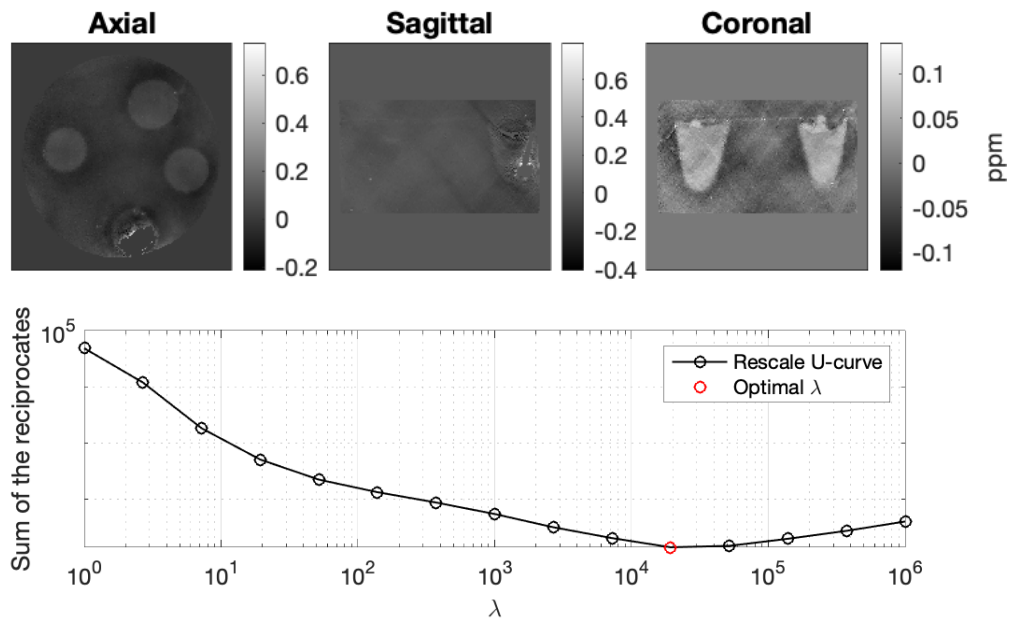


Fig. G3.2 Reconstructed susceptibility images (upper) of $A\beta$ phantom and its U-curve (bottom). Optimal regularisation parameter $\lambda = 1.93 \times 10^4$.

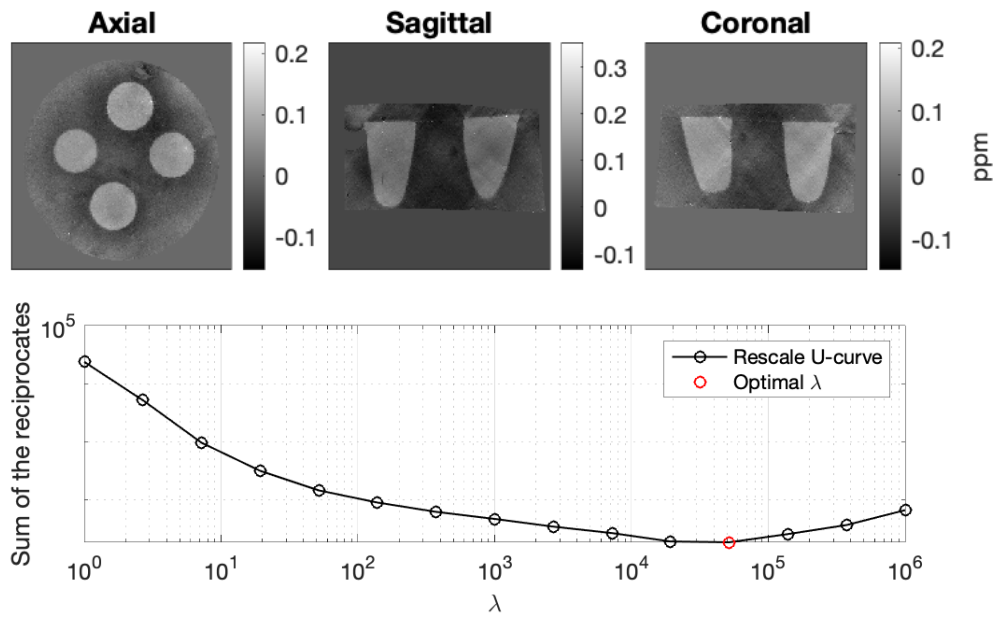


Fig. G3.3 Reconstructed susceptibility images (upper) of Ftn phantom and its U-curve (bottom). Optimal regularisation parameter $\lambda = 5.18 \times 10^4$.

Appendix H Summary of linear regression analyses between R_2^* and ferritin levels, and between susceptibility and ferritin level in A β +Ftn, Ftn and A β phantoms

Table H1. Summary of linear regression analysis

Phantom	Correlation	k	C	SSE	R^2	Adjusted R^2	RMSE
A β +Ftn	Median R_2^* -ferritin	42.48	21.84	44.76	0.8943	0.8415	4.7308
	Mean R_2^* -ferritin	58.08	21.59	24.89	0.9661	0.9491	3.5278
	Median susceptibility-ferritin	0.1473	0.0013	0.0003	0.9473	0.9209	0.0113
	Mean susceptibility-ferritin	0.1502	0.0073	0.0003	0.9473	0.9209	0.0113
Ftn	Median R_2^* -ferritin	14.65	14.73	0.7061	0.9846	0.9769	0.5942
	Mean R_2^* -ferritin	15.00	14.84	0.7818	0.9837	0.9756	0.6252
	Median susceptibility-ferritin	0.0123	0.0441	$8.2e^{-05}$	0.2806	-0.0791	0.0064
	Mean susceptibility-ferritin	0.0100	0.0466	$8.2e^{-05}$	0.2806	-0.0791	0.0064
A β	Median R_2^* -ferritin	-10.44	19.90	3.7542	0.3156	-0.0266	1.3701
	Mean R_2^* -ferritin	-10.64	20.05	3.391	0.346	0.020	1.302
	Median susceptibility-ferritin [†]	-0.004	0.0313	$1.1e^{-05}$	0.0202	-0.9597	0.0033
	Mean susceptibility-ferritin [†]	-0.0029	0.0313	$3.1e^{-05}$	0.0036	-0.9927	0.0056

A linear correlation $y = kx + C$ was fitted for the observed data individually, where y was the observed value of R_2^* (s^{-1}) or susceptibility (ppm), x indicated the nominal concentration of the ferritin or A β (mg/mL), and the slope coefficient k and a constant offset C were estimated for each fit. [†] Correlation was fitted without the measurements in A β 1 ROI, due to the susceptibility artifact.

Appendix I Ethical approval documentation

The list of documentations for the ethical approval granted for the study presents here:

- I1. Signed BSREC application form
- I2. Data flow map
- I3. Invitation email
- I4. Poster and leaflet
- I5. Participant information sheet (PIL)
- I6. MRI information sheet
- I7. Consent form
- I8. MRI safety screening form
- I9. Sample MRI scan list
- I10. BSREC full approval
- I11. GafREC application form
- I12. GafREC approval letter – use of facility only
- I13. GafREC approval letter – retrospective data
- I14. GafREC insert letter for COVID19 response

Biomedical and Scientific Research Ethics Committee (BSREC):
Application Form for Research Ethical Approval

Date: 24 th Jun 2019		Version: 001	
SECTION 1. APPLICANT DETAILS			
1.1 APPLICANT			
Applicant's Title (optional):	Miss		
Applicant's Forename:	Jierong		
Applicant's Surname:	Luo		
School or Department:	School of Engineering		
Warwick e-mail address:	J.Luo.1@warwick.ac.uk		
Contact telephone number:	+44 (0) 7414474558		
Applicant's Status:			
STUDENT:		STAFF:	
Undergraduate Student	<input type="checkbox"/>	Professor	<input type="checkbox"/>
Taught Postgraduate Student	<input type="checkbox"/>	Associate Professor	<input type="checkbox"/>
Postgraduate Research Student	<input checked="" type="checkbox"/>	Assistant Professor	<input type="checkbox"/>
		Research Fellow	<input type="checkbox"/>
Name of course/qualification:	PhD in	Teaching Fellow	<input type="checkbox"/>
Engineering		Other	<input type="checkbox"/>
		Please specify:	
1.2 SUPERVISOR (COMPLETE FOR ALL STUDENT PROJECTS)			
Supervisor's Title:	Dr		
Supervisor's Forename:	Joanna		
Supervisor's Surname:	Collingwood		
Supervisor's Post:	Reader		
Supervisor's Faculty/School and Department:	School of Engineering		
Supervisor's Warwick e-mail address:	J.F.Collingwood@warwick.ac.uk		
<i>Clinical Supervisors must provide a <u>Warwick</u> email address</i>			
Supervisor's contact telephone number:	024 7652 3152		
1.3 OTHER INVESTIGATORS/COLLABORATORS (INTERNAL & EXTERNAL)			
Please list all other known collaborators, internal and external to Warwick, including the name of the company/organisation or Investigator's Warwick department/school and their role in the project:			
The research team consists of Miss Jierong Luo and following co-investigators and external collaborators from the University Hospitals Coventry and Warwickshire (UHCW):			
Dr. Joanna Collingwood Reader			

School of Engineering, University of Warwick

Role: Supervising the research project, trial design, and managing data in the project

Dr. Sarah Wayte

Lead MRI Clinical Scientist

Radiology Physics Department, UHCW

Role: MR Physics Lead and MR Safety Expert at UHCW, engage in trial design, safety screening participants, data acquisition and transferring image data in the project

Andrew Weedall

MRI Clinical Scientist

Radiology Physics Department, UHCW

Role: MR Physicist at UHCW, take part in safety screening participants, data acquisition and transferring image data in the project

Michael Diokono

MRI Research Radiographer

Radiology Physics Department, UHCW

Role: MR Research Radiographer at UHCW, take part in safety screening participants, data acquisition and transferring image data in the project

1.4 REFERRALS

Has the Project been referred to BSREC from another REC or delegated process?

Yes No

If yes, please provide the reason:

Referred by HSSREC as project involves the NHS

Referred by department as not within the remit for delegated approval

Other

Please provide details:

SECTION 2. PROJECT DETAILS

2.1 Project Title:

Validation of a Quantitative Susceptibility Mapping Sequence to Measure Brain Iron Concentrations

2.2 Estimated start date:

July 2019

2.3 Estimated completion date of project:

June 2021

2.4 Does the project involve the NHS or social care:

Yes: No:

2.5 Type of Project:

https://warwick.ac.uk/services/ris/research_integrity/researchethicscommittees/biomed/study_design/

Research

NHS Service evaluation or Development

NHS Clinical Audit

Other- please specify:

2.6 Research Sponsor:

N/A

If **not** research in the NHS, please state N/A

2.7 Funder:

N/A

If unfunded, please state N/A

2.8 IDEATE/Funder reference (if applicable) If your study is funded, please provide a reference	PhD fully funded by University of Warwick, Chancellor Scholarship
2.9 Links with other BSREC applications Is the project linked to any other BSREC application? If yes: Project title: Chief Investigator: BSREC Reference (if known): Nature of linkage:	Yes: <input type="checkbox"/> No: <input checked="" type="checkbox"/>

SECTION 3: BACKGROUND/LAY SUMMARY

Please provide a lay summary of the project:

The summary should be easily understood by someone who is not an expert in the area. Definitions and explanation of terms should be provided (avoid technical language).

To include:

- *context for the proposed study*
- *a brief literature review supported by appropriate references*
- *a description of the proposed study and population to be studied building on review of previous studies/evidence*
- *the scientific benefit of the proposed study*

Iron is essential to normal brain function, and the storage of iron in tissue is known to be associated with normal ageing (Hallgren, B., et al. 1958). Furthermore, the disruption of iron metabolism in the central nervous system is found to be related to multiple neurodegenerative disorders, such as Alzheimer's disease, Parkinson's disease, and multiple sclerosis (MS) (Collingwood, J. F., et al. 2014). Therefore, it is important to understand the role of iron in the normal ageing brain, in order to compare with the pathological changes of iron in the brains.

Magnetic resonance imaging (MRI) has proved an iron-sensitive technique to study brain iron on living subjects, because the tissue iron can substantially affect the magnetic properties of the tissue and thereby produce contrast in MRI. Different methods have been developed to quantify the iron concentration by using MRI (Haacke, E. M., et al. 2005, Ghassaban, K., et al. 2019). Emerging in recent years, quantitative susceptibility mapping (QSM) is becoming the most promising, clinically accessible technique to quantitatively measure tissue iron (Deistung, A., et al. 2013; Schweser, F., et al. 2016).

The concentration of iron in the brain has previously been quantified successfully at University Hospitals Coventry and Warwickshire (UHCW) using the transverse relaxation method reported in the literature (Haacke, E. M., et al. 2005). This method of iron quantification takes around twenty minutes and can cover only part of the brain. As QSM has become available in clinical settings, it has the potential to quantify brain iron concentration in the whole brain with an acquisition time below ten minutes, but the validation is required on the local scanner.

Therefore, it is necessary to develop and validate the QSM pulse sequence, as a cutting edge MR technique for iron quantification, on the clinical MR scanner (3.0T GE Healthcare) at UHCW. The establishment and validation of the iron-sensitive pulse sequence QSM which can cover the entire brain is crucial and fundamental, and is an essential part of a bigger clinical project that concerns MS pathological alternations and the role of iron in disease development.

The study proposed here aims to validate the QSM technique for brain iron quantification, on up to 10 healthy living participants, using 3.0T clinical MRI scanners at UHCW. This study also seeks to quantify the regional iron distribution and its function with ageing in the living healthy brains by the QSM analysis.

SECTION 4 RISK AND ETHICAL CONSIDERATIONS CHECKLIST

Complete the checklist ticking 'Yes' or 'No' to all questions.

Where you have ticked 'Yes' to a question below, you will need to specifically address the ethical issues raised by that point and detail what safeguards will be put in place to minimise the potential risks/harm in the relevant section of the application form or in the space provided.			
		Yes	No
A	<p>Does the study involve participants who are particularly vulnerable or unable to give informed consent or in a dependent position (e.g. children, your own students, over-researched groups, people with learning difficulties, people with mental health problems, young offenders, people in care facilities, prisoners)?</p> <p><i>(If yes, please provide details in section 7 – Informed Consent)</i></p>	<input type="checkbox"/>	<input checked="" type="checkbox"/>
B	<p>Will participants be taking part in the study without their consent or knowledge at the time, or will deception of any sort be involved (e.g. covert observation of people in non-public places)?</p> <p><i>(If yes, please provide details in section 7 – Informed Consent)</i></p>	<input type="checkbox"/>	<input checked="" type="checkbox"/>
C	<p>Is there a risk that the highly sensitive nature of the subject might lead to disclosures from the participant concerning their involvement in illegal activities or other activities that represent a threat to themselves or others (e.g. sexual activity, drug use, or professional misconduct)?</p> <p>If yes, please provide details:</p>	<input type="checkbox"/>	<input checked="" type="checkbox"/>
D	<p>Could the study induce psychological distress or anxiety, or produce humiliation, or cause harm, or lead to negative consequences beyond the risks encountered in normal life?</p> <ul style="list-style-type: none"> • <i>Applicable to studies involving sensitive topics, vulnerable participants as well as studies involving driving experiments, simulators, computational or physiological experiments. For the latter, please detail potential risks associated with any equipment and how these will be monitored and addressed in the space below.</i> • <i>Please also consider the risk to individuals if any personally identifiable data collected as part of the study is accidentally disclosed. Please see guidance note for more information.</i> <p>If yes, please provide details:</p>	<input type="checkbox"/>	<input checked="" type="checkbox"/>
E	<p>Does the study involve substantial physical exertion?</p> <p>If yes, please provide details:</p>	<input type="checkbox"/>	<input checked="" type="checkbox"/>
F	<p>Does the study involve the administration of any substance?</p> <p>If yes, please provide details:</p>	<input type="checkbox"/>	<input checked="" type="checkbox"/>
G	<p>Does the study involve physically intrusive procedures, use of bodily materials or human tissue, or DNA/RNA analysis?</p> <p>If yes, please provide details:</p>	<input type="checkbox"/>	<input checked="" type="checkbox"/>
H	<p>Is any reward, apart from travelling and other expenses, to be given to participants?</p> <p>If yes, please provide details and justification for this, to ensure this is appropriate, and not seen as a bribe or to coerce participants into taking part:</p>	<input type="checkbox"/>	<input checked="" type="checkbox"/>
I	<p>Could the proposal give rise to researchers having any conflicts of interest?</p> <p>https://warwick.ac.uk/services/finance/resources/regulations/fp1</p> <ul style="list-style-type: none"> • <i>Consider relationships/previous personal interactions with participating organisations, participants etc.</i> <p>If yes, please provide details including how this will be managed:</p>	<input type="checkbox"/>	<input checked="" type="checkbox"/>
J	<p>Will any part of the project be undertaken overseas?</p> <p>If yes, please state which Country/Countries, the locations at which the project will be undertaken, e.g. public place, school, company, hospital, University, researcher's office, including the services of an overseas cloud hosting provider for storage or a</p>	<input type="checkbox"/>	<input checked="" type="checkbox"/>

	market research company etc. and the local permissions in place for this (where required): Please see University Guidance for data processing overseas: https://warwick.ac.uk/services/idc/dataprotection/internationaldatatransfers/		
K	Will the researchers go to any areas where their <u>safety may be compromised</u>? If yes, please provide details, including what measures will be put in place to minimise risks and ensure the researcher's safety. A risk assessment should be submitted with the application:	<input type="checkbox"/>	<input checked="" type="checkbox"/>
L	Will <u>pregnant women</u> be participants in the study? <ul style="list-style-type: none"> Please note, while you may not purposefully be recruiting pregnant women to the study, consider if any special measures would need to be put into place or if it is appropriate for these individuals to take part, e.g. safety risks If yes, please provide details:	<input type="checkbox"/>	<input checked="" type="checkbox"/>
M	Will the study involve children <u>under 5 years</u> old? If yes, please provide details:	<input type="checkbox"/>	<input checked="" type="checkbox"/>
N	Is the research commissioned by the <u>military</u>? If yes, please provide details:	<input type="checkbox"/>	<input checked="" type="checkbox"/>
O	Is the research commissioned under an <u>EU security call</u>? If yes, please provide details:	<input type="checkbox"/>	<input checked="" type="checkbox"/>
P	Does the research involve the acquisition of <u>security clearances</u>? If yes, please provide details:	<input type="checkbox"/>	<input checked="" type="checkbox"/>
Q	Does the research concern <u>terrorist or extreme groups</u>? If yes, please provide details:	<input type="checkbox"/>	<input checked="" type="checkbox"/>
R	Does the study involve any additional <u>ethical considerations</u> or <u>risks</u> to participants or the researcher that are not listed above? If yes, please provide details: Incidental findings might be revealed during the study, such as unsuspected abnormalities on MRI scans, and the general practitioner of participant could be contacted. The risks of unexpected findings, and necessary actions of the investigators in the events will be explicit in the Participant Information Leaflet (PIL) and the consent form.	<input checked="" type="checkbox"/>	<input type="checkbox"/>

* Please refer to the University webpages on [Prevent Duty](#)

SECTION 5: STUDY DESIGN, METHODOLOGY & ANALYSIS

5.1 Clearly state the research aim(s) of the project:

To include:

- a clear explanation and justification for the research question(s)/aim(s)

The study aims to set up and validate an MRI pulse sequence that is applicable to QSM on the GE healthcare 3.0 T clinical scanner at University Hospital Warwickshire and Coventry (UHWC), and to develop a protocol of MRI acquisition and post-processing that allows the robust quantification of brain iron concentration in vivo using QSM. In addition, this project also looks at the regional iron distribution and its function with ageing in the living healthy brains by the QSM analysis. The protocols for MRI scans, and the QSM processing and analysis will be established as a non-intrusive, quantitative technique of iron measurement for future studies of neurodegenerations.

5.2 What are the objective(s) for the project:

- Objectives are intermediate steps that will help you to meet your research aim(s)

To design a QSM-applicable MRI pulse sequence, the initial parameters will be set up according to the literatures (Langkammer, C., et al. 2012), then tested, and optimised by using the phantoms for the local MRI scanners, to achieve the best clinically feasible image quality for QSM analysis.

To evaluate the accuracy reproducibility and reliability of the pulse sequence, it will be used to scan phantoms that contains known iron concentrations, and the quantitative correlation between the iron concentration and the susceptibility will be investigated by regression analysis.

To study the brain iron concentration of scanned participants using QSM, quantitative susceptibility maps will be generated, and the results will be compared with those from previously reported studies.

The quantitative relation of brain iron concentration and the measurement of tissue susceptibility will be validated by correlating the susceptibility measurements to the regional brain iron concentration that is estimated by its function of participants' age, as described in the literature (Hallgren, B., et al. 1958).

5.3 Study design and data collection methods:

To include:

- a clear description of the study design and data collection methods
- a suitable design should reflect the aim(s) of the study
- This may include ethnography/observations, interviews, focus groups, questionnaires, document analysis etc.
 - **Ethnography/Observations**- what/who will be observed, by whom, for how long? What equipment (if any) will be used for recording etc.?
 - **Interviews**- who is conducting the interviews, how, where and when- by telephone/in person/skype; will they be recorded- how? How long will they last? How will the interview guide be developed? etc.
 - **Focus groups**- who is leading, how will they be organised, when and where will they take place, how will they be recorded? How long will they last? etc.
 - **Questionnaires**- who has designed the questionnaire, who will distribute it, how long will it take to complete etc.
 - **Document analysis**- what documents will be requested, where from, by whom, what permissions are in place for this etc.
 - **Experimental** – what tests/lab work will be undertaken on participants, by whom, is specialist training required before undertaking?
 - **Secondary analysis of previously collected data**- analysis of data that has been previously collected by a third party for research or other purposes, that is not publicly available e.g. healthcare, student, financial records. Please state whether the data set is identifiable or anonymised.

a. Study design

a1. Scan protocol setting up and testing on phantoms

A QSM-applicable sequence will be set up for MRI acquisition on the local scanners, using parameters that are comparable to recently reported brain iron studies (Schweser, F., et al. 2016). Raw phantom image data will then be reconstructed, processed and analysed. At this stage, optimised parameters will be applied on MR phantoms to achieve the best clinically feasible image quality, which will be assessed until MRI data is suitable for QSM. We aim to control the total scan time of the QSM sequence to be under 10 minutes.

a2. Participant recruitment and eligibility

Approximately 10 healthy adult participants with age below 80 years old will be recruited, give consent, and screened according to the criteria before enrolling in this study, as described in "Section 6: Recruitment". Only necessary information (i.e. age and gender) of the participants will be collected for analysis, as described in the following sections "5.4 Data Analysis" and "Section 8".

Neurological screening: During consent, all participants will be asked if they suffer from any known neurological disorder in an attempt to exclude participants with neurological disorders. The MRI scans of enrolled participants will be review by a radiologist later, to exclude any visible neurological abnormality.

a3. MRI and validation of iron concentration

MRI of phantoms and healthy participants will be performed, followed by QSM analysis and measurement, to validate the reported correlation between iron and the tissue susceptibilities quantified by QSM. The susceptibility will be measured on a series of MR phantoms that contain a range of known iron concentrations, including the range of physiologically-relevant iron level in human brains. Then, the iron concentrations will be correlated with the measured susceptibilities. Repeated measurements will be conducted to assess the reproducibility and uncertainty.

After testing the phantoms, the eligible healthy participants will undergo MRI at UHCW. The MRI scanning will be performed by an appropriately trained radiographer, under supervision of an MRI clinical scientist, Dr. Sarah Wayte or Andrew Weedall. The MRI data will be transferred to the University of Warwick to be processed and analysed by Miss Jierong Luo, as described in "5.4 Data Analysis".

b. Data collection methods

b1. Participant information collection

Only the participant information that is necessary to this study will be collected and used in the project during recruitment and enrolment, as described in "5.4 Data Analysis", "Section 6" and "Section 8". The collection of participant information via consent forms, MRI Safety Screening Forms will be conducted by Miss Jierong Luo.

b2. MRI data collection

An MRI scan appointment will be arranged with each participant after the informed consent, and the participant will be asked to attend the appointment for scanning on the day. To help participants to understand MRI and its procedure, all participants will be given an MRI Information Sheet (Appendix 1) before attending their sessions, and the demonstrations and instructions will be given by professionals before and during the MRI scan, in the department of radiology, UHCW. During the scanning session, participants will be able to communicate with the scan operator at any time if necessary. The scanning session will take approximately 15 minutes, but could take up to 30 minutes. All MRI data will be collected by using the 3.0 T GE scanners at UHCW, performed by an approved radiographer.

5.4 Data Analysis

To include:

- *Specifically what data sets will be collected (name, date of birth, email address, ethnicity, health status, financial records, IP address etc.)*
- *whether this data will be collected directly from participants (e.g. via questionnaires/interviews) or indirectly, from a third party (previously collected data set) and how i.e. web form, online application, paper form*
- *Detail the analysis methods that will be undertaken e.g. content analysis, framework analysis, interpretative phenomenological analysis etc. and any statistical analyses.*
- *Describe how and by whom any data will be transcribed, coded, de-identified, stored, transferred, accessed, archived*
- *Any software used in the analysis should be specified and detailed how it will be used in the project*

a. Data collection

Personal data: The name, age, gender, email address and phone number will be collected directly from participants after informed consent. The other personal data collected as part of the study via the MRI safety screening questionnaire include the participant's name, address, date of birth, health status and medical history that might involve pacemakers, electronic implants, metal fragments, historical operations and treatments relevant to MRI safety. The participant's general practitioner (GP) information will also be acquired in case that the study reveals any unsuspected abnormality of the enrolled participant.

Imaging data: Brain magnetic resonance (MR) images of enrolled participants will be collected for QSM reconstruction, by using 3.0 T clinical scanners during their visits for scanning. Participants will be scanned under their trial number, gender and age only. Therefore, the data to be collected will only contain the brain anatomy of participants and imaging information that are necessary for subsequent analysis.

b. Data processing

Image processing and analysis: Image reconstruction, post-processing and analysis will be performed on the software Orchestra (GE Healthcare), MATLAB (Mathworks) and scientific biomedical image analysis tools, such as Fiji (ImageJ) (Schindelin, J., et al. 2012). Magnitude and phase images will be reconstructed and processed by using the reconstruction pipeline provided by the manufacture GE healthcare and by MATLAB algorithms and toolboxes for QSM analysis. Phase processing will consist of careful phase unwrapping and background removal for an accurate susceptibility estimation. Further processing and analysis of the susceptibility of reconstructed images, such as region of interest (ROI) analysis and voxel-based analysis, will be carried out on MATLAB and Fiji.

Statistics analysis: Statistics analysis will be conducted by using statistics tools and packages, such as SPSS (IBM), Origin (OriginLab), MATLAB and R. Descriptive statistics of the susceptibility measurements and the distributions of susceptibilities will be examined, which will be analysed for scan reproducibility and measurement uncertainty, by comparing the repeated measurements of MR phantoms (Bityukov, S. I., et al. 2016). Then regression analysis will be conducted to find and validate the relationship between the susceptibility and the iron concentration, in both phantoms and human brains respectively. The validation will be performed by correlating the susceptibility to the regional iron concentrations that can be estimated as a function of age from prior-published post-mortem data (Hallgren, B., et al. 1958; Haacke, E. M., et al. 2005).

Analysis of variance will be performed to detect the difference of measured susceptibilities between varied brain regions of all subjects. The correlation of the susceptibility of brain regions with subject's age will also be studied by regression analysis, and the relationships will be compared with the previously reported regional dependence of iron levels on age (Hallgren, B., et al. 1958).

c. Data management

The study data and the personal data collected as part of the research will be carefully managed by the research team to ensure the confidentiality of participants.

c1. Obtain consent

Informed consent will be obtained from each participant by initialing and signing a consent form before they could enrol in the study, given and collected by Miss Jierong Luo. After collecting the consent form, Miss Jierong Luo will allocate a unique trial number to each participant, to de-identify the individual. All consent forms will be stored in a locked filing cabinet in Dr Joanna Collingwood's office in the School of Engineering, University of Warwick.

c2. MRI safety screening

Each participant will be required to complete an MRI safety screening questionnaire form (Appendix 2) before they can take part in the study and undergo an MR scan. The participant will be given the MRI safety screening form prior to their MR appointment, and informed that the MR staff at UHCW will go through the safety questionnaire with them in detail immediately prior to their MRI scan. However, they will be asked to inform Miss Jierong Luo if they will be answering 'yes' to questions 1 to 7, prior to an MRI appointment time being allocated, as this may exclude them from having an MRI scan and participation in the study. Any question regarding MRI safety will be referred to the MRI staff at UHCW.

The screening questionnaire will be completed by the participant and an MR staff member together, immediately prior to the MRI scan. If the participant passes the safety screening, the MRI safety screening form will be stored in a locked filing cabinet at UHCW until the MR scan of the participant is reviewed by a radiologist; otherwise the screening form will not be kept and will be destroyed.

c3. MR scan

The participants will be scanned under their unique trial number at UHCW by the research team, so all research data will not be personally identifiable. The scans will be reviewed by a radiologist, and if an abnormality is found, the participant's GP will be contacted, and the MRI safety screening form will be retained for one year at UHCW, before being destroyed. If no abnormality is present, the MRI safety screening form will be destroyed.

c4. Data analysis

MRI data generated at UHCW will be transferred to the School of Engineering, University of Warwick for analysis, by Miss Jierong Luo. The research data will include the MR data that is coded with the participant trial number, and the necessary participant information (age and gender). Processing and the analysis of data will be performed by Miss Jierong Luo, and the analysis methods are detailed in "Section 5.3" and "Section 5.4b".

c5. Report and dissemination

The reporting of this research will be incorporated in the PhD thesis of Miss Jierong Luo to be submitted in 2021, and will be disseminated in journals and scientific events, including conferences and public engagements. All results published will be pseudonymised: trial numbers will be replaced with new identifiers "Subject #" by Miss Jierong Luo.

SECTION 6: RECRUITMENT

6.1 State the total number of planned participants and the sampling strategy; provide justification for this:

To include:

- *The rationale behind the proposed size of the sample*
- *Will the sample size provide enough data to answer the research question?*
- *If sampling will be continued until saturation is reached, then this should be stated and linked to the research question*
- *Sampling strategy- is this random, snowball, purposive, convenience etc.*
- *What is the rationale for this- it should reflect the methodological framework for the study*

We aim to recruit and enrol approximately 10 healthy adult participants for the study, with age up to 80 years old, and approximately uniformly distributed within the age range between 20 and 80 years.

A key aim of the study is to establish an MRI protocol of QSM-applicable pulse sequence on the scanners at UHCW, that can be applied to and reliably measure brain iron in living participants. Ultimately, the study will focus on measuring the quality, reproducibility and reliability of the scans, by testing the sequence on phantoms and participants. To investigate the viability of iron quantification by using QSM, the validation and calibration of the tissue susceptibility measured by QSM with the iron concentration will be the main consideration in this study. A comparable study (Choi, J. Y., et al. 2019) has been reported recently, and the researchers investigated the reproducibility in QSM for clinical use of ROI analysis by applying and testing the sequence on 10 healthy volunteers. In the study proposed here, MR scans will be obtained from and repeatedly tested on MR phantoms before applying the sequence on participants, in order to provide robust results to establish this approach on the UHCW scanners while keeping the number of participants minimised.

Recruiting a small group of healthy individuals locally from the University of Warwick is appropriate for this study design. Taking into account the known dependence of iron levels on age (Hallgren, B., et al. 1958), a stratified sampling method will be applied in this study, aiming to recruit participants whose ages cover the range from 20 to 80 years. This sampling method will enhance the regression analysis as part of the study design by providing an age range that is close to a uniform distribution, as the participant's age will be treated as an independent variable to be correlated with the susceptibility measurements, and to be used to estimate the iron concentration in different brain regions of the healthy participant.

6.2 Where applicable, state the breakdown of participants by type and number of each type of participant, e.g. children (include age), parents, teachers, health care professionals etc.:

Type of Participant:

Number:

Healthy adults (up to 80 years old)

~10

6.3 Please provide clear inclusion criteria:

Participants must be adults no older than 80 years old at screening, and pass the MRI safety screening by answering the safety questionnaire. All participants should have no known neurological disorders (e.g. Parkinson's disease, multiple-sclerosis, a brain haemorrhage, a brain infarct, or a brain tumour), and no cardiac pacemaker or other electronic implants that could compromise MRI safety.

6.4 Please provide clear exclusion criteria:

Volunteers who are not in the age group concerned, or who do not pass the MRI safety screening, or are considered not suitable or not recommended due to MR safety by the MR staff will be excluded from the study. Participants who have historical neurological disorders, or neurological disorders that become known during the study later can also be excluded. Pregnant volunteers will be excluded from the study.

6.5 Please detail how participants will be recruited to the study:

To include:

- *How participants will be identified/screened and approached; by whom?*
- *Where participants will be recruited from and when?*
- *Detail the source of any personal information that may be used to identify participants. If this information will be accessed by someone outside the team who would have access to this information as part of their day to day role, the reason for this should be explained, and permissions detailed e.g. healthcare, student records etc.*
- *Will any vulnerable groups be recruited?*
- *What materials will be used to recruit participants- please provide copies of posters, leaflets, invitation emails, etc.*
- *Where will the above materials be advertised: list and provide details of locations, websites, social media etc.*
- *Will any recruitment tools be used e.g. SONA- please specify and provide details.*

In this research project, we aim to recruit and enrol participants within the first 6 months from the start of the study. Participants will be recruited among the students and staff of University of Warwick, and Miss Jierong Luo will act as the main contact and take the overall responsibility of the recruitment at this site. Advertising and recruiting materials, including posters, leaflets, and invitation emails, will be used for the recruitment.

Posters and leaflets: Hard copies of posters and leaflets will be placed at multiple approved display areas in buildings at the University of Warwick, to cover a range of various departments and disciplines. The materials will be distributed on departmental notice boards, and their electronic copies will be also advertised internally via departmental media feeds (e.g. newsletters).

Invitation emails: A brief and concise invitation email that includes a lay summary in bullet points of the proposed study will be circulated among the students and staff of the University.

To ensure MR safety, all participants recruited from the site need to undergo screening by completing the MRI safety questionnaire at UHCW with an MR staff of the research team. The personal information collected via the questionnaire (see "Section 5") will be accessed and managed, as described in "Section 8".

SECTION 7: INFORMED CONSENT

7.1 Please detail the process for obtaining informed consent.

*Informed consent **must** be obtained prior to the participant undergoing any research activities that are specifically for the purposes of the study. This should involve discussion with potential participants or their legally acceptable representative; the presentation of written materials e.g. participant information leaflet(s) –PIL(s) and consent form, and the opportunity to ask questions.*

To include:

- *How and when informed consent will be obtained- written, verbal etc. provide details and justification. Justification must also be provided if informed consent will **not** be sought or if consent will be assumed (please note this needs to be appropriate to the study type).*
- *Who will be taking consent? What training has been undertaken for this?*
- *When and how potential participants will be issued with the information leaflet, in what format and how long they will be given to consider taking part?*
- *Does the study involve children- if so, will consent be obtained from parents, if not provide clear justification why not.*
- *Are the informed consent materials appropriate for the target audience- consider age / language / literacy levels / cultures etc.*

Informed consent will be obtained before the participant enrolment of the study. The potential participant will be given a consent form, together with a participant information leaflet, an MRI information sheet, and an MRI safety screening form, in order to help them to understand the purposes of the study, the nature of the MR examination, and their eligibility for participating in the study. Before making their decisions, each potential participant will be able to ask questions and discuss about the study and the information materials. The potential participant will be given a minimum of 3 days to consider taking part in the study.

Miss Jierong Luo, who has successfully completed the Research Integrity online training module to fully understand matters of consent and related guidelines, will obtain informed consent in all cases.

All the information leaflets are written in plain English, for the target audience who presumably has no prior knowledge of MRI and the study. All the informed consent materials are attached to this application, and listed below:

- a. Consent form: Through which all participants must initial and sign to give consent to the researchers and take part in the study.
- b. Participant information leaflet (PIL): It is a 6-page information leaflet for potential participants, to provide an overview of the study and its aims, how it will take place, and important information that may affect the decision to participate. It includes what exactly will happen if they choose to take part into the study, the protection of their rights during and after the study, and the anonymity of them and their data.
- c. MRI information sheet: It is a one-page leaflet that provides necessary information about MRI, how it works, and what participants will be expected to do during an MR scan. Some necessary technical information will be given to readers to understand the technique and the potential risks.
- d. MRI safety screening form: It is a one-page questionnaire about MRI safety, and necessary information from the participant will be required to ensure a safe MR scan to be conducted. If the participant answers 'yes' to questions 1 to 7 on the screening questionnaire, they will be advised by Dr. Sarah Wayte at UHCW to confirm if they are safe and eligible to undergo an MRI scan for the study.

7.2 Please detail how participants withdraw from the study if they have requested to do so.

The process by which an individual can withdraw their participation from the study without giving a reason or experiencing any detrimental effects e.g. should they not wish to continue with their participation in an interview or focus group.

To include:

- Consideration for any data already collected up until this point- whether it is possible for this to be removed. E.g. it may not be possible to identify data once submitted for an anonymous survey. This needs to be clear in the participant information leaflet (PIL).
- Researchers should specify up to what point participants can withdraw their data from a study and **how** a participant would request this- this also needs to be clear in the participant information leaflet (PIL).
- Consideration should be given to when data will be anonymised, analysed, published etc. make sure it is possible/feasible for data to be withdrawn if this is being offered to participants. It may be appropriate to provide a time frame for withdrawal.

If participants no longer wish to continue with their participation at any point during the study, they can request to withdraw from the study any time without having to give a reason, and the participants can request to withdraw their data any time before the research data is being integrated for analysis. The contact of the MR research team will be provided on the PIL to each participant at the beginning of their participation, to ensure they can reach the research team and request withdrawal if they wish to. Miss Jierong Luo will act as the contact and take responsibility for withdrawal requests.

If a withdrawal from the study is requested, a response to the request from the research team will be made, and all research activities about this participant will cease within 24 hours. If a request is made to withdraw the research data that is already obtained, a response to the request from the research team will be made within 24 hours, and the withdrawal of requested research data will be completed within two weeks after the response.

Once the image processing is completed and the research data is integrated for statistical analysis, it is not feasible anymore for the research team to withdraw any research data. A time frame for withdrawal is provided in the Data flow map as an attachment to the application.

SECTION 8: DATA COLLECTION, USE & STORAGE (DPA 2018 & GDPR)

For projects involving processing of personally identifiable data, please answer the questions below to map the data flow to indicate the data controllers and data processors. This can be submitted as a separate document if necessary, please see accompanying guidance note from the Information Data Compliance team.

8.1 Does the project involve the collection, analysis or storage of personally identifiable data?

Yes No

'Personal data' is any information relating to an identified or identifiable natural person- a 'data subject'.

An identifiable natural person is one who can be identified, directly or indirectly, in particular by reference to an identifier (such as a name, an identification number, location data, financial data, opinion, an online identifier), or to one or more factors specific to the physical, physiological, genetic, mental, socio-economic, cultural, race, religion, trade union membership, political beliefs, medical, gender or social identity of that natural person.

If yes, please provide details of what will be collected: The name, age, gender, email address and phone number will be collected from participants as part of consent. The name, address, date of birth of the participant will be collected as other personally identifiable data on the MRI safety screening questionnaire. For the MRI safety purpose some information about the medical history of the participants, that might reveal the identity of individuals will also be collected. In case any unsuspected abnormality is found during the study, the GP of participant and GP' address will also be acquired. The imaging data collected from participants may reveal part of their facial features, which is minimised to be within the upper part of the head and will not be personally identifiable.

After collection, the personal information and all materials that contain personally identifiable data will be securely stored until deleted or destroyed. Only the age, gender, and MRI data of participants will be used for analysis in the study.

8.2. Does the project involve the collection, analysis or storage of any personally identifiable special category data or criminal offence data? Yes No

Special category data includes personal data which is by its nature, particularly sensitive in relation to fundamental rights and freedoms of individuals such as: racial or ethnic origin, political opinions, religious or philosophical beliefs, trade union membership, genetic data, biometric data (for the purpose of identifying a natural person), data concerning health or data concerning a natural person's sex life or sexual orientation. This type of data merits specific protection as the context of its processing. Failure to handle this data correctly could result in significant risks to the fundamental rights and freedoms of the individuals.

If yes, please provide details of what will be collected and for what purpose:

What measures are being implemented to reduce or eliminate the risk to these participants' data for the duration of the period that their personal data is collected and stored? Please see accompanying guidance note for more information.

8.3 Does the project involve the collection or analysis of personal data relating to children under 13 or vulnerable groups? Yes No

UK law provides that for data protection purposes an individual aged under 13 years old is considered a child. For the purposes of the GDPR, a child is someone aged under 16 years old, although Member States are able to reduce this age. Please consider Member State law as Parental/Guardian consent will be required for a child participating in the research.

If yes, please provide details of what will be collected:

For what purpose do you need to process the children's or vulnerable person's data?

What measures are being implemented to reduce or eliminate the risk to these participants' data for the duration of the period that their personal data is collected and stored?

8.4 Who will have access to the study data?

Include individuals internal and external to the University and what level of access they have to the data e.g. anonymised, pseudonymised, identifiable etc.

Please note you will need to hold a University approved data sharing/processing agreement with each third party (external to the University) with whom data is to be shared.

Personal information: During the stage of consent and screening, Miss Jierong Luo, who obtain informed consent will have access to the individually identifiable information of participants, including knowing the name, age, date of birth, personal contact (i.e. phone number and email address), and if they meet the inclusion criteria for the study and the MRI safety screening. To be collected on the consent form, the email address and phone number of participant are required to arrange an appointment time for the MR examination, and to answer any MRI safety queries effectively.

The rest of the MRI research team will also have the access to the email address and phone number of the participant until MRI scan of the participant is acquired, then the information as part of the consent form will be retrieved and securely stored as detailed in "Section 8.8". The MRI safety screening forms and the personal data on the forms will be destroyed as soon as MRI scan of the participant is obtained and no abnormality is found.

Research data: The research team will have access to the pseudo-anonymised MR data coded by the trial number, while it stays at UHCW. As soon as possible after the MR data are generated (usually within 24 hours), Miss Jierong Luo will collect and transfer the pseudonymised MR data, using a password-protected memory stick or portable hard drive specific for the study, to the University of Warwick to be analysed and securely stored. During the analysis, only Miss Jierong Luo and Dr. Joanna Collingwood will have the access to the research data, including the MR data, and the age and gender of participant that has been scanned.

8.5 During the project, will data be hosted on any external platforms or use new technology?

Yes No

e.g. Apps, online survey tools (qualtrics, Bristol online surveys etc.), recruitment tools (Prolific, SONA etc.), cloud hosting tools.

If yes, please provide details of the system(s) and how they operate:

Have you contacted Information Security (informationsecurity@warwick.ac.uk) regarding whether these technologies will be required to go through the Information Assurance workbook approval process? <https://warwick.ac.uk/services/idc/informationsecurity/faqs/purchasingissues/> Yes No

How and when will the data be deleted and who by?

8.6 Will any research activities be audio or video recorded? Yes No

This needs to be clear in the participant information leaflet and consent form.

If yes, please provide details of what will be recorded, how long it will be kept, how it will be stored securely and how it will be deleted:

8.7 Will data be shared with any organisation external to the University for processing? Yes No

e.g. external transcription services, external statistics support, archiving etc.

If yes, please provide details of the sharing arrangements: clarify whether the data shared will be identifiable, the external organisation to which it will be sent and what contracts/arrangements are in place to safeguard the data and ensure the data processors/controllers will comply with data protection requirements:

8.8 Please detail how, where, in what format and for how long the research data will be stored securely, including on back up storage.

e.g. hard/electronic copies, locked filing cabinets in researcher's office, encrypted files, password protected devices, Warwick servers. Please also consider consent forms here. These should be stored separately to research data.

a. Personal information

Consent forms: All consent forms will be completed, collected and stored as hard copies by Miss Jierong Luo in a locked filing cabinet in Dr. Joanna Collingwood's office in the School of Engineering, University of Warwick, for five years after the completion of the study, and then they will be destroyed.

MRI safety screening forms: The form will be completed at UHCW immediately before the MRI examination; and they will be stored as hard copies by Dr Sarah Wayte, in a locked filing cabinet in an locked office, at UHCW, until to be destroyed when the MR scans of participant are reviewed by a radiologist and no abnormality is found. If any abnormalities are found from the MR scans, the GP of the participant will be contacted and the MRI safety screening form will be retained in the locked filing cabinet in UHCW for one year after the MR scan.

b. Research data for analysis

MR data and non-identifiable participant information: The MR data will be generated as pseudonymised electronic files at UHCW, then transferred to the University of Warwick for processing, analysis and storage, described as below. The age and gender of participant will be stored electronically as DICOM (Digital Imaging and Communications in Medicine) headers of the MRI after scanning. After generation in UHCW, it will be transferred as part of the MR data to the University of Warwick for analysis and storage, in an access-restricted Warwick server for Dr Joanna Collingwood's research group, and the files will be stored in a password-protected folder under the name of Joanna Collingwood, which is specified for the study and can only be accessed by Dr Joanna Collingwood and Miss Jierong Luo.

No research data will be stored in UHCW.

8.9 For this project, will data be processed, (to include the collation, collecting, distributing, sharing, accessing, reviewing, amending, deletion) transferred or stored in any Countries outside UK?

Yes No

e.g. the use of transcribing service outside the UK, market research company, cloud hosting provider

If yes, please provide details of the country/countries and the collection/transfer/storage arrangements:

8.10 Describe compliance and proportionality measures in place to satisfy the requirements of the Data Protection Act 2018 and the GDPR.

e.g. how will you ensure: fairness and transparency to research participants, data quality, data minimisation (only collect data which is necessary for the purpose(s) of the study), purpose limitation (no further processing of the data for purposes incompatible to those for which it was collected), de-identification of the data as soon as possible, appropriate technical and organisational measures in place to avoid unauthorised access and accidental loss or damage to data etc. Please see the accompanying guidance note from the Information Data Compliance Team to help answer this question.

a. Data minimisation

Only the data that are required for the study will be collected from the minimum number of participants. The full name of participant needs to be obtained as part of the consent process and MRI safety screening. As a necessary procedure of MRI, other personal information of participant is required on the MRI safety screening form, to ensure the MR safety of participants during the scanning, including necessary information of participant's health status and medical history that might involve pacemakers, electronic implants, and

metal fragments, such as historical operations and treatments. The information of the pregnancy of participants will be required on the MRI safety screening form to exclude any pregnant participant, for MR safety purpose. The participant's GP and GP's contact details will also be acquired in case that the study reveals any unsuspected abnormality of the enrolled participant.

As key factors of brain iron level, the age and gender of participant are required for analysis of the study. A list of the MR scans of participants, including trial numbers, age and gender will be retained by Miss Jierong Luo and stored securely and separately to the research data on a password-protected server of University of Warwick.

b. Pseudonymisation

A unique trial number will be given to each participant on the consent form by Miss Jierong Luo, at the beginning of the study. As all participants will be scanned only under their trial number, and so the obtained MR data is automatically pseudonymous. The consent form, as the key to re-identify individuals, will be securely stored in a locked filing cabinet in Dr. Joanna Collingwood's office, at University of Warwick.

c. Transparency and fairness

Together with the information of the study, details of what and how personal data will be collected and the intended use, share and storage of the data will be explicit in the PIL. All data will be obtained openly, honestly and fairly, and participants will be informed of the pseudonymisation and deletion process of their personal data via the PIL and by the research team. Possible reuse of data for future research, which will be conducted by either the same investigators or continued by another team member, will be clearly stated in the PIL and the consent form.

d. Technical measures

All hard copy materials that contain personal data, including consent forms and MRI safety screening forms will be separated from research data, and securely stored in locked filing cabinets in offices which are either locked or attended at all times. The MRI data will be obtained using a trial number, age and gender only. The research data will be transferred to the University of Warwick using a password-protected portable hard drive, then securely stored in a password-protected folder on the University secure server with restricted access. Data processing and analysis will be performed by Miss Jierong Luo, on the University managed PC.

8.11 Is it anticipated that there will be any future use of the data? Yes No

If yes, please provide details (if known at this stage). This should be clear in the Participant Information Leaflet and on the consent form if there is potential for future use of this data:

Possible future use of the research data will be conducted by either the same investigator after PhD or continued by another team member, which could include validation, comparison, further processing and analysis of the MR data by using various methods and algorithms.

SECTION 9: DISSEMINATION

Please describe the dissemination arrangements for the study:

To include:

- *What will happen to the results at the end of the study?*
- *Will this study have any pathways to impact? ('Pathways to Impact' are activities designed to ensure any potential impact is realised, measured and evidenced.)*
- *How and where will the results be reported/published?*
- *Are there any plans to notify/debrief the participants of the outcome of the study, either by provision of the publication, or via a specifically designed newsletter, presentation etc.?*
- *If it is possible for the participant to specifically request results from the researcher when would this information be provided e.g. after the Final Study Report had been compiled or after the results had been published?*

This project will be incorporated in the PhD thesis of Miss Jierong Luo, to be submitted in 2021. The results of the study will be presented at scientific events (e.g. conferences, public engagement), and disseminated in journals of relevant research fields, such as MRI, neuroimaging, radiology, and brain iron research. As part of published results, all individuals will be fully unidentifiable in the reports, as described in "Section 5" and "Section 8".

SECTION 10: FURTHER INFORMATION (OPTIONAL)

Please provide any further details/information relevant to this application that may aid the ethical review process.

To include:

- For complex studies with multiple work packages, collaborators or steering groups, applicants may wish to submit a protocol or supplementary documents in addition to this application form detailing the roles and responsibilities of each party.
- Projects that require further approvals e.g. HRA approval for research in the NHS may also wish to submit a protocol for review.
- Peer review
- Patient and public involvement
- Flow diagram
- Data management plan

For the study proposed here, an application is to be submitted to seek the ethics review from GafREC (Governance arrangements for Research Ethics Committee) in order to obtain the approval for the use of the MRI scanner at UHCW.

Materials for the informed consent, advertisements, and a data flow map are enclosed as part of this application.

SECTION 11: SUPPORTING DOCUMENTS

BSREC will need to review **all** participant facing documents associated with this application.

There may be more than one type of each document for each study, i.e. multiple participant information leaflets if there are different participant groups, or work packages.

Please specify below, which documents have been submitted with this application (where applicable):

- Participant information leaflet(s)
- Consent form(s)
- Poster(s)/advertisement(s)
- Invitation email(s)
- Questionnaire(s)/Survey question(s)
- Interview schedule(s)/topic guide(s)
- Data Collection form
- Data flow map
- Data Management Plan
- Risk assessment
- Protocol (optional- needs to be consistent with the application)
- Other, please specify: MRI Information Sheet, MRI Safety Screening Form, Sample MRI scan list

SECTION 12. SIGNATURES AND DECLARATIONS

12.1 RESEARCHER/APPLICANT

The information in this form together with any accompanying information is complete and correct to the best of my knowledge and belief and I take full responsibility for it.

I undertake to abide by the University of Warwick's Research Code of Practice in undertaking this study.

I understand that BSREC grants ethical approval for projects, and that the seeking and obtaining of all other necessary approvals and permissions prior to starting the project is my responsibility.

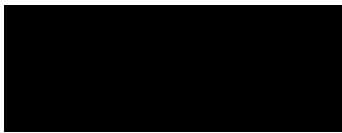
I confirm I am familiar with and will conduct my project in line with the General Data Protection Regulation (GDPR) and Data Protection Act 2018 (DPA 2018), reporting any data breaches to the University's Information and Data Director: DPO@warwick.ac.uk.

I understand that I must not begin research and related projects with human participants, their data or tissue until I have received full approval from the relevant Research Ethics Committee of the University of Warwick.

I understand that any changes that I would like to make to this study after receiving approval from BSREC, including changes to the research team or study end date must follow BSREC procedures as detailed on the BSREC web pages.

Name of Researcher: Jierong Luo

Signature:



Date:

21/06/2019

Send a signed copy of the form to bsrec@warwick.ac.uk, along with copies of all study documentation, including questionnaires, interviews schedules/topic guides, posters/leaflets, invitation emails etc.

12.2 SUPERVISOR SECTION

I confirm that I have read this application and will be acting as the student researcher's supervisor for this project.

The proposal is viable and the student has the appropriate skills to undertake the research. Participant recruitment procedures, including the Information Leaflet(s) to be provided and the process for obtaining informed consent, are appropriate, and the ethical issues arising from the project have been addressed in the protocol.

I have reviewed any questionnaires, interview schedules/topic guides where relevant, and these are appropriate for the project.

I understand that BSREC grants ethical approval for projects, and that the seeking and obtaining of all other necessary approvals and permissions prior to starting the project is the responsibility of the student.

I confirm I am familiar with and will ensure the student will conduct the project in line with the General Data Protection Regulation (GDPR) and Data Protection Act 2018 (DPA 2018) reporting any data breaches to the University's Information and Data Director: DPO@warwick.ac.uk.

I understand that research and related projects with human participants, their data or tissue must not commence without full approval from the relevant research ethics committee of the University of Warwick.

Name of Supervisor: Joanna Collingwood

Signature: 

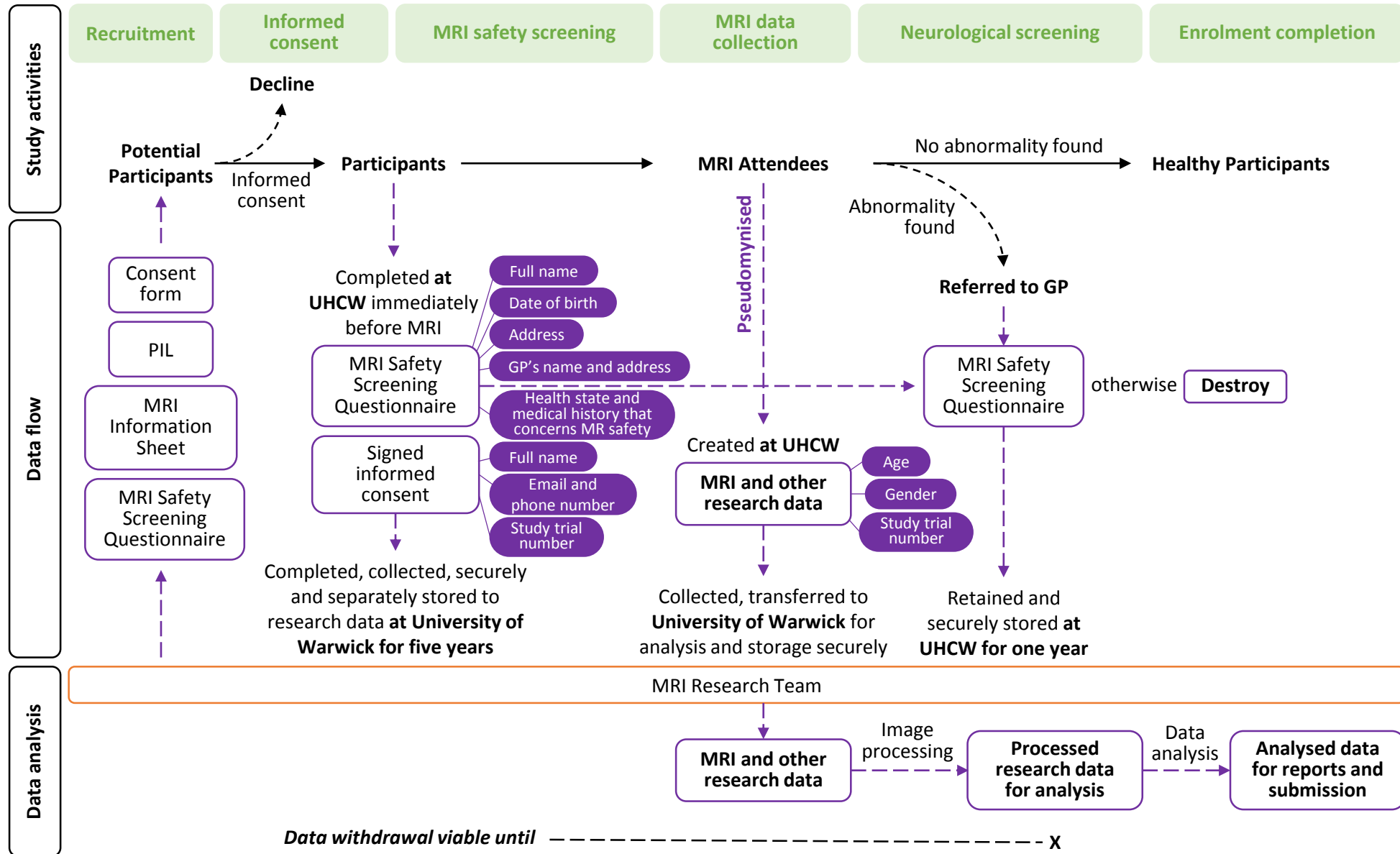
Date: 21/06/19

NB: An e-mail from the Academic Supervisor that states the above, in lieu of a signature on this form, may be sent to: bsrec@warwick.ac.uk

If you have not already done so, you are strongly recommended to undertake the Research Integrity Online Training Course. All details relating to this course can be found [here](#).

Validation of a Quantitative Susceptibility Mapping Sequence to Measure Brain Iron Concentrations

Data Flow Map



Invitation Email

Dear friends,

You are invited to take part in a research study, **Validation of a Quantitative Susceptibility Mapping Sequence to Measure Brain Iron Concentrations**.

What is the study about?

This study involves imaging your brain by using magnetic resonance imaging (MRI), which is a safe, non-invasive, and non-ionising medical imaging technique. By applying an advanced MRI technique, quantitative susceptibility mapping (QSM), we aim to investigate and validate QSM analysis on local clinical MRI scanners (3.0T GE healthcare) of the University Hospital Coventry and Warwickshire (UHCW), for quantitatively measuring iron concentration in the brain.

Why?

As the regional brain iron is a potential biomarker of ageing and multiple neurodegenerative disorders, including Alzheimer's disease, Parkinson's disease, and multiple sclerosis. QSM has been used increasingly in brain imaging in recent years, however, it is not yet undertaken at UHCW. Therefore, this study aims to validate a QSM-applicable sequence on the local scanners in UHCW. As an essential development work to support future research studies, including proposed research into multiple sclerosis, the MRI technique of QSM will help understanding of the pathological alternations and the role of iron in disease development.

How?

If you are an adult no older than 50 years old and have no known brain disorder (e.g. Parkinson's disease, multiple sclerosis, a brain haemorrhage, a brain infarct, or a brain tumour) and wear no cardiac pacemaker or other electronic implants, and if you are interested in taking part in the study, you can contact us directly or write to:

Jierong Luo
School of Engineering
University of Warwick
Coventry
CV4 7AL
Email: J.Luo.1@warwick.ac.uk
Tel: 024 7657 5487

If you have any questions about the study or if you would like to know more information, you are welcome to contact us by using the information provided above. Thank you for your time!

This study is as part of a PhD project by Miss Jierong Luo (School of Engineering, University of Warwick), and it is not funded by any external body. It is collaborative research with University Hospitals Coventry and Warwickshire (UHCW).

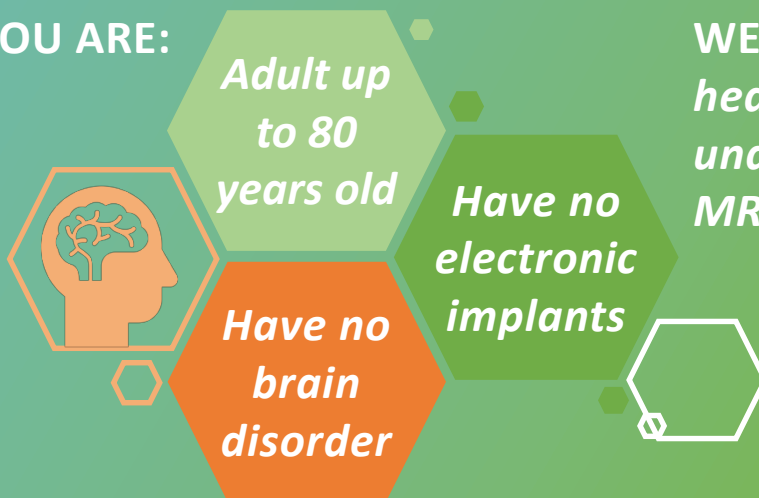
Best regards,

Jierong

TAKE PART IN OUR RESEARCH TO HELP UNDERSTANDING BRAIN DISORDERS

We're carrying out a research study to validate an advanced medical imaging technique **quantitative susceptibility mapping (QSM)** using Magnetic Resonance Imaging (MRI) on local clinical MRI scanners of the University Hospital Coventry and Warwickshire (UHCW), to measure **brain iron – a biomarker of ageing and multiple neurodegenerative disorders.**

IF YOU ARE:



WE NEED

healthy volunteers to undergo a single brain MRI scan at UHCW

AND IF YOU

are interested in taking part or have questions or would like more information



PLEASE CONTACT US

Jierong Luo
University of Warwick
Coventry
CV4 7AL
J.Luo.1@warwick.ac.uk



Participant Information Leaflet

Study Title:	Validation of a Quantitative Susceptibility Mapping Sequence to Measure Brain Iron Concentrations
Investigator(s):	Jierong Luo, Joanna Collingwood (University of Warwick); Sarah Wayte, Andrew Weedall, Michael Doikono (University Hospitals Coventry and Warwickshire)

Introduction

You are invited to take part in a research study. Before you decide, you need to understand why the research is being done and what it would involve for you. Please take the time to read the following information carefully. Talk to others about the study if you wish.

Please ask us if there is anything that is not clear or if you would like more information. Take time to decide whether or not you wish to take part.

Who is organising and funding the study?

This study is as part of a PhD project by Miss Jierong Luo (School of Engineering, University of Warwick), and it is not funded by any external body. It is collaborative research trial with University Hospitals Coventry and Warwickshire (UHCW).

What is the study about?

This is a research project that uses a medical imaging technique, magnetic resonance imaging (MRI), to compute the tissue susceptibility and measure iron in the brain. By applying an advanced MRI technique, quantitative susceptibility mapping (QSM), we aim to investigate if QSM can quantitatively measure iron concentration in different brain regions with good reliability and robustness.

As an emerging technique, QSM has been used increasingly in brain imaging in recent years, however, it is not currently undertaken at UHCW. Therefore, this study aims to validate a QSM-applicable sequence on the local scanners in the Hospital. The images will be obtained using a standard MRI scanner and applying a standard pulse sequence optimised to image the tissue susceptibility that is generated by brain iron. Your MRI scan will then be processed and analysed at the University of Warwick, to test and measure iron concentration in the brain.

What would taking part involve?

This study involves imaging your brain by using MRI, which is a safe, non-invasive, and non-ionising medical imaging technique.

If you agree to take part in the study, you will be required to undertake a single MRI scan in the Radiology Department at UHCW. You have been given an MRI information sheet, which should give you more information about the MRI examination; you can also find some useful information about this on the NHS page of MRI: <https://www.nhs.uk/conditions/mri-scan/>.

Before making an MRI appointment

Please look at the MRI Safety screening form, a safety questionnaire that has been given to you with this document. If you will answer 'yes' to questions 1 to 7 on the form, please contact us, and we will discuss with the MRI team at UHCW. *If you have any doubts or questions regarding the MRI safety screening form, please also contact us.*

Making an MRI appointment

If you will answer 'no' to questions 1 or 7 on the MRI safety screening form, or if you have answered 'yes' but the MRI team at UHCW has confirmed it should be safe to proceed with your MRI, then you will be contacted by Miss Jierong Luo and given a short list of when an MRI appointment is available at the site, and you may choose the date and time that are convenient for you. Once your appointment has been made, you will receive a confirmation from us.

Attending the MRI appointment

Note: There are no lifestyle or dietary restrictions for undergoing the MRI scan. You are free to drive to and from the hospital before and after your scan. No changes to regular medications, no blood-taking or injections are required prior to or during this scan.

On the day of your appointment, you should visit the MRI department within the x-ray department of UHCW as arranged to undergo your MRI scan.

At the appointment, you will be asked to complete the MRI safety screening form together with a member of the MR staff before the MR scan, to ensure that having an MRI scan is safe for you. (Please bring the MRI safety screening form you have been given along to your appointment.)

If you pass the safety screening and ready to undergo your scan, then instructions will be provided to help you understand and complete the MRI scan. Your MRI scan will be performed by a trained radiographer, and should take approximately 15 minutes, but may take up to 45 minutes. During scanning, you will be required to lie down on your back and to keep as still as possible during some of this time, and you can communicate with the scan operator at any time if necessary.

After the appointment

The images collected in this study will be reviewed by a radiologist. If we are concerned by the appearance of your images, we will inform your GP.

Your MRI scanimages will be taken to the University of Warwick for processing, analysis and storage.

Do I have to take part?

Participation in this study is completely voluntary.

Before you make the decision of whether to take part in this study or not, a member of the research team will ask a few short questions to ensure that you are eligible for the participation of the study. You should then be talked through the aims of the study; any questions you may have that concerns the study will be answered with honesty. You will then be given at least 3 days to consider if you wish to take part. If so, we will then discuss and go through with you the consent form, which you will initial and sign if you are happy to participate in the study.

You can also choose to withdraw your participation at any time, without giving a reason by contacting one of the research team. Further details about withdrawing from the study are provided later on in this document.

What are the possible benefits of taking part in this study?

As the regional brain iron is a potential biomarker of ageing and multiple neurodegenerative disorders, including Alzheimer's disease, Parkinson's disease, and multiple sclerosis (MS), this study aims to validate the QSM analysis for brain iron quantification, on local clinical MRI scanners (3.0T GE healthcare) of UHCW. If applicable, the MRI technique of QSM will be an essential part of a bigger clinical project that concerns MS pathological alternations and the role of iron in disease development.

What are the possible disadvantages, side effects or risks, of taking part in this study?

With no known hazard, MRI is entirely non-invasive and involves no exposure to hazardous radiation, unlike some other medical imaging technique (e.g. X-ray imaging).

MRI uses strong magnetic fields and radio-frequency pulses, so it can be unsafe for certain individuals, for example those with cardiac pacemakers, cochlear implants or other implanted electronic devices. We are also excluding pregnant participants from this trial, as the possible effects of MRI scans on the baby are not completely known. You will be taken through the MRI safety screening form with an member of the MRI staff at UHCW immediately prior to your examination to ensure that the MRI scan is safe for you.

MRI is comfortable for most people, but those who suffer from claustrophobia (fear of enclosed spaces) might find it uncomfortable to stay in a tube-shaped scanner.

Your participation and data will be kept confidential, but if your MR scan reveals any unsuspected abnormality, we will inform your general practitioner (GP) and your images may be withdrawn from the study.

Expenses and reimbursary

Local transportation charges (e.g. bus fares) and parking charges at UHCW for the study will be reimbursed after your participation.

Will my taking part be kept confidential?

Your participation will be kept confidential. All the data obtained from you as part of this study will be stored securely and handled with care by the research team.

In the study, your participation will be pseudonymous - you will be given a unique study number after signing on the informed consent form, so your identity will be protected from the beginning of the study; after that, all research activities about you will be carried out under the study number. The only file that keeps the link of the code with your identity will be securely stored at the University of Warwick.

Only the research team can access your data in the study; when the study is completed, all data that are collected from you will be fully pseudonymised in the study to be reported and submitted, and you will not be identified in the report directly or indirectly.

What will happen to the data collected about me?

The collection of research data is carried out under a study trial number that is given to you at the beginning of the study, so all research data will be pseudonymised, and will contain no personally-identifiable information of you. Following data will be collected from you:

- 1) Your age and gender
- 2) The MRI scan of your brain

The data will then be processed and analysed, and to be used to generate the tissue susceptibility maps, and to evaluate the brain iron. To validate the QSM-applicable sequence, necessary statistics analysis will be carried out using the data.

Your personal information that is collected on the consent form will be stored separately and securely to the research data, in the University of Warwick, until being destroyed to safeguard your identity.

The MRI safety screening form will be stored securely at UHCW. If no abnormality is seen on your images the form will be destroyed. If an abnormality is seen, the form will be retained for 1 year before being destroyed.

As a publicly-funded organisation, the University of Warwick has to ensure that it is in the public interest when we use personally-identifiable information from people who have agreed to take part in the research. This means that when you agree to take part in a research study, such as this, we will use your data in the ways needed to conduct and analyse the research study.

We will be using information from you in order to undertake this study and will act as the data controller for this study. We are committed to protecting the rights of individuals in line with data protection legislation. The University of Warwick will keep identifiable information about you for 5 years after the study has finished.

Can I withdraw the data that has been collected from me?

After your data has been collected for the study, you can still request to withdraw your data from the study at any time before the data is to be integrated into analysis for reports. *Please note that because of the practical reasons above, we would not be able to withdraw your data from the stage of analysis onwards.*

If you wish to withdraw the data that has already been collected from you, you can write your request to Miss Jierong Luo, whose contact is provided later on in this document. A response to your request will be made by us within 24 hours, and please allow one week for the data withdraw procedure. We will contact you once your data is totally removed from the study.

Data Sharing

Your data will not be shared outside the University for this study. However, as part of the study, we need to acquire your MRI data using the facilities of UHCW, which will be carried out under a study trial number that will be given to you, and the data will be transferred securely to the University of Warwick as soon as possible. After the stage, no research data will be stored in UHCW.

Your rights to access, change or move your information are limited, as we need to manage your information in specific ways in order for the research to be reliable and accurate. The University of Warwick has in place policies and procedures to keep your data safe.

This data may also be used for future research, including impact activities following review and approval by an independent Research Ethics Committee and subject to your consent at the outset of this research project.

For further information, please refer to the University of Warwick Research Privacy Notice which is available here:

*<https://warwick.ac.uk/services/idc/dataprotection/privacynotices/researchprivacynotice>
or by contacting the Information and Data Compliance Team at GDPR@warwick.ac.uk.*

What will happen if I don't want to carry on being part of the study?

Your participation in this study is entirely voluntary, and you are free to withdraw – stop being part of the study at any time without giving a reason, and a decision of the withdrawal would not affect you in any way. If you wish to stop your participation in the study, you can contact us directly or write your request to:

Jierong Luo
School of Engineering
University of Warwick
Coventry
CV4 7AL
Email: J.Luo.1@warwick.ac.uk
Tel: 024 7657 5487

A response to your request will be made by us within 24 hours, and all research activities on you will cease as soon as we receive your request. You will be notified once your request is fulfilled.

Please note withdrawing participation is separate to withdrawing data that has already been collected during the study. If you wish to withdraw your data that has been collected, please refer to a previous section “**Can I withdraw the data that has been collected from me?**” for the procedure and the timeline of withdrawing your data.

What will happen to the results of the study?

As part of a PhD project, the results will be incorporated in the PhD thesis of Miss Jierong Luo, to be submitted in 2021. The results of the study will be presented at scientific events (e.g. conferences, public engagements), and disseminated in journals of relevant research fields. All results will be fully pseudonymised.

Who has reviewed the study?

This study has been reviewed and given a favourable opinion by the University of Warwick's **Biomedical & Scientific Research Ethics Committee (BSREC): Insert your HSSREC/BSREC reference number here (given to you during the course of the review process).**

Who should I contact if I want further information?

If you have any questions about the study or if you would like to have further information, you can contact the person below:

Jierong Luo
School of Engineering
University of Warwick
Coventry
CV4 7AL
Email: J.Luo.1@warwick.ac.uk
Tel: 024 7657 5487

Joanna Collingwood
School of Engineering
University of Warwick
Coventry
CV4 7AL
Email: J.F.Collingwood@warwick.ac.uk
Tel: 024 7652 3152

Who should I contact if I wish to make a complaint?

Any complaint about the way you have been dealt with during the study or any possible harm you might have suffered will be addressed. Please address your complaint to the person below, who is a senior University of Warwick official entirely independent of this study:

Head of Research Governance

Research & Impact Services

University House

University of Warwick

Coventry

CV4 8UW

Email: researchgovernance@warwick.ac.uk

Tel: 024 76 522746

If you wish to raise a complaint on how we have handled your personal data, you can contact our Data Protection Officer, Anjeli Bajaj, Information and Data Director who will investigate the matter: DPO@warwick.ac.uk.

If you are not satisfied with our response or believe we are processing your personal data in a way that is not lawful you can complain to the Information Commissioner's Office (ICO).

Thank you for taking the time to read this Participant Information Leaflet

MRI Information Sheet

Magnetic Resonance Imaging (MRI) is a medical imaging technique used for diagnosing and managing the disease in the hospital. The method can be used to produce anatomical images from within the body. The method is entirely non-invasive and involves no exposure to hazardous radiation (unlike, for example, X-ray imaging).

MRI has no known hazard and comfortable for most people, with only a few exceptions. People who have electrically, magnetically or mechanically activated implants (such as cardiac pacemakers), or those with metal in their body (such as clips on blood vessels in their brain, or other metal fragments) should not have an MRI because the devices may move or not function properly. However, persons with metal dental fillings may have an MRI. MRI is not usually recommended for the pregnant patient, because the long-term effects of the strong magnetic field on the developing baby is unknown. Those who suffer from claustrophobia (fear of enclosed spaces) will probably find an MR study uncomfortable. Before you are enrolled in an MRI study, the investigator will perform a thorough screening to be sure that MRI is safe for you.

The magnetic resonance (MR) scanner is a powerful tube-shaped magnet that uses radio waves to create computerized images of the brain and body. Because the magnet is always on, you will be instructed not to bring any metal objects into the magnet suite, as these objects may become airborne and injure someone. The MR scanner magnet will also erase the magnetic strip on credit cards, so you should leave your wallet outside as well.

To perform a safe and successful MR scan, a radiographer will instruct you before and during the scanning. Because the MRI study involves imaging procedures that are very sensitive to motion, you will be asked to keep as still as possible during the examination. You may expect the MRI examination to be noisy and will be given earplugs to wear. You will be able to talk or listen to the radiographer during the examination. You will be given a button which you can squeeze to alert the radiographer if you want the scanning to stop at any time.

The images collected in this study will be reviewed by a radiologist. If a radiologist is concerned by the appearance of your images, we will inform your GP.



CONSENT FORM

STRICTLY CONFIDENTIAL

Participant Identification Number for this study:

Title of Project: *Validation of a quantitative susceptibility mapping sequence to measure brain iron concentrations*

Name of Researcher(s): *Jierong Luo, Joanna Collingwood (University of Warwick); Sarah Wayte, Andrew Weedall, Michael Doikono (University Hospitals Coventry and Warwickshire, UHCW)*

Name of Participant (print):

Tel:

E-mail:

Please initial all boxes

- 1. I confirm that I have read and understood the information sheet (Participant Information Leaflet) for the above study. I have had the opportunity to consider the information, ask questions and have had these answered satisfactorily.
- 2. I have read and understood the MRI information sheet, and the nature of the examination is clear to me.
- 3. I have given an MRI safety screening form and I have been given an opportunity to discuss any issues arising from it. I understand that it is obligatory for me to complete the MRI safety screening before undergoing any MRI scan.
- 4. I confirm that to my knowledge I have had no brain disorders (e.g. Parkinson's disease, multiple-sclerosis, brain haemorrhage, brain infarct, or brain tumour).
- 5. I understand that data collected during the study will be looked at by the research team from the University of Warwick, and UHCW. I give permission for them to have access to my data.
- 6. I consent to my general practitioner being contacted in the event that the scan reveals any unsuspected abnormality.
- 7. I understand that my participation is voluntary and that I am free to withdraw at any time without giving any reason.
- 8. I am happy for my data to be used in future research.
- 9. I agree to take part in the above study.

Name of Participant

Date

Signature

Name of Person taking consent

Date

Signature

MRI Safety Screening Form
STRICTLY CONFIDENTIAL

Name: _____

GP's Name: _____

Address: _____

GP's Address: _____

Date of Birth: _____

	NO	YES
1. Do you have a heart pacemaker or artificial heart valve or have you had a heart operation? Please give details:		
2. Have you had any operations on your head or spine? Please give details:		
3. Have you had any operations which involved the use of metal implants (e.g. clips, plates, or pins) or do you have ANY implant(s) anywhere in your body? Please give details:		
4. Have you EVER had any metal fragments in your eyes?		
5. Do you have any metal fragments (e.g. bullets or shrapnel) in your body		
6. Do you have a skin patch (e.g. HRT patch)?		

Female participants only	NO	YES
7. Is there a possibility that you might be pregnant?		
8. Do you have an IUD (coil) or sterilisation clips?		

The following questions will help us manage your MR examination:	NO	YES
9. Have you ever had a fit/blackout or suffered from Epilepsy?		

Signature of Participant _____

Date _____

To be completed by MR Staff only

Potential contra-indications _____

accepted for scanning by _____.

Weight: _____ st _____ lb.	_____ kg	Trial Number
----------------------------	----------	--------------

Biomedical and Scientific Research Ethics Committee
Kirby Corner Road
Coventry
CV4 8UW

Thursday, 18 July 2019

Miss Jierong Luo
Engineering
University of Warwick
Coventry
CV4 7AL

Dear Miss Luo,

Ethical Application Reference: BSREC 74/18-19

Title: Validation of a Quantitative Susceptibility Mapping Sequence to Measure Brain Iron Concentrations

Thank you for submitting your ethics application to the Biomedical and Scientific Research Ethics Committee (BSREC) for consideration. We are pleased to advise you that, under the authority delegated to us by the University of Warwick Research Governance and Ethics Committee, **full approval for your project is hereby granted.**

Before conducting your research it is strongly recommended that you complete the on-line Research Integrity training:

www.warwick.ac.uk/ritraining. Support is available from the BSREC Secretary.

In undertaking your study, you are required to comply with the University of Warwick's Research Code of Practice:

https://warwick.ac.uk/services/ris/research_integrity/code_of_practice_and_policies/research_code_of_practice/

You are also required to familiarise yourself with the University of Warwick's Code of Practice for the Investigation of Research Misconduct:

https://warwick.ac.uk/services/ris/research_integrity/research_misconduct/codeofpractice_research_misconduct/

You must ensure that you are compliant with all necessary data protection regulations:

<https://warwick.ac.uk/services/idc>

Please ensure that evidence of all necessary local permissions is provided to BSREC prior to commencing your study.

Please also be aware that BSREC grants **ethical approval** for studies. The seeking and obtaining of all other necessary approvals is the responsibility of the investigator.

Any substantial changes to any aspect of the project will require further review by the Committee and the PI is required to notify the Committee as early as possible should they wish to make any such changes. The BSREC Secretary should be notified of any minor amendments to the study.

May I take this opportunity to wish you the very best of luck with this study.

Yours sincerely

pp.



Dr David Ellard
Chair, Biomedical and Scientific Research Ethics Committee

GafREC Proposal

Title of Project	Validation of a Quantitative Susceptibility Mapping Sequence to Measure Brain Iron Concentrations	
Name of Researcher	Jierong Luo	
Contact details	Email: J.Luo.1@warwick.ac.uk	Telephone: +44 (0) 7414474558
Department	Department of Engineering, University of Warwick	

1. Background

Iron is essential to normal brain function, and the storage of iron in tissue is known to be associated with normal ageing (Hallgren, B., et al. 1958). Furthermore, the disruption of iron metabolism in the central nervous system is found to be related to multiple neurodegenerative disorders, such as Alzheimer's disease, Parkinson's disease, and multiple sclerosis (MS) (Collingwood, J. F., et al. 2014). Therefore, it is important to understand the role of iron in the normal ageing brain, in order to compare with the pathological changes of iron in the brains.

Magnetic resonance imaging (MRI) has proved an iron-sensitive technique to study brain iron in living subjects, because the tissue iron can substantially affect the magnetic properties of the tissue and thereby produce contrast in MRI. Different methods have been developed to quantify the iron concentration by using MRI (Haacke, E. M., et al. 2005, Ghassaban, K., et al. 2019). Emerging in recent years, quantitative susceptibility mapping (QSM) is becoming the most promising, clinically accessible technique to quantitatively measure tissue iron (Deistung, A., et al. 2013; Schweser, F., et al. 2016).

The concentration of iron in the brain has previously been quantified successfully at University Hospitals Coventry and Warwickshire (UHCW) using the transverse relaxation method reported in the literature (Haacke, E. M., et al. 2005). This method of iron quantification takes around twenty minutes and can cover only part of the brain. As QSM has become available in clinical settings, it has the potential to quantify brain iron concentration in the whole brain with an acquisition time below ten minutes, but validation is required on the local MR scanner.

2. Significance of research

To establish and validate an iron-sensitive pulse sequence QSM on the 3.0 T MR scanner at University Hospital, Coventry, which can cover the entire brain in under ten minutes. If successful, the QSM technique will form an essential part of larger clinical projects. For example, a trial into MS pathological alternations and the role of iron in disease development, lead by Dr Tarunya Arun.

3. Aims and objectives

The study aims to set up and validate an MRI pulse sequence that is applicable to QSM on the GE healthcare 3.0 T MR scanner at University Hospital, Coventry (UH), and to develop a protocol of MRI acquisition and post-processing that allows the robust quantification of brain iron concentration *in-vivo* using QSM. In addition, this project also looks at the regional iron distribution and its function with ageing in the living healthy brains by the QSM analysis. The protocols for MRI scans, and the QSM processing and

analysis will be established as a non-invasive, quantitative technique of iron measurement for future studies of neurodegenerations.

4. Methodology

a. Study design

a1. Scan protocol setting up and validation on phantoms

A QSM-applicable sequence will be set up for MRI acquisition on the 3.0 T MR scanner, using parameters that are comparable to recently reported brain iron studies (Schweser, F., et al. 2016). Images of the phantom will then be reconstructed, processed and analysed at the University of Warwick. At this stage, optimised parameters will be applied on MR phantoms to achieve the best clinically feasible image quality, which will be assessed until MRI data is suitable for QSM. We aim to control the total scan time of the QSM sequence to be under 10 minutes.

The susceptibility will be measured on a series of MR phantoms with a range of physiologically-relevant iron level for human brains. Then, the iron concentrations will be correlated with the measured susceptibilities. Repeated measurements will be conducted to assess the reproducibility and uncertainty.

a2. MRI validation of QSM in participants

MRI of up to twenty healthy participants will be performed, followed by QSM analysis and measurement, to validate the reported correlation between iron and the tissue susceptibilities quantified by QSM.

The resulting images will be used to study the brain iron concentration of scanned participants using the QSM reconstruction, and the generated quantitative susceptibility maps will be measured, then the results will be compared with those from previously reported studies. The quantitative relation of brain iron concentration and the measurement of tissue susceptibility will be validated by correlating the susceptibility measurements to the regional brain iron concentration that is estimated by its function of participants' age, as described in the literature (Hallgren, B., et al. 1958).

b. Study population

We aim to recruit and enrol up to 20 healthy adult participants for the study, with age up to 80 years old, and approximately uniformly distributed within the age range between 20 and 80 years.

c. Eligibility

- Staff or students at the University of Warwick
- Aged between 20 and 80 years
- Do not have a known neurological disorder (including Parkinson's disease, multiple-sclerosis, a brain haemorrhage, a brain infarct, or a brain tumour)
- Not pregnant
- Answer 'no' to questions 1 to 7 of the MRI safety screening form (attached and in BSREC approved documentation, reference: BSREC 74/18-19)

d. Outcome Measures

From the phantom measurements, physiologically relevant iron concentrations will be correlated with measured susceptibilities, and the reproducibility and uncertainty of the QSM technique will be established.

From the scanning of the healthy volunteers, the establishment of a MR sequence with adequate resolution and signal to noise, which can scan the whole brain in under ten minutes. In addition, a quantitative relationship between susceptibility measurements and regional brain iron concentration which follow the relationship with the participants' age describe by Hallgren et al.

5. Consent

The participant information leaflet, MRI information sheet and MRI safety screening form (reference: BSREC 74/18-19) will be given to potential participants by Miss Jierong Luo, to understand the nature of the study and their participation. Potential participants will have the opportunity to ask questions and discuss the study, and will be given at least three days to consider if they wish to take part. Informed consent will be obtained by Miss Jierong Luo, via the consent form, before a participant can take part in the study. The protocol for obtaining informed consent is detailed in Section 7 of the BSREC application for this study (reference: BSREC 74/18-19).

6. Duration

We aim to start the project in July 2019 and the anticipated completion date is June 2021. We would hope to start scanning the first participants towards the end of August 2019, and would aim to have completed the participant scanning by January 2020.

7. Analysis/Statistics

All data analysis will be carried out at the University of Warwick. Full details are provided in the BSREC application form, Section 5.4b (reference: BSREC 74/18-19).

8. Publication/Dissemination

This project will be incorporated in the PhD thesis of Miss Jierong Luo, to be submitted in 2021. The results of the study will be presented at scientific events (e.g. conferences, public engagement), and disseminated in journals of relevant research fields, such as MRI, neuroimaging, radiology, and brain iron research.

Research & Development Department
University Hospitals Coventry & Warwickshire NHS Trust
4th Floor Rotunda, ADA40014
University Hospital
Clifford Bridge Road
Coventry
CV2 2DX

Commercial enquiries: 02476 964995
Governance/Non-commercial enquiries: 02476 966195
Research Funding & Grant enquires: 02476 964958
Email: R&DSponsorship@uhcw.nhs.uk

30 October 2019

Miss Jierong Luo
Engineering
University of Warwick
Coventry
CV4 7AL

Dear Jierong,

Project Title: Validation of a Quantitative Susceptibility Mapping Sequence to Measure Brain Iron Concentrations

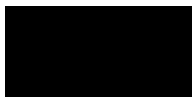
R&D Ref: GF0360

Thank you for sending in the required documents and completing the GafREC form for the above study. Having reviewed the details of your proposed project, research limited to the use of or access to NHS premises and facilities is excluded from NHS Research Ethics Committee (REC) review therefore; I can confirm that we are happy for you to carry out this project within UHCW NHS Trust.

Please be aware that should you wish to change the project in anyway, you must notify our office using the above reference.

I have logged your study on behalf of the Trust, which means you can proceed. I wish you every success with your project.

Yours Sincerely,



Jasmeet Bhambra
R&D Clinical Trials Officer.

Research & Development Department
University Hospitals Coventry & Warwickshire NHS Trust
4th Floor Rotunda, ADA40014
University Hospital
Clifford Bridge Road
Coventry
CV2 2DX

Commercial enquiries: 02476 964995
Governance/Non-commercial enquiries: 02476 966195
Research Funding & Grant enquires: 02476 964958
Email: R&DSponsorship@uhcw.nhs.uk

30 October 2019

Miss Jierong Luo
Engineering
University of Warwick
Coventry
CV4 7AL

Dear Jierong,

Project Title: Validation of a Quantitative Susceptibility Mapping Sequence to Measure Brain Iron Concentrations

R&D Ref: GF0360

Thank you for sending in the required documents and completing the GafREC form for the above study. Having reviewed the details of your proposed project, research involving previously collected, non-identifiable information including research undertaken by staff within a care team using previously collected information during the course of care of their own patients or clients, are excluded from NHS Research Ethics Committee (REC) review therefore; I can confirm that we are happy for you to carry out this project within UHCW NHS Trust.

Please be aware that should you wish to change the project in anyway, you must notify our office using the above reference.

I have logged your study on behalf of the Trust, which means you can proceed. I wish you every success with your project.

Yours Sincerely,



Jasmeet Bhambra
R&D Clinical Trials Officer.

Volunteer Information – COVID 19 Adjustments

We are constantly monitoring what is happening with the coronavirus pandemic and all planned imaging is subject to developments.

For the safety of everyone, please **do not attend your MR appointment** or come to the hospital if:

- you think you might have coronavirus or are showing any COVID related symptoms
- or you've been in close contact with someone with coronavirus

In these instances, please Call 111 to speak to someone about coronavirus and please **inform Jierong Lou**.

Please let us know if you have any health conditions (including diabetes, COPD, asthma or a BMI over 35) which put you at higher risk of contracting COVID-19 as we will be unable to include you in the trial at the moment.

On attending your Radiology MRI appointment

We want to reassure you that our hospitals are safe environments and we are working hard to protect the patients in our care, our visitors, **our volunteers** and our staff. We are making changes to our hospitals and the way that we work to minimise the risk of spreading any infection. Please note that:

Our hospital sites may look a little different than before. These changes include notices asking you to follow social distancing measures whilst on site, washing your hands regularly and using the available hand sanitisers. The way we ask patients, volunteers, visitors and staff to move around the site has also changed including one-way systems and possible changes to entrances and exits and we ask that you follow this clearly marked advice. We also ask that when you are in any hospital building you wear a mask and if you are not able to bring one, these can be provided.

- To help us adhere to social distancing measures, please do not come into the department more than 10 minutes before your scheduled appointment
- We would also encourage you to leave the site as soon as you can following your appointment
- If you travel to the site by car and arrive early, we ask that you wait in your car until the appropriate time to make your way into the outpatient area
- Where possible, please come to the appointment alone. If you need to be accompanied, we ask that this is kept to one person and should be someone from your household or social bubble.

You can find more information and latest updates on our website, www.uhcw.nhs.uk. Thank you for your continued support that will help us better protect staff, volunteers, visitors and patients from infection.

